

**CHEMICAL EVOLUTION FROM DIFFUSE CLOUDS TO DENSE CORES**

LÁSZLÓ SZŰCS

Molecular tracers of physical conditions  
in molecular cloud simulations

Referees:

PD. Dr. Simon Glover  
Prof. Dr. Thomas Henning

November 2014



DISSERTATION

submitted to the  
Combined Faculty of Natural Sciences and Mathematics  
of the Ruperto-Carola-University of Heidelberg, Germany  
for the degree of

DOCTOR OF NATURAL SCIENCES

Put forward by

László Szűcs

born in: Szentes, Hungary

Oral examination: 22 January 2015



Én fölnéztem az est alól  
az egek fogaskerekére -  
csilló véletlen szálaiból  
törvényt szőtt a mult szövőszéke  
és megint fölnéztem az égre  
álmaim gőzei alól  
s láttam, a törvény szövedéke  
mindíg fölfeslik valahol.

Attila József, *Eszmélet*



## ABSTRACT

Star formation is linked to molecular gas, which predominantly resides in giant molecular clouds within the galaxy. The chemical composition of these clouds and the newborn stellar population within them are in an intricate relation. On one hand, the star formation rate and the mass function of the resulting stars are sensitive to the gas temperature, which is affected by molecular heating and cooling processes. On the other hand, the ionizing and photodissociative radiation from the young stars may initiate the formation of more complex molecules through ion-molecular reactions, or it may very efficiently destroy them. Furthermore, the molecular clouds are not just the birth environments of stars and stellar systems but also provide the raw material for their formation. Precursors of the large chemical diversity that we experience in our Solar System have been found in numerous molecular clouds and dense cores, heated by new-born protostars. The molecular emission also provides us with an insight into the physical conditions of the star forming material, and traces the velocity, (column) density, temperature and the dynamical history of the gas.

Therefore, understanding the main chemical pathways for formation and destruction of molecular coolants, determining the chemical initial conditions of high- and low-mass star formation, finding species that preserve the dynamic history of the gas and calibrating the chemical tracers of cloud properties are amongst the major interests of today's astrophysics and astrochemistry. New observatories, like ALMA (Atacama Large Millimeter/submillimeter Array) and NOEMA (Northern Extended Millimeter Array) will provide previously unseen sensitivity, resolution and amount of data to address these issues. The new complexity of observational data requires, however, increasingly complex, multi-dimensional and time dependent theoretical models to explain and predict them. Fortunately, parallel to the advancement of observational facilities, the theoretical understanding of the relevant physical and chemical processes, as well as the numerical methods and computational resources developed swiftly, allowing us to model a variety of processes (magneto-hydrodynamics, chemistry, radiation propagation) self-consistently within a single simulation.

In this thesis I present three-dimensional, turbulence-supported hydrodynamical simulations of Giant Molecular Clouds and dense cores, linked with implicit or explicit chemical models, and describe synthetic molecular emission maps to be compared with observations. First, I investigate how the active chemical fractionation and isotope-selective photodissociation affects the  $^{12}\text{CO}/^{13}\text{CO}$  isotope ratio and implicitly the  $^{13}\text{CO}$  emission based CO column density estimates. Then I benchmark the most frequently used CO emission based molecular mass measurement techniques for a large range of cloud properties. Finally, I present a new approach for modelling the formation and destruction of complex molecules, many of which form exclusively on grain surfaces, in three-dimensional, time dependent hydrodynamical simulations, that was previously only possible with major simplifications either dynamics-wise or chemistry-wise.



## ZUSAMMENFASSUNG

Sternentstehung ist eng verbunden mit molekularem Gas, welches vorwiegend in riesigen Molekülwolken der Galaxien vorkommt. Die chemische Zusammensetzung dieser Wolken und die neu entstandene Sternpopulation stehen in einem komplexem Zusammenhang. Einerseits hängen die Sternentstehungsrate und Massenfunktion der entstandenen Sterne von der Gastemperatur ab, die von molekularen Heiz- und Kühlprozessen beeinflusst wird. Andererseits kann die ionisierende und photodissoziative Strahlung der jungen Sterne die Entstehung von komplexen Molekülen durch Ionen-Molekül-Reaktionen anstoßen oder aber diese auch sehr effizient zerstören. Darüber hinaus sind Molekülwolken nicht nur die Geburtsstätten von Sternen und Sternsystemen, sondern sie stellen auch das Rohmaterial für deren Entstehung zur Verfügung. Vorläufer der großen chemischen Vielfalt, die wir in unserem Sonnensystem finden, wurden in zahlreichen Molekülwolken und dichten Molekülwolkenkernen gefunden, geheizt durch einen neu entstandenen Protostern. Die molekulare Emission erlaubt auch Einblicke in die physikalischen Bedingungen im sternbildenden Material und zeigt Geschwindigkeiten, dichten, Temperaturen und Folgen der dynamische Vergangenheit des Gases auf.

Aufgrund dessen gehört das Verständnis der chemischen Hauptentwicklungswege für Entstehung und Zerstörung von kühlenden Molekülen, die Bestimmung der chemischen Anfangsbedingungen der Entstehung von massereichen wie massearmen Sternen, die Suche nach Verbindungen, welche die dynamische Vergangenheit des Gases erhalten und die Kalibration chemischer Markerverbindungen zu den wichtigen Interessensgebieten der heutigen Astrophysik und Astrochemie. Neue Observatorien wie ALMA und NOEMA werden bisher unerreichte Empfindlichkeit, Auflösung und Datenumfang erreichen, mit denen diese Fragen angegangen werden können. Die neue Komplexität der Beobachtungsdaten verlangt zur Erklärung und Vorhersage jedoch auch zunehmend komplexe, mehrdimensionale und zeitabhängige theoretische Modelle. Glücklicherweise hat sich, parallel zu den Fortschritten bei der Beobachtung, auch das theoretische Verständnis der relevanten physikalischen und chemischen Prozesse ebenso wie die numerischen Methoden und Rechenkapazitäten rasch weiterentwickelt und erlaubt nun die Modellierung zahlreicher Prozesse (Magnetohydrodynamik, Chemie, Strahlungsausbreitung) innerhalb einer einzigen Simulation in selbst-konsistenter Weise.

In dieser Arbeit werden dreidimensionale, turbulenzgestützte hydrodynamische Simulationen von Riesenmolekülwolken und dichten Molekülwolkenkernen vorgestellt, verbunden mit impliziten oder expliziten chemischen Modellen, ebenso wie synthetische Emissionskarten zum Vergleich mit Beobachtungen. Zuerst wird untersucht, wie die aktive chemische Fraktionierung und isotop-selektive Photodissoziation das  $^{12}\text{CO}/^{13}\text{CO}$  Isotopenverhältnis beeinflusst und damit implizit auch die  $^{13}\text{CO}$ -basierten Schätzungen der CO-Säulendichten. Danach werden die am häufigsten verwendeten CO-Emissions-basierten Techniken zur Bestimmung der molekularen Massen für einen weiten Bereich von Wolkeneigenschaften auf den Prüfstand gestellt. Schließlich wird ein neuer Ansatz für dreidimensionale, zeitabhängige hydrodynamische Simulationen vorgestellt, wie die Bildung und Zerstörung von komplexen Molekülen modelliert werden kann, von denen sich viele ausschließlich auf Staubkornoberflächen bilden - etwas, das bisher nur mit großen Vereinfachungen entweder für die Dynamik oder Chemie möglich war.



## PUBLICATIONS AND AUTHORSHIP

The results presented in this thesis have previously appeared or will appear in the following publications:

*Szűcs, Glover & Klessen, MNRAS (2014), vol 445, 4055*

*Szűcs, Glover & Klessen, in prep.*

*Szűcs, Glover, Semenov & Klessen, in prep.*

The details of authorship, each chapter listed individually:

Chapter 1: I wrote all the text and made all figures, except Fig. 1.2 and Fig. 1.5, which were reproduced with the permission of the original authors.

Chapter 2: I wrote all the text and prepared all figures. I set up the simulations, run them and analysed the resulting data. The chemical network presented in the chapter was developed and implemented in the hydrodynamic simulation by S. Glover.

Chapter 3: I wrote all the text and prepared all figures. I performed all simulations and analysed the resulting data.

Chapter 4: I wrote all the text and prepared all figures. The `ALCHEMIC` chemical modelling code was written by D. Semenov. We partially modified it together to be compatible with the output of the hydrodynamic simulations, while the treatment of the time-dependent physical conditions was implemented by me. I have run all the simulations and the tests.



# CONTENTS

<b>1</b>	<b>Introduction</b>	<b>1</b>
1.1	Molecular cloud evolution and star formation	1
1.2	The ISM as self-gravitating fluid	4
1.2.1	Equations of hydrodynamics in the Lagrangian scheme	5
1.2.2	Smoothed Particle Hydrodynamics (SPH)	6
1.2.3	Gravitational potential	8
1.2.4	Cooling and heating	10
1.3	Chemistry at the dawn of star formation	12
1.3.1	Chemical processes in the ISM	12
1.3.2	Carbon chemistry	15
1.3.3	Oxygen chemistry	17
1.3.4	Nitrogen chemistry	17
1.3.5	Chemistry on grain surfaces	18
1.3.6	Chemical models	19
1.3.6.1	The NL99 network	21
1.3.6.2	The osu_03_2008 based network	22
1.4	Shielding and the attenuation of the interstellar radiation	22
1.5	The journey of light – from molecules to the observer	24
1.5.1	The formal radiative transfer equation	25
1.5.2	The TreeCol algorithm	26
1.5.3	Line radiative transfer in LTE	29
1.5.4	The Sobolev approximation	31
1.6	The aims of this thesis	32
<b>2</b>	<b>The <math>^{12}\text{CO}/^{13}\text{CO}</math> ratio</b>	<b>33</b>
2.1	Introduction	33
2.2	Simulations	37
2.2.1	Chemistry	38
2.2.2	Attenuation of the ISRF	39
2.2.3	Thermal model	39
2.2.4	Initial conditions	40
2.3	The $^{12}\text{CO}/^{13}\text{CO}$ column density ratio	41
2.3.1	Correlation with the total column density	44
2.3.2	Correlation with the $^{12}\text{CO}$ column density	46
2.3.3	Fitting formula	48
2.3.4	Application for $^{13}\text{CO}$ observations	51
2.4	The $^{13}\text{CO}$ line emission	52
2.4.1	Line profiles	54
2.4.2	Emission maps	57
2.5	Comparison to previous works	60
2.6	Summary	63

<b>3</b>	<b>Molecular cloud mass measurement methods</b>	<b>65</b>
3.1	Introduction . . . . .	65
3.2	Simulations . . . . .	68
3.3	CO isotope emission maps . . . . .	69
3.4	Methods for cloud mass estimation . . . . .	73
3.4.1	Column density determination . . . . .	73
3.4.2	Virial mass . . . . .	76
3.4.3	The CO-to-H <sub>2</sub> conversion factor . . . . .	77
3.5	Results . . . . .	80
3.6	Discussion . . . . .	83
3.6.1	Inferring H <sub>2</sub> column density from CO isotope emission . . . . .	84
3.6.2	Why does the virial mass estimate work? . . . . .	86
3.6.3	The CO-to-H <sub>2</sub> factor at low visual extinctions and on small scales . . . . .	88
3.7	Summary . . . . .	93
<b>4</b>	<b>Chemistry as post-processing</b>	<b>95</b>
4.1	Introduction . . . . .	95
4.2	A recipe for post-processing . . . . .	97
4.2.1	Hydrodynamic simulation . . . . .	98
4.2.2	Chemical networks . . . . .	99
4.2.3	Solving the chemical network . . . . .	99
4.2.4	Initial abundances . . . . .	101
4.3	A prestellar dense core . . . . .	102
4.4	Preliminary results . . . . .	105
4.4.1	Carbon chemistry . . . . .	105
4.4.2	High density tracers and organic molecules . . . . .	107
4.5	Summary and further plans . . . . .	110
<b>5</b>	<b>Summary</b>	<b>113</b>
<b>A</b>	<b>The reaction rates of the NL99 chemical network</b>	<b>115</b>
<b>B</b>	<b>On the gridding of smoothed particle hydrodynamic simulations</b>	<b>117</b>
B.1	Interpolation to a regular grid . . . . .	117
B.2	Grid resolution test . . . . .	117
<b>C</b>	<b>The effect of the initial chemical composition</b>	<b>121</b>
<b>D</b>	<b>Dendrograms</b>	<b>123</b>
	<b>Bibliography</b>	<b>125</b>

# 1 INTRODUCTION

## 1.1 MOLECULAR CLOUD EVOLUTION AND STAR FORMATION

A growing amount of observational (e.g. Kennicutt, 1989; Bigiel et al., 2008; Evans et al., 2009) and theoretical (e.g. Krumholz et al., 2011; Glover and Clark, 2012b) evidence suggests that current-day star formation is accompanied by molecular gas on every size scale, from galactic scales to parsec-sized star forming-regions. However, the exact link between molecular gas and star formation is not entirely clear. It is likely that both the gravitational collapse, which eventually produces stars, and the conversion from atomic to molecular composition take place at a similar column density or surface density threshold, at  $N_{\text{H}} \approx 1.5 \times 10^{21} \text{ cm}^{-2}$  and  $\Sigma \approx 10 M_{\odot} \text{ pc}^{-2}$ , respectively (Hartmann et al., 2001), where  $N_{\text{H}}$  is the hydrogen nuclei column density and  $\Sigma$  is the mass surface density. Nevertheless, the strong connection and the mutual feedback and regulation is evident. Therefore, to understand how and why stars and stellar systems form, we need to understand the physical and chemical state and evolution of their birth environment, the molecular gas, which also provides their building blocks.

The molecular gas in our Galaxy and others like it is predominantly organized in giant molecular clouds, with total cloud masses ranging from a few  $10^4 M_{\odot}$  to  $10^7 M_{\odot}$  (e.g. Blitz et al., 2007). About 80 per cent of the total molecular mass reservoir resides in clouds more massive than  $10^5 M_{\odot}$ . The estimated typical lifetime of a GMC is on the order of a few 10 Myrs (e.g. Kawamura et al., 2009; Miura et al., 2012), and they are supported against collapse by turbulent motions rooted in their formation mechanism and by magnetic fields, which are thought to be an important, but not dominant source of support (Bourke et al., 2001; Mac Low and Klessen, 2004; Troland and Crutcher, 2008). The gravity and the support is in many cases close to equilibrium, thus explaining the fact that the lifetime is long when compared to the free-fall time. Small scale density enhancements, such as cores or filaments, might however, become gravitationally unstable in shorter time scales and form stars within a few Myr. The cloud is then dispersed on 10 - 20 Myr time scales due to the radiation and kinetic feedback from the young stellar population within (e.g. Dale et al., 2012; Colín et al., 2013). A slightly more detailed picture of low-mass star formation, from the origin of the GMC is illustrated in Fig. 1.1 (based on van Dishoeck and Blake, 1998):

The formation of molecular clouds (panel a) on 10-100 parsec scales is likely to be the result of instabilities in the cold neutral medium (CNM; Dickey and Lockman, 1990), which is characterized by number densities  $30 - 100 \text{ cm}^{-3}$ , temperatures  $< 300 \text{ K}$  and neutral atomic hydrogen composition (Wolfire et al., 1993, e.g.) and it is supported by large scale magnetic fields (e.g. Vázquez-Semadeni, 2010). The instabilities might be seeded by feedback from earlier stellar populations in forms of stellar winds, jets and super nova explosions. These mechanisms then drive convergent flows in which certain regions reach high enough densities and masses that the mass-to-magnetic flux ratio becomes supercritical (also around  $N_{\text{H}} \approx 1.5 \times$

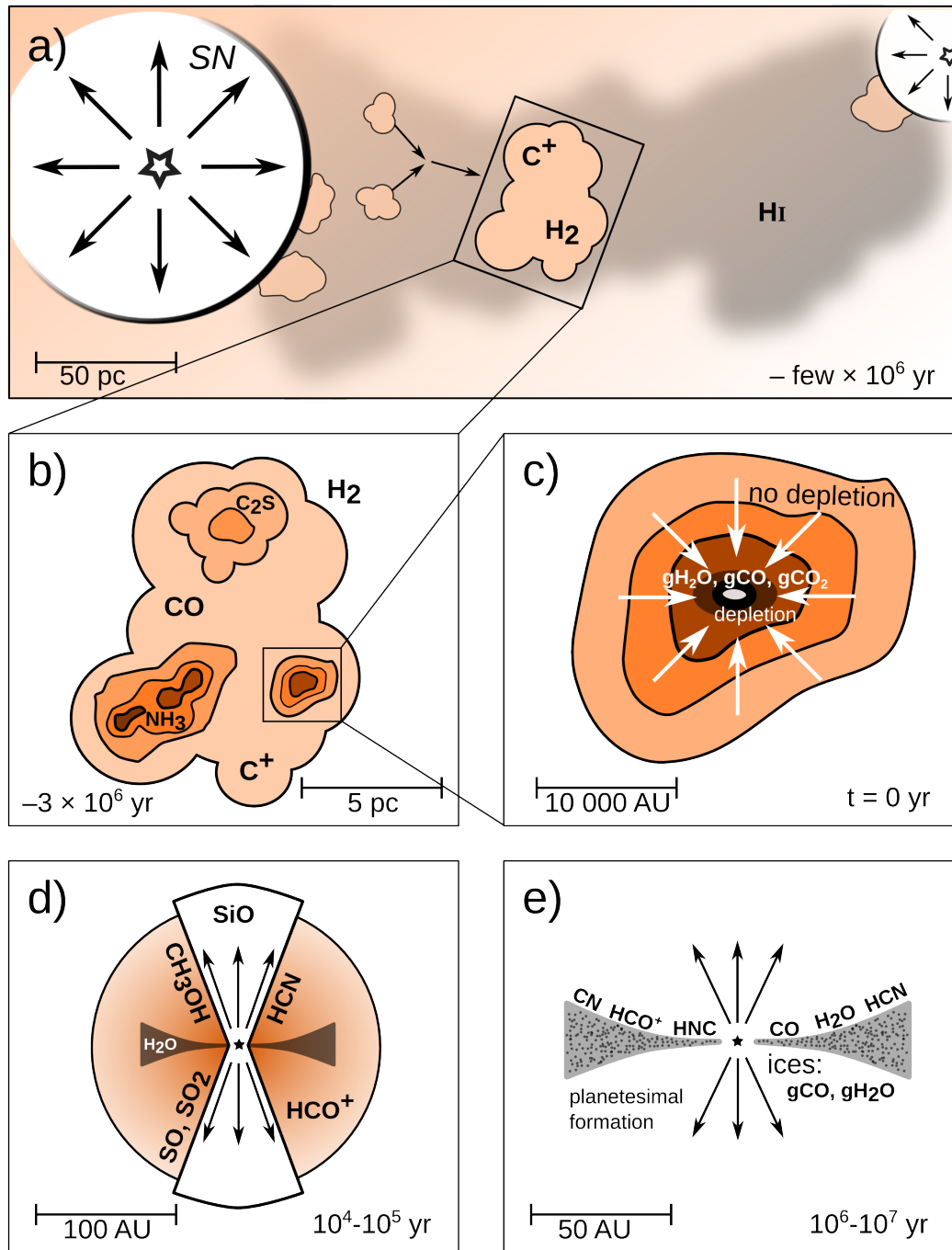


Figure 1.1: The evolution of the interstellar matter and chemistry, from diffuse HI clouds to a planet forming protoplanetary disk around a low-mass star. (a) MCs might form in localized convergent flows induced by stellar feedback, as well as a result of cloud collisions in dynamic environments, e.g. the galactic spiral arms (Dobbs et al., 2013). (b) Dense cores form in the molecule-dominated cloud, which is supported by turbulence and magnetic fields. (c) on small scales the support is overcome by gravity, the collapse begins. The gas-phase tracer molecules freeze-out onto dust grains. (d) The young, embedded protostar accretes with a high rate, while it also powers molecular winds and/or protostellar jets. (e) The mass outflow and the radiation clears out the envelope leaving a T Tauri star and its planet forming disk behind. A planetary system forms on a time scale of few Myr. Based on van Dishoeck and Blake (1998).

$10^{21} \text{ cm}^{-2}$ ) and the magnetic field can no longer prevent the collapse (Hennebelle and Pérault, 2000; Vázquez-Semadeni, 2010). In addition, as the density rises, molecules, such as  $\text{H}_2$  and  $\text{CO}$ , start to form (Bergin et al., 2004; Clark et al., 2012b). Besides these molecules, the ionized carbon ( $\text{C}^+$ ) and the atomic oxygen ( $\text{O}$ ) are also abundant and govern the gas temperature due to their efficient fine-structure line emission. The rising gas density initiates thermal instabilities, which in turn aid the mass and density enhancement. The cloud support by then is taken over by the turbulence inherited from the convergent flows and the contraction continues in a quasi static state, close to virial equilibrium. This formation mechanism may produce molecular clouds up until about  $10^4 M_\odot$ . This mechanism naturally explains the observed morphologies (e.g. shells at a variety of scales in the Orion-Monoceros molecular cloud complex, Dobbs et al., 2013) and the small age spread of molecular clouds in the direct vicinity of the Solar System (Hartmann et al., 2012).

The larger GMCs are likely form via the accumulation of these small clouds in spiral arms, where the collisional time scales are noticeably reduced. This can also explain the observed quasi-periodic spacing between molecular cloud complexes in spiral arms. Small clouds also show more uniform galactic distribution, while the large GMCs tend to cluster around spiral arms (Koda et al., 2009). Other possible formation processes include gravitational instability, magneto-Jeans instability, Parker instability, etc. For a complete review we refer to Dobbs et al. (2013).

Once the typical GMC conditions are reached (panel b) the average number density,  $\langle n \rangle$ , is around a few hundred particles per  $\text{cm}^3$ , while the temperature is typically below 30 K. The chemical composition is dominated by  $\text{H}_2$  and  $\text{C}^+$  at the cloud edge, and  $\text{H}_2$  and  $\text{CO}$  deeper in. Molecular clouds exhibit a large amount of substructure in the forms of parsec scale filament and clumps ( $n \approx 10^3 \text{ cm}^{-3}$ ) and sub-parsec scale cores ( $n \gtrsim 10^4 \text{ cm}^{-3}$ ). In these dense regions additional chemical tracers, such as  $\text{NH}_3$  and  $\text{C}_2\text{S}$  start to appear. During this evolutionary stage, the cloud is supported by turbulence, and it is quasi static on large scales. On small, clumps and cores scales the cloud may collapse hierarchically to form – typically low mass – stars.

As the turbulent support is overcome in the few  $M_\odot$  mass cores, the collapse begins (panel c). The density reaches  $10^5 - 10^6 \text{ cm}^{-3}$  and the temperature remains initially low at around 15-20 K. The dust particles take over the cooling role from the molecules and the previously dominant gas-phase molecules, such as  $\text{CO}$ , freeze out onto the grains. This enhances previously suppressed species, e.g.  $\text{N}_2\text{H}^+$ . As magnetic support of the cloud and the non-ideal magneto-hydrodynamic effects (e.g. ambipolar diffusion) become more important, the chemistry, by regulating the ionization fraction of the cloud still remains important for the dynamics. The collapse progresses at close to the free-fall rate (e.g. Hartquist et al., 1993).

The young, embedded protostar accretes with a high rate ( $\dot{M} \approx 10^{-6} M_\odot \text{ yr}^{-1}$ ; Dullemond et al., 2007), while it also powers molecular winds and/or jets (panel d). As the envelope heats up, the previously frozen-out species return to the gas phase, initiating a rich chemical diversity. The outflows remove the excess angular momentum of matter, thus sustaining the high accretion rate. The shocks in the outflows splutter grains, and thus increasing the  $\text{SiO}$  abundance, and may dissociate molecules. The lifetime of this stage is  $10^4 - 10^5 \text{ yr}$ .

The mass outflow and the radiation clears out the envelope and leaving a T Tauri star and its planet-forming residual disk behind. The chemistry remains

important for regulating the ionization state inside the disk, thus affecting the angular momentum transport through the magnetorotational instability (e.g. [Gammie, 1996](#); [Armitage, 2010](#)). The chemistry close to the surface of the disk resembles the  $C^+ - CO$  chemistry of photon dominated regions at the GMC cloud edges, while deeper in the disk, molecules like CO and  $H_2O$  freeze out onto dust grains again. The chemical composition of the disk may inherit some properties from the earlier stages of star formation. For instance, [Cleeves et al. \(2014\)](#) finds hints for that the disk ionization conditions might not be suitable for producing the deuterium-to-hydrogen ratio observed in water and ices within the Solar System, thus their origin predates the formation of the Sun. A developed planetary system forms and the protoplanetary disk dissipates on a few Myr time scale.

In this thesis, we focus on the intermediate stages of the molecular cloud evolution (stages b and c in [Fig. 1.1](#)), when turbulent motions, molecular and dust heating and cooling and self-gravity govern the cloud state. The cloud is already dominated by molecular gas, but the first generation of stars have not been born yet. In this evolutionary stage we may study the large scale distribution of mass, turbulence and molecules, and at the same time, we may obtain an insight into the physical and chemical state of prestellar and dense cores.

## 1.2 THE ISM AS SELF-GRAVITATING FLUID

The interstellar matter is very dilute even at its peak density compared to gases and fluids on Earth. In molecular clouds, for example, the number density,  $n$ , ranges from a few hundred to  $\sim 10^7 \text{ cm}^{-3}$  (e.g. [Shu et al., 1987](#)), while the number densities of air and water are 10 to 12 orders of magnitude higher (i.e.  $n_{\text{air}} \approx 2.5 \times 10^{19} \text{ cm}^{-3}$  and  $n_{\text{water}} \approx 3.3 \times 10^{21} \text{ cm}^{-3}$  at 1 atm pressure and 300 K temperature). Another noteworthy difference is that fluids in terrestrial conditions are usually neutral, while the interstellar matter remains partly ionized even in the depths of GMCs. In additions, flows in earthbound laboratories are often generated by obstructions of solid bodies, while fluid motions in the ISM are typically due to gravitational forces, interactions with radiation fields or violent events, such as explosions or implosions. These differences might prompt the question of whether and when can we use hydrodynamics, a theory historically developed to describe fluid motions in Earth-like conditions, to model the dynamics of the interstellar matter ([Shu, 1991](#)).

The fluid approximation is appropriate to describe an assembly of particles if their mean free path,  $\ell$  is much smaller than  $L$ , the characteristic macroscopic length scale of the problem. For neutral atoms  $\ell$  can be given as

$$\ell = (n\sigma)^{-1}, \quad (1.1)$$

where  $\sigma$  is the elastic collisional cross section. The collisional cross section for  $H_2$  molecules is on the order of  $10^{-16} \text{ cm}^2$  ([Srivastava et al., 1975](#)). Assuming that the mean number density in a GMC is on the order of a  $100 \text{ cm}^{-3}$ , we get a mean free path on the order of  $10^{14} \text{ cm}$ . This is indeed much smaller than the relevant GMC scales on the order of  $10^{18} \text{ cm}$ , thus the fluid approximation holds.

According observations ([Williams et al., 1998](#)) and theoretical considerations ([Shu et al., 1987](#)), electric charge carriers are at least 5-7 orders of magnitude under-abundant compared to the neutral  $H_2$  molecule. Even so, the small quantities of

charge carriers are sufficient to efficiently couple the gas to the interstellar magnetic field, and thus affect the gas motions. These effects can be taken into account in the framework of magnetohydrodynamics (MHD). In the present thesis we ignore MHD effects. This may result in an overestimated turbulent cloud support, but the effect should be less than a factor of 2 (Crutcher, 1999).

In the following sections we will also show that additional physical processes, such as gravity or cooling, can be easily introduced to the hydrodynamic equations to provide a better description of the interstellar gas.

The remainder of this section introduces the basic equations of fluid dynamics and describes the Smoothed Particle Hydrodynamics (SPH) method, utilized throughout the thesis, to solve them.

### 1.2.1 EQUATIONS OF HYDRODYNAMICS IN THE LAGRANGIAN SCHEME

In the Lagrangian formalism the fluid dynamics is described from the perspective of a fluid element travelling along a flow line. In this scheme, we introduce the comoving derivative as  $d/dt \equiv \partial_t + \vec{v} \cdot \nabla$ , where  $\vec{v}$  is the fluid element velocity vector and  $\nabla = \left( \frac{\partial}{\partial x}, \frac{\partial}{\partial y}, \frac{\partial}{\partial z} \right)$  in Cartesian coordinates. Using this definition, the continuity equation takes the following form (Monaghan, 1992):

$$\frac{d\rho}{dt} + \rho \nabla \cdot \vec{v} = 0 \quad (1.2)$$

In the physical sense this means that the density of the gas parcel changes when the gas flows are converging or diverging. The continuity equation is an expression of mass conservation. The momentum conservation equation in its Lagrangian form expresses the fact that the pressure gradient acts as a force on the parcel, accelerating it:

$$\frac{d\vec{v}}{dt} - \frac{\nabla P}{\rho} = 0 \quad (1.3)$$

The momentum equation can also be interpreted as the equation of motion for the gas parcel. In its generalized form additional forces acting on the parcel, such as gravity and viscous dissipation (a force proportional to velocity squared), can be added to this equation:

$$\frac{d\vec{v}}{dt} - \frac{\nabla P}{\rho} - \frac{\nabla \Phi}{\rho} - \frac{\nabla \Psi}{\rho} = 0, \quad (1.4)$$

where  $\Phi$  is the gravitational potential and  $\nabla \Psi$  represents the viscosity. For a continuous density distribution,  $\Phi$  is given by the Poisson equation:

$$\nabla^2 \Phi = 4\pi \mathcal{G} \rho, \quad (1.5)$$

where  $\mathcal{G}$  is the gravitational constant. The internal energy change of the parcel is given by the energy equation, which expresses the conservation of energy:

$$\frac{du}{dt} = -\frac{p \nabla \cdot \vec{v}}{\rho} - \Lambda, \quad (1.6)$$

where  $u$  is the internal specific energy and  $\Lambda$  denotes net rate at which the gas gains ( $\Lambda < 0$ ) or loses ( $\Lambda > 0$ ) internal energy due to radiative and chemical heating

and cooling.  $\Lambda$  depends on the attenuation of the incident radiation as well as on the chemical state of the gas. We give a detailed description of these processes in section 1.3.6 and section 1.4. The physical meaning of the energy equation, in the absence of external heating and chemical cooling, is that the internal energy of the parcel changes only due to adiabatic contraction or expansion.

To solve the above described hydrodynamic or Navier-Stokes equations, we need to specify an equation of state, which relates the internal energy to the pressure. For ideal gas it is given by

$$p = (\gamma_{\text{ad}} - 1)u\rho, \quad (1.7)$$

where  $\gamma_{\text{ad}}$  is the ratio of specific heats and it depends on the gas composition. For diatomic molecules (e.g.  $\text{H}_2$  gas)  $\gamma_{\text{ad}} = 7/5$ , while for a mixture of 10 per cent helium content and  $\text{H}_2$  gas it is  $10/7$ , assuming that the  $\text{H}_2$  rotational degrees of freedom are populated, but the vibrational degrees of freedom are not (Glover and Mac Low, 2007a).

In astrophysics, there are three main prescriptions for solving this differential equation system numerically: smoothed particle hydrodynamics (SPH), grid-based Riemann solvers and moving-mesh based codes. The SPH methods work in the Lagrangian frame, solving the above introduced form of the hydrodynamic equations. The Riemann solvers, hence the name, are designed to solve the Riemann problem at each cell boundary on a regular or adaptive grid, using the coordinate-based Eulerian frame. The moving-mesh solution is a combination of the previous two, combining the adaptable resolution of the first and the better shock solution of the latter.

In the present thesis, we use the SPH scheme of numerical hydrodynamics to model molecular cloud evolution and the early stages of star formation. In the next section we describe the SPH formalism in more detail, following Springel (2005).

### 1.2.2 SMOOTHED PARTICLE HYDRODYNAMICS (SPH)

The SPH method uses discrete particles to solve the fluid dynamic equations. In this scheme the continuous fluid quantities are defined by an interpolation kernel (Lucy, 1977). The particles, are described by the  $\vec{r}_i$  coordinate vector, the  $\vec{v}_i$  velocity vector and the  $m_i$  masses. The latter by definition ensures mass conservation, thus the continuity equation is unnecessary in this formalism. The thermodynamic condition of the particles can be given either by the internal energy per unit mass ( $u_i$ ), as described above or by the entropy per unit mass ( $s_i$ ). Springel (2005) prefers  $s_i$  as the independent thermodynamic variable, because this choice ensures that both the energy and the entropy are conserved (Springel and Hernquist, 2002).

In this formalism, the density of the  $i$ th particle is calculated according to

$$\rho_i = \sum_{j=1}^N m_j W(|\vec{r}_{ij}|, h_i), \quad (1.8)$$

where  $N$  is the number of SPH particles used to describe the fluid,  $\vec{r}_{ij} = \vec{r}_i - \vec{r}_j$  and  $W(r, h)$  is the smoothing kernel. Springel (2005) chooses spline smoothing and the

kernel is defined as

$$W(r, h) = \frac{8}{\pi h^3} \times \begin{cases} 1 - 6(\frac{r}{h})^2 + 6(\frac{r}{h})^3 & \text{if } 0 \leq \frac{r}{h} \leq 0.5 \\ 2 \times (1 - \frac{r}{h})^3 & \text{if } 0.5 < \frac{r}{h} \leq 1 \\ 0 & \text{if } \frac{r}{h} > 1 \end{cases} \quad (1.9)$$

The variable  $h$  denotes the smoothing length of the particle and is chosen such that the number of particles within a smoothing length from the particle center is nearly constant at  $N_{\text{sph}}$ , so that

$$\frac{4\pi}{3} h_i^3 \rho_i = N_{\text{sph}} \langle m \rangle, \quad (1.10)$$

where  $\langle m \rangle$  is the average particle mass. In principle the smoothing length gives the length scale on which the fluid motions are resolved.  $h$  is adaptive (i.e. high particle density by design means small smoothing length), therefore the resolution is also adaptive, constituting a major strength of the SPH formalism. This makes the method a suitable choice for ISM simulations, where large dynamic ranges in size have to be considered.

Springel and Hernquist (2002) shows that the moment equation for a SPH particle, if viscous dissipation is not considered (i.e. for a reversible flow), with the Eq. 1.8 definition for density, can be written as

$$\frac{d\vec{v}_i}{dt} = - \sum_{j=1}^N m_j \left[ f_i \frac{P_i}{\rho_i^2} \nabla W_{ij}(h_i) + f_j \frac{P_j}{\rho_j^2} \nabla W_{ij}(h_j) \right], \quad (1.11)$$

where  $W_{ij}(h) = W(|\vec{r}_i - \vec{r}_j|)$  and  $f_i$  is a correction factor defined as

$$f_i = \left( 1 + \frac{h_i}{3\rho_i} \frac{\partial \rho_i}{\partial h_i} \right). \quad (1.12)$$

These equations already describe the fluid dynamics in the case of time reversible flows. The gas flows in the ISM, however, are non-reversible: the kinetic energy dissipates in shocks and complex, chemical state dependent heating and cooling processes alter its temperature and entropy. The viscous dissipation could be accounted for by adding an artificial viscosity term to the equation of motion:

$$\left. \frac{d\vec{v}_i}{dt} \right|_{\text{visc}} = - \sum_{j=1}^N m_j \Psi_{ij} \nabla \langle W_{ij} \rangle, \quad (1.13)$$

where  $\langle W_{ij} \rangle$  is the average of the  $W_{ij}(h_i)$  and  $W_{ji}(h_j)$  kernels and  $\Psi_{ij}$  is the viscosity factor, mentioned earlier. It is zero for distant particles, and greater than zero when the particles approach each other in physical space. Its value for close particles is inversely proportional to the mean density of the particle pair and proportional to the viscosity strength parameter (Springel, 2005). The most widely used parametrization of  $\Psi_{ij}$  is given by Monaghan and Gingold (1983) and Balsara (1995), thus for more details we refer to them.

Self-gravity is extremely important in most astrophysical applications. We can add its contribution to the momentum equation (Eq. 1.11) according to

$$\left. \frac{d\vec{v}_i}{dt} \right|_{\text{grav}} = - \sum_{j=1}^N m_j \nabla \Phi(\vec{r}_{ij}). \quad (1.14)$$

It is usual to define a gravitational softening length  $\epsilon$  to limit the importance of close particle encounters, in a similar fashion as in collisionless  $N$ -body system, thus  $\Phi = \Phi(\vec{r}, \epsilon)$  (Springel, 2010). Here we keep the softening length constant at 5 AU for particles which interact only via gravitational forces (i.e. sink or star particles, see also in section 2.2), while for the SPH particles, it is variable and set according the smoothing length of the particle (Clark et al., 2011).

Finally, we need to give the energy equation in terms of the entropy as well. The equation of state for ideal gas as function of entropy can be written as

$$P_i = A_i \rho_i^{\gamma_{\text{ad}}}, \quad (1.15)$$

where  $A_i = A(s_i)$  is the entropic function, which depends directly only on entropy. The entropy can be converted to internal specific energy as

$$u = A(s) \frac{\rho^{\gamma_{\text{ad}} - 1}}{(\gamma_{\text{ad}} - 1)}. \quad (1.16)$$

The ideal gas temperature is then given by

$$T_{\text{g}} = \frac{u \rho}{(\gamma_{\text{ad}} - 1) n_{\text{tot}} k_{\text{B}}}, \quad (1.17)$$

where  $n_{\text{tot}}$  is the particle number density. The energy equation is then given by

$$\frac{du_i}{dt} = \sum_{j=1}^N m_j \vec{v}_{ij} \left( f_i \frac{P_i}{\rho_i^2} \nabla W_{ij}(h_i) + \frac{1}{2} \Psi_{ij} \nabla \langle W_{ij} \rangle \right) - \Lambda_i, \quad (1.18)$$

where  $\langle W_{ij} \rangle$  is the average of the  $W_{ij}(h_i)$  and  $W_{ji}(h_j)$  kernels. The first term in the sum accounts for the internal energy change due to adiabatic expansion or contraction, while the second is the viscosity term. The latter enhances entropy by converting the kinetic energy into heat. The term  $\Lambda_i$  represents the net heating or cooling rate. Equations 1.11, 1.13, 1.14 and 1.18, along with the implicit gravitational potential and net cooling/heating rate give a complete description the time evolution of a self-gravitating gas with thermal processes in SPH formalism. We solve the equation system using the GADGET-2 code (Springel, 2005).

In the next sections we give details on the calculation of two major ingredients, the gravitational potential and the net cooling/heating rate.

### 1.2.3 GRAVITATIONAL POTENTIAL

To solve the momentum equation (Eq. 1.11) we need to know the gravitational potential at the location of particle  $i$ . For the assembly of discrete SPH particles, this is given by

$$\Phi_i = \sum_{j=1}^N \frac{\mathcal{G} m_j}{|\vec{r}_j - \vec{r}_i|}. \quad (1.19)$$

The computational cost of this direct sum scales with the square of the number of particles in the assembly. This could very quickly dominate the simulation time, even for a few tens of thousands of particles. For larger simulations (e.g. the numerical simulations presented in this thesis use from 2 to 20 million particles) a more efficient method is required.

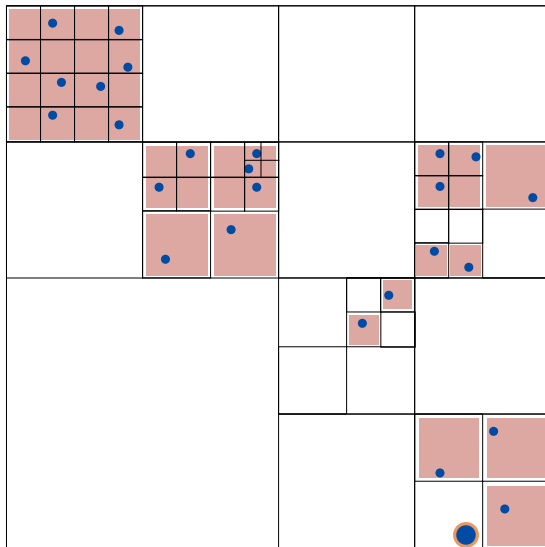


Figure 1.2: A schematic representation of the oct-tree constructed in GADGET-2 for the gravitational force calculation in case of a distribution of particles (blue dots). In three-dimension a node has eight daughter nodes, here in the two-dimensional representation only four of these are plotted. The black lines indicate the node boundaries, while the red shaded zones show how the nodes would be used for the gravitational force calculation for the orange-blue particle in the lower right corner. The figure is adopted from [Clark et al. \(2012a\)](#).

One method to overcome this difficulty involves the construction of a hierarchical tree ([Barnes and Hut, 1986](#)). The GADGET-2 code utilizes an oct-tree ([Springel, 2005](#)). In this case the procedure is as follows (see also the left panel of Fig. 1.2).

The simulation volume is split into nested boxes, so-called nodes (black lines in the figure). The “root” node is at the bottom of the hierarchy, containing all resolution elements (i.e. SPH particles, represented by blue dots) in the simulation. The root or “parent” node is then split into 8 “child” nodes. In the next step the previous child nodes act as parents and they are again split to 8 child nodes. This procedure is repeated until each node contains exactly one SPH particle. These nodes, at the top of the hierarchical structure, are called “leaves” (a similar terminology as used for dendrograms, see chapter 4). At each level in the hierarchy, the tree stores information about the positions, masses and sizes of the nodes contained within.

The gravitational potential calculation is speed up by considering the contribution of distant nodes to the potential, instead of taking each particles within them individually into account. The usual criterion for deciding if the node is far away or not is its angular size, seen from the particle in question. In practice,  $\Phi_i$  is calculated starting from the bottom of the hierarchy. Each node is tested whether it fulfils the solid angle criteria. If it does, the contribution of the node is added to the potential. If not, then the node is opened, and its child nodes are tested again. As an example, the red-shaded nodes in figure 1.2 show the nodes used for the calculation of the potential at the location of the blue dot with orange outline (right bottom corner).

A common choice for the angular size criteria is 0.5 rad. With this, the true

Table 1.1: Cooling and heating processes included in the thermal model. For the complete list of references we refer to Table 1. in [Glover et al. \(2010\)](#)

<i>Cooling</i>	<i>Heating</i>
C fine structure lines	Photoelectric effect
C <sup>+</sup> fine structure lines	H <sub>2</sub> photodissociation
O fine structure lines	UV pumping of H <sub>2</sub>
H <sub>2</sub> rovibrational lines	H <sub>2</sub> formation on dust grains
CO rovibrational lines	Cosmic-ray ionization
Gas-grain energy transfer	
Recombination on grains	
Atomic resonance lines	
H collisional ionization	
H <sub>2</sub> collisional dissociation	
Compton cooling	

gravitational potential can be recovered within 1 per cent error ([Clark et al., 2012a](#)). The oct-tree gravitational potential solver scales as  $N \log N$  with the number of resolution elements considered.

The oct-tree can be also used to calculate column densities, which are important for modelling (photo)chemical processes ([Clark et al., 2012a](#)). We discuss this briefly in section 1.5.2.

#### 1.2.4 COOLING AND HEATING

To solve the energy equation (Eq. 1.6) we need to know  $\Lambda$ , the net rate of gas heating and cooling.  $\Lambda$  can be written as the sum of a heating and a cooling term:

$$\Lambda = \Lambda_{\text{cool}} - \Gamma_{\text{heat}}. \quad (1.20)$$

We summarize all the considered cooling and heating processes in table 1.1. For their detailed description and reference articles we point the reader to section 2.3 in [Glover and Mac Low \(2007a\)](#) and section 2.3 in [Glover et al. \(2010\)](#). We also refer to figure 2.2 for the density/depth dependence of heating and cooling processes in our simulations.

Here, we briefly describe the adopted model for the photoelectric heating ([Bakes and Tielens, 1994; Wolfire et al., 2003](#)) and the rovibrational CO cooling ([Neufeld and Kaufman, 1993; Neufeld et al., 1995](#)) processes. The former process is responsible for the heating of diffuse and translucent clouds, while the latter is the most important coolant at higher extinctions, until the dust cooling takes over the role of dominant cooling process above a few times  $10^4$  particles per  $\text{cm}^3$ . The example of CO cooling also shows well why hydrodynamical models of molecular clouds need to include a reasonable treatment of chemistry.

The most important heating process in diffuse and translucent clouds is due to the photoelectric process. Absorption of an energetic ultraviolet (UV) photon

may lead to the ejection of an electron from carbon grains and polycyclic aromatic hydrocarbons (PAHs). The electron carries some of the photon energy away in the form of kinetic energy. This excess kinetic energy then leads to the heating of the gas. [Bakes and Tielens \(1994\)](#) developed a theoretical model to measure the net heating rate from this process, assuming a grain size distribution, and exploring a range of UV field strengths, gas temperatures and electron abundances. They find that grains smaller than 100 nm are responsible for most of the heating effect, while the large grains absorb a significant fraction of UV photons, attenuating the UV field, but without electron ejections. They also give an analytical expression for the photoelectric heating rate ( $\Gamma_{pe}$ ), that we also adopt in this thesis. The expression is given as

$$\Gamma_{pe} = 1.3 \times 10^{-24} n \epsilon 1.7G \exp(-2.5 A_V) \text{ ergs s}^{-1} \text{ cm}^{-3}, \quad (1.21)$$

where  $n$  is the number density of gas, the  $G$  is the unattenuated interstellar UV radiation field strength in the unit of the Draine field ([Draine, 1978](#)), while the exponential accounts for the attenuation due to absorption by larger dust grains. The 1.7 coefficient stands for the conversion between the Draine and the Habing ([Habing, 1968](#)) fields, while the numerical value of the rate coefficient is given in terms of the latter. The heating efficiency depends on the ratio of the ionization and recombination rates and it is denoted by  $\epsilon$ . According [Bakes and Tielens \(1994\)](#) and [Wolfire et al. \(2003\)](#) the efficiency can be written as

$$\epsilon = \frac{4.9 \times 10^{-2}}{1 + 4 \times 10^{-3} \psi^{0.73}} + \frac{3.7 \times 10^{-2} (T_g/10^5)^{0.7}}{1 + 2 \times 10^{-4} \psi}, \quad (1.22)$$

where  $\psi = G_0 T_g^{1/2} / n_e$  with  $n_e$  denoting the electron number density.

A similarly important thermal process is the CO cooling by rovibrational line emission. Following [Glover et al. \(2010\)](#), we use the tabulated cooling functions of [Neufeld and Kaufman \(1993\)](#) and [Neufeld et al. \(1995\)](#). They calculated the cooling rate of CO as a function of gas temperature, density and the effective optical depth using the large velocity gradient (LVG) approximation of radiative transfer. They give the rotational CO cooling rate as

$$\Lambda_{CO,rot} = L_{CO,rot} n_{CO} n_{tot,eff}, \quad (1.23)$$

where  $L_{CO,rot}$  is the cooling rate coefficient,  $n_{CO}$  is the CO number densities, while  $n_{tot,eff}$  represents the total number density of possible collisional partners for CO. The latter includes molecular and atomic hydrogen and a cross-section-weighted electron number density (see eq. 13 in [Glover et al., 2010](#)). The cooling rate coefficient is tabulated and it depends on both the temperature and the effective optical depth. The vibrational cooling rate is calculated similarly.

As Eq. 1.23 illustrates, the molecular cooling rates directly depend on the number densities (i.e. abundances) of chemical species. The gas temperature, thus the internal energy and the pressure of gas depends on the cooling rate. This in turns influences the gas dynamics through the energy and momentum equations. Therefore, if we aim to model the gas dynamics of the interstellar matter, we need to have a good approximation for its chemical state.

### 1.3 CHEMISTRY AT THE DAWN OF STAR FORMATION

The interstellar gas, from its diffuse phase to the dense dark cores, provide sites for a rich chemistry. The detection of about 180 interstellar or circumstellar and more than 50 extragalactic molecules, as of November 2014<sup>1</sup>, is a strong proof for that. These molecules show a large diversity from simple diatomic species (such as H<sub>2</sub> and CO: see e.g. Carruthers, 1970; Wilson et al., 1970, respectively) in diffuse clouds, to saturated organic molecules (e.g. CH<sub>3</sub>CH<sub>2</sub>OH, Zuckerman et al., 1975) in high mass star forming regions and fullerenes made of up to 70 carbon atoms in circumstellar shells (Cami et al., 2010). The large variety of molecules implies that there must be many more relevant, but still undetected species, which are involved in their formation and destruction processes. Therefore, if we want to understand how the detected species are produced, we have to build comprehensive (numerical) models with a large number of species and interconnected reactions (i.e. reaction networks).

The influence of the chemical state of the gas on its thermal and magnetic properties (i.e. through cooling and heating processes and by controlling the ionization degree), which in turns control the fragmentation, thus star formation, emphasizes the significance of interstellar chemistry. Furthermore, chemical species can also serve as tracers of physical conditions in each stage of star formation. The most common examples are CO, which is often used as a molecular gas and gas dynamics tracer, NH<sub>3</sub>, which is a good indicator of the gas temperature, N<sub>2</sub>H<sup>+</sup>, hinting for CO depletion from the gas phase at high densities, and SiO, which has been established as a shock tracer.

In this section we give a general overview of important chemical processes and describe the formation routes of abundant carbon, oxygen and nitrogen bearing species. We also introduce the chemical model and reaction networks used in the remainder of this thesis.

#### 1.3.1 CHEMICAL PROCESSES IN THE ISM

The chemical networks developed for modelling diffuse cloud, dense core and protoplanetary disk environments typically contain from a few hundred to a few thousand (Semenov et al., 2010; Röllig and Ossenkopf, 2013) chemical reactions. However, most of these reactions could be classified in four main categories; bond formation, bond destruction, bond rearrangement and ionization. The main reaction types within these categories with the formal reactions and examples are summarized in Table 1.2. Here, we briefly describe these processes. For a more complete description, however, we refer to the reviews of van Dishoeck (1998), van Dishoeck and Blake (1998) and Tielens (2013).

The typical densities in the above mentioned astrophysical environments, excluding the inner regions of protoplanetary disks and planetary atmospheres, are low (from a few hundred to 10<sup>6</sup> particle per cm<sup>-3</sup>) and therefore the probability of reactions involving the (almost) simultaneous interaction of three or more species are highly unlikely. Thus, most astrochemical reactions happen between two reactants. The rate of the reaction between species  $i$  and  $j$  is given by  $R_{\text{chem},ij} = k_{ij} n_i n_j$  in

---

<sup>1</sup><http://www.astro.uni-koeln.de/cdms/molecules>

Table 1.2: Types of molecular processes (adapted from van Dishoeck, 1998; Semenov, 2004)

<i>Bond formation</i>	<i>Formal reaction</i>	<i>Example</i>
Radiative association	$A + B \rightarrow AB + h\nu$	$C^+ + H \rightarrow CH^+ + h\nu$
Associative detachment	$A^- + B \rightarrow AB + e^-$	$H^- + H \rightarrow H_2 + e^-$
Surface formation	$A + B_{\text{grain}} \rightarrow AB + \text{grain}$	$H + H_{\text{grain}} \rightarrow H_2 + \text{grain}$
<i>Bond destruction</i>		
Photodissociation	$AB + h\nu \rightarrow A + B$	$CO + h\nu \rightarrow C + O$
Dissociative recombination	$AB^+ + e^- \rightarrow A + B$	$HCO^+ + e^- \rightarrow CO + H$
Collisional dissociation	$AB + M \rightarrow A + B + M$	$H_2 + H \rightarrow H + H + H$
<i>Bond rearrangement</i>		
Ion-molecule exchange	$A^+ + BC \rightarrow AB^+ + C$	$C^+ + OH \rightarrow HCO^+$
Charge transfer	$A^+ + BC \rightarrow A + BC^+$	$C^+ + HCO \rightarrow C + HCO^+$
Neutral-neutral	$A + BC \rightarrow AB + C$	$O + CH \rightarrow CO + H$
<i>Ionization</i>		
Photoionization	$AB + h\nu \rightarrow AB^+ + e^-$	$C + h\nu \rightarrow C^+ + e^-$
CRP ionization	$AB + CRP \rightarrow AB^+ + e^-$	$He + CRP \rightarrow He^+ + e^-$

$\text{cm}^3 \text{s}^{-1}$ , where  $k_{ij}$  is the reaction rate coefficient in  $\text{cm}^{-3} \text{s}^{-1}$  and  $n$  is the concentration in  $\text{cm}^{-3}$ . Usually, the rate coefficient, in terms of its temperature dependence and possible barrier energies, is given by the Arrhenius equation

$$k(T_g) = \alpha \left( \frac{T_g}{300} \right)^\beta \exp \left( -\frac{\gamma}{T_g} \right), \quad (1.24)$$

where  $\alpha$  is the reaction rate coefficient at room temperature (300 K), the  $\beta$  parameter characterizes the temperature dependence and  $\gamma$  is the activation barrier of the reaction in K (0 for exothermic reactions).

The basic problem of bond formation is that the total energy of the system formed by species  $i$  and  $j$  upon collision is larger than when they are incorporated in a single, stable molecule (e.g. Bates, 1951). The excess energy needs to be removed for the bond to form. The two main processes through which this could happen are the radiative association, when the excess energy is removed by the emission of one or more photons, and grain surface formation, when the excess energy is absorbed by the dust grain itself. The characteristic time for photon emission in the radiative association case is typically long compared to the collision time scale and it might involve forbidden transitions, thus in many molecule formation pathways this reaction acts as a bottleneck. A typical example for radiative association is the formation of  $\text{CH}_2^+$  from the reaction of  $\text{CH}^+$  with  $\text{H}_2$ . The rate of grain surface formation depends on the sticking probability of the species upon collision

with the grains, the grain surface properties, the mobility of the species on the grain, the probability of reaction if they meet and the probability of release back to the gas phase. The best example for surface formation is  $\text{H}_2$ , which forms predominantly this way, while the gas phase formation path requires a forbidden electronic transition between the dissociative and the ground states.

In diffuse and translucent clouds, the dominant process for bond destruction is photodissociation by interstellar UV photons. In most conditions the Lyman limit at 91.2 nm (13.6 eV) provides the upper limit in energy for the dissociative and ionizing radiation. Molecules like  $\text{H}_2$ , CO and CN are dissociated only by very short wavelength photons, between 92.1 and 112 nm in the so called Lyman-Werner bands, while others, such as CH and OH can be destroyed by much lower energy photons, down to 300 nm wavelength. The flux of photons in these wavelength ranges (i.e. the radiation field strength) become attenuated quickly at larger cloud depths, due to the high absorption and scattering opacities of small dust grains, at short wavelengths. As an effect the dissociation rate decreases with cloud depth. Usually, the depth and radiation field strength dependence of the rate coefficient, in one-dimensional slab geometry, is given according

$$k_i^{\text{ph}} = \alpha_{\text{fs}} G \exp(-\gamma_{\text{ph}} A_V), \quad (1.25)$$

where  $\alpha_{\text{fs}}$  is the free space rate coefficient at the standard Draine radiation field strength ( $G_0$ , [Draine, 1978](#)),  $G$  is the unattenuated fields strength in the units of  $G_0$ ,  $\gamma_{\text{ph}}$  describes how rapidly the rate coefficient falls with the depth, while and  $A_V$  is direct indicator of depth, denoting the visual extinction due to dust grains towards the radiation source.

Under the assumption of “typical” dust properties (a gas-to-dust ratio of 100 and interstellar reddening,  $R_V = 3.1$ , [Bohlin et al., 1978](#); [Draine and Bertoldi, 1996](#)), the visual extinction can be given as a function of the hydrogen nuclei column density ( $N_{\text{H,tot}}$ ) as

$$A_V = \frac{N_{\text{H,tot}}}{1.59 \times 10^{21} \text{ cm}^{-2}} \text{ mag}. \quad (1.26)$$

In the remainder of the thesis we use this definition for  $A_V$ .

The photodissociation of  $\text{H}_2$  and CO occurs through discrete absorption in the 91 nm - 120 nm, UV wavelength range ([Draine and Bertoldi, 1996](#); [Visser et al., 2009a](#)). Due to their relatively high abundances and thus column densities, these molecules are able to shield themselves and each other (although the  $\sim 4$  orders of magnitude lower abundance of CO makes the shielding of  $\text{H}_2$  by CO negligible) from the incident UV radiation. The details of this are given in section 1.4.

Besides photodissociation, molecules can be dissociated by high energy cosmic ray particles (CRP), CRP-induced photons ([Prasad and Tarafdar, 1983](#)) and by dissociative recombination reactions. Due to the very high energies (between  $10^{11}$  and  $10^{21}$  eV) of CRPs, their flux is not attenuated like that of the UV photons. In fact in the densest, most shielded zones of molecular clouds, CRP and CRP-induced photons are expected to contribute strongly to the gas heating and and to drive the chemistry through ionization, which lead to subsequent ion-molecular reactions. In the same regions, CRP-produced ions, such as  $\text{He}^+$  and  $\text{H}_3^+$ , are also effective in destroying the bonds of neutral molecules. Finally, in circumstances when the relative speed of molecules are high (e.g. in shocks), dissociation by direct collisions might also become efficient.

Photoionization happens similarly to photodissociation and therefore the attenuation of the radiation field due to dust absorption is treated similarly in both cases.

The more complex chemical species are produced through the bond rearrangement process. This could occur involving ion-molecular or two neutral reactants. In the former case, given that the reaction is exothermic, the rate coefficient is described by the Langevin equation, and so does not depend on the gas temperature, but only on the polarizability of the neutral molecule and the reduced mass of the system. The typical rate coefficient values are high, therefore the ion-molecule reactions dominate the gas phase chemistry in cold and well-shielded molecular cloud interiors and dark cores (Herbst and Klemperer, 1973; Watson, 1973).

Neutral-neutral reactions are generally thought to be slow compared to the ion-neutral reactions. Experiments, however, found that radical-radical (i.e. molecules with unpaired valence electrons, for example  $\text{CN} + \text{O}_2 \rightarrow \text{OCN} + \text{O}$ ) and unsaturated molecule (e.g.  $\text{CN} + \text{C}_2\text{H}_2 \rightarrow \text{HC}_3\text{N} + \text{H}$ ) reactions have rates only a factor of  $\sim 5$  below those of the ion-molecule reactions (van Dishoeck, 1998).

In the following subsections we overview the most important species and reactions involving the three most abundant elements besides hydrogen in the ISM; carbon, oxygen and nitrogen. A graphical overview of their reactions are also given in Figure 1.3.

### 1.3.2 CARBON CHEMISTRY

In diffuse clouds and at the edges of GMCs, carbon is dominantly in the form of  $\text{C}^+$ , due to the fact that its ionization potential smaller is than of the atomic hydrogen (13.6 eV). The carbon chemistry is primarily initiated by reactions with the  $\sim 4$  orders of magnitude more abundant  $\text{H}_2$  molecule. The fast ion-neutral reaction between  $\text{C}^+$  and  $\text{H}_2$  is inhibited by a high activation energy barrier, thus the reaction proceeds through the much slower radiative association reaction, forming  $\text{CH}_2^+$  (see Fig.1.3). The  $\text{CH}_2^+$  cation then reacts quickly with  $\text{H}_2$  to form  $\text{CH}_3^+$ . The small hydrocarbon cations might react with atomic oxygen to form  $\text{HCO}^+$ , leading to CO after recombination or they dissociatively recombine to neutral hydrocarbons ( $\text{CH}_2$  and  $\text{CH}$ ). These neutrals might then react with atomic oxygen to form CO, with atomic nitrogen to form HCN or with  $\text{C}^+$  to form acetylenic species (i.e. species with carbon-to-carbon triple bonds), that can build up longer carbon chains.

In dark, dense clouds, where the photoionization of carbon and the photodissociation of CO is highly attenuated, CO becomes the preferred carbon-bearing species. CO is a stable molecule and it is much less reactive than  $\text{C}^+$ , thus the gas-phase carbon chemistry becomes less rich after the transition. At densities higher than  $\text{few} \times 10^5 \text{cm}^{-3}$  and temperatures below  $\sim 20 \text{K}$ , CO eventually freezes-out onto dust grains (e.g. Caselli et al., 1999).

More complex carbon-bearing molecules, such as  $\text{H}_2\text{CO}$  and  $\text{CH}_3\text{OH}$ , are thought to form from CO hydrogenation on grain surfaces (Tielens and Hagen, 1982; Tielens, 2013). They can be returned to the gas phase by thermal- or photodesorption (see section 1.3.5).



### 1.3.3 OXYGEN CHEMISTRY

The initial steps of oxygen chemistry differ qualitatively from that of carbon. The ionization potential of O is slightly above the Lyman limit, thus hydrogen ionization evens shields it from the ionizing radiation. Thus, in the diffuse gas, the oxygen is predominantly in neutral atomic form. The formation of oxygen-bearing molecules is then initiated by the relatively slow charge exchange reaction with  $H^+$ . In the next step,  $O^+$  quickly reacts with  $H_2$  to produce  $OH^+$ ,  $H_2O^+$  and  $H_3O^+$ . The latter two then dissociatively recombine to form  $H_2O$  and  $OH$ . These neutrals then react with  $C^+$  to produce  $CO^+$ ,  $HCO^+$  and eventually  $CO$  (Fig.1.3).

At higher depths, where most hydrogen is already converted to molecular form, the cosmic ray ionization of  $H_2$  leads to  $H_3^+$  formation. This in turn can already react with neutral oxygen to form  $OH^+$ . The formation chain from  $OH^+$  continues similarly as described above.

The excess oxygen, which is not incorporated in  $CO$  is either converted to  $O_2$  by the reaction of  $OH$  with  $O$ , or forms  $H_2O$  on grain surfaces. For the latter, [Tielens and Hagen \(1982\)](#) suggested the following reactions channels: As the first step, atomic oxygen is accreted to the grain. This is mobile and quickly moves around on the grain surface to react with another oxygen atom to form  $O_2$ . A further accreted oxygen atom will react with  $O_2$  to form ozone ( $O_3$ ). Next, the atomic hydrogen on the surface preferentially react with  $O_3$  to form  $OH$ , which in turns react with  $H_2$ , producing  $H_2O$ . The leftover  $O_2$  from the ozone-hydrogen bond rearrangement might participate in further hydrogenations, until  $H_2O_2$  is produced. A subsequent hydrogenation then leads to the formation of  $H_2O$  and  $OH$ . The  $OH$  produces  $H_2O$  as well, if it reacts again with  $H_2$ . In these pathways multiple poorly known barrier are involved. These are often expected to be overcome by tunnelling (e.g. [Mokrane et al., 2009](#)).

### 1.3.4 NITROGEN CHEMISTRY

In diffuse clouds, nitrogen is expected to be in an initially neutral state, due to its large ionization potential. The neutral nitrogen may react with  $CH$  or  $OH$  to form  $CN$  or  $NO$ , respectively. Their radical-radical reaction with an additional  $N$  leads to  $N_2$  formation. The  $N_2$  is very stable and models predict that most nitrogen is locked up in molecular form.

Further reactions between  $N_2$  and  $H_3^+$  produce  $N_2H^+$ . In diffuse clouds the major destruction channel for  $N_2H^+$  is dissociative recombination, with  $N_2$  as the most probable and  $NH$  a less likely result. At higher densities  $N_2H^+$  is mostly destroyed by the proton transfer reaction with  $CO$ , producing  $HCO^+$  and  $N_2$ . When  $CO$  is depleted from the gas phase,  $N_2H^+$  is expected to be more abundant. Therefore it is often used as a tracer for  $CO$  freeze-out and high density in protostellar cores (e.g. [Lippok et al., 2013](#)) and protoplanetary disks (e.g. [Qi et al., 2013](#)).

The gas-phase  $NH_3$  (ammonia) production is thought to start with the dissociative charge transfer reaction between  $N_2$  and  $He^+$ , decaying to  $N^+$  and  $N$ . These species then react with  $H_2$  and  $H_3^+$ , respectively, to form  $NH^+$  or  $NH_2^+$ . The subsequent proton abstraction from  $H_2$  then leads to the formation of  $NH_3^+$  and  $NH_4^+$ . The latter then recombines to form  $NH_3$ . This reaction chain, however, has 2 bottlenecks: the first is the endothermic nature of the  $N^+ + H_2$  reaction, while the second is the large activation barrier of the last hydrogen abstraction (Fig.1.3). These difficulties

might be overcome when the ortho/para state of  $\text{H}_2$  is considered (Tielens, 2013). Another often assumed pathway for ammonia formation is on grain surfaces. In short, the channel progresses through accretion and hydrogenation of N, with an immediate release to the gas phase upon the final hydrogen abstraction.

### 1.3.5 CHEMISTRY ON GRAIN SURFACES

Although dust grains are under-abundant compared to the gas, with a typically assumed gas-to-dust ratio of 100, they still have a large impact on the interstellar chemistry (e.g. Semenov, 2004; Tielens, 2013). One main effect, as mentioned earlier, is the attenuation of the UV radiation field, thus protecting gas-phase molecules from photodissociation. A similarly important property of grains is their much larger than molecular geometrical cross section, which makes grains important sites for chemical processes. In cold and dense environments grains act as sinks for many gas-phase species, while allowing others to increase their abundance (e.g.  $\text{N}_2\text{H}^+$  after CO accretion). Grain surfaces might also serve as catalysts for chemical reactions that are slowed by barriers in the gas phase (most notably  $\text{H}_2$  formation, Hollenbach and Salpeter, 1971; Jura, 1975). Finally, they also affect the ionization state of the gas by sweeping up electrons from the gas-phase.

The rate at which the  $i$ th gas-phase species accretes to grains can be derived from cross section considerations and it is written as

$$k_i^{\text{acc}} = \pi a_d^2 v_i^{\text{th}} n_d S, \quad (1.27)$$

where  $v_i^{\text{th}} = \sqrt{8k_B T_g / \pi m_i^{\text{spec}}}$  is the thermal velocity of the species  $i$ , which has a mass of  $m_i^{\text{spec}}$  and  $k_B$  is the Boltzmann constant. The dust properties are described by  $a_d$ , the (average) grain radii and  $n_d$ , the dust number density per unit volume.  $S$  denotes the sticking coefficient (i.e. the probability of sticking upon collision), which is close to 1 for most species.

One can imagine the progress of grain surface reactions as follows: The grain surface is covered with small potential valleys, called reaction sites (e.g. an  $a_d = 0.1 \mu\text{m}$  silicate grain has on the order of  $10^6$  such sites), where the accreted species might be trapped by relatively weak van der Waals forces or by stronger chemical bonds. The light species, such as H,  $\text{H}_2$  or O are mobile on the surface, thus can move from site to site (due to thermal hopping or tunnelling), while the more massive molecules are usually immobile. A reaction might occur when the mobile species visits a site occupied by another reactant. The reaction rate coefficient is then given by the product of the rate at which the mobile species scans through the surface with a random walk, and the probability of reaction upon meeting. The newly formed molecule is typically in an excited state with enough energy to leave the reaction site, and thus return to the gas-phase.

There are two major methods for modelling reactions on grain surfaces. One utilizes the rate equation approach (e.g. Hasegawa et al., 1992; Semenov et al., 2010), described in the following section. The other models the stochastic nature of the random walk on the grain surface by a Monte Carlo approach (e.g. Tielens and Hagen, 1982). The two methods yields significant differences in the rate coefficients, with the latter providing a more realistic representation of the true physical process. To account for the shortcomings of the former method, (Caselli

et al., 1998) developed the so called modified rate equation method. Recently, Vasyunin et al. (2009) showed that the modified rate equation method can reproduce the stochastic results almost perfectly, if the tunnelling of H and H<sub>2</sub> is not considered, while it underestimates the abundances of e.g. H<sub>2</sub>O, NH<sub>3</sub> and CO, in some cases by up to an order of magnitude, when tunnelling is accounted for.

The grain surface species can be released back to the gas phase by three main mechanisms. The most simple of these is thermal desorption. This takes place when the temperature of the grain is high, and the molecule accumulate more energy then the  $k_B T^D$  binding energy. The thermal evaporation rate of grain surface species  $i$  is given by

$$k_i^{\text{th}} = \nu_0 \exp(-T_i^D / T_d), \quad (1.28)$$

where  $\nu_0$  is the characteristic vibrational frequency of  $i$  (Hasegawa et al., 1992).

Another important desorption mechanism is due to the heating of grains by high energy, deep-penetrating cosmic-ray particles. The cosmic ray desorption rate, according Hasegawa et al. (1992), is given by

$$k_i^{\text{CRP}} = 3.16 \times 10^{19} \nu_0 \exp(-T_i^D / T_{\text{CRP}}), \quad (1.29)$$

where  $T_{\text{CRP}}$  is the peak temperature of the grain due to the momentary CRP heating.

Finally, in diffuse clouds and in hot cores the desorption by UV photons might also became effective process for removing grain surface species. The rate of this process is determined by the probability per incident UV photon that surface species  $i$  will be removed by photodesorption (i.e. the photoevaporative yield,  $Y$ ), and the local radiation field strength (attenuated by the dust column towards the radiation source):

$$k_i^{\text{ph}} = GY \exp(-2A_V), \quad (1.30)$$

see Walmsley et al. (1999) and Semenov (2004).

### 1.3.6 CHEMICAL MODELS

The main input parameters of chemical models are the gas density, the gas and the dust temperatures, the radiation field strength, the initial composition and the elemental abundances, the primary cosmic-ray ionization rate and the grain properties. In multi-dimensional hydrodynamical cases, all of these parameters, except the grain properties, are location and time-dependent quantities. The expected results from the chemical models are the abundances of major species, as a function of location and time. These abundances then can be used to compute cooling and heating rates, which are then inserted as  $\Lambda$  into the hydrodynamical equations (see section 1.2.2) or to calculate column densities and emission maps. These then can be compared to observations.

The network of chemical reactions can be formalized mathematically as a system of coupled ordinary differential equations (ODEs). These equations are often called the equations of chemical kinetics. Each equation in the system describes the concentration change of a chemical species due to chemical reactions in the gas phase or on the dust surface, and due to accretion onto or release from dust grains. For the  $i$ th species, it takes the following forms (e.g. Herbst, 1993; Semenov et al., 2010):

$$\frac{dn_i}{dt} = \sum_{l,m} k_{lm} n_l n_m - n_i \sum_{l \neq i} k_l n_l - k_i^{\text{acc}} n_i + k_i^{\text{des}} n_i^s \quad (1.31)$$

$$\frac{dn_i^s}{dt} = \sum_{l,m} k_{lm}^s n_l^s n_m^s - n_i^s \sum_{l \neq i} k_l^s n_l^s + k_i^{\text{acc}} n_i^s - k_i^{\text{des}} n_i^s, \quad (1.32)$$

where  $n_i$  and  $n_i^s$  are the gas-phase and surface concentrations of species  $i$  (in  $\text{cm}^{-3}$ ). The first terms in the equations account for the production of the gas-phase and the grain surface species, with rate coefficients  $k_{lm}$  and  $k_{lm}^s$ , respectively. Similarly, the second terms give their destruction rates,  $k_l$  and  $k_l^s$  due to reactions with species  $l$ . The rate coefficients have units  $\text{s}^{-1}$  in case of first order kinetics (only one chemical species is involved in the reaction, e.g. photodissociation) and  $\text{cm}^3 \text{s}^{-1}$  for second order kinetics (two chemical species are involved in the reaction). The last two terms account for interactions with dust grains: A species might accrete onto grains with the rate  $k_i^{\text{acc}}$  or it might desorb from them with the rate  $k_i^{\text{des}}$ . In the equation for the gas-phase species (Eq. 1.31) the accretion term appears as a sink, with a negative rate, while the desorption term at the same time provides a source term, with a positive contribution. In case of the grain surface species (Eq. 1.32), the roles and the signs are switched.

The rate coefficients in the ODEs cover a large range in values: The fast recombination reactions have rates coefficients on the order of  $10^{-7} \text{cm}^3 \text{s}^{-1}$ , while for the slower, neutral-neutral reaction rate coefficients are typically on the order of  $10^{-11} \text{cm}^3 \text{s}^{-1}$ . The Jacobi matrix of the system for astronomically relevant chemical reaction networks contains a significant number of zero value elements. Therefore, the typical chemical kinetic ODE systems are stiff and sparse, requiring specialized algorithm for the solution.

We use the publicly available DVODPK<sup>2</sup> (Differential Variable-coefficient Ordinary Differential equation solver with Preconditioned Krylov method GMRES for the solution of linear systems) ODE solver package in both the GADGET-2 implicit chemistry module and also in the ALCHEMIC chemical modelling code (Semenov et al., 2010), used for post-processing (see chapter 4).

Besides the ODE solver, the most important ingredients of a chemical model are the chemical rate coefficients. Most astrochemical networks are based on four major chemical rate databases: the UDFA<sup>3</sup> (Umist Database For Astrochemistry, McElroy et al., 2013), the OSU database (Ohio State University, Smith et al., 2004), the network incorporated in the MEUDON<sup>4</sup> Photon Dominated Region (PDR) code (Le Petit et al., 2006) and the KIDA<sup>5</sup> (Kinetic Database for Astronomy, Wakelam et al., 2012), which is a broad, community-driven database. Besides these general databases and networks, some applications require much more specific selection of reactions. Good examples of these are the reduced network of Glover et al. (2010) for hydrodynamical applications, the extensive deuterium fractionation model of Albertsson et al. (2013) with multi-deuterated species and the high temperature gas-phase model of Harada et al. (2010) for modelling chemical abundances in accretion disks surrounding Active Galactic Nuclei.

<sup>2</sup><http://computation.llnl.gov/casc/odepack/>

<sup>3</sup><http://udfa.ajmarkwick.net/>

<sup>4</sup><http://pdr.obspm.fr/PDRcode.html>

<sup>5</sup><http://kida.obs.u-bordeaux1.fr/>

One should, however, always keep in mind that only about 10 per cent of the chemical reactions rates have been accurately measured in the laboratory at temperatures and densities similar to typical GMC conditions (few  $\times$  10K and a few thousand particle per  $\text{cm}^3$ ). The rest of the rates are extrapolations from high temperature and density rate measurements and the results of quantum chemical calculations. In addition, the branching ratios (i.e the probability ratios of the possible reaction outcomes) of most low temperature reactions are unmeasured (Wakelam et al., 2010). These uncertainties introduce a factor of a few dispersion to the modelled abundances and column densities, although species such as CO,  $\text{C}^+$ ,  $\text{H}_3^+$ ,  $\text{H}_2\text{O}$ ,  $\text{N}_2\text{H}^+$  and  $\text{NH}_3$  seem to be less affected (e.g. Vasyunin et al., 2008; Wakelam et al., 2010).

In the forthcoming chapters of this thesis, two chemical networks are implemented, one for the implicit chemical model in hydrodynamic calculation, with limited number of species and reactions, and one more complete network, containing freeze-out and grain surface reactions alongside the extensive gas-phase network. The former specialized network was developed to model CO chemistry in hydrodynamic simulations, with the emphasis on computational cost efficiency (Nelson and Langer, 1999; Glover and Clark, 2012a). The latter complex model is based on the osu\_03\_2008 rate files of the Ohio State University database (Smith et al., 2004; Garrod and Herbst, 2006; Semenov et al., 2010). In the next subsections we review briefly both networks.

#### 1.3.6.1 THE NL99 NETWORK

The Nelson and Langer (1999) chemical network (NL99 hereafter) was designed as a fast, approximate model for tracking the conversion of  $\text{C}^+$  first into C, and then to CO, in hydrodynamical simulations of low mass molecular clouds.  $\text{C}^+$  is produced in poorly shielded regions due to photoionization, while it is destroyed by recombination to neutral carbon, by ion-neutral reaction with  $\text{H}_2$ , producing light hydrocarbons, or with the composite  $\text{OH}_x$  species (standing for OH,  $\text{H}_2\text{O}$ ,  $\text{O}_2$  and their ions), forming  $\text{HCO}^+$ .

The network allows the formation of CO through channels involving the composite hydrocarbon radical  $\text{CH}_x$  (representing CH and  $\text{CH}_2$ ), the composite  $\text{OH}_x$  and via the dissociative recombination of  $\text{HCO}^+$ . At low visual extinctions, the main channel for CO destruction is photodissociation. We adopt the free-space dissociation rate, the self- and  $\text{H}_2$  shielding coefficients and the visual extinction dependence from Visser et al. (2009a), see section 1.4. Deeper in the cloud the main destruction path involve the ion-molecular reaction with  $\text{He}^+$  and the conversion to  $\text{HCO}^+$  by charge transfer reaction with  $\text{H}_3^+$ . Due to the importance of ion-molecular reactions, the electron abundance of the gas is important. Besides the ionization of H and C, the low ionization potential metals (e.g. sodium and magnesium) are also contributing to the electron budget. In the NL99 network these are combined to an artificial species M and this may release one electron due to a photoionization event.

The original form of the NL99 network assumes fully molecular hydrogen, and does not model its formation and destruction self-consistently. In realistic molecular cloud conditions, however, the  $\text{H}_2$  formation time can be comparable to the free-fall time of the cloud (see e.g. Glover and Mac Low, 2007a; Clark et al., 2012b,

and Appendix C). Therefore we also incorporate the H<sub>2</sub> network of [Glover and Mac Low \(2007a,b\)](#), to be able to give a more realistic account for the atomic-to-molecular transition. In this model dust grains act as catalysators for the H<sub>2</sub> formation ([Hollenbach and McKee, 1979](#)). The main paths for H<sub>2</sub> destruction are the photodissociation ([Draine and Bertoldi, 1996](#), and section 1.4) and collisional dissociation with H and H<sub>2</sub>.

The network involves 9 self-consistently calculated (H<sup>+</sup>, H<sub>2</sub>, C<sup>+</sup>, CH<sub>x</sub>, OH<sub>x</sub>, CO, HCO<sup>+</sup>, He<sup>+</sup>, M<sup>+</sup>) and 5 conserved species (H, C, He, M, e<sup>-</sup>), with 32 reactions between them. In chapter 3 we extend the network with 4 additional evolved (<sup>13</sup>C<sup>+</sup>, <sup>13</sup>CO, <sup>13</sup>CH<sub>x</sub> and H<sup>13</sup>CO<sup>+</sup>) and one conserved (<sup>13</sup>C) isotopic species. The full set of reactions, without the isotope chemistry (see section 2.2.1), is summarized in Appendix A.

### 1.3.6.2 THE OSU\_03\_2008 BASED NETWORK

We adapt the osu\_03\_2008 rate file based gas-phase and grain surface chemistry network of [Semenov et al. \(2010\)](#) for modelling the chemistry of H-, O-, C-, S- and N-bearing molecules. In its current form it contains 191 neutrals, 6 anions and 265 cations in the gas-phase, 196 grain surface species, with the addition of electrons and dust grains in neutral, positively or negatively charged states, amounting to a total of 661 species.

The network incorporates all the gas phase reactions described in subsections 1.3.2, 1.3.3, 1.3.4 and summarized in Figure 1.3. The photochemistry is treated similarly as in the case of the NL99 network: the photodissociation rate coefficients take the attenuation of dust into account according to Eq. 1.25. The exceptions are H<sub>2</sub> and CO. In their case the self-shielding (and shielding by H<sub>2</sub> in case of CO) is also taken into account, as described in section 1.4.

The grain surface chemistry is based on the standard rate equation method ([Hasegawa et al., 1992](#)). The surface species are only allowed to sweep the grain surface by thermal hopping between surface sites. The desorption energies are adopted from ([Garrod and Herbst, 2006](#)).

The total number of reactions is 7383.

## 1.4 SHIELDING AND THE ATTENUATION OF THE INTERSTELLAR RADIATION

As we have seen in the previous section the ionizing and dissociating UV radiation plays a key role in the chemistry in diffuse and translucent clouds. With the increasing depth in the cloud these ionization and photodissociation events, in combination with dust absorption and scattering, attenuate the flux of energetic UV photons, thus decreasing the photochemical rates. For most molecule, the major process of shielding is due to dust absorption, and can be described by Eq. 1.25, where the  $\gamma_{\text{ph}}$  parameter depends on the species in question (e.g.  $\gamma_{\text{ph}} = 3.74, 3.53, 1.7, 3.1$  for H<sub>2</sub>, CO, CH and OH, respectively).

The H<sub>2</sub> and CO molecules are dissociated due to absorption at discrete frequencies. Furthermore both molecules have a very high abundance, so in addition to the dust shielding they can shield themselves and each other from the photodissociating radiation.

We take the free-space photodissociation rate of  $\text{H}_2$  to be  $3.3 \times 10^{-11} \text{ G s}^{-1}$ . The  $\text{H}_2$  self-shielding from the Lyman-Werner band radiation is described according [Draine and Bertoldi \(1996\)](#) as

$$\Theta_{\text{H}_2} = \frac{0.965}{(1 + x/b_5)^2} + \frac{0.035}{(1 + x)^{1/2}} \exp[-8.5 \times 10^{-4}(1 + x)^{1/2}], \quad (1.33)$$

where  $x = N_{\text{H}_2}/5 \times 10^{14} \text{ cm}^{-2}$  and  $b_5 = b/10^5 \text{ cm s}^{-1}$ , with the Doppler broadening parameter  $b$ . The formula is expected to overestimate the shielding if the gas flow is supersonic and the  $\text{H}_2$  column density is lower than  $10^{17} - 10^{18} \text{ cm}^{-2}$ . At higher column densities the line width is dominated by Lorentz broadening instead of the Doppler broadening, thus the shielding becomes independent of velocity gradient and dispersion.

The shielding of CO is a more complicated process. Besides the self-shielding, the shielding by the  $\text{H}_2$  column also has an important contribution. CO is expected to saturate at column densities higher than  $10^{15} \text{ cm}^{-2}$ , above which the photodissociation rate drops rapidly ([van Dishoeck and Black, 1988](#); [Lee et al., 1996](#); [Visser et al., 2009a](#)). This is an isotope selective process; due to the slightly shifted absorption lines (a result of slightly different molecular masses), each CO isotope has to build up the saturation column density on its own. The effects of this on the chemical state of the cloud are investigated in [chapter 2](#).

In this thesis, we adopt the CO shielding coefficient,  $\Theta_{\text{CO}}$ , tabulated by [Visser et al. \(2009a\)](#) as functions of CO and  $\text{H}_2$  column densities. The excitation temperature and the Doppler broadening are also important parameters of their modes, but we keep them constant at  $b(\text{CO}) = 0.3 \text{ km s}^{-1}$  and  $T_{\text{ex}}(\text{CO}) = 5 \text{ K}$ . Similarly to the  $\text{H}_2$  shielding prescription, this results in an overestimated shielding coefficient if the velocity dispersion is high and the column density is low.

In the three-dimensional space, a partial of gas within the cloud is irradiated from a  $4\pi sr$  solid angle. The attenuation in a given direction is then given by the total,  $\text{H}_2$  and CO column densities along that line of sight. There are several approximations to treat this in numerical simulations. The simplest approach is the local approximation, when it is assumed that the effective column density is given by the local volume density multiplied by a characteristic length (e.g. [Dobbs et al., 2006](#)). A more sophisticated approach, the so-called ‘‘six-ray’’ approximation, calculates the column densities in both the positive and negative directions along each of the three coordinate axis (e.g. [Nelson and Langer, 1997](#); [Yoshida et al., 2003](#)). Here we use an advanced version of the six-ray approach, the so called TreeCol method ([Clark et al., 2012a](#)), which accounts for the whole  $4\pi sr$  sky, covering it with a large number of rays (see [section 1.5.2](#)).

Once the column densities are known, the effective photochemical rate coefficients are calculated according:

$$k_{\text{ph,eff}} = \frac{1}{N_{\text{ray}}} \sum_{i=1}^{N_{\text{ray}}} \alpha_{\text{fs}} G \exp(-\gamma_{\text{ph}} A_{\text{V},i}), \quad (1.34)$$

where the coefficients have the same meaning as in [Eq. 1.25](#). We emphasize the important difference between averaging the photochemical rate coefficients and calculating the effective rate coefficient as a function of the column density and visual extinction average. The latter method is unphysical.

In case of  $\text{H}_2$  photodissociation the expression, with the self-shielding coefficient  $\Theta_{\text{H}_2}$ , takes the following form:

$$k_{\text{H}_2,\text{ph,eff}} = \frac{1}{N_{\text{ray}}} \sum_{i=1}^{N_{\text{ray}}} 3.3 \times 10^{-11} \Theta_{\text{H}_2}(N_{\text{H}_2,i}) G \exp(-3.74A_{V,i}) \text{ s}^{-1} \quad (1.35)$$

Similarly accounting for CO shielding by  $\text{H}_2$  and self-shielding we write:

$$k_{\text{CO,ph,eff}} = \frac{1}{N_{\text{ray}}} \sum_{i=1}^{N_{\text{ray}}} 2.6 \times 10^{-10} \Theta_{\text{CO}}(N_{\text{H}_2,i}, N_{\text{CO},i}) G \exp(-3.53A_{V,i}) \text{ s}^{-1}. \quad (1.36)$$

## 1.5 THE JOURNEY OF LIGHT – FROM MOLECULES TO THE OBSERVER

A reliable model of light propagation in molecular clouds, or as a matter of fact in any other astrophysical environments, is important for a variety of reasons: The radiative transfer models provide diagnostic links between observations and theoretical model predictions. Furthermore, radiative cooling (e.g through molecular lines) and radiative heating (e.g. due to the photoelectric effect of UV photons) are crucial processes in determining the thermal balance of the gas, thus its pressure and dynamics. Finally, the chemistry up to moderate visual extinction values is driven by photoionization, and dissociation by UV photons constitutes the main molecular destruction process.

In principle the propagation of electromagnetic radiation and its interaction with matter is described by the Maxwell equations. In practical cases, however, these are too complicated and often even not feasible to solve. We can still give a solution for the light propagation, by invoking the radiative transfer approximations. In this, we assume that the characteristic size of the object in which the light propagates is much larger than the wavelength of the radiation, thus the radiation can be treated within the framework of geometrical optics. Additionally, the densities are so low in the interstellar matter, that the index of refraction is virtually 1 everywhere. Thus we can assume that radiation propagates along straight rays. As the ray propagates through the matter, photons might be added to or removed from the ray. Spontaneous and induced emission enhance the ray, while scattering and absorption events diminish it.

However, even in this approximation, the modelling of light propagation is challenging. The processes adding or removing photons from the ray themselves are dependent on the state of matter, determined by the radiation arriving along other rays from the  $4\pi$  sr solid angle around the gas parcel. To know the state of matter in the parcel we need to know the radiation field. To establish the radiation field, the rate of addition and removal of photons needs to be known. To calculate these rates, we need to know the state of the matter, thus the circle closes. Especially when multi-dimensional models are considered, which sometimes even evolve with time (such is the case with our hydrodynamical simulations), further approximations need to be introduced. After the introduction of the radiative transfer formalism, we describe three such approximate methods for modelling the radiation field within the cloud. The first, the so-called TreeCol algorithm (Clark et al., 2012a) only considers the removal of photons from the ray and utilizes a small number of rays to cover the whole sky around the parcels of gas (i.e. each

SPH particle). Due to its computational cost efficiency we use this “on the fly” within the hydrodynamical models. The second approximation assumes that the gas is in local thermal equilibrium (LTE; e.g. [Carroll and Ostlie, 2007](#)), thus the emission/absorption state of the gas only depends on the kinetic gas temperature. Finally we describe the Sobolev ([Sobolev, 1957](#)) approximation, which takes sub-thermal excitation into account, but localizes the calculation of photon escape probabilities (i.e. the photon addition rate).

### 1.5.1 THE FORMAL RADIATIVE TRANSFER EQUATION

Usually a ray is quantified by its specific intensity. To arrive at its definition we shall consider the ray depicted in Fig. 1.4. A ray propagating at an angle  $(\theta, \phi)$  in a Cartesian coordinate system, passes through a surface area  $dA$  with a angle and diverges into a solid angle  $d\Omega$ . Angle  $\theta$  is measured perpendicular to the  $dA$  surface, thus its projection to the plane perpendicular to the direction of the ray is  $dA \cos \theta$ , while angle  $\phi$  is measured in the plane of the surface. The ray carries  $E_\nu d\nu$  energy in a frequency interval  $d\nu$  via the surface in the time interval  $dt$ . In this case, the specific radiation energy flux is given by  $F_\nu = E_\nu d\nu / (d\nu dt dA \cos \theta)$ . The specific intensity in turn is defined as the specific flux per solid angle, so we write

$$I_\nu \equiv \frac{dI}{d\nu} \equiv \frac{E_\nu d\nu}{d\nu dt dA \cos \theta d\Omega'} \quad (1.37)$$

The typical unit of intensity is  $\text{erg s}^{-1} \text{cm}^{-2} \text{Hz}^{-1} \text{sr}^{-1}$ . The advantage of this definition is that  $I_\nu$  is constant along any ray as it is passing through empty space, in contrast with the specific flux, which decreases with the square of distance travelled. The mean intensity,  $\langle I_\nu \rangle$  also often written as  $J_\nu$ , is defined as the integral of the specific intensity over all directions divided by the  $4\pi \text{sr}$  the solid angle,

$$\langle I_\nu \rangle = \frac{1}{4\pi} \int_{\phi=0}^{2\pi} \int_{\Theta=0}^{\pi} I_\nu \phi_\nu \sin \theta d\theta d\phi, \quad (1.38)$$

where  $\phi_\nu$  gives the probability of emission or absorption for a photon with frequency  $\nu$ . This coefficient is often called the line profile. In case of frequency independent radiation processes it is a constant over the whole frequency range. For isotropic emission  $\langle I_\nu \rangle = I_\nu$ , while for isotropic black body radiation  $\langle I_\nu \rangle = B_\nu$ .

The formal radiation transfer equation gives the change of  $I_\nu$  as the ray travels a small  $ds$  distance:

$$\frac{dI_\nu}{ds} = j_\nu - \alpha_\nu I_\nu, \quad (1.39)$$

where  $j_\nu$  is the emissivity and  $\alpha_\nu = \rho \kappa_\nu$  is the absorption coefficient. The absorption coefficient is given as the product of the gas density and the opacity ( $\kappa_\nu$ ), the cross section of absorbers per unit mass. The transfer equation is often written in terms of the optical depth ( $\tau$ ):

$$\frac{dI_\nu}{d\tau} = S_\nu - I_\nu, \quad (1.40)$$

where  $d\tau = \rho \kappa_\nu ds$  and  $S_\nu = j_\nu / \alpha_\nu$  is the source function, the ratio of the emission and absorption rates. If the intensity does not change, then the specific intensity is equal to the local source function. If the intensity is larger than the source function,

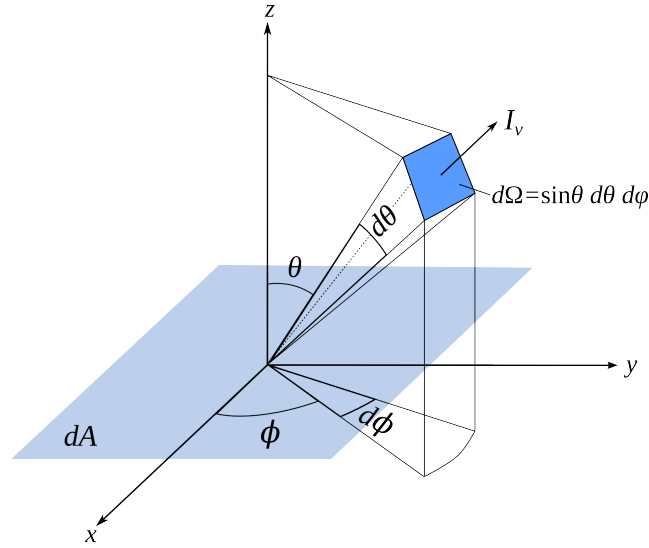


Figure 1.4: A ray of light with frequency between  $\nu$  and  $\nu + \Delta\nu$  passes through a  $dA$  surface area at an angle  $\theta$  into a solid angle cone  $d\Omega$ . The specific intensity ( $I_\nu$ ) is the monochromatic energy flux through the cone per solid angle. Adapted from [Carroll and Ostlie \(2007\)](#).

then it decreases with distance (or optical depth), while if it is smaller then increases. This shows the tendency of radiation to approach the source function. In LTE the source function is equal to the Planck function.

### 1.5.2 THE TREECOL ALGORITHM

Occasionally, the object under investigation might act only as absorber of a certain type of radiation. If the emissivity is neglected the solution for the radiative transfer equation takes the form of

$$I_\nu(s) = I_{\nu,0} \exp(-\kappa_\nu \rho s) = I_{\nu,0} \exp(-\tau(s)). \quad (1.41)$$

If we narrow our study to a specific wavelength range, e.g. the photons which fall to the Lyman-Werner band, and the properties of the medium are affected equally by each photons in the range, then the frequency dependence of the equation may be neglected.

One such case is the attenuation of interstellar UV photons in the Lyman-Werner band. In the early stages of molecular cloud evolution, when stars have not formed yet, the only source of UV radiation is the diffuse interstellar radiation field. The photoelectric heating rate and the rate of photochemical reactions driven by the UV photons, at least to first order are proportional to the total incident intensity in the band. When  $I_0$  is known, the problem of radiation transport simplifies to the calculation of optical depth, or analogously, for a homogeneous and isotropic  $\kappa$  the column density ( $N_{\text{col}} \propto \rho ds$ ). In the knowledge of the column density the attenuation of radiation field by dust (Eq. 1.25) and the molecular shielding factors (e.g. Eq. 1.33 for  $\text{H}_2$ ) can be calculated. As we pointed out in the previous sections, these processes have important effects on the gas dynamics. Therefore we want to model them alongside the integration of the hydrodynamical and chemical

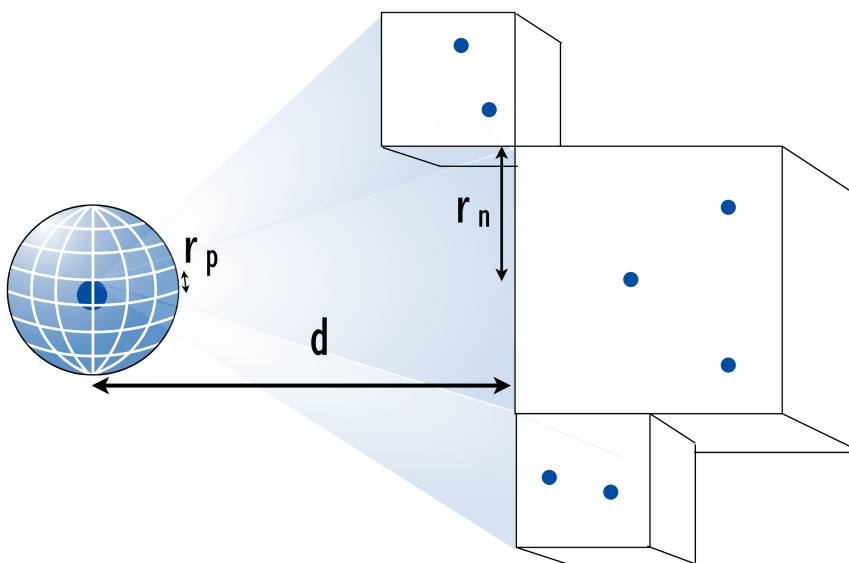


Figure 1.5: Schematic illustration of the TreeCol concept. The  $4\pi sr$  map of column densities is being mapped in case of the particle on the left, while the gravitational tree is walked to calculate the gravitational force acting on it. The tree already contains the information necessary (i.e. the node mass, location and apparent size seen from the particle center) for the column density calculation. The figure was originally published in Clark et al. (2012a).

equations. This task is only feasible with reasonable computational resources if a very efficient algorithm for column density calculation is put into use.

The TreeCol (Clark et al., 2012a) algorithm is one such method (i.e. the frequency dependent raytracing scales as  $N_\nu \log N^{5/3}$ , where  $N_\nu$  is the number of frequencies traced, while TreeCol as  $N \log N$ ). It maps the column density distribution onto a spherical grid around a particle (or voxel). It can be used in numerical simulations, which implement hierarchical trees for the gravitational force calculation. The basic idea of TreeCol is to divide the  $4\pi sr$  “sky” around a particle into equal area pixels, and then add up the column density contribution of each hierarchical structure in the tree to the pixel to which they fall.

As a first step, the equal area representation of the spherical surface around the particle is utilized. For this the HEALPIX<sup>6</sup> (Hierarchical Equal Area isoLatitude Pixelization of a sphere, Górski et al., 2005) algorithm is used. The requirement of equal area pixels restricts the choice of pixels (i.e. rays to be consistent with the previously used terminology) number, according  $N_{\text{ray}} = 12 \times N_{\text{side}}^2$ , where  $N_{\text{side}}$  is a power of 2, thus  $N_{\text{ray}} = 12, 48, 192$  and so on.

Once the pixelization of the sky is defined, the hierarchical tree is walked. In section 1.2.3 we already described how the oct-tree works for the gravitational potential estimation. TreeCol follows the same procedure. Once a node is found to fulfil the angular size criterion, the coordinates of the node are used to calculate

<sup>6</sup><http://healpix.jpl.nasa.gov/>

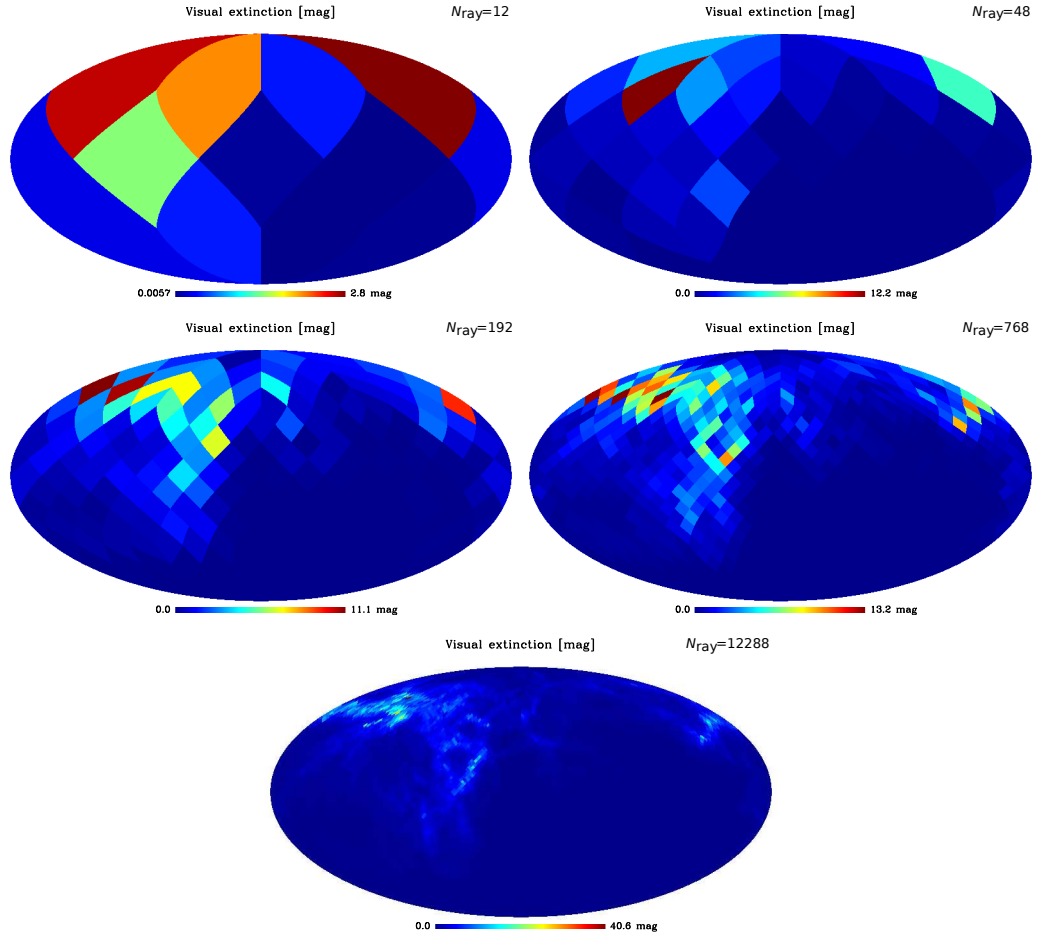


Figure 1.6: HEALPIX projection of the total column density distribution of the sky in simulation (d) (see Table 2.1), calculated with increasing number of rays. We find that 48 equal area pixel is enough to retrieve the true mean visual extinction with about 5 per cent accuracy.

the overlap between the node and the HEALPIX pixelation. The column density contribution, which is defined as the node density times the radial extent of the node, is added to the pixel column density value in a fraction corresponding to their overlap. One should also mention that the method assumes the nodes to be always seen as squares on the sky of the particle, regardless of their true orientation in three-dimensional space. It is also assumed that the overlapping region of the node and pixels can be defined based on simple orthogonal coordinates in the plane of the sky (i.e. spherical trigonometry is not considered).

Figure 1.6 illustrates how the visual extinction distribution of the sky looks for a particle in one of our simulation (model d in chapters 2 and 3 with progressive resolution). In the simulation we chose 48 pixels per particle. Clark et al. (2012a) showed that this number is sufficient to approximate the true distribution with less than 15 per cent error. The algorithm is used in the simulations to estimate the total ( $N_{\text{H,tot}} \simeq N_{\text{H}} + 2N_{\text{H}_2} + N_{\text{H}^+}$ ),  $\text{H}_2$  and CO column densities for each particles. This data is then used for the calculation of shielding in the photochemical rates.

### 1.5.3 LINE RADIATIVE TRANSFER IN LTE

Often the gas parcels within the cloud themselves are contributing to or even the sole sources of the radiation intensity. In such cases the emissivity cannot be neglected. Furthermore, the frequency dependence of the intensity, while it provides information on the velocity structure of the emitting or absorbing medium, might be a major focus of interest. A common example for these is the ro-vibrational line emission from interstellar molecules. In chapters 2 and 3 we model the low-lying rotational transitions of CO isotopes using snapshots from the hydrodynamic simulations as physical models and then compare these to observations or analyse them adopting observational techniques. Therefore, we see it necessary to explain the basics of molecular excitation and radiation transport.

Molecules are not rigid, suspended objects. They are capable of rotational, vibrational and translational motions. The rotational and vibrational modes are associated with certain discrete energy levels. A molecule can jump between these levels either due to collision with other molecules or by absorbing or emitting a photon. The frequency of the absorbed or emitted photon is discrete too and it depends on the difference in the energies associated with the starting and final states. For instance, the transition from excited state  $i$  to ground state  $j$  results in the emission of a photon with a frequency defined according

$$h\nu_{ij} = E_i - E_j, \quad (1.42)$$

where  $E_i$  and  $E_j$  are the energies of states  $i$  and  $j$ . When more than one molecule of a kind is considered, we define the relative population of level  $i$  as

$$f_i = n_i / \sum_{j=1}^{N_{\text{lev}}} n_j, \quad (1.43)$$

where  $n_i$  denotes the number density of the molecule in energy state  $i$  and the sum stands for the total number density of the molecule (including all energy levels). In statistical equilibrium  $f_i$  is determined by the equation of detailed balance:

$$\sum_{j>i} [f_j A_{ji} + (f_j B_{ji} - f_i B_{ij}) \langle I_{ji} \rangle] - \sum_{j<i} [f_i A_{ij} + (f_i B_{ij} - f_j B_{ji}) \langle I_{ij} \rangle] + \sum [f_j C_{ji} - f_i C_{ij}] = 0, \quad (1.44)$$

where the first summation accounts for the increase in  $f_i$  due to decay from higher energy levels, the second summation stands for the decrease in the relative population of  $i$  due to its decay to lower energy levels, while the last summation represents the change of relative populations due to collisions. The  $A_{ij}$ ,  $B_{ij}$  and  $B_{ji}$  coefficients are the Einstein coefficients of spontaneous emission for a transition from level  $i$  to  $j$ , stimulated emission from level  $i$  to  $j$  and absorption from level  $j$  to  $i$ . The  $C_{ij}$  collisional rate depends on the rate coefficient  $K_{ik}$  and the number density of the collisional partner(s).

The equation of detailed balance is coupled to the transfer equation (Eq. 1.40) through the source function,  $S_{ij}$ , which is given in this case as

$$S_{ij} = \frac{f_i A_{ij}}{f_j B_{ij} - f_i B_{ij}'}, \quad (1.45)$$

and the integrated mean intensity,  $\langle I_{ij} \rangle$ , which is calculated according to Eq. 1.38. The fact that the emission happens at discrete frequencies is taken into account of by the  $\phi_{ij}(v)$  line profile;

$$\phi_{ij}(v) = \frac{c}{av_{ij}\sqrt{\pi}} \exp \left[ -\frac{c^2(v - v_{ij} - \vec{v} \cdot \hat{n}v_{ij}/c)^2}{a^2v_{ij}^2} \right], \quad (1.46)$$

where  $c$  is the light speed,  $\vec{v}$  is the gas velocity,  $\hat{n}$  is the normal vector of the ray and  $\vec{v} \cdot \hat{n}$  is the amplitude of gas velocity, projected onto the ray. The line broadening parameter,  $a$  depends on the temperature and the microturbulent, unresolved motions ( $v_{\text{mt}}$ ) of the gas,

$$a^2 = v_{\text{mt}}^2 + \frac{2k_{\text{B}}T_{\text{g}}}{m_{\text{mol}}}. \quad (1.47)$$

It is difficult to solve the coupled equations 1.40, 1.44 and 1.45, because gas parcels with large physical separations are linked and interact through the mean intensity. One option for solving the problem employs repeated iterations, until the molecular level populations at each point in the considered domain (in the molecular cloud) reaches a steady state. This is computationally expensive and often not feasible in high resolution cases. An alternative solution is the localization of the problem.

One way to localize the problem is to assume, the gas is in Local Thermal Equilibrium (LTE). The LTE approximation hold if the gas density is high and the (de)excitation is dominated by collisions. In this case the molecular level population follows the Boltzmann distribution and can be described by a single parameter, the local kinetic (i.e. gas) temperature:

$$f_i = \frac{1}{Z(T_{\text{g}})} g_i \exp \left( -\frac{E_i}{k_{\text{B}}T_{\text{g}}} \right), \quad (1.48)$$

where  $Z(T_{\text{g}})$  is the partition function, which is a summation over all possible energy levels:

$$Z(T_{\text{g}}) = \sum_{j=1}^{N_{\text{lev}}} g_j \exp \left( -\frac{E_j}{k_{\text{B}}T_{\text{g}}} \right), \quad (1.49)$$

where  $g_i$  and  $g_j$  are the statistical weights of states  $i$  and  $j$ . The statistical weight accounts for degenerate states, which have the same energy. The validity of the LTE approximation depends on the value of the density compared to the molecules critical density. The critical density for the  $i \rightarrow j$  transition of a species is defined as  $n_{\text{crit}} \approx A_{ij} / \langle \sigma_{\text{ccs}} v \rangle$ , where  $\sigma_{\text{ccs}}$  is the collisional cross section and  $v$  is the gas velocity. According the Leiden Atomic and Molecular Database<sup>7</sup>, the Einstein coefficient for spontaneous emission, in case of the transition between the lowest excited state and the ground state of CO is  $7.2 \times 10^{-8} \text{s}^{-1}$ . The typical collisional cross section is about  $10^{-15} \text{cm}^2$  and the typical speeds are on the order of  $10^4 \text{cm s}^{-1}$ . Using these values, the critical density for the CO  $J = 1 \rightarrow 0$  transition is on the order of  $10^3 \text{cm}^{-3}$ . A similar value can be derived, for instance, for the NH<sub>3</sub> molecule. If the density is higher than the critical, then the excitation and deexcitation is dominated by collisions between molecules, and thus the LTE approximation works well.

<sup>7</sup><http://home.strw.leidenuniv.nl/~moldata/>

Although their critical densities are very similar, the LVG approximation works better for ammonia than for CO. The reason lies in their chemistry: CO molecules might already effectively form in a dilute gas with a density of a few hundred particles per  $\text{cm}^3$ , while for  $\text{NH}_3$  formation a considerably higher density is required, partly due to its grain-surface formation route. In fact, [Pineda et al. \(2008\)](#) finds in the Perseus molecular cloud, that about 60 per cent of the CO emission originates from subthermally excited regions.

#### 1.5.4 THE SOBOLEV APPROXIMATION

As we mentioned in the previous section, the assumption of LTE is often invalid for the most frequently used molecular tracer, the CO molecule. To model the emission of this molecule reliably, we need to use an approximation which accounts for the absorption and emission of photons when the level populations are computed but is still fast enough that we can apply it to large three-dimensional models.

In this thesis we use the Sobolev or Large Velocity Gradient (LVG) approximation ([Sobolev, 1957](#); [Mihalas et al., 1978](#); [Ossenkopf, 1997](#); [Shetty et al., 2011a](#)). In this approach, the equation of detailed balance (Eq. 1.44) is solved by assuming that the mean intensity ( $\langle I_{ij} \rangle$ ) originates completely from the photons emitted locally, and the photons emitted elsewhere in or outside of the cloud cannot excite molecules in the parcel under consideration. The mean intensity is proportional to the source function:

$$\langle I_{ij} \rangle = S_{ij}(1 - \beta_{\text{LVG}}), \quad (1.50)$$

where  $\beta_{\text{LVG}}$  denotes the photon escape probability. Note that in LTE the source function is equal to the mean intensity, thus a small escape probability would result in falling back to the LTE case. The escape probability depends on the optical depth ( $\tau$ ) of the transition and it is given according to

$$\beta_{\text{LVG}} = \frac{1}{\tau} \int_0^{\tau} \exp(-\tau') d\tau' = \frac{1 - \exp(-\tau)}{\tau}. \quad (1.51)$$

The optical depth is estimated from the local density ( $n$ ), the local population levels and the velocity gradient with the neighbouring cells ([van der Tak et al., 2007](#); [Shetty et al., 2011a](#)):

$$\tau = \frac{c^3}{8\pi v_{ij}^3} \frac{A_{ij} n}{1.065 \langle |dv/dr| \rangle} \left( f_j \frac{g_i}{g_j} - f_i \right), \quad (1.52)$$

where  $\langle |dv/dr| \rangle$  is effective velocity gradient, i.e. in a Cartesian grid it is the mean value of velocity gradients with the six direct neighbour cells.

The fundamental idea of the approximation is evident from Eq. 1.52: if there is a large velocity difference between neighbouring parcels, then the photons emitted in one parcel cannot interact with the same molecule in another parcel, due to the large Doppler shift between the former parcel's emission and the latter's absorption. The larger the velocity gradient the lower the optical depth becomes. In turn, the escape probability increases. Thus the Sobolev approximation works the best, if the velocity gradients with the surrounding parcels are large (hence the name).

The Sobolev approximation was originally developed for modelling stellar atmospheres. [Ossenkopf \(1997\)](#) showed that the method also works well in lower

density GMCs, even if the requirement of large velocity gradients are not strictly met. In this thesis we use the Sobolev approximation implemented in the RADMC-3D multi-dimensional radiative transfer code<sup>8</sup> by Shetty et al. (2011a).

## 1.6 THE AIMS OF THIS THESIS

The main theme of this thesis is to use numerical simulations of giant molecular clouds, which take the turbulent nature of the gas, the light propagation and attenuation and the chemical evolution into account, for the purpose of testing and constraining frequently used observational and theoretical approximations and measurement methods. For the first time, we also present theoretical predictions for column densities, abundance ratios and radial distributions of complex molecules, which are otherwise neglected in dynamical simulation, due to the numerous chemical species and thus long computational time required for their reliable modelling. We organize the chapters of the thesis as follows:

In chapter 2 we investigate the  $^{12}\text{CO}/^{13}\text{CO}$  isotope ratio in low mass GMC, by taking the preferential photodissociation of  $^{13}\text{CO}$  and the temperature dependent chemical fractionation reaction into account. In both observational (Pineda et al., 2008) and theoretical (Beaumont et al., 2013) studies the value of the ratio is often taken to be constant over all lines of sight. We aim to investigate whether this assumption is, on average, an acceptable simplification or whether there are systematic deviations, which need to be considered.

In chapter 3 we explore a wider range in cloud properties, and benchmark a number of CO emission based observational methods for cloud mass and column density determination, such as the LTE column density inference of the  $^{13}\text{CO}$  column density (Pineda et al., 2008, 2010), the virial mass analysis (e.g. Kauffmann et al., 2013) and the CO-to- $\text{H}_2$  conversion factor (e.g. Bolatto et al., 2013). We are aiming to test which method gives the best estimates under which conditions.

In chapter 4 we extend the number of chemical species studied, by utilizing a more complete chemical model than in the previous chapters. We choose a dense core region in the simulation volume and follow the detailed chemical evolution of the particles constituting it as a post-processing step. We aim to compare the CO chemistry with increasingly complex chemical networks and to derive volume and column densities of species, such as  $\text{NH}_3$ ,  $\text{N}_2\text{H}^+$ ,  $\text{HCO}^+$ ,  $\text{CH}_3\text{OH}$  and  $\text{HCOOCH}_3$ . We compare the results to recent measurements of the chemical composition of infrared dark clouds (IRDCs) (Gerner et al., 2014).

Finally, in chapter 5 we summarize the results of the thesis.

---

<sup>8</sup><http://www.ita.uni-heidelberg.de/~dullemond/software/radmc-3d/>

## 2 THE $^{12}\text{CO}/^{13}\text{CO}$ RATIO IN TURBULENT MOLECULAR CLOUDS

*Adapted from Szűcs, Glover & Klessen, MNRAS (2014), vol 445, 4055<sup>1</sup>*

### ABSTRACT

The  $^{13}\text{CO}$  molecule is often used as a column density tracer in regions where the  $^{12}\text{CO}$  emission saturates. The  $^{13}\text{CO}$  column density is then related to that of  $^{12}\text{CO}$  by a uniform isotopic ratio. A similar approximation is frequently used when deriving  $^{13}\text{CO}$  emission maps from numerical simulations of molecular clouds. To test this assumption we calculate the  $^{12}\text{CO}/^{13}\text{CO}$  ratio self-consistently, taking the isotope selective photodissociation and the chemical fractionation of CO into account. We model the coupled chemical, thermal and dynamical evolution and the emergent  $^{13}\text{CO}$  emission of isolated, starless molecular clouds in various environments. Selective photodissociation has a minimal effect on the ratio, while the chemical fractionation causes a factor of 2-3 decrease at intermediate cloud depths. The variation correlates to both the  $^{12}\text{CO}$  and the  $^{13}\text{CO}$  column densities. Neglecting the depth dependence results in  $\leq 60$  per cent error in  $^{12}\text{CO}$  column densities derived from  $^{13}\text{CO}$ . The same assumption causes  $\leq 50$  per cent disparity in the  $^{13}\text{CO}$  emission derived from simulated clouds. We show that the discrepancies can be corrected by a fitting formula. The formula is consistent with millimetre-wavelength isotopic ratio measurements of dense molecular clouds, but underestimates the ratios from the ultraviolet absorption of diffuse regions.

### 2.1 INTRODUCTION

The carbon monoxide molecule (CO) and its isotopes are the most widely used gas-phase tracers of total column density in the interstellar medium (ISM). In contrast to the hydrogen molecule, CO is asymmetric and hence has a permanent dipole moment ( $\mu_{\text{dp}} = 0.112 \text{ Debye} = 3.736 \times 10^{-31} \text{ Cm}$ ). Its dipole transitions between rotational levels can be excited at temperatures (few  $\times 10$  K) and densities ( $\approx 300 \text{ cm}^{-3}$ ) typical of giant molecular clouds (GMCs). The emission from the lowest transitions is relatively easily detectable at millimetre wavelengths. Due to its high fractional abundance ( $\chi_{\text{CO}} \approx 10^{-4}$ , in equilibrium at high density) the emission of the most abundant CO isotope ( $^{12}\text{CO}$ ) is usually optically thick, therefore only lower limits of the total column density could be derived. To achieve better total column density estimates, less abundant CO isotopes are used (usually  $^{13}\text{CO}$  and  $\text{C}^{18}\text{O}$ ). The simplest and most often used method is the following (e.g. [Pineda et al., 2008](#); [Wilson et al., 2009](#); [Pineda et al., 2010](#)): The  $^{12}\text{CO}$  emission is assumed to

---

<sup>1</sup>See page [xi](#) for details on authorship.

be fully optically thick and in local thermodynamic equilibrium (LTE), allowing the excitation temperature of  $^{12}\text{CO}$  to be calculated. If the excitation temperature is the same for  $^{13}\text{CO}$  and if  $^{13}\text{CO}$  is optically thin, a simple relation between the integrated intensity along the line of sight,  $W(^{13}\text{CO})$ , and the column density of  $^{13}\text{CO}$ ,  $N(^{13}\text{CO})$  can be derived (e.g. see equation 9 in [Pineda et al., 2008](#)). The  $^{13}\text{CO}$  column densities are then usually converted into  $^{12}\text{CO}$  column densities using a uniform  $^{12}\text{CO}/^{13}\text{CO}$  isotope ratio. Finally, the  $^{12}\text{CO}$  column density is transformed to total column density assuming a given conversion factor between CO and  $\text{H}_2$ . The high uncertainties and environmental dependence of this final step have been extensively studied in the literature ([Shetty et al., 2011a,b](#); [Glover and Mac Low, 2011](#); [Feldmann et al., 2012](#), and references within). We discuss this method for column density estimation further in section 3.4.

However, the  $^{12}\text{CO}/^{13}\text{CO}$  ratio may vary considerably. Typically it is chosen to be equal to the measured  $^{12}\text{C}/^{13}\text{C}$  ratio ([Pineda et al., 2010](#)). The carbon isotope ratio, however, shows large regional variations. Based on observations of millimetre-wavelength emission of CO isotopes, [Langer and Penzias \(1990\)](#) found a systematic gradient with galactocentric distance in the carbon isotope ratio, ranging from 24 in the Galactic Center to about 70 at  $\sim 12$  kpc. They found the average ratio to be 57 at the solar galactocentric distance, which shows  $^{13}\text{C}$  enhancement compared to the value of 89 measured in the Solar System ([Geiss, 1988](#)). Observations of CO absorption in ultraviolet electronic and near-infrared vibrational transitions (e.g. [Scoville et al., 1983](#); [Mitchell and Maillard, 1993](#); [Goto et al., 2003](#); [Sonnentrucker et al., 2007](#); [Sheffer et al., 2007](#)) find up to a factor of 3 higher ratios in the solar neighbourhood. Nevertheless, the most frequently adopted ratios are between 57 ([Langer and Penzias, 1990](#)) and 69 ([Wilson, 1999](#)), the measured average values for the interstellar medium within a few kpc of the Sun.

The gradient with galactocentric distance and the  $^{13}\text{C}$  enhancement in the Solar neighbourhood compared to the Solar System value could be interpreted in the framework of the carbon isotopic nucleosynthesis.  $^{12}\text{C}$  is the primary product of the triple-alpha process during the post Red Giant Branch (RGB) evolution of massive stars. The rarer  $^{13}\text{C}$  is produced from  $^{12}\text{C}$  as a secondary product in the CNO cycle during the RGB phase of low and intermediate mass stars. Due to the longer lifetime of low and intermediate mass stars – which are the main contributors of  $^{13}\text{C}$  enrichment – the  $^{12}\text{C}/^{13}\text{C}$  ratio is expected to decrease with time and to depend on the star formation history ([Audouze et al., 1975](#)).

More important for our problem, however, is the fact that the CO isotope ratio could vary by a factor of a few even if the elemental  $^{12}\text{C}/^{13}\text{C}$  ratio is constant in a region under investigation, due to isotope-selective chemical processes. For example, [van Dishoeck and Black \(1988\)](#) describe qualitatively the CO isotopic chemistry in molecular clouds as follows (see Fig. 2.1). The preferred pathways of CO production are the ion-neutral reaction of  $\text{C}^+$  and OH producing  $\text{HCO}^+$ , which dissociatively recombines to CO and H, and the neutral-neutral reaction of CH or  $\text{CH}_2$  with an oxygen atom. These reactions are not isotope-selective and work (with varying efficiency) in every region of the molecular cloud. In the diffuse regions (gray,  $A_V < 0.5 \text{ mag}^2$ ) the photodissociation of CO by interstellar far-ultraviolet (FUV) photons dominates over the production reactions and most of the carbon

---

<sup>2</sup>The exact visual extinction values depend on the strength of the incident radiation field and the density distribution.

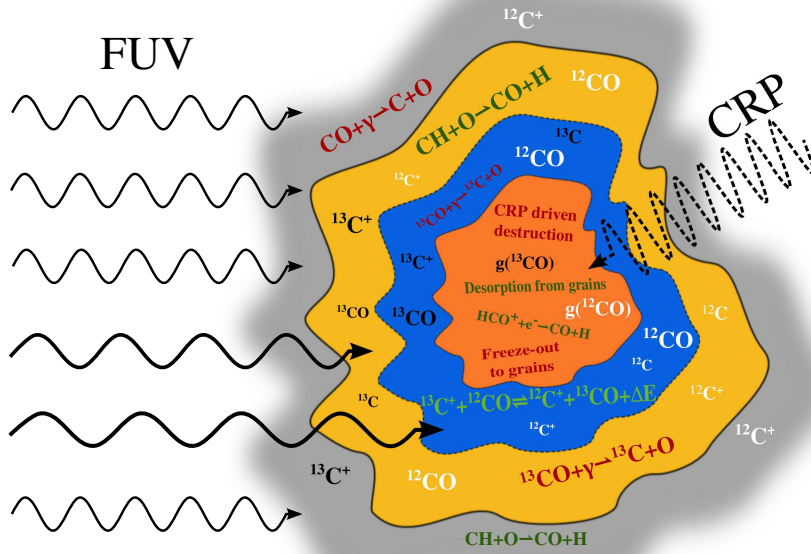
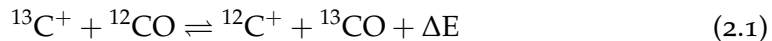


Figure 2.1: Qualitative picture of carbon isotopic chemistry in molecular clouds. The outer diffuse layer (gray) is followed by the translucent (yellow and blue) and the inner, dense regions (orange). The font size of the chemical species relates to the abundance of the species in the region. The font size of chemical reactions indicates the importance of the reaction in the region, the green and red colors represent reactions producing and destroying CO. When a particular isotopic species is not indicated, then both species are affected. Based on [van Dishoeck and Black \(1988\)](#).

is in ionized form. In translucent regions (yellow,  $1 \text{ mag} < A_V < 2 \text{ mag}$ ) the CO production rates start to compete with the photodissociation. The  $^{12}\text{CO}$  column density becomes high enough to effectively self-shield itself from the incident interstellar FUV photons. However,  $^{13}\text{CO}$ , due its slightly shifted absorption lines at UV wavelengths and the lower abundance, is less effectively self-shielded. This difference in self-shielding, in principle, leads to isotope-selective photodissociation. In practice, the selective photodissociation is expected to be dominant only in low density ( $n < 10^2 \text{ cm}^{-3}$ ) domains or in dense regions with very strong radiation fields (see [Röllig and Ossenkopf, 2013](#)). Further in (blue,  $2 \text{ mag} < A_V < 5 \text{ mag}$ ), due to the shielding by dust absorption and the increasing  $^{13}\text{CO}$  column density, both isotopic species are effectively protected from FUV photons. In this region ionized carbon is still abundant and the



fractionation reaction ([Watson et al., 1976](#)) becomes important. At temperatures typical to the corresponding cloud depths, the exothermic reaction (to the right, leads to energy release) is preferred, resulting in more  $^{13}\text{CO}$  production, and consequently in a reduced isotope ratio. This reaction provides the main  $^{13}\text{CO}$

production and destruction paths in this region. On the other hand, the destruction of  $^{12}\text{CO}$  is determined by the competing effects of photodissociation, chemical fractionation and dissociative charge transfer with  $\text{He}^+$ , while its production is mainly due to the neutral-neutral reaction of light hydrocarbons with oxygen. At the highest column densities (orange,  $A_V > 5$  mag) the CO chemistry is governed by non-isotope-selective reactions. The gas phase production of both CO isotopes happens through  $\text{HCO}^+$  recombination and desorption from dust grains, while the main destruction channels are the dissociative charge transfer with  $\text{He}^+$  and  $\text{H}_3^+$ , photodissociation by cosmic-ray induced photons, and freeze-out onto grains. As a result, the isotope ratio approaches to the elemental ( $^{12}\text{C}/^{13}\text{C}$ ) ratio. Due to these processes we expect that the CO isotope ratio varies significantly even within the same GMC. In fact, observational studies report a factor of a few region-by-region variation. In the case of the Taurus molecular cloud, the indirect measurements of Goldsmith et al. (2008) and Pineda et al. (2010) find isotope ratios between 30 and the canonical value of 69, suggesting  $^{13}\text{CO}$  enrichment.

The direct determination of the  $^{12}\text{CO}/^{13}\text{CO}$  ratio is usually difficult and restricted to a certain column density range. For instance, the ultraviolet and millimetre-wavelength absorption measurements, such as presented by Sheffer et al. (2007), Sonnentrucker et al. (2007) and Liszt and Lucas (1998), require suitable galactic or extragalactic background sources and CO column densities, which fall into the optically thin, diffuse regime ( $N(^{12}\text{CO}) < \text{few} \times 10^{16} \text{ cm}^{-2}$ ). Observations of millimetre-wavelength emission from GMCs (e.g. Pineda et al., 2008; Goldsmith et al., 2008; Pineda et al., 2010), however, usually trace the higher CO column density regions, where the isotope ratio-column density correlation is not constrained by observations, and therefore as a “best guess” a uniform isotope ratio is adopted.

The inverse problem emerges when  $^{13}\text{CO}$  emission is inferred from (magneto-) hydrodynamical simulations. The computational cost of the chemical modelling scales with the cube of the number of species considered (Glover and Clark, 2012a). Even when only 14 self-consistently calculated (i.e. not described by conservation laws), non-equilibrium species are included in the network, the chemistry will often be the dominating factor in terms of computational cost, taking up to 90 per cent of the total computational time (Glover et al., 2010; Glover and Clark, 2012a). For the practical reason of cost efficiency usually only the most common isotope,  $^{12}\text{CO}$  is included in the chemical networks. When observable quantities, like emission from rarer CO isotopes are inferred from such simulations (e.g. Beaumont et al., 2013) the canonical isotope ratio is adopted and assumed to be constant through the whole simulation domain.

In this chapter we investigate the effect of *selective photodissociation* and *chemical fractionation* on the  $^{12}\text{CO}/^{13}\text{CO}$  isotopic ratio in different environments and for different cloud properties, using turbulent hydrodynamical simulations that include a self-consistent chemical and cooling model and an approximate treatment of the attenuation of the interstellar radiation field (ISRF). One of our aims is to test and improve the frequently used assumption of uniform  $^{12}\text{CO}/^{13}\text{CO}$  ratio in the context of inferring  $^{13}\text{CO}$  emission from simulations which neglect isotopic chemistry. We also provide a prescription for deriving the isotope ratio from the  $^{13}\text{CO}$  column density (e.g. calculated from observations).

In section 2.2 we describe the numerical setup and the initial conditions of our simulations. Section 2.3 discusses the correlation between various (total,  $^{12}\text{CO}$

Table 2.1: Model parameters and used snapshots

Model	$n_0$ [cm <sup>-3</sup> ]	Metallicity [ $Z_\odot$ ]	ISRF [ $G_0$ ]	Time [Myr]
a	300	0.3	1	2.046
b	300	0.6	1	1.930
c	300	1	0.1	2.124
d	300	1	1	2.150
e	300	1	10	2.022
f	1000	1	1	0.973
g	300	1	1	2.150

Summary of model parameters. Each model cloud has  $10^4 M_\odot$  and an SPH mass resolution of  $0.5 M_\odot$ . In each case the analysed snapshots are chosen to represent the molecular clouds preceding sink particle formation.  $Z_\odot$  and  $G_0$  refer to the Solar metallicity and Draine radiation field strength (1.7 in units of the [Habing \(1968\)](#) field) respectively. Models from a) to f) have fully molecular initial conditions while model g) was calculated with atomic initial composition.

and  $^{13}\text{CO}$ ) column densities and the isotope ratio for different cloud conditions. We also propose a formula for inferring  $^{13}\text{CO}$  column/number densities from  $^{12}\text{CO}$  in simulations neglecting fractionation chemistry, and one for calculating the isotope ratio from observations of  $^{13}\text{CO}$ . Then in section 2.4, we post-process the simulations with line radiative transfer to quantitatively compare the emergent  $^{13}\text{CO}$  line profiles and emission maps in case of self-consistently calculated, column density dependently inferred and uniform isotope ratios. Section 2.5 compares our results to previous theoretical works and to observations of the  $^{12}\text{CO}/^{13}\text{CO}$  column density ratio. We summarize the results and draw our final conclusions in section 2.6.

## 2.2 SIMULATIONS

We use a modified version of the smoothed particle hydrodynamics (SPH) code `GADGET-2`<sup>3</sup>, described by [Springel \(2005\)](#). The modifications include a sink particle algorithm ([Bate et al., 1995](#); [Jappsen et al., 2005](#); [Federrath et al., 2010](#); [Glover and Clark, 2012b](#)), a simplified model of the gas phase chemistry with radiative heating and cooling ([Glover and Clark, 2012a](#)) and an approximate treatment of the attenuation of the ISRF ([Clark et al., 2012a](#)). Stellar feedback from the formed sink particles is not included, an effect which could influence the CO isotope ratio in high density regions significantly. Therefore, we restrict our analysis and discussion to cloud properties before sink particle formation (i.e. to molecular clouds in an early stage of evolution).

<sup>3</sup><http://www.mpa-garching.mpg.de/gadget/>

### 2.2.1 CHEMISTRY

We adopt the chemical network of [Nelson and Langer \(1999\)](#) (hereafter NL99) supplemented with the hydrogen chemistry of [Glover and Mac Low \(2007b\)](#). The network was designed to follow CO formation and destruction over a wide density range in molecular clouds. It takes multiple CO formation pathways into account: a formation channel involving the composite  $\text{CH}_x$  ( $\text{CH}$  and  $\text{CH}_2$ ) species, another involving the composite  $\text{OH}_x$  ( $\text{OH}$ ,  $\text{H}_2\text{O}$  and  $\text{O}_2$ ) species and a third route via the dissociative recombination of  $\text{HCO}^+$ . The destruction of CO could happen due to photodissociation, dissociative charge transfer with  $\text{He}^+$  or through proton transfer from  $\text{H}_3^+$  resulting in the conversion of CO to  $\text{HCO}^+$ . See Table 1 in [Glover and Clark \(2012a\)](#) for the full list of reactions and the Appendix B of [Glover et al. \(2010\)](#) for the adopted reaction rate coefficients.

Initially the NL99 network does not account for the  $^{13}\text{C}$ ,  $^{13}\text{C}^+$ ,  $^{13}\text{CO}$  and  $\text{H}^{13}\text{CO}^+$  isotopes. Therefore we add these species and the corresponding reactions, which are non-isotope-selective, from the original network. We do not apply rescaling on the reaction rate coefficients of these reactions. In addition, to allow conversion of  $^{12}\text{CO}$  to  $^{13}\text{CO}$ , we implemented the  $^{13}\text{CO}$  fractionation reaction (equation 2.1, with the left to right rate coefficient of  $r_{\text{frac,CO,lr}} = 2 \times 10^{-10} \text{cm}^3 \text{s}^{-1}$  and the temperature dependent right to left rate coefficient of  $r_{\text{frac,CO,rl}} = 2 \times 10^{-10} \exp(-35 \text{K}/T_{\text{gas}}) \text{cm}^3 \text{s}^{-1}$ . Although, [Smith and Adams \(1980\)](#) suggests an order of magnitude higher rate coefficient, [Sheffer et al. \(2007\)](#) finds that the smaller value of [Watson et al. \(1976\)](#) is more consistent with the observations, therefore we adopt the latter. The free-space  $^{12}\text{CO}$  and  $^{13}\text{CO}$  photodissociation rate coefficients in the absence of absorbing material are taken to be equal with the value of  $r_{\text{pd,CO,thin}} = 2.6 \times 10^{-10} \text{s}^{-1}$  ([Visser et al., 2009a](#)) for the interstellar radiation field strength equal to  $1 \times G_0$ . In addition to the reactions included in the [Nelson and Langer \(1999\)](#) chemical network, we also include the cosmic-ray induced photodissociation of CO ([Prasad and Tarafdar, 1983](#); [Gredel et al., 1987](#)) and the cosmic-ray induced photoionization of C. The reaction rate of the former (i.e. not the rate coefficient) is taken to be  $R_{\text{CRP,pd,CO}} = 0.21 \times x_{\text{H}_2} \times \sqrt{T_{\text{gas}} x_{\text{CO}}}$  and the rate coefficient of the latter is  $r_{\text{CRP,pi,C}} = 2800 \times \zeta_{\text{H}}$  ([Maloney et al., 1996](#)). The cosmic ray ionization rate of H is denoted by  $\zeta_{\text{H}}$  and  $x_{\text{H}_2}$  and  $x_{\text{CO}}$  are the fractional abundances of the corresponding molecules.

In cold and dense molecular clouds the freeze-out onto dust grains becomes the most effective process for removing CO from the gas phase ([Bacmann et al., 2002](#); [Tafalla et al., 2004](#)). The chemical network presented here does not include this process. This simplification results in the overestimation of gas phase CO abundance, and consequently the CO emissivity in the high density regions. We argue, however, that due to optical depth effects and a relatively low velocity dispersion in the simulated clouds, this probably has a small impact on the CO emission. The freeze-out becomes important only above  $A_{\text{v}} \approx 6$  mag and by this depth, even the  $^{13}\text{CO}$  emission becomes optically thick, obscuring the freeze-out regions. In any case, the main focus of this work is to constrain the  $^{12}\text{CO}/^{13}\text{CO}$  ratio, which should not be affected by the non-isotope-selective freeze-out process.

### 2.2.2 ATTENUATION OF THE ISRF

As we describe in the introduction, the differential shielding of  $^{12}\text{CO}$  and  $^{13}\text{CO}$  is expected to play a role in determining the isotope ratio. To account for this effect the column densities – from the centre of a given SPH particle to the outer surface of the cloud – of the critical species ( $\text{H}_2$ , dust,  $^{12}\text{CO}$  and  $^{13}\text{CO}$ ) need to be calculated. We use the TreeCol method presented by [Clark et al. \(2012a\)](#). In short, TreeCol is a cost efficient algorithm to calculate total and species specific column densities while “walking” the gravitational tree structure (used in GADGET-2 to compute the gravitational interaction of far-away particles). It constructs a HEALPIX ([Górski et al., 2005](#)) sphere with 48 equal-area pixels for each SPH particle and accumulates the contribution of the line of sight nodes for the considered pixel. We trace the total (H nuclei),  $\text{H}_2$ ,  $^{12}\text{CO}$  and  $^{13}\text{CO}$  column densities. The visual extinction ( $A_V$ ) due to the dust is calculated using the formula ([Bohlin et al., 1978](#); [Draine and Bertoldi, 1996](#)),

$$A_V = \frac{N_{\text{tot}}}{1.8699 \times 10^{21} \text{cm}^2} \times f_{\text{dg}}, \quad (2.2)$$

where  $N_{\text{tot}}$  is the total H nuclei column density and  $f_{\text{dg}} = Z/Z_{\odot}$  is the factor correcting for the simulation metallicity.

We model the attenuation of the ISRF by multiplying the optically thin photodissociation rates with shielding factors depending on the column density and visual extinction. The  $\text{H}_2$  photodissociation rate is attenuated due to dust absorption and  $\text{H}_2$  self-shielding. The dust shielding factor can be calculated in the plane-parallel approximation by

$$\Theta_{\text{dust}} = \exp(-\gamma A_V) \quad (2.3)$$

with  $\gamma = 3.74$  ([Draine and Bertoldi, 1996](#)). The self-shielding factor depends on the  $\text{H}_2$  column density and is calculated according to equation (37) in [Draine and Bertoldi \(1996\)](#). In the case of  $^{12}\text{CO}$  and  $^{13}\text{CO}$ , the shielding is due to dust absorption, the  $\text{H}_2$  Lyman-Werner lines and CO self-shielding. The shielding factor due to dust absorption for both isotopic species is given by equation (2.3) with  $\gamma = 3.53$ . The tabulated CO shielding by  $\text{H}_2$  and self-shielding factors are adopted from [Visser et al. \(2009a\)](#). We used the same relation between the column density and the CO self-shielding factor for both CO isotopes when calculating the self-shielding, but with the corresponding isotope column density.

We refer to section 2.2 in [Glover et al. \(2010\)](#) for a more detailed description of the adopted treatment of photochemistry.

### 2.2.3 THERMAL MODEL

We calculate the thermal balance and temperatures of gas and dust self-consistently, taking a number of cooling and heating processes into account. The temperature structure of the cloud has a large impact on the chemical fractionation (due to the temperature barrier for the right-to-left path), a moderate effect on the selective photodissociation (more strongly isotope selective in colder gas; discussed in detail in [Visser et al. \(2009a\)](#), but not considered here) and significant influence on CO excitation, therefore a realistic thermal model is necessary.

The adopted thermal model – with the complete list of heating and cooling processes and rates – is presented in section 3.2.4 of [Glover and Clark \(2012b\)](#).

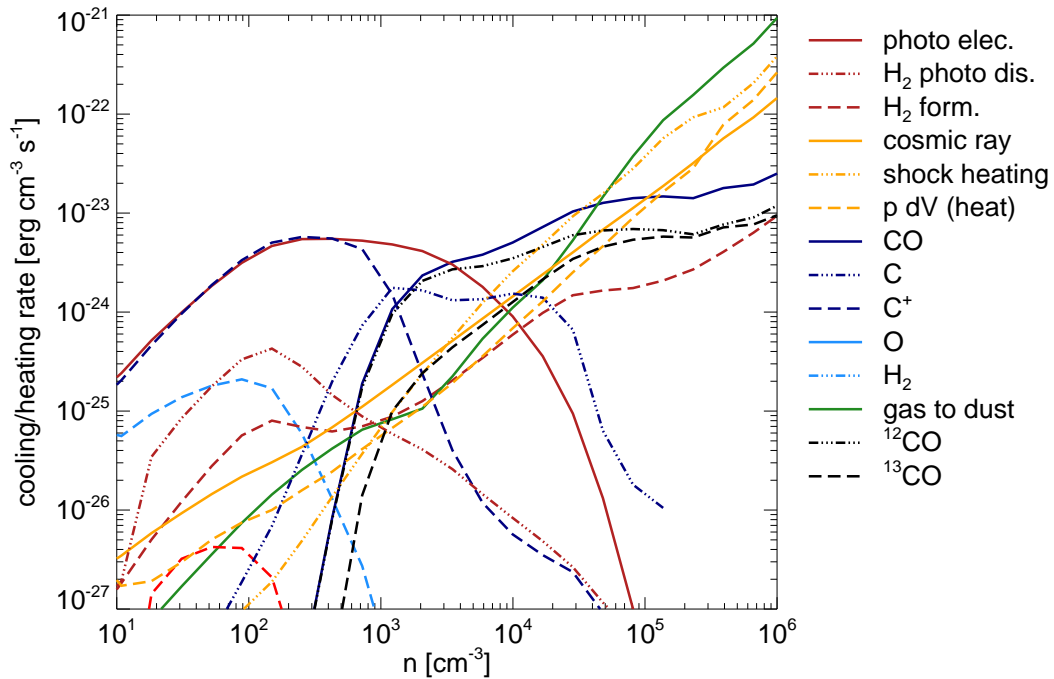


Figure 2.2: The median cooling (dashed lines) and heating (solid lines) rates as a function of hydrogen nuclei number density for the fiducial model (d). The cooling rates of C-bearing molecules are calculated separately for the  $^{12}\text{C}$  and  $^{13}\text{C}$  isotopologues but their combined rates are shown here. The exception is CO, for which we also plot the isotopic contributions separately. For the detailed description of the cooling and heating processes see [Glover and Clark \(2012b\)](#).

Fig. 2.2 summarizes the contributions of thermal processes to the thermal balance in our simulations. The dominant heating processes are the photoelectric, shock, cosmic ray, and pdV (expansion and contraction) heating. The major coolants at low and intermediate densities are  $\text{C}^+$  and CO, while at high density cooling is dominated by the dust. We consider the  $\text{C}^+$  and CO isotopes separately when calculating the cooling rates. Thanks to its lower optical depth,  $^{13}\text{CO}$  might become as effective coolant as  $^{12}\text{CO}$  at densities higher than  $10^4 \text{ cm}^{-3}$ . However, the effect of this on the thermal balance is negligible, since at these densities, dust cooling is already the dominant process.

#### 2.2.4 INITIAL CONDITIONS

Our basic initial setup is identical to [Glover and Clark \(2012b\)](#). We start the simulations with a uniform density sphere with  $10^4 M_\odot$  total mass. The initial volume density of the sphere is set to 300 or  $1000 \text{ cm}^{-3}$ , resulting in an approximate cloud radius of 6 pc or 4 pc, respectively. The initial velocities of the SPH particles are chosen so that the initial velocity field has a steep power spectrum with  $P(k) \propto k^{-4}$ , using the “cloud-in-cell” scheme ([Hockney and Eastwood, 1988](#); [Mac Low et al., 1998](#)). The velocity field is scaled such that the total kinetic energy equals to the gravitational potential energy, corresponding to 3D root-mean-square (rms)

velocities ( $\sigma_{\text{rms},3\text{D}}$ ) of  $2.81 \text{ km s}^{-1}$  and  $3.43 \text{ km s}^{-1}$  for the different initial densities. We do not apply turbulent driving during the simulations and the turbulence is allowed to dissipate freely through shocks and numerical viscosity. Consequently, the overall rms velocity of the cloud decreases with time. In the first  $\sim 0.3 \text{ Myr}$  the rms velocity stagnates; afterwards, it decreases with time as  $\sigma_{\text{rms},3\text{D}}(t) \propto t^{-0.24}$ . By the time of the analysed snapshots it reaches the values of  $2$  and  $2.6 \text{ km s}^{-1}$ . The initial gas and dust temperature are uniform at  $20 \text{ K}$  and  $15 \text{ K}$ , respectively.

In case of the solar metallicity ( $Z_{\odot}$ ) runs, the adopted initial abundances of  $^{12}\text{C}$ ,  $^{13}\text{C}$  and  $\text{O}$  relative to hydrogen nuclei are  $x_{^{12}\text{C}} = 1.4 \times 10^{-4}$ ,  $x_{^{13}\text{C}} = 2.3 \times 10^{-6}$  and  $x_{\text{O}} = 3.2 \times 10^{-4}$  respectively (Sembach et al., 2000). In the case of “fully molecular” initial composition (models a to f), all hydrogen atoms are in  $\text{H}_2$  form, while when “atomic” initial conditions are adopted (model g, see discussion in Appendix C), then all hydrogen is atomic and neutral. In both cases we assume that all carbon is in ionized form. The helium is neutral and its fractional abundance is  $0.079$ , equivalent to  $24$  per cent mass fraction, in all simulations. The total abundance of low ionization potential metals (Na, Mg, etc.) is  $x_{\text{M}} = 1 \times 10^{-7}$ . These are initially assumed to be fully ionized. The electron abundance of the cloud is set to give an overall neutral medium. To investigate the metallicity dependence of our results, we also perform simulations with scaled initial abundances geared towards the SMC ( $0.3 \times Z_{\odot}$ ) and the LMC ( $0.6 \times Z_{\odot}$ ). In each run the carbon isotopic abundance ratio is  $60$ , a value consistent with the frequently adopted measurements (Lucas and Liszt, 1998) in the Solar vicinity. Besides the abundances we also scale the dust-to-gas ratio with a factor,  $f_{\text{dg}} = Z/Z_{\odot}$ . In the solar metallicity case the dust-to-gas ratio is taken to be  $0.01$ .

We assume that the cloud is illuminated by an isotropic, standard radiation field, described by Draine (1978) in the UV and by Black (1994) at longer wavelengths. The default field strength is  $G_0 = 1.7$  in units of the Habing (1968) field, corresponding to  $2.7 \times 10^{-3} \text{ erg cm}^{-2} \text{ s}^{-1}$  integrated flux in the  $91.2\text{--}240 \text{ nm}$  wavelength range. To test various galactic environments we scaled the radiation field strength between  $0.1 \times G_0$  and  $10 \times G_0$  with the fiducial value of  $1 \times G_0$ .

In the most shielded regions of GMCs, several important CO destruction pathways are activated by the deep penetrating cosmic ray particles, which also provide an important gas heating mechanism there. The adopted cosmic ray ionization rate of atomic hydrogen is  $\zeta_{\text{H}} = 10^{-17} \text{ s}^{-1}$ . The ones for  $\text{H}_2$  and atomic He are  $2 \times \zeta_{\text{H}}$  and  $1.09 \times \zeta_{\text{H}}$ , respectively.

We performed  $6+1$  hydrodynamic cloud simulations in total. The parameters explored are summarized in Table 2.1. In the analysis that follows in section 2.3 we take simulation d) as the fiducial model.

### 2.3 THE $^{12}\text{CO}/^{13}\text{CO}$ COLUMN DENSITY RATIO

In this section we analyse the  $N(^{12}\text{CO})/N(^{13}\text{CO})$  isotopic column density ratio resulting from our simulations. We look for correlations between the isotope ratio and the total,  $^{12}\text{CO}$  and  $^{13}\text{CO}$  column densities. Hereafter, if not indicated otherwise, the column densities are meant as the number of atoms/molecules of a species or the gas mass in a given line of sight, per  $\text{cm}^2$ , integrated from the “observer” to infinity.

We used the grid interpolated quantities (see Appendix B). The column density

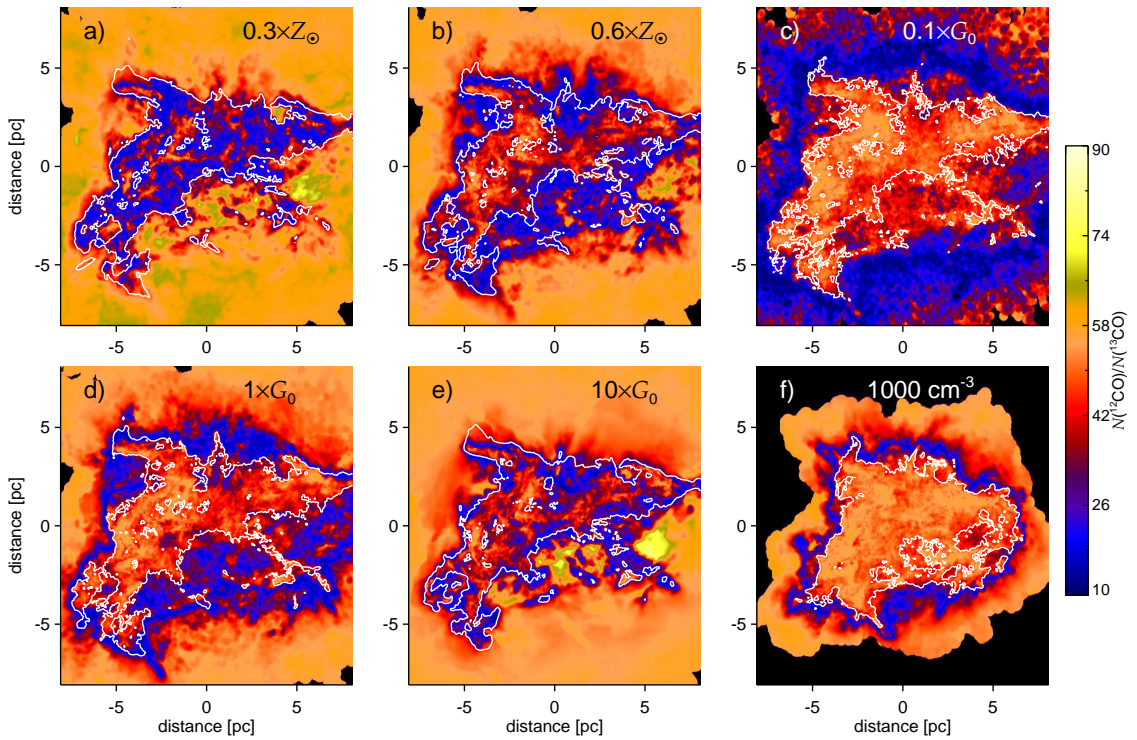


Figure 2.3:  $N(^{12}\text{CO})/N(^{13}\text{CO})$  column density ratio maps for varying ISRFs, metallicities and initial volume densities. The white contour represents the  $5 \times 10^{21} \text{ cm}^{-2}$  level in total column density. The same colour scale applies for all the ratio maps. Yellow and blue colors mark regions dominated by the effects of selective photodissociation and chemical fractionation, respectively, while orange marks regions in which the CO is not significantly fractionated. Lines of sight which do not intersect any SPH particles are marked with black.

maps were calculated by integrating the volume density along the  $z$  direction of the grid. Although the apparent shape of the molecular cloud does depend on the viewing direction, the quantities and relationships discussed below are independent of the choice of viewing direction. Fig. 2.3 shows the ratio of  $^{12}\text{CO}$  and  $^{13}\text{CO}$  column density maps for different radiation fields, metallicities and initial volume densities. The white contour line indicates the total column density level of  $5 \times 10^{21} \text{ cm}^{-2}$ . The shape of this contour line does not change substantially with varying radiation field strength or metallicity, indicating that the overall density structure is not affected significantly within the studied parameter range (see also Fig. 2.5).

The simulated ratio maps are in general agreement with the picture of the CO isotopic chemistry described in the introduction. In the outer parts of the clouds, the total column densities are low and the shielding of neither isotopic species is effective. Deeper in the cloud (see model a and e), the selective photodissociation of  $^{13}\text{CO}$  might dominate, increasing the  $^{12}\text{CO}/^{13}\text{CO}$  ratio up to  $\sim 75$  (yellow region). Further in, where the substance of the cloud dwells, the fractionation reaction takes over and significantly decreases the ratio to  $\sim 25$  and below (blue region). At the core of the cloud, the radiation field photodissociates CO or ionizes C with a very

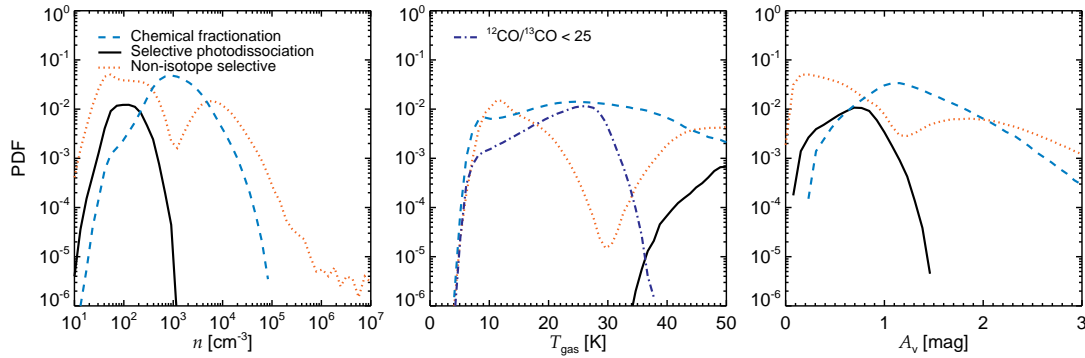


Figure 2.4: The number density, gas temperature and mean visual extinction PDFs of the non-fractionated ( $50 < ^{12}\text{CO}/^{13}\text{CO} < 65$ ), chemical fractionation dominated ( $^{12}\text{CO}/^{13}\text{CO} \leq 50$ ) and isotope selective photodissociation dominated ( $^{12}\text{CO}/^{13}\text{CO} \geq 65$ ) zones, weighted by the mass. Simulation e) is shown here, but all the other models qualitatively follow the same distributions.

low rate, and so neither of the isotope-selective processes are effective. In these regions the  $N(^{12}\text{CO})/N(^{13}\text{CO})$  ratio increases again and approaches the initially set  $^{12}\text{C}/^{13}\text{C}$  ratio (marked by the orange color). Qualitatively all simulations follow this scheme. However, the quantitative details – e.g the transitional column densities – differ considerably from simulation to simulation.

To investigate the typical physical conditions of the three zones (non-fractionated or dominated by the effects of selective photodissociation or chemical fractionation) we plot their number density, gas temperature and mean visual extinction probability density functions (PDFs) in Fig. 2.4. The non-fractionated gas shows bimodal distributions in all three quantities. At low number densities, CO is poorly shielded from the effects of the ISRF and both CO isotopes are photodissociated at approximately the same rate. In this regime, photodissociation is non-selective and does not significantly alter the  $^{12}\text{CO}/^{13}\text{CO}$  ratio. At high number densities ( $n > 10^4 \text{ cm}^{-3}$ ), the ISRF is strongly attenuated and almost all of the available carbon is locked up in CO. In this regime, the  $^{12}\text{CO}/^{13}\text{CO}$  ratio is necessarily close to the elemental  $^{12}\text{C}/^{13}\text{C}$  ratio. The effects of isotope-selective photodissociation peak at number densities around  $100 \text{ cm}^{-3}$ , high temperatures and moderate visual extinctions (between 0.5 and 1 mag). However, even in this parameter regime, only a small fraction of the gas has an isotope ratio 65 or higher. This high ratio gas resides in a thin layer around the bulk of the cloud. Normally this thin layer is not visible in the column density maps, since such maps trace a mass-weighted ratio along a given line of sight. In certain cases (see models a and e), high ratios could still be found, if most of the gas in the line of sight is relatively dilute (a few hundred particles per  $\text{cm}^3$ ) and moderately shielded (about 0.5 mag visual extinction). Chemical fractionation dominates in gas which has a characteristic number density between  $10^3$  and  $10^4 \text{ cm}^{-3}$  and mean visual extinction around unity. The chemically fractionated gas shows a wide temperature range. However, the temperature distribution of the highly fractionated gas (ratio lower than 25, dotted dashed line on the middle panel of Fig. 2.4) has an abrupt cut-off around 30 K.

The dependence of the  $^{12}\text{CO}/^{13}\text{CO}$  ratio on the physical conditions in the cloud

that we find from our study is in a good qualitative agreement with the large parameter study of photon dominated region (PDR) models in [Röllig and Ossenkopf \(2013\)](#). We conclude that effect of the isotope selective photodissociation is negligible when column density isotope ratios are considered. Hereafter, we mainly focus on the effect of chemical fractionation.

### 2.3.1 CORRELATION WITH THE TOTAL COLUMN DENSITY

The mass-weighted PDFs of the total, the  $^{12}\text{CO}$  and the  $^{13}\text{CO}$  column densities for simulations a) and d) are presented in Fig. 2.5. The figure shows the mass fraction of the cloud at a given column density. The CO isotope column densities are weighted with the total mass, therefore the corresponding curves show the cloud mass fraction locked in CO isotopes as a function of the total column density.

The overall density distributions in these simulations are roughly identical. The CO isotope distributions, however, show large differences: due to less effective shielding, in simulation a) both CO isotopes form at a factor of a few higher total column densities and the total  $^{12}\text{CO}$  mass (the integral of the red curve multiplied by the total cloud mass) is also a factor of 17 lower,  $0.6 M_{\odot}$  and  $10.2 M_{\odot}$  for simulation a) and d) respectively. The total  $^{13}\text{CO}$  mass is reduced by a similar factor. Consequently, depending on cloud properties and environment, CO isotopes trace different total column densities and cloud mass fractions. Also note the relatively large fraction of the so called CO-dark gas, i.e. mass not traced at all by CO ([Wolfire et al., 2010](#); [Smith et al., 2014](#)).

The upper sub-panels in Fig. 2.5 show the mean  $N(^{12}\text{CO})/N(^{13}\text{CO})$  ratio as a function of the total column density. The description of the algorithm that we used to produce these curves is given in section 2.3.3. The gradients of the curves represent the transitions between regions dominated by photodissociation, chemical fractionation and strong attenuation. The total column densities corresponding to these transitions are strongly dependent on the strength of the ISRF and the metallicity of the cloud. In case of simulation d) the  $5 \times 10^{21} \text{ cm}^{-2}$  total column density contour (see Fig. 2.3) approximately indicates the transition between the regions dominated by chemical fractionation and strong attenuation. In the case of simulation a), the reduced metallicity decreases both the CO column density and the extinction due to dust that a parcel of gas in the cloud “sees”, resulting in less effective attenuation of the radiation field. The transition between the chemical fractionation-dominated and the attenuation-dominated regions is shifted to a total column density that is an order of magnitude larger. In this case, the  $5 \times 10^{21} \text{ cm}^{-2}$  contour line traces the transition between the regions dominated by non-selective photodissociation and chemical fractionation. Simulations with reduced metallicity or increased ISRF (b and e) behave similarly to model a), while simulation f) has transitional column densities similar to model d). In case of c), due to the weak radiation field, a substantial amount of CO is able to form even at low visual extinctions. This results in an extended chemical fractionation dominated region at very low total column densities (i.e. most likely below any reasonable detection limit) and a very strong shielding, and hence close to elemental ratios in the (observable) inner regions.

Regardless of the model dependent transitional total column densities, the isotope ratio seems to be consistent within a few per cent in the corresponding regions

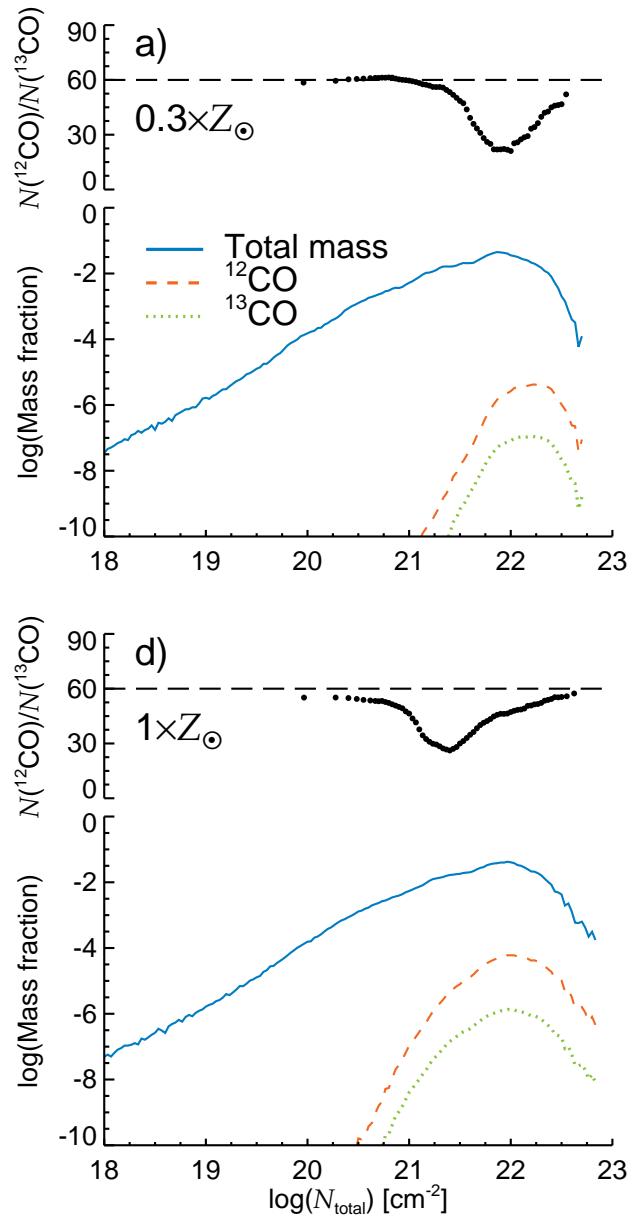


Figure 2.5: Total,  $^{12}\text{CO}$  and  $^{13}\text{CO}$  mass fraction distributions and the  $N(^{12}\text{CO})/N(^{13}\text{CO})$  ratio as a function of the total column density for low metallicity (a) and the fiducial (d) simulations. The total column density distributions are roughly identical, while CO forms at a factor of 3 higher column densities in the case of a). The total CO mass is also reduced by about an order of magnitude. The dip in the isotope ratio curve is shifted by almost a order of magnitude to higher total column densities. Note that the column density ratio is not expected to be equivalent to the ratio of the  $^{12}\text{CO}$  and  $^{13}\text{CO}$  mass distributions, as in the latter case the area associated with a column density value is also taken into account.

of the cloud for each simulation. In the region dominated by non-selective photodissociation the ratio is close to the initially set  $^{12}\text{C}/^{13}\text{C}$  ratio of 60. In the region of chemical fractionation, the ratio drops to  $\sim 20$ . Finally, in the most shielded regions the CO isotope ratio approaches 60 again. Note, however, that the results from the outermost regions of the cloud are – due to large smoothing lengths and low SPH resolution – somewhat uncertain. These regions are usually also undetectable in CO emission, because of their very low column densities.

Fig. 2.5 also shows that the region of  $^{13}\text{CO}$  enhancement coincides with the highest CO mass fraction in case of simulation a) and with lower mass fractions in case of d). This indicates a higher importance of isotope-selective reactions when the radiation field is high and/or the metallicity is low.

We conclude that the total column density and the isotope ratio correlate, but the correlation strongly depends on the cloud properties and environment.

### 2.3.2 CORRELATION WITH THE $^{12}\text{CO}$ COLUMN DENSITY

We find a tighter correlation between the  $^{12}\text{CO}$  column density and the CO isotope ratio. Fig. 2.6 shows the mass-weighted, two dimensional probability density distribution of  $N(^{12}\text{CO})$  and the isotope ratio for the 6 simulations (from a to f). The colours indicate the mass fraction of the cloud with a given parameter combination. Consistent with Fig. 2.5, most of the cloud mass lies at different  $^{12}\text{CO}$  column densities, depending on the model parameters. If the metallicity is low or the radiation field is strong, then CO forms at, and therefore traces, higher total column densities.

The most remarkable feature of Fig. 2.6 is that the location and depth of the dip in the isotope ratio shows only weak parameter dependence. The three dimensional nature ( $N(^{12}\text{CO})$  vs. isotope ratio vs. mass fraction) of these probability density distribution diagrams, however, makes it hard to directly compare them. Therefore, we project them into 2D space, keeping in mind that we are interested in the relationship of  $N(^{12}\text{CO})$  and the isotope ratio, and that we are aiming to derive a functional form. We construct curves according the following procedure: Starting from the low  $^{12}\text{CO}$  column densities we bin  $N(^{12}\text{CO})$  adaptively into strips. The normalized total mass fraction of a strip is required to be at least 0.002, a value chosen to provide well sampled isotope ratio distribution in the strip. We then collapse the strip in the  $N(^{12}\text{CO})$  dimension by adding up mass fractions in isotope ratio bins. This gives the mass fraction in a  $N(^{12}\text{CO})$  strip as the function of isotope ratio. We fit a Gaussian to this curve to determine the mean value and the width of the distribution (i.e. the standard deviation). Finally, we determine an effective  $N(^{12}\text{CO})$  within the strip, by weighting based on the mass fraction contribution of a  $N(^{12}\text{CO})$  pixel column to the strip. We repeat this procedure until the upper limit of the  $^{12}\text{CO}$  column density is reached. The small, filled, black circles in the panels in Fig. 2.6 and the coloured filled symbols in Fig. 2.7 show the mean isotope ratios as a function of  $^{12}\text{CO}$  column density derived this way. Fig. 2.6 demonstrates that the derived mean ratios follow the probability density distribution well, justifying our approach.

The mean isotope ratio curves show a very good overall agreement in all cases (see Fig. 2.7). However, there is a weak correlation between the curve shape and the physical parameters. A higher initial density ( $n_0$ ) might result in higher isotope

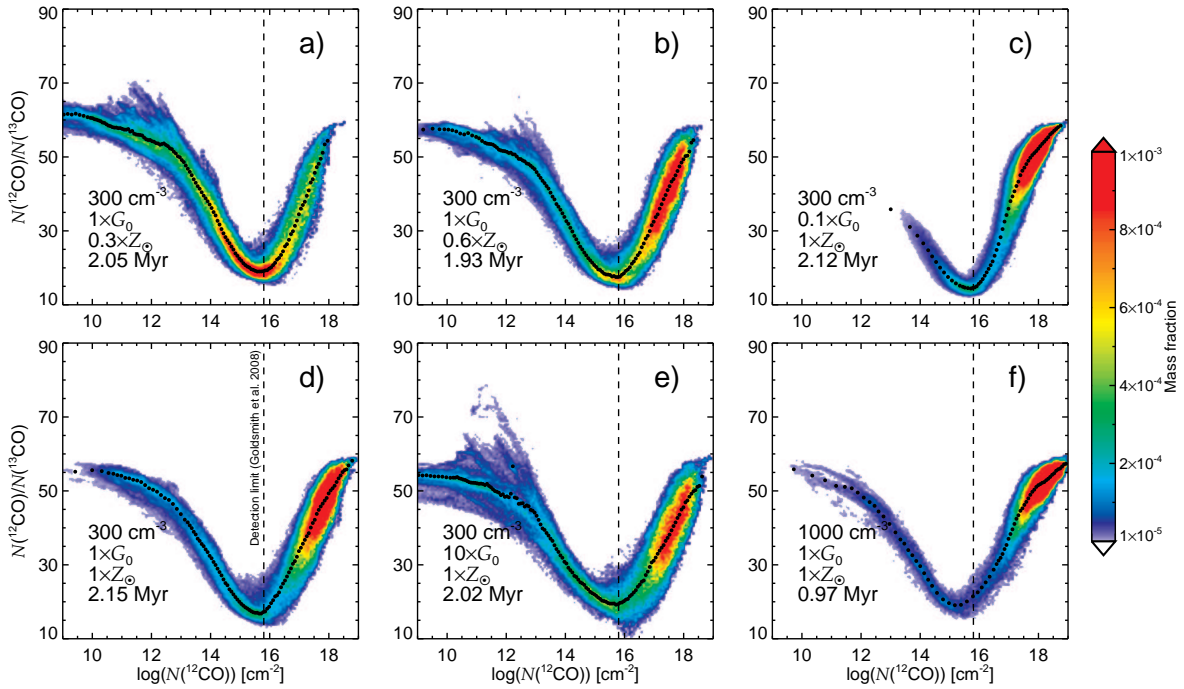


Figure 2.6: CO isotope column density ratio as a function of the  $^{12}\text{CO}$  column density, calculated using the “real” column densities (i.e. directly from the hydrodynamic simulation). Model parameters are indicated in the legend, the vertical line shows the approximate detection limit achieved by Goldsmith et al. (2008) in the case of the Taurus molecular cloud region. The colour indicates the mass fraction of the cloud with the specified  $^{12}\text{CO}$  column density and isotope ratio, which depends significantly on the model parameters. At low column densities, isotope-selective photodissociation might increase the ratio up to 70 in some cases. At higher column densities, the fractionation reaction takes over, resulting in a pronounced dip. The observations are sensitive to the inner regions of the cloud, where the fractionation reaction becomes less effective as the  $\text{C}^+$  abundance decreases, and the ratio increases to the initial value. The black dotted curves represent the fitted relation between the quantities (see Section 2.3.3).

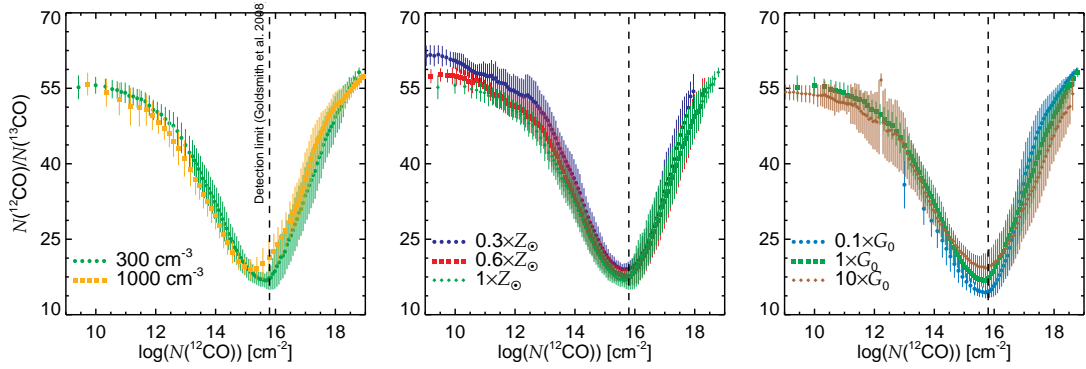


Figure 2.7: CO isotope column density ratio as a function of the  $^{12}\text{CO}$  column density derived by the procedure described in section 2.3.2. From left to right the panels compare the effect of varying the initial density, metallicity and radiation field. We emphasize that the main features of the curves only weakly depend on the physical parameters. Model parameters not indicated in the legend are kept at the fiducial value.

ratios at high  $^{12}\text{CO}$  column densities. As the metallicity decreases from  $1Z_{\odot}$  to  $0.3Z_{\odot}$  the isotope selective photodissociation seem to increase the  $^{12}\text{CO}/^{13}\text{CO}$  ratio slightly above the elemental at CO column densities below  $10^{11}\text{cm}^{-2}$  (middle panel). The decreasing radiation field strength seems to decrease the minimum isotope ratio from  $19.23 \pm 2.98$  to  $14.40 \pm 1.17$  (right panel).

The depth of the dip in the isotope ratio curve is expected to depend on the gas temperature (and therefore the heating and cooling processes) of the corresponding cloud regions. The chemical fractionation has an energy barrier for the right to left reaction path (see equation 2.1 and section 2.2.1), which is approximately 35 K. At temperature much higher than this, the reaction could proceed in both directions with similar rate, resulting in a less enhanced  $^{13}\text{CO}$  abundance and a isotope ratio closer to the  $^{12}\text{C}/^{13}\text{C}$  ratio (e.g. Röllig and Ossenkopf, 2013).

We emphasize, however, that these trends are not statistically significant in our simulations, and the model-by-model deviations of the isotope ratio curves are typically comparable to the standard deviations of the ratio. From this point on, we dispense with further investigation of the trends in the mean isotope ratio curves with physical parameters and assume that there is an unequivocal correlation between the  $^{12}\text{CO}$  column density and the  $^{12}\text{CO}/^{13}\text{CO}$  ratio which is independent of the parameters we vary in the simulations.

### 2.3.3 FITTING FORMULA

To derive a functional form for the  $N(^{12}\text{CO})$ -isotope ratio relationship we fit the curves presented in Fig. 2.7 individually and together using the non-linear least-squares Marquardt-Levenberg algorithm implemented in GNUPLOT<sup>4</sup> (Williams and Kelley, 2011). The combined data was constructed from all models except models c) and g), due to the low numerical resolution at low column densities in the former and for the sake of consistency in the latter case. We fitted 4th, 5th and 6th order polynomial functions taking the standard deviation of each data point into

<sup>4</sup><http://gnuplot.sourceforge.net/>

Table 2.2: Coefficients of the best fitting polynomials in case of the  $^{12}\text{CO}$  column density–isotope ratio correlation

Model	$a_{0,12}$	$a_{1,12}$	$a_{2,12}$	$a_{3,12}$	$a_{4,12}$	$a_{5,12}$
a	44118.20±946.40	-16028.90±336.30	2308.65±47.51	-164.3870±3.336	5.78127±0.1164	-0.080301±0.00162
b	39398.60±990.50	-14339.70±348.80	2069.68±48.80	-147.7000±3.390	5.20628±0.1170	-0.072481±0.00160
c	-129934.00±22970.00	39353.20±7218.00	-4717.00±904.00	279.7200±56.410	-8.20654±1.7540	0.095312±0.02170
d	23435.20±1973.00	-8696.25±675.90	1277.96±91.93	-92.6067±6.206	3.30431±0.2079	-0.046415±0.00277
e	16928.80±919.10	-6337.57±320.20	939.74±44.29	-68.6503±3.041	2.46668±0.1037	-0.034852±0.00141
f	6002.58±2009.00	-2530.75±701.70	416.65±96.97	-33.2072±6.631	1.28180±0.2244	-0.019203±0.00301
combined	23619.40±1657.00	-8801.37±566.20	1298.19±76.76	-94.3795±5.162	3.37743±0.1723	-0.047569±0.00228

Table 2.3: Coefficients of the best fitting polynomials in case of the  $^{13}\text{CO}$  column density–isotope ratio correlation

Model	$a_{0,13}$	$a_{1,13}$	$a_{2,13}$	$a_{3,13}$	$a_{4,13}$	$a_{5,13}$
a	3430.54±304.30	-1389.82±132.70	220.92±22.84	-16.7171±1.941	0.59055±0.0815	-0.007564±0.00135
b	4607.55±476.30	-1955.96±206.00	328.11±35.16	-26.7192±2.961	1.05021±0.1230	-0.015883±0.00202
c	57181.50±28280.00	-22455.80±9957.00	3494.39±1397.00	-269.0400±97.540	10.24410±3.3920	-0.154282±0.04700
d	9050.64±665.40	-3887.04±280.10	659.215±46.52	-54.7241±3.813	2.21884±0.1542	-0.035134±0.00247
e	4956.36±272.80	-2159.25±117.60	372.237±19.98	-31.2920±1.674	1.27851±0.0691	-0.020294±0.00113
f	12412.20±796.60	-5319.18±323.70	901.857±51.93	-75.1591±4.112	3.07318±0.1608	-0.049292±0.00249
combined	8519.51±411.00	-3677.23±174.70	626.981±29.30	-52.3141±2.423	2.13123±0.0988	-0.033897±0.00159

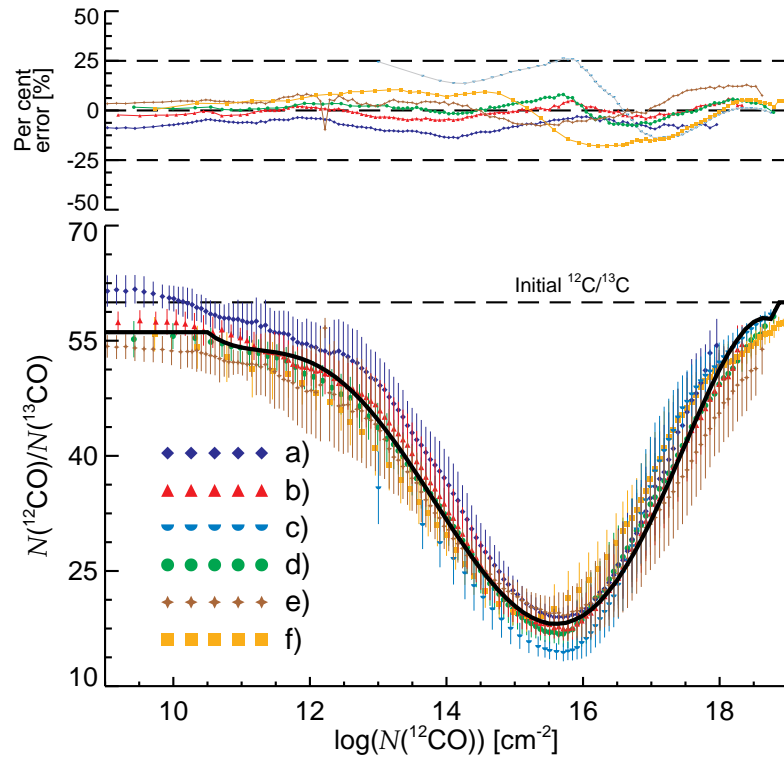


Figure 2.8: Similar to Fig. 2.7. Here we compare the  $N(^{12}\text{CO})$ -isotope ratio curves derived from the simulation (coloured dotted lines) to the adopted fitting formula (black solid line). The upper panel shows the percentage error of the formula when compared to the model data.

account. The best fit 4th order polynomial over-predicts the ratios for  $10^{15} \text{ cm}^{-2} < N(^{12}\text{CO}) < 10^{17} \text{ cm}^{-2}$ , and under-predicts in every other case. The 6th order polynomial does not provide a significantly better fit than the 5th order polynomial, therefore we chose to use the best fitting 5th order polynomial for the further analysis. The best fitting polynomial coefficients are presented in Table 2.2 for the individual and the combined data.

We adopt the best fit coefficients for the combined model with the modifications that the ratio at  $^{12}\text{CO}$  column densities lower than  $3.2 \times 10^{10} \text{ cm}^{-2}$  is equal to the ratio at  $N(^{12}\text{CO}) = 3.2 \times 10^{12} \text{ cm}^{-2}$  and we set the ratio to 60 above an upper limit of  $N(^{12}\text{CO}) = 10^{19} \text{ cm}^{-2}$ . The final form of our fitting formula is

$$r(N_{12}) = \begin{cases} r(N_{12} = 3.2 \times 10^{10}) & \text{if } N_{12} < 10^{12} \\ a_{0,12} + a_{1,12} \log_{10}(N_{12}) \\ + a_{2,12} \log_{10}(N_{12})^2 \\ + a_{3,12} \log_{10}(N_{12})^3 \\ + a_{4,12} \log_{10}(N_{12})^4 \\ + a_{5,12} \log_{10}(N_{12})^5 & \text{if } 3.2 \times 10^{10} \leq N_{12} \leq 10^{19} \\ 60 & \text{if } N_{12} > 10^{19} \end{cases} \quad (2.4)$$

where  $r$  is the  $^{12}\text{CO}/^{13}\text{CO}$  ratio and  $N_{12}$  is the  $^{12}\text{CO}$  column density in units of  $\text{cm}^{-2}$ . To justify this choice we compare the function derived from the combined models to the individual models. The bottom panel of Fig. 2.8 shows the unmodified curves from section 2.3.2 for all models with the standard deviations represented by the vertical lines. The black line represent the fitting function. The top panel show the per cent error between the data points from the models and the approximate value from the formula,  $\Delta = (\text{function} - \text{data})/\text{data} \times 100$ . The deviation with which the formula reproduces the data tends to be the largest in the fractionation reaction dominated region ( $10^{15}\text{cm}^{-2} < N(^{12}\text{CO}) < 10^{16}\text{cm}^{-2}$ ) going up to about 25 per cent. Note however, the difference on the whole  $^{12}\text{CO}$  column density range ( $\leq 15$  per cent) is comparable to the standard deviation (i.e. the thickness) of the combined distribution.

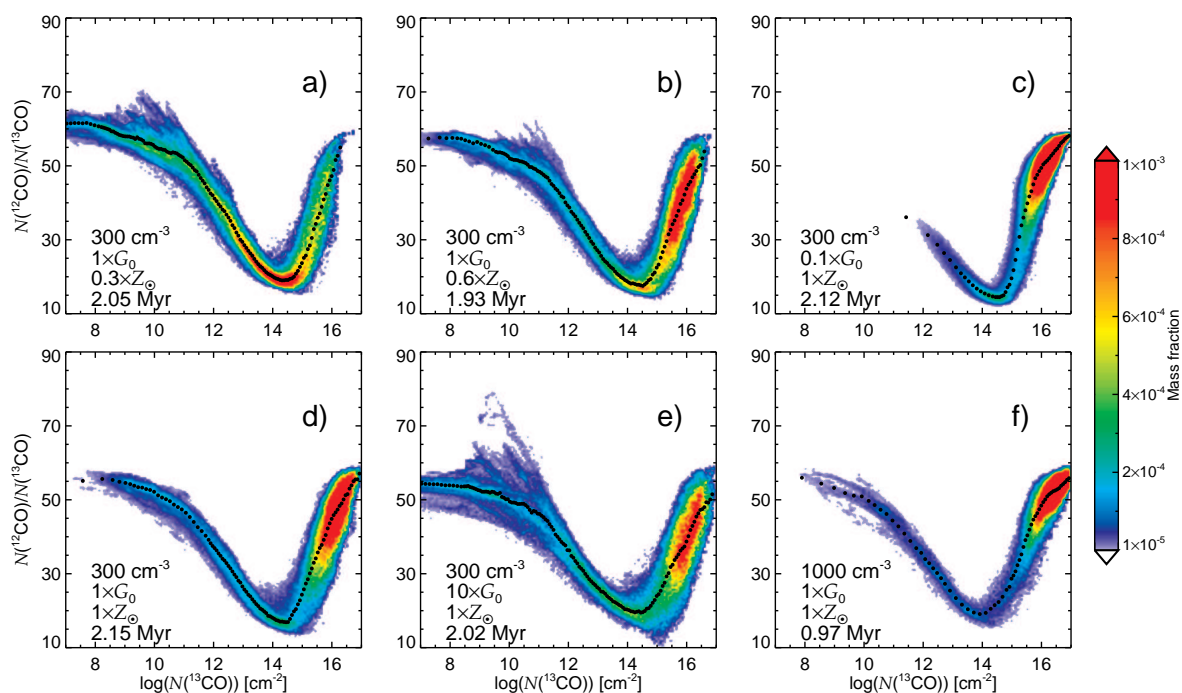


Figure 2.9: CO isotope column density ratio as a function of the  $^{13}\text{CO}$  column density. Colours and the dashed line have the same meaning as in Fig. 2.6. The main difference compared to Fig. 2.6 is the steeper slope at column densities larger than the characteristic column density of the dip in the isotope ratio.

### 2.3.4 APPLICATION FOR $^{13}\text{CO}$ OBSERVATIONS

The  $^{12}\text{CO}/^{13}\text{CO}$  isotopic ratio shows a similar correlation with the  $^{13}\text{CO}$  column density as presented in section 2.3.2 and a fitting formula could also be derived following the procedure described in section 2.3.3 (see Fig. 2.9). We adopt a similar functional form:  $r(N_{13}) = a_{0,13} + a_{1,13} \log_{10}(N_{13}) + a_{2,13} \log_{10}(N_{13})^2 + a_{3,13} \log_{10}(N_{13})^3 + a_{4,13} \log_{10}(N_{13})^4 + a_{5,13} \log_{10}(N_{13})^5$ , where  $r$  and  $N_{13}$  are the isotope ratio and the  $^{13}\text{CO}$  column density, respectively. The best fitting coefficients for the individual runs and the combined sample are presented in Table 2.3. The fitting

Table 2.4: Total  $^{12}\text{CO}$  mass in the simulations

Model	$^{12}\text{CO}$ mass [ $M_{\odot}$ ]			Per cent error [%]	
	“Real”	Uniform ratio	Fitting formula	Uniform ratio	Fitting formula
a	0.604	0.955	0.544	+58.2	-9.9
b	3.461	5.020	3.372	+45.0	-2.6
c	18.081	21.772	16.789	+20.4	-7.1
d	10.230	13.308	10.293	+30.1	+0.6
e	4.275	6.144	4.684	+43.7	-9.6
f	18.572	21.335	19.185	+14.9	+3.3
g	7.050	11.534	8.745	+63.6	+24.0

The total  $^{12}\text{CO}$  masses are derived with various assumptions on the  $^{12}\text{CO}$  column density (see section 2.3.4). Positive per cent errors mean overestimation of the self-consistent value. Model g) is discussed in Appendix C

formula is valid for  $^{13}\text{CO}$  column densities in the range  $3 \times 10^{10} \text{ cm}^3 - 5 \times 10^{16} \text{ cm}^3$ . We do not consider lines of sight with column densities less than the lower value and set the isotope ratio to 60 in case of column densities higher than the upper limit. We exclude runs c) and g) from the combined sample.

Table 2.4 shows the total  $^{12}\text{CO}$  mass in the simulations, calculated with various methods. In case of the “real” mass, we use the self-consistently calculated  $^{12}\text{CO}$  distribution. In the uniform ratio case we take the  $^{13}\text{CO}$  column density map and scale it with a uniform  $^{12}\text{CO}/^{13}\text{CO}$  factor of 60. In the case of the fitting formula, we derive  $^{13}\text{CO}$  column density dependent isotope ratio, and scale  $N(^{13}\text{CO})$  with the corresponding value. The assumption of a uniform isotope ratio always results in an overestimation of the “real”  $^{12}\text{CO}$  mass. If the fitting formula is applied then the overestimation could be reduced from up to  $\sim 58$  per cent to less than 10 per cent.

This correlation could be used to infer isotope ratios and improve  $^{12}\text{CO}$  column density estimates based on  $^{13}\text{CO}$  observations. We note however, that the  $^{13}\text{CO}$  column density estimation methods are influenced by various sources of errors. At high column densities even the rarer isotopes become optically thick, thus provide only lower limit on the isotope column density. At low column densities, the often assumed local thermodynamic equilibrium is not suitable to calculate molecular level populations precisely, resulting in an underestimation of the column density (e.g. Padoan et al., 2000; Molina, 2013)

## 2.4 THE $^{13}\text{CO}$ LINE EMISSION

In the previous sections we showed that (photo-)chemical processes have a large impact on the  $^{12}\text{CO}/^{13}\text{CO}$  ratio in GMCs and that there is a clear correlation between  $N(^{12}\text{CO})$ ,  $N(^{13}\text{CO})$  and the ratio. We now explore how these effects are reflected in the observable emission line profiles and maps. Could the assumption of uniform isotope ratio still give back approximately the right answer when optical depth effects and detection limits are considered? We try to answer this question

Table 2.5: Total  $^{13}\text{CO}$  mass in the simulations

Model	$^{13}\text{CO}$ mass [ $M_{\odot}$ ]			Per cent error [%]	
	“Real”	Uniform ratio	Fitting formula	Uniform ratio	Fitting formula
a	0.016	0.010	0.017	-36.8	+6.9
b	0.086	0.059	0.084	-31.1	-1.7
c	0.374	0.310	0.386	-17.0	+3.3
d	0.230	0.176	0.220	-23.1	-3.3
e	0.105	0.073	0.095	-30.4	-9.8
f	0.366	0.319	0.358	-13.0	-2.2
g	0.192	0.118	0.156	-38.9	-18.9

The total  $^{13}\text{CO}$  mass in the analysed simulation domain when its number density is self-consistently calculated or inferred from  $^{12}\text{CO}$  with a uniform isotope ratio or using our fitting formula. Negative (positive) per cent errors mean underestimation (overestimation) of the self-consistent value.

quantitatively by comparing line profiles and emission maps produced from self-consistent calculations with those obtained by either adopting a uniform isotope ratio, or one that depends on  $N(^{12}\text{CO})$ .

The numerical models are transformed to the observational plane by line radiative transfer modelling. We calculate the emission in a  $\pm 6 \text{ km s}^{-1}$  velocity range around the  $J = 1 \rightarrow 0$  transition of  $^{13}\text{CO}$  ( $\lambda_0 = 2720.41 \mu\text{m}$ ). For the  $^{13}\text{CO}$  number density we adopt three distributions: one produced by self-consistent simulations, a second produced by rescaling the  $^{12}\text{CO}$  distribution with a uniform isotopic ratio of 60 and a third produced by rescaling the  $^{12}\text{CO}$  distribution using the isotope ratios we obtained from our fitting formula. In the last case, we assume that the isotope ratio is constant along a given line of sight.

In the interstellar medium, the assumption that molecule energy levels are populated according to a thermal distribution (i.e. local thermodynamic equilibrium), is often invalid. To account for non-LTE conditions we use the Large Velocity Gradient (LVG) approximation, described in detail in [Sobolev \(1957\)](#), [Ossenkopf \(1997\)](#) and [Shetty et al. \(2011a\)](#). The non-thermal excitation/de-excitation is mainly driven by collisions with other molecules or atoms. As the most abundant particle in the dense ISM, the hydrogen molecule is the most probable collisional partner for CO. We account for the two spin isomers of the hydrogen molecule and calculate the level population of  $^{13}\text{CO}$  in two cases: using an ortho- $\text{H}_2$ /para- $\text{H}_2$  ratio of 3 (the high temperature equilibrium ratio) and of  $3 \times 10^{-5}$  (the thermal ratio at 15 K). The collisional rates are adopted from the Leiden Atomic and Molecular Database<sup>5</sup> ([Schöier et al., 2005](#); [Yang et al., 2010](#)). In addition to the LVG approximation, in which the photon escape probability in a cell is given by the velocity gradient with the neighbouring cells, we also use the so called “Doppler catching” method to correct for numerical artifacts when the Doppler shift between neighbouring cells is larger than the intrinsic line width ([Shetty et al., 2011b](#)).

<sup>5</sup><http://home.strw.leidenuniv.nl/~moldata/>

We use the radiation transfer tool, RADMC-3D<sup>6</sup> (Dullemond, 2012) and the physical conditions (number densities, gas temperature, etc.) self-consistently computed in the hydrodynamic simulations to calculate the molecular energy level populations in the above described approximation. Once the level populations are known, the line emission is obtained using the ray-tracing module of RADMC-3D. The required input parameters include the number density of the modelled species ( $^{13}\text{CO}$  in our case), the number density of the collision partners (ortho- and para-hydrogen molecules), the gas temperature, resolved (i.e. systematic and turbulent) and unresolved (“micro-turbulent”) velocity of the gas, and the line properties (energy levels, statistical weights, Einstein A-coefficients and collision rate coefficients). The SPH data of number densities, gas velocity and temperature are interpolated to a regular grid of  $(512 \text{ pixel})^3$  as described in Appendix B.1. The “micro-turbulent” velocity field, accounting for the small scale velocities unresolved on the grid, is set uniformly according Larson’s law by  $v_{\text{mturb}} = 1.1 \times (0.032 \text{ [pc]})^{0.38} = 0.297 \text{ km s}^{-1}$  (Larson, 1981), where 0.032 pc is the linear size of a pixel. Generally, a higher microturbulent velocity results in smoother line profiles. For a detailed discussion on how the choice of microturbulent velocity affects the emission see Appendix A in Shetty et al. (2011b). The line properties are adopted from Yang et al. (2010). The intensity of emission is calculated in position-position-velocity cubes with a velocity resolution of  $0.09 \text{ km s}^{-1}$ .

We consider three different distributions for the  $^{13}\text{CO}$  number density when producing the synthetic emission cubes. The first of these is taken directly from our simulation, and hence fully accounts for the effects of chemical fractionation and selective photodissociation. The second distribution is generated by scaling the  $^{12}\text{CO}$  number densities from the simulation by a uniform factor of  $1/60$ . Finally, the third distribution is produced by scaling the  $^{12}\text{CO}$  number densities by a variable factor derived using the isotope ratio- $^{12}\text{CO}$  column density fitting function (equation 2.4). In the latter case, we first calculate the  $^{12}\text{CO}$  column density along the  $z$  direction, then use the fitting formula described in section 2.3.3 to estimate the average line-of-sight isotope ratio. In the final step, the  $^{13}\text{CO}$  number density is calculated from the  $^{12}\text{CO}$  number density and the  $^{12}\text{CO}$  column density dependent isotope ratio. Table 2.5 summarizes the total  $^{13}\text{CO}$  mass for every model and each method used to calculate the  $^{13}\text{CO}$  number density distribution. These values represent the input number density distributions for the radiation transfer calculations (i.e. no radiation transfer effects are considered). It is clear from the per cent errors that the fitting formula gives a better representation of the “real”  $^{13}\text{CO}$  mass: the uniform scaling of the  $^{12}\text{CO}$  number density results in an error ranging from 13 to 40 per cent, while when using the fitting formula, the deviation is typically less than 10 per cent. When adopting a uniform isotope ratio, we always underestimate the total  $^{13}\text{CO}$  mass. The fitting formula may result in under- or overestimation with comparable absolute errors.

#### 2.4.1 LINE PROFILES

The results of the radiative transfer calculations are position-position-velocity intensity cubes in units of  $\text{erg cm}^{-2}\text{s}^{-1}\text{Hz}^{-1}\text{ster}^{-1}$ . As the first step the intensity is

---

<sup>6</sup><http://www.ita.uni-heidelberg.de/~dullemond/software/radmc-3d/>

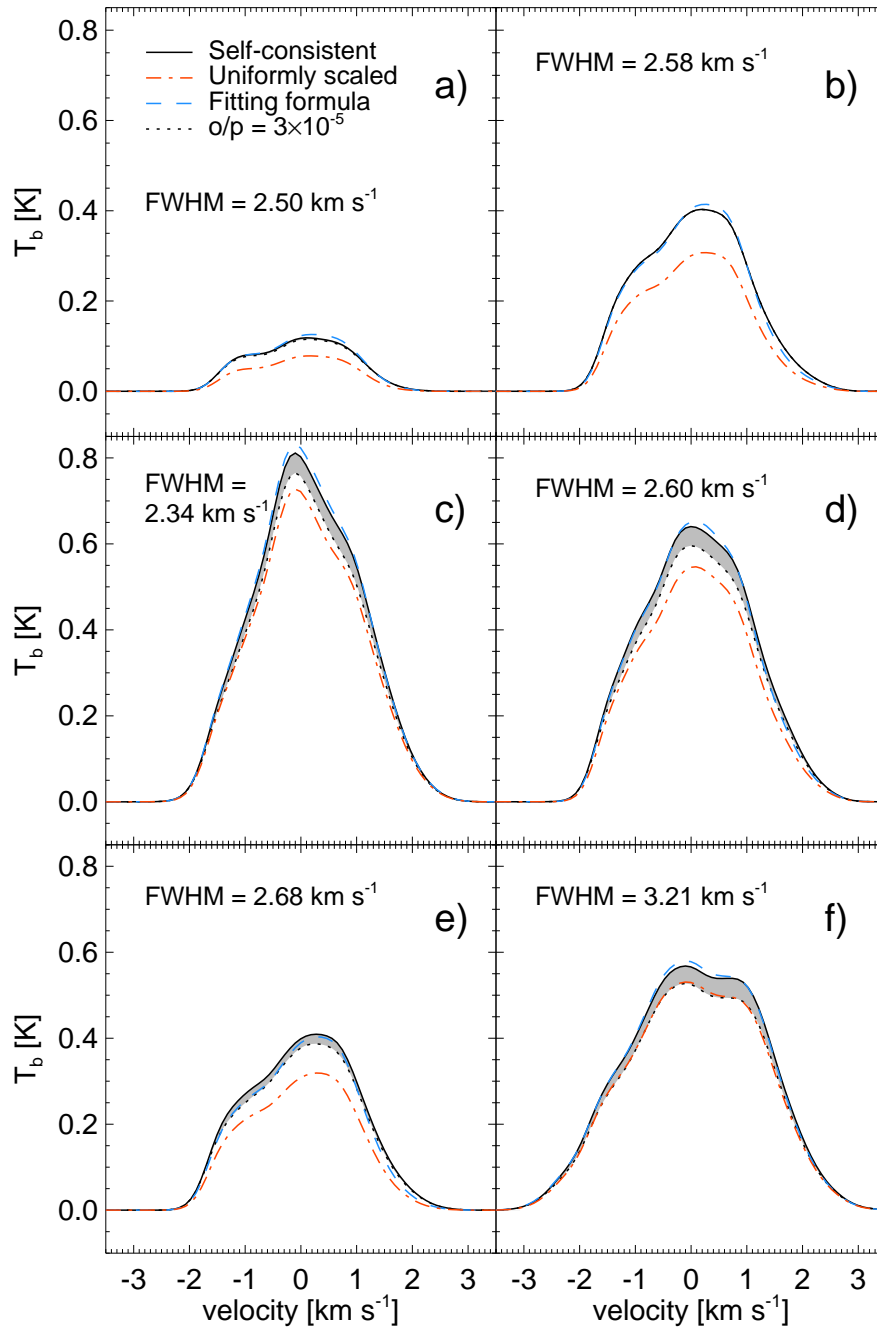


Figure 2.10: Cloud-averaged emission line profiles of the  $^{13}\text{CO}$   $J=1-0$  transition for the six simulations. The solid line shows the self-consistent  $^{13}\text{CO}$  number density model with the  $\text{H}_2$  ortho-to-para ratio of 3. The dotted line shows the same model, but with ortho- $\text{H}_2$ /para- $\text{H}_2 = 3 \times 10^{-5}$  (thermal distribution at 15 K). In reality the ortho-para ratio is between these limiting values, i.e. here in the gray shaded area. The dotted-dashed and the dashed lines represents uniformly scaled and fitting formula models, with ortho- $\text{H}_2$ /para- $\text{H}_2 = 3$ . The FWHM of the self-consistent model is indicated on the panels.

Table 2.6: Intrinsic and  $^{13}\text{CO}$  emission line inferred line of sight velocity dispersions.

Model	$\sigma_{1D,intrinsic}$ [km s $^{-1}$ ]	$\sigma_{1D,measured}$ [km s $^{-1}$ ]		
		Self- consistent	Uniform ratio	Fitting formula
a	1.39	1.06	1.03	1.04
b	1.26	1.10	1.08	1.06
c	0.93	0.99	0.98	0.97
d	1.09	1.11	1.08	1.07
e	1.32	1.14	1.11	1.09
f	1.61	1.37	1.35	1.35

converted to brightness temperature ( $T_b$ , in K), a quantity usually measured in molecular line observations.

The  $T_b(x, y, v)$  cubes are integrated along the spatial dimensions to obtain the overall  $^{13}\text{CO}$  J=1-0 line profile of the cloud. The resulting spectra are shown in Fig. 2.10. For each model, the self-consistent case is calculated using ortho- $\text{H}_2$ /para- $\text{H}_2$  ratios of 3 and  $3 \times 10^{-5}$  for comparison. We find that the choice of the  $\text{H}_2$  spin isomer ratio has less than 10 per cent effect on the integrated intensity of the line and typically a few per cent effect on the line width. Due to the small difference, the uncertain ortho/para ratio (Tielens, 2013) in real clouds and that we are focusing on a comparative study, we consider models with the somewhat unrealistic ratio of 3 in the rest of the discussion.

We find peak brightness temperatures and full-width-at-half-maximum<sup>7</sup> (FWHM) values consistent with those observed in molecular clouds with similar masses (e.g. the Perseus molecular cloud complex, see Fig. 4 and Table 2 in Pineda et al., 2008). The peak brightness temperature correlates with the total CO mass in a given simulation (Table 2.5). In the case of models a) to e), the line width increases as a larger amount of radiation energy is deposited at greater cloud depths due to less effective shielding (i.e. lower metallicity) or higher ISRF strength. In the case of the high density model (f), the line width is larger due to the initially larger kinetic energy and  $\sigma_{\text{rms}}$ .

The line profiles produced by the uniform isotopic ratio and fitting formula models are also shown in Fig. 2.10. The fitting formula model recovers the self-consistent line shapes and peak brightness temperatures within  $\sim 2$  per cent error, while the choice of a uniform ratio might result in up to 30 per cent error in the peak intensity.

The one dimensional velocity dispersion ( $\sigma_{1D,m}$ ) is inferred from the line width assuming a Gaussian line shape by  $\sigma_{1D,m} = \text{FWHM}/2.35$ . The velocity dispersion calculated this way is always smaller than the real line of sight dispersion, and scarcely depends on the adopted  $^{12}\text{CO}/^{13}\text{CO}$  ratio.

<sup>7</sup>Calculated by the interpolation mode of the IDL procedure [http://www.astro.washington.edu/docs/idl/htmlhelp/library21.html#fullwid\\_halfmax](http://www.astro.washington.edu/docs/idl/htmlhelp/library21.html#fullwid_halfmax)

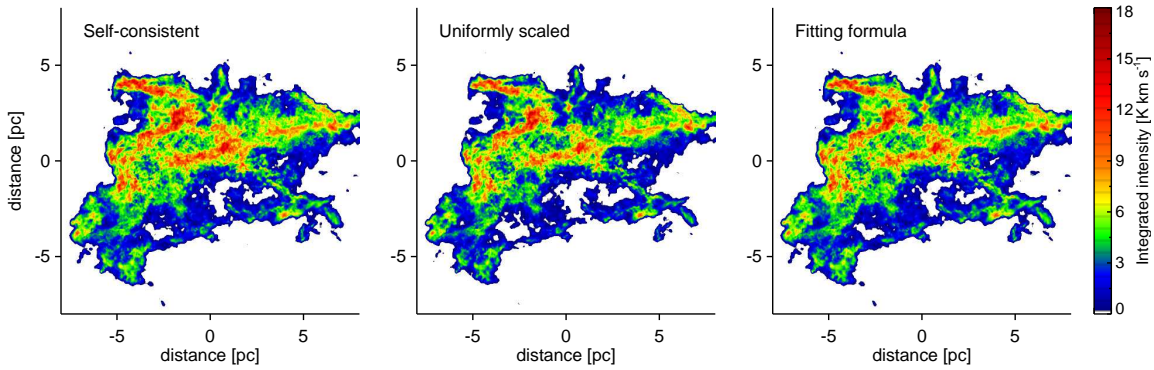


Figure 2.11: Velocity integrated  $^{13}\text{CO}$   $J = 1 \rightarrow 0$  emission maps derived from run d) in case of the three methods. Pixels in a given map with intensity values less than the chosen detection limit of  $0.2 \text{ K km s}^{-1}$  are shown in white. The area associated with an emission value is more extended in the self-consistent map than when a uniform  $^{12}\text{CO}/^{13}\text{CO}$  isotopic ratio is assumed. The difference is most prominent at the edge of the cloud (blue region) and in the region of moderate intensity (4-7  $\text{K km s}^{-1}$ , green and yellow). The latter region contributes the most to the total, spatially and velocity integrated intensity of the cloud. The map produced using our fitting formula agrees well with the self-consistent case.

#### 2.4.2 EMISSION MAPS

The  $T_b(x, y, v)$  cubes integrated in velocity space, along the line of sight give the zeroth moment maps,  $W(^{13}\text{CO})$ , in units of  $\text{K km s}^{-1}$ . For the purpose of the comparison we consider pixels with  $W(^{13}\text{CO}) > 0.2 \text{ K km s}^{-1}$  in each map. This limit is comparable to the  $0.18 \text{ K km s}^{-1} 3\sigma$  level of Goldsmith et al. (2008) in the Taurus molecular cloud. This detection limit approximately translates to a  $N(^{12}\text{CO})$  of  $6 \times 10^{15} \text{ cm}^{-2}$ , suggesting a negligible effect of preferential photodissociation and a more important role of chemical fractionation. We do not consider additional noise in the synthetic maps. See Fig. 2.11 for the zeroth moment maps of run d), calculated with the different assumptions on the  $^{12}\text{CO}/^{13}\text{CO}$  isotope ratio.

Fig. 2.12 compares the total intensity of pixels falling in a brightness temperature bin (with the bin size of  $0.5 \text{ K km s}^{-1}$ ) as a function of brightness temperature for the self-consistent (filled histogram with black outline) and approximate maps (orange dotted and blue dashed for the uniform ratio and fitting formula respectively). The bins with the high total intensity values contribute the most to the total emission. The contribution is determined by the enclosed area of contours associated with the lower and upper boundaries of a bin and the “mean” bin intensity. In case of simulation d), for example, the total intensity at high brightness temperatures is low because of the small area occupied by high intensity pixels. At low brightness temperatures, the corresponding area is large, but the mean intensity of pixels is low. The largest intensity contribution comes from pixels with values around  $5 \text{ K km s}^{-1}$ , due to the large area occupied and the relatively high mean intensity. The  $5 \text{ K km s}^{-1}$  brightness temperature corresponds to  $N(^{13}\text{CO}) \approx 1 \times 10^{16} \text{ cm}^{-2}$ ,  $N(^{12}\text{CO}) \approx 5 \times 10^{17} \text{ cm}^{-2}$ , and approximately  $8.6 \times 10^{21} \text{ cm}^{-2}$  total column density

(in simulation d). Taking the relatively large area into account, a significant fraction of the  $^{13}\text{CO}$  and total cloud mass is associated with this intensity range.

To quantify the deviations from the self-consistent distribution, we plot the per cent errors of the approximate maps on the upper panels of Fig. 2.12. At the highest intensities the per cent error shows large fluctuation in both approximate cases. On one hand, the number of pixels in these bins are usually below- or at a few times 10. On the other hand, the  $^{12}\text{CO}/^{13}\text{CO}$  ratio slightly falls below 60 even at the highest intensities/column densities (see Fig. 2.8). Hereafter we exclude bins containing fewer than 100 pixels (a solid, vertical black lines on the per cent error panels) from the comparison.

Generally, the assumption of uniform isotope ratio results in an up to  $\sim 50$  per cent underestimation at intermediate and high intensities ( $W > 5 \text{ K km s}^{-1}$ ) and slight overestimation at low intensities ( $\sim 1 \text{ K km s}^{-1}$ ). The fitting formula offers a better fit with an error usually lower than  $\sim 10$  per cent. These errors are comparable to the errors on the scaled (i.e. uniformly or  $^{12}\text{CO}$  column density dependently) input  $^{13}\text{CO}$  mass (Table 2.5) used in the radiation transport modelling.

The reason for the relatively large difference between the self-consistent and uniformly-scaled maps is that the area associated with a certain  $^{13}\text{CO}$  column density is systematically underestimated when the uniform isotope ratio is adopted. When the chemical fractionation reaction is taken into account, we find higher  $^{13}\text{CO}$  number densities at given total and  $^{12}\text{CO}$  column densities on the intermediate range. In terms of excitation conditions, this means a slight reduction in the number density of collisional partners for the  $^{13}\text{CO}$  molecules. On the other hand, the kinetic temperature is also slightly higher in these regions. On average, this results in a larger volume with similar excitation conditions and emerging brightness temperature. When self-consistent and uniformly scaled maps are visually compared we find a more extended emission in the former case (see Fig. 2.11). When using the fitting formula, the extended emission is almost completely recovered.

The error distributions on the upper panels of Fig. 2.12 show environment dependent trends: in case of simulation c) and f) the per cent error is moderate in both cases (below 10 per cent). In these simulations the isotope-selective reactions play a relatively minor role due to the weak ISRF or the high density (the gas is well shielded close to the cloud edge) and the CO isotope ratio is close to the initial  $^{12}\text{C}/^{13}\text{C}$  ratio in regions where most of the CO mass dwells (see Fig. 2.3). There is however a qualitative difference between runs c) and f): in the case of run c) the chemical fractionation-dominated region is extended, but due to its low column density, falls below the detection limit. In run f), on the other hand, the corresponding region is very compact. In simulation a), b), d) and e) the chemical fractionation is important and the fitting formula recovers the self-consistent distribution better.

We conclude that above the  $0.2 \text{ K km s}^{-1}$  detection limit only chemical fractionation has a non-negligible effect on the isotope ratio, and therefore on the synthetic  $^{13}\text{CO}$  emission maps. The assumption of a uniform isotope ratio in most cases leads to an error as high as 30-40 per cent in the peak brightness temperature and up to 50 per cent in  $W(^{13}\text{CO})$  at brightness temperatures above  $\sim 5 \text{ K km s}^{-1}$ . This approach is a good approximation only when the ISRF is weak, or when the initial density is high. The FWHMs and derived velocity dispersions are insensitive to the adopted isotope ratio. The fitting formula provides a better fit to the self-consistent

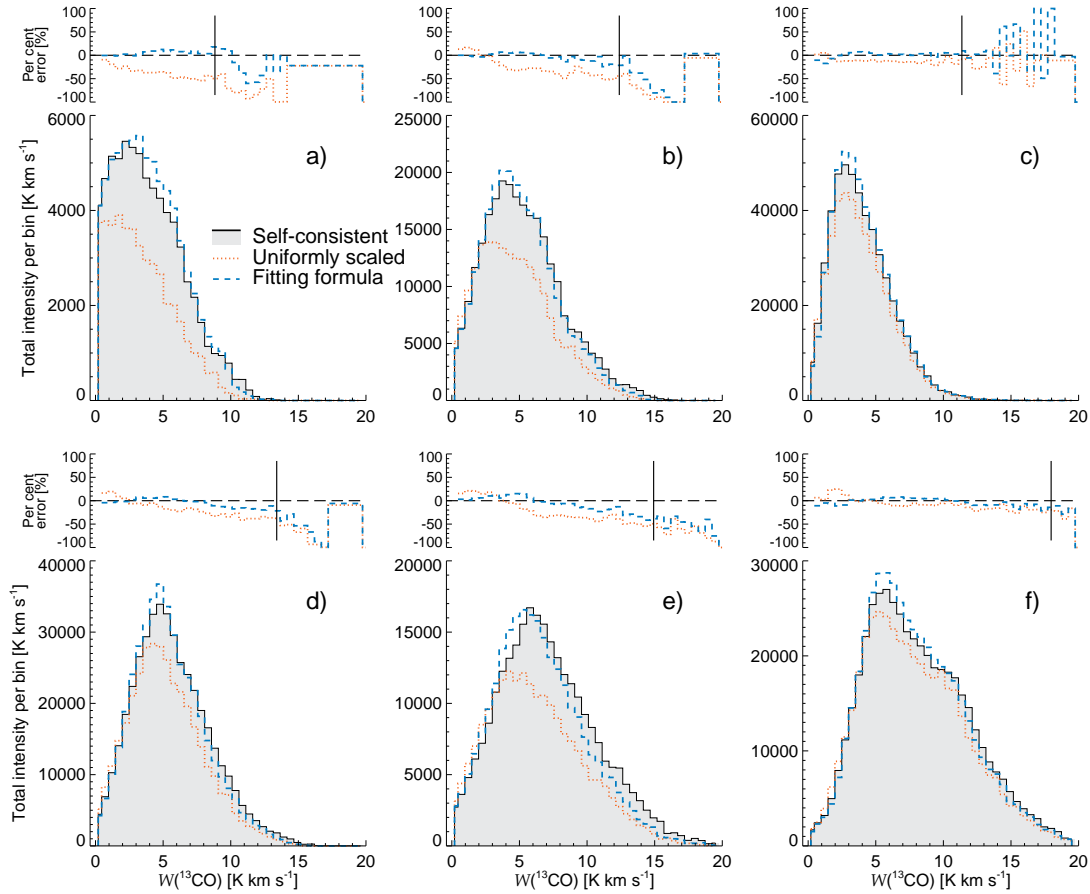


Figure 2.12: Comparison of the  $^{13}\text{CO}$  ( $J = 1 \rightarrow 0$ ) brightness temperature distributions in the 6 simulations (from a to f). The figure shows which brightness temperatures are contributing the most to the total intensity of the cloud. The filled histograms with the black outlines show the self-consistent models. The orange dotted and blue dashed lines represent the distributions from the uniformly scaled and fitting formula approximations. The per cent errors of the latter compared to the self-consistent distribution are shown on panels above the intensity distributions. The vertical black line marks the intensity below which each bin contains more than 100 pixels. We only considered pixels with  $W(^{13}\text{CO}) > 0.2\text{K km s}^{-1}$ .

map in all cases and we recommend its usage in all quantitative investigations.

## 2.5 COMPARISON TO PREVIOUS WORKS

The previous works of Liszt (2007) and Röllig and Ossenkopf (2013) focus on CO fractionation in photon dominated regions. The former study concludes that the CO isotope ratio in low density PDRs ( $n < 10^2\text{cm}^{-3}$ ) is determined by the competing processes of selective photodissociation and chemical fractionation and that the ratio does not reflect local properties, such as the CO excitation temperature and gas density. Röllig and Ossenkopf (2013) find a different behaviour in dense PDRs ( $n > 10^3\text{cm}^{-3}$ ) embedded in strong interstellar radiation fields: with the exception of very specific conditions, the  $^{12}\text{CO}/^{13}\text{CO}$  ratio is always smaller than the  $^{12}\text{C}/^{13}\text{C}$  elemental ratio, indicating that isotope-selective photodissociation is much less effective than chemical fractionation. The common feature of these studies is that they use simplified geometry and density distributions and scale the radiation field strength and the density to probe a large parameter range.

We present cloud simulations with self-consistently calculated density, velocity and temperature structure, which is expected to be consistent with isolated, small ( $M \approx 10^4 M_{\odot}$ ) molecular clouds before the start of star formation, providing an intermediate evolutionary step between the diffuse gas and dense dark cores irradiated by bright young clusters.

The CO isotope ratio in our simulations shows a general behaviour consistent with the results of Röllig and Ossenkopf (2013). The upper and lower panels of Fig. 2.13 present the fractional abundances of carbon bearing species and their isotopic abundance ratios as the function of visual extinction respectively. The figure could be directly compared to Fig. 3 and 4 in Röllig and Ossenkopf (2013) (note that here we show a cloud with an ISRF 10 times lower than in their figures). At low and high visual extinctions most of the carbon atoms are locked in  $\text{C}^+$  and CO, respectively. The transition of the main isotope is at  $\sim 1.5$  mag visual extinction. The conversion of  $^{13}\text{C}^+$  to  $^{13}\text{CO}$  takes place at a slightly lower visual extinction, due to the Eq. 2.1 fractionation reaction becoming the main  $^{13}\text{CO}$  production pathway (Röllig and Ossenkopf, 2013). Increasing radiation field strength or decreasing metallicity shifts these transitions towards higher  $A_V$  values. Compared with the Röllig and Ossenkopf (2013) models, the most important difference is that they find typically an order of magnitude lower  $\text{C}^+$ -CO transitional visual extinction values with similar ISRF strength models. This difference is a result of much higher number densities at the cloud surface, adopted in their models. Their models also produce lower temperatures at similar visual extinction, enhancing the chemical fractionation reaction in those regions. As a result, they find the “dip” in the  $^{12}\text{CO}/^{13}\text{CO}$  ratio curve shifted towards lower total/ $^{12}\text{CO}$  column densities with high end rise coinciding with the UV absorption measurements (see below).

We also find regions where the isotope selective photodissociation dominates and the  $^{12}\text{CO}/^{13}\text{CO}$  ratio is increased above the elemental abundance ratio (see yellow zones in Fig. 2.3). Similarly to Liszt (2007), the typical density is low (around  $\sim 100\text{cm}^{-3}$ ) and the temperature is above 40 K (see Fig. 2.4). The enhanced CO isotope ratio gas, however is confined to a narrow layer around the denser cloud body, and appears only in the column density ratio maps, when in the given line of sight there is no substantial amount of dense gas.

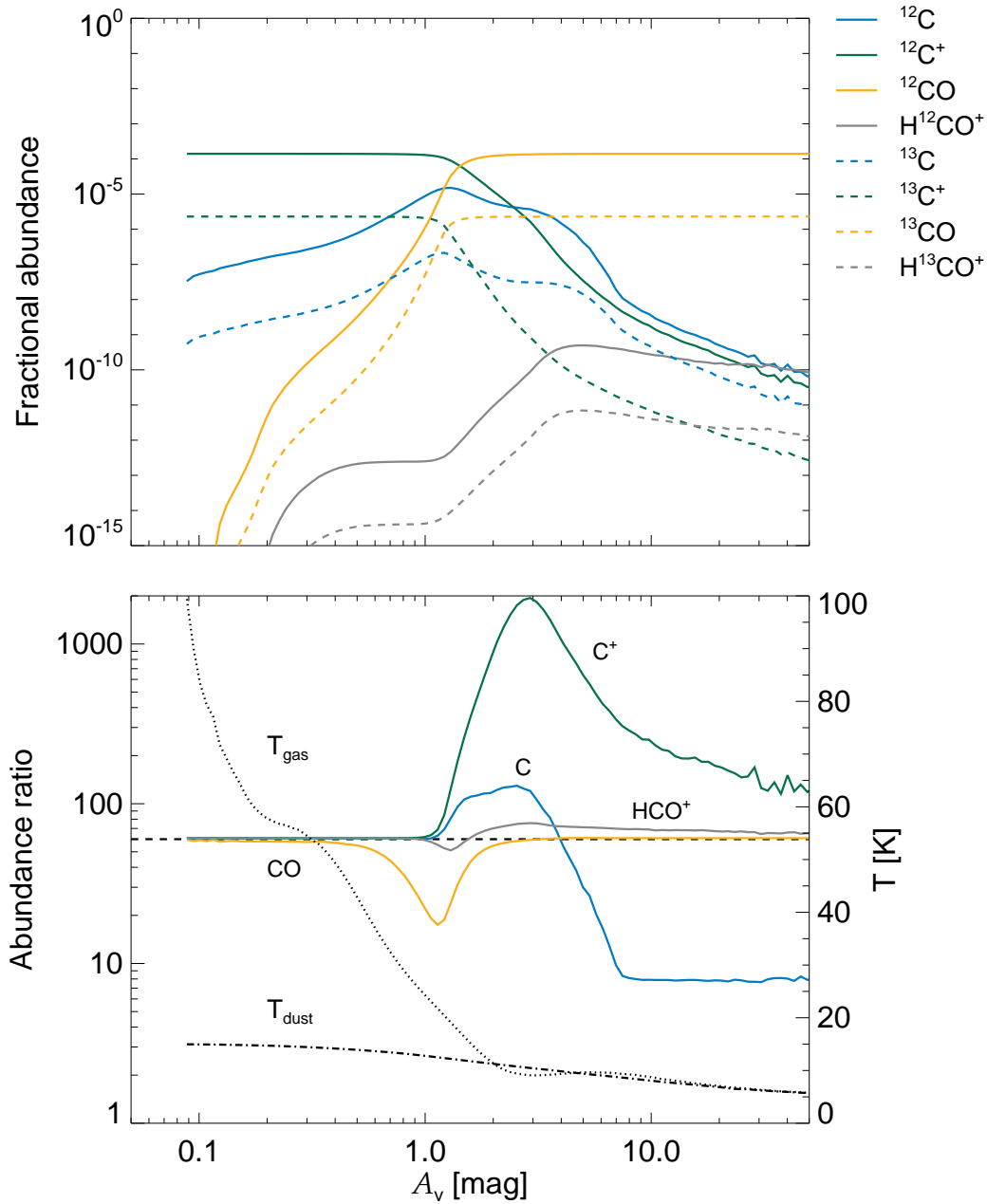


Figure 2.13: The upper panel shows the fractional abundances (relative to total hydrogen nuclei) of the main carbon bearing species and their isotopes as functions of the mean visual extinction in the case of run d). The lower panel shows the median isotopic abundance ratios as a function of visual extinction. The dashed line shows the elemental carbon isotope ratio. The dotted and dotted-dashed lines are the median gas and dust temperature at a given visual extinction.

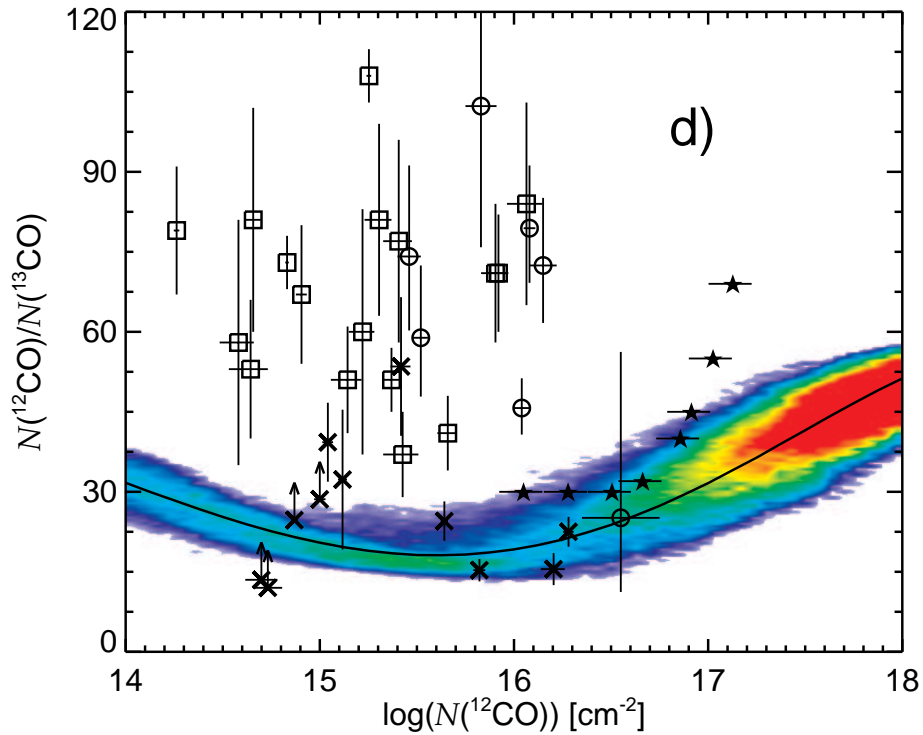


Figure 2.14:  $^{12}\text{CO}/^{13}\text{CO}$  column density ratios from the literature compared to run d) and the adopted fitting formula (black solid line). The ultraviolet absorption measurements are from Sheffer et al. (2007, open square) and Sonnentrucker et al. (2007, open circle). The millimetre-wavelength data are from Liszt and Lucas (1998, “x” symbol). The filled stars are *not direct measurements* but values derived by emission line profile fitting presented in Goldsmith et al. (2008). The colour scale and its meaning is the same as in Fig. 2.6. In contrast to the UV absorption measurements, the millimetre-wavelength data and the fitted ratios are largely consistent with the fitting formula and the distribution in the simulation.

On the observational side, Burgh et al. (2007), Sheffer et al. (2007) and Sonnentrucker et al. (2007) provide ultraviolet absorption measurements of the  $\text{H}_2$ ,  $^{12}\text{CO}$ ,  $^{13}\text{CO}$  column densities and consequently the  $^{12}\text{CO}/^{13}\text{CO}$  isotopic ratio. Liszt and Lucas (1998) also determined the CO isotope ratio in nine selected line of sights by measuring millimetre-wavelength absorption and emission. Both the UV absorption and millimetre-wavelength measurements are limited to  $^{12}\text{CO}$  column densities in the range of  $10^{14} \text{ cm}^{-2} < N(^{12}\text{CO}) < 4 \times 10^{16} \text{ cm}^{-2}$ . At higher column densities the  $^{12}\text{CO}$  absorption/emission saturates, preventing the direct measurement of its column density. In this high CO column density regime, Goldsmith et al. (2008) fitted the brightness temperature distribution of  $^{12}\text{CO}$  and  $^{13}\text{CO}$  emission from the Taurus molecular cloud, using a grid of PDR models with the assumption of an increasing  $^{12}\text{CO}/^{13}\text{CO}$  abundance ratio with increasing  $N(^{12}\text{CO})$ . Although this method carries significant uncertainties, their results provide valuable constraints

on the isotope ratio at high CO column densities.

The aforementioned observations are summarized and compared with the fitting formula and run d) in Fig. 2.14. The UV measurements are inconsistent with the proposed fitting formula, while the millimetre-wavelength measurements and the fitted ratios are largely consistent with it. When interpreting UV absorption data one should keep in mind that they preferentially probe low average column density clouds, more consistent with the dilute, moderate temperature PDRs of Liszt (2007). At the same time, the dense, strongly irradiated PDR models of Röllig and Ossenkopf (2013) are also partly consistent with the UV measured isotope ratio, due to the relatively cold gas at low column densities, which allows significant chemical fractionation. On the other hand, these PDR models have more difficulty explaining the low ratios at high  $^{12}\text{CO}$  column densities, found in millimetre-wavelength measurements. These measurements most likely trace higher average column density clouds similar to the models presented here.

## 2.6 SUMMARY

In this chapter we investigated the effects of selective photodissociation and chemical fractionation on the  $^{12}\text{CO}/^{13}\text{CO}$  ratio in realistic hydrodynamical simulations of isolated molecular clouds, considering a range of cloud properties. We aimed to quantitatively test the validity of the frequently assumed uniform isotope ratio, when  $^{13}\text{CO}$  intensities are calculated from hydrodynamical simulations neglecting isotopic chemistry or when  $^{12}\text{CO}$  column density/mass is inferred from observations of  $^{13}\text{CO}$  emission.

We find a close correlation between the  $^{12}\text{CO}$  column density and the isotope ratio, which shows only a weak dependence on cloud conditions within the considered parameter range. The isotope-selective-photodissociation is effective and increases the isotope ratio up to 70 in some regions. However, the mass fraction of the gas with higher than elemental ratio is negligible, and has virtually no effect on the column density ratio and on the observables. The chemical fractionation reaction – by enhancing the  $^{13}\text{CO}$  abundance – reduces the isotope ratio to values as small as 20 in the  $10^{15} \text{ cm}^{-2} < N(^{12}\text{CO}) < 10^{17} \text{ cm}^{-2}$  range and has a significant effect on the millimetre-wavelength emission. At high CO column densities neither of the isotope-selective reactions are effective, therefore the ratio increases to the value of the elemental isotopic abundance ratio. The isotope ratio varies similarly with the  $^{13}\text{CO}$  column density.

The correlations depend only weakly on environmental conditions, such as ISRF strength or metallicity. This is because the ability of gas to form CO correlates with its ability to shield itself from the interstellar radiation field. If the irradiation is stronger or the metallicity is lower, the regions of significant  $^{12}\text{CO}$  and  $^{13}\text{CO}$  formation shift towards higher total column densities by a similar amount. Furthermore, the characteristic gas temperature of regions where CO reside are very similar in every simulation, providing a consistent condition for the chemical fractionation.

If  $^{12}\text{CO}$  number densities are provided (e.g. from a simulation of a molecular cloud, such as in Glover and Clark, 2012b), and if we want to calculate the corresponding  $^{13}\text{CO}$  number densities, then using a uniform  $^{12}\text{CO}/^{13}\text{CO}$  ratio results in the  $^{13}\text{CO}$  number densities being underestimated by as much as 30-40 per cent (see Table 2.5). This can lead to errors of up to 50 per cent in some regions of the derived

$^{13}\text{CO}$  integrated intensity maps (see Fig. 2.12). The peak brightness temperature is affected by about 30 per cent in this case. However, the adopted isotope ratio has only a few per cent influence on the line width and therefore the derived velocity dispersion. In section 2.3.3 we derive a fitting formula based on the simulation results to address this issue in a computational cost efficient way (i.e. to infer the correct ratio without the need of the full fractionation chemistry model). When the fitting formula is applied, then the  $^{13}\text{CO}$  column/number density and emission can be recovered with errors smaller than 10 per cent.

If we have instead  $^{13}\text{CO}$  column densities (e.g. derived from observations), then using a uniform  $^{12}\text{CO}/^{13}\text{CO}$  ratio to convert them to  $^{12}\text{CO}$  column densities may result in the overestimation of the  $^{12}\text{CO}$  column densities by up to 50-60 per cent (see Table 2.4). In section 2.3.4 we construct a fitting formula describing the correlation of the isotope ratio and the  $^{13}\text{CO}$  column density. By applying this formula the errors could be reduced to  $\sim 10$  per cent. We note however, that the error introduced by using a fixed  $^{12}\text{CO}/^{13}\text{CO}$  ratio may be smaller than other sources of errors in the determination of the  $^{13}\text{CO}$  column density (such as the assumption that the excitation temperatures of  $^{12}\text{CO}$  and  $^{13}\text{CO}$  are the same and that the  $^{13}\text{CO}$  emission is optically thin), which can lead to uncertainties of as much as a factor of 4 (see Padoan et al., 2000, and the following chapter). Nevertheless, in the  $10^{14} \text{ cm}^{-2} < N(^{13}\text{CO}) < 10^{16} \text{ cm}^{-2}$  range, where the aforementioned assumptions are valid and the chemical fractionation is effective, the fitting formula provides more accurate conversion to  $^{12}\text{CO}$  than the assumption of uniform scaling.

The proposed fitting formulas are consistent with millimetre-wavelength  $^{12}\text{CO}/^{13}\text{CO}$  column density ratio measurements, and underestimate the ratio measured in ultraviolet absorption by a factor of 2-3 (see Fig. 2.14). The reason for the discrepancy with the ultraviolet data is probably that the UV measurements are tracing a qualitatively different population of clouds, more consistent with PDR models (diffuse clouds or highly irradiated massive clumps) than with giant molecular clouds.

Finally, we conclude that the fitting formulas proposed above are good representations of the  $^{12}\text{CO}/^{13}\text{CO}$  isotopic ratio distributions of our hydro-chemical simulations and that they can be used to infer  $^{13}\text{CO}$  properties from (magneto-) hydrodynamical simulations in a computationally cost-efficient manner, and more precise  $^{12}\text{CO}$  column density estimates from millimetre-wavelength  $^{13}\text{CO}$  observations, provided that the molecular clouds under investigation are similar to those presented here.

### 3 BENCHMARKING THE CO EMISSION BASED CLOUD MASS MEASUREMENT METHODS

*Adapted from Szűcs, Glover & Klessen, in prep.<sup>1</sup>*

#### ABSTRACT

In this chapter we discuss numerical simulations of molecular clouds with self-consistent CO gas-phase and isotope chemistry in various environments. The simulations are post-processed with a line radiative transfer code to obtain  $^{12}\text{CO}$  and  $^{13}\text{CO}$  emission data in their  $J = 1 \rightarrow 0$  rotational transition. The emission maps are analysed with commonly used observational methods and then the inferred quantities (mass and column density) are compared to the true values.

We generally find that all methods examined here trace the true GMC molecular mass within a factor of 2 uncertainty if the cloud metallicity is not too low. The  $^{13}\text{CO}$  column density method is affected by chemical and optical depth issues, and even though it provides a reasonable estimate for the molecular mass, it measures the true  $\text{H}_2$  column density distribution very poorly. The virial mass estimate seems to work the best in the considered metallicity and radiation field strength range, although this is not surprising, since the simulations are close to virial equilibrium. A single CO-to- $\text{H}_2$  conversion factor appears to be a robust choice over relatively wide ranges of cloud conditions, while methods which try to take its metallicity dependence into account systematically overestimate the true cloud masses.

#### 3.1 INTRODUCTION

The giant molecular clouds (GMCs) mass and its distribution are fundamental parameters in the understanding of the structure of the interstellar medium (ISM) and the star formation process itself. Often, emission from the millimetre-wave rotational transitions of carbon monoxide (CO) isotopes and the mass or column density inference methods built upon their measurements provide the most accessible measure of these fundamental quantities. The methods which are the most often used are the local thermodynamic equilibrium (LTE) column density measurement of the rarer  $^{13}\text{CO}$  isotope (e.g. Goldsmith et al., 2008; Pineda et al., 2008, 2010), the virial mass estimation (e.g. Solomon et al., 1987; MacLaren et al., 1988; Dame et al., 2001; Hughes et al., 2010) and the CO-to- $\text{H}_2$  (often called  $X_{\text{CO}}$ ) conversion factor (e.g. Dickman, 1978; Sanders et al., 1984; Bolatto et al., 2011). Their mass estimates are then used to measure the star formation efficiency of the (molecular) gas (e.g. Solomon and Sage, 1988; Kennicutt, 1998), the galactic and extragalactic GMC mass functions (Colombo et al., 2014; Zaragoza-Cardiel et al., 2014) and the ratio of kinetic to gravitational energy (e.g. Solomon et al., 1987; Colombo et al., 2014), thus

---

<sup>1</sup>See page xi for details on authorship.

inferring the fates of individual clouds (Kauffmann et al., 2013). The measured column density distribution may provide an insight into the Mach-number of the turbulent velocity field that shaped it (Brunt, 2010; Burkhart and Lazarian, 2012). Any uncertainty in the mass and column density measurements are expected to propagate to these more complex quantities. Therefore, the reliability of the mass and column density measurement methods, especially considering the systematic errors introduced by often necessary simplifications, remains a major issue in the field of star formation.

Until recently, the nearby molecular clouds (e.g. Taurus and Perseus), which are well characterized by multiple tracers, provided the best testing grounds for constraining the intrinsic uncertainties in the methods. Pineda et al. (2008), for example, used high dynamic range visual extinction maps to determine the  $\text{H}_2$  column density and  $^{12}\text{CO}$ ,  $^{13}\text{CO}$  and  $\text{C}^{18}\text{O}$  millimetre observations to constrain the CO-to- $\text{H}_2$  conversion factor and the  $^{13}\text{CO}/\text{H}_2$  abundance ratio in the Perseus molecular cloud. They show that the  $^{12}\text{CO}$  and  $^{13}\text{CO}$  emission saturates at visual extinctions of 4 mag and 5 mag respectively and that about 60% of the emission emerges from sub-thermally excited regions. These results clearly challenge the assumptions regarding optical depths and LTE conditions upon which some measurement methods strongly rely. Such regional studies are, however, restricted to the few nearby molecular clouds and they only provide probe to a narrow range in physical conditions and environments. CO-based techniques, on the other hand, are used in diverse conditions, from low metallicity to starburst environments. In addition, the interpretation of observational studies is difficult, since these studies themselves are biased by the effects they ought to measure.

The recent development in computational science and the increasing understanding of the most important physical and chemical processes in the ISM, enables us to perform numerical simulations with increasing realism. Comparing the true column densities and cloud masses from such simulations to those derived from the simulations with applying the observational methods, might provide the most complete census on the sources of errors affecting the measurements.

One of the first studies using three-dimensional hydrodynamic numerical simulations to quantify errors in observational assumptions was presented by Padoan et al. (2000). They computed turbulent magneto-hydrodynamical (MHD) simulations with supersonic and super-Alfrénic turbulence, post-processed them with non-LTE radiative transfer modelling and then compared the true CO column densities to those inferred from the LTE analysis of the molecular emission. They find that none of the assumptions in the LTE method holds over most of the simulated volume, and that the method underestimates the true column densities by a factor of a few. Their simulations are adequate to illustrate the effects arising from the assumption regarding the excitation conditions (i.e. LTE), but neglect several relevant mechanisms, such as the self-gravity of the gas, calculation of the thermal balance (they consider isothermal gas) and a model for the chemical composition. These neglected processes might be as important sources of error in the mass estimates as the radiation transfer effects in certain circumstances.

In this chapter we aim to follow the latter, simulation-based, method for constraining and quantifying the main sources of error in the observational techniques of mass and column density estimation. As a next step in realism compared to Padoan et al. (2000), we present and analyse turbulent hydrodynamic simulations

Table 3.1: Model parameters and used snapshots

Model	$n_0$ [cm <sup>-3</sup> ]	Metallicity [ $Z_{\odot}$ ]	ISRF [ $G_0$ ]	$\alpha_{\text{vir}}$	Time [Myr]
$M_{\text{cloud}} = 10^4 M_{\odot}$					
a	300	0.3	1	1.08	2.046
b	300	0.6	1	1.10	1.930
c	300	1	0.1	1.04	2.124
d	300	1	1	1.04	2.140
e	300	1	10	1.07	2.022
f	1000	1	1	1.51	0.973
g	300	1	1	1.49	0.998
$M_{\text{cloud}} = 10^5 M_{\odot}$					
h	100	1	1	0.90	1.297
i	100	1	100	0.89	1.374
j	100	0.3	1	0.81	1.445

Summary of model parameters. From a) to f) and from h) to j) the analysed snapshots were chosen to be the last before sink particle formation, while g) represents an earlier state of the fiducial cloud (model d).  $Z_{\odot}$  and  $G_0$  refer to the Solar metallicity and the Draine radiation field strength (1.7 in units of the Habing (1968) field) respectively. The virial parameter,  $\alpha_{\text{vir}}$  is defined as the ratio of 2 times the kinetic energy and the potential energy.

with self-gravity, an improved approximation of interstellar radiation field (ISRF) attenuation and self-consistent models of chemistry and gas heating/cooling. In addition to the LTE column density estimation technique, we extend our investigation to additional CO-based methods, such as virial mass estimation and the CO-to-H<sub>2</sub> conversion factor. Most of these methods are calibrated for near-by, “Solar-like” or “Milky Way-like” clouds, thus they are expected to work reasonably well for such conditions. To test the applicability of the methods for different conditions, we explore a range of molecular cloud parameters (metallicity, cloud mass, virial state) and environments (ISRF strength).

The chapter is organized as follows: In section 3.2 and section 3.3 we describe the basic details of the hydrodynamic simulations and the adopted radiative transfer model, respectively. Section 3.4 gives a short overview on the CO-based mass measurements methods and provides details on how the techniques are applied to the synthetic emission maps. The results are presented in section 3.5 and in Fig. 3.3. In the discussion (section 3.6) we pinpoint the reasons for the success or the failure of each of the methods and try to put the results into a broader context. Finally, section 3.7 closes the chapter with a summary.

### 3.2 SIMULATIONS

We performed turbulent cloud simulations using the smoothed particle hydrodynamics (SPH) code GADGET-2<sup>2</sup> (Springel, 2005). In addition to the base code, which deals with the hydrodynamics of a self-gravitating gas, we also include gas-phase chemistry with radiative heating and cooling (Glover and Clark, 2012a), an approximate treatment for the ISRF attenuation (Clark et al., 2012a) and sink particle formation (Bate et al., 1995; Jappsen et al., 2005; Federrath et al., 2010). For the detailed description of the code, the considered physical and chemical processes and the simulation setup see section 2.2. However, we summarize the most important technicalities here as well and underline the differences in initial conditions compared to the previous chapter.

The modelled molecular clouds incorporate a range of initial number densities, metallicities, incident radiation field strengths and total cloud masses (see Table 3.1). In the beginning of each simulation, the cloud is characterized by a spherical shape with a radius set by the total cloud mass ( $M_{\text{cloud}}$ ) and a uniform number density ( $n_0$ ). Similarly, the initial gas and dust temperatures are uniform at 20 K and 10 K, respectively. The initial turbulent bulk motions follow a steep  $P(k) \propto k^{-4}$  power spectrum over a factor of 16 dynamic range, with the maximum scale size equal to the respective cloud radius. The total initial turbulent energy of the  $10^4 M_{\odot}$  models is chosen to be equal to the total gravitational energy, that is  $\alpha_{\text{vir},0} = 2$ . The  $10^5 M_{\odot}$  models are initially in virial equilibrium ( $\alpha_{\text{vir},0} = 1$ ). The energy deposited on large scales cascades down quickly to smaller scales and a power spectrum consistent with fully developed turbulence builds up. The turbulent energy is allowed to dissipate through shocks, providing an important mechanism for heating the gas. We do not replenish the dissipated turbulent energy, i.e. turbulent driving is not considered.

The simulations start with an initial chemical composition which is rich in hydrogen molecules (with fractional abundance of  $x_{\text{H}_2} = 0.5$ ), but poor in CO and the main sources of free electrons are carbon ions and other low ionization potential metals (e.g. Na, Mg). This composition is inspired by the self-consistent cloud formation models of Clark et al. (2012b) and Smith et al. (2014). In the solar metallicity case, the adopted initial fractional abundances of  $^{12}\text{C}$ , O and metals relative to the hydrogen nuclei are  $x_{^{12}\text{C}} = 1.4 \times 10^{-4}$ ,  $x_{\text{O}} = 3.2 \times 10^{-4}$  (Sembach et al., 2000) and  $x_{\text{M}} = 1 \times 10^{-7}$ . These scale linearly with the metallicity parameter of the given model. The He abundance is  $x_{\text{He}} = 0.079$  (corresponding to He mass fraction of 0.24) regardless of the metallicity. In the previous chapter we referred to those initial conditions as “fully molecular” (see also Appendix C)

The chemical evolution of the turbulent gas is followed implicitly in the hydrodynamic simulation, using the gas-phase chemical network NL99 (Nelson and Langer, 1999), designed for the modelling of CO formation in a GMC environment, with an addition of H<sub>2</sub> formation on grain surfaces (Glover and Mac Low, 2007b, see also Chapter 2). Glover and Clark (2012a) showed that the NL99 network reproduces the C<sup>+</sup>, C, CO transition very well when compared to the more complex network of Glover et al. (2010), whilst saving a factor of 3 in computational costs. They also calculate the C/CO ratio in their simulations with the NL99 network, and find a value consistent with observations. We extend the NL99 model by differentiating between

---

<sup>2</sup><http://www.mpa-garching.mpg.de/gadget/>

the  $^{12}\text{C}$  and  $^{13}\text{C}$  isotopes. With the additional reaction of chemical fractionation and an isotopologue species dependent photodissociation shielding prescription, this allows us to model the  $^{12}\text{CO}$  and  $^{13}\text{CO}$  elemental abundances and the physical condition dependent conversion between them self-consistently. The initial  $^{12}\text{C}/^{13}\text{C}$  isotopic ratio is set to 60, a value consistent with the measured average in the solar neighbourhood (Lucas and Liszt, 1998). For the further details of the CO isotope chemistry and its implementation in our hydrodynamic simulations we refer to sections 2.2 and 2.3.

The modelled GMCs are assumed to be irradiated by an isotropic interstellar radiation field. The spectral shape of the ISRF is described by Draine (1978) and Black (1994) at ultraviolet and longer wavelengths, respectively. The fiducial radiative energy flux ( $G_0$ ) is equivalent to 1.7 in units of the Habing (1968) field, or  $2.7 \times 10^{-3} \text{ erg cm}^{-2} \text{ s}^{-1}$  integrated over the 91.2–240 nm wavelength range. The  $\text{H}_2$  and CO molecules can be relatively easily dissociated by the ultraviolet photons of the ambient radiation field in the optically thin gas. As the  $\text{H}_2$  and CO column densities build up, the molecules closer to the surface protect their peers located at higher depths from the dissociating radiation. To account for these shielding effects we employ  $\text{H}_2$ ,  $^{12}\text{CO}$  and  $^{13}\text{CO}$  column density dependent scaling factors to adjust the photodissociation rates of these species. The adopted model for  $\text{H}_2$  self-shielding is described in Draine and Bertoldi (1996). The factors of CO self-shielding and CO shielding by the Werner-band of  $\text{H}_2$  molecules are taken in a tabulated form from Visser et al. (2009a). The column densities were calculated by the TREECOL algorithm (Clark et al., 2012a). In sections 1.4 and 1.5.2 of the introduction, we give a detailed summary of our treatment of shielding.

The SPH mass resolution is kept consistent in both the  $10^4 M_\odot$  and the  $10^5 M_\odot$  simulation (at  $0.5 M_\odot$ ) by increasing the SPH particle number from  $2 \times 10^6$  to  $2 \times 10^7$ . The factor of 10 increase in particle number increases the simulation run time by a factor of 4, therefore we restrict the explored parameters to the fiducial, the low metallicity and the strong radiation field. Although a significant population of giant molecular clouds as massive as  $10^6 - 10^7 M_\odot$  is observed in the Milky Way and other galaxies in the Local Group (Rosolowsky, 2005), we are unable to model such large clouds due to the very large computational cost.

### 3.3 CO ISOTOPE EMISSION MAPS

For the further analysis, we select the last snapshots just before the formation of the first sink particles. The exception is model (g), where we consider earlier stages of the cloud evolution to test the methods in the case of higher virial parameter values. Nevertheless, we note that observational studies find much higher virial parameters than the highest considered here (Kauffmann et al., 2013), and that clouds with  $\alpha_{\text{vir}} = 1$  and 1.5 are indistinguishable within the usual observational uncertainty. The SPH data is interpolated to a  $512^3$  zone regular grid using the procedure described in Appendix B.1. This conversion step is necessary, because the radiation transport code used to produce emission maps takes gridded data as input. See Appendix B.2 for a discussion on the effects of the grid resolution on the emergent emission.

We calculate position-position-velocity (PPV) emission maps in the  $J = 1 \rightarrow 0$  rotational transitions of  $^{12}\text{CO}$  ( $\lambda_{0,12\text{CO}} = 2600.76 \mu\text{m}$ ) and  $^{13}\text{CO}$  ( $\lambda_{0,13\text{CO}} = 2720.41 \mu\text{m}$ ). The spatial size of the maps is  $16 \text{ pc} \times 16 \text{ pc}$  with a linear resolution of  $0.032 \text{ pc}$

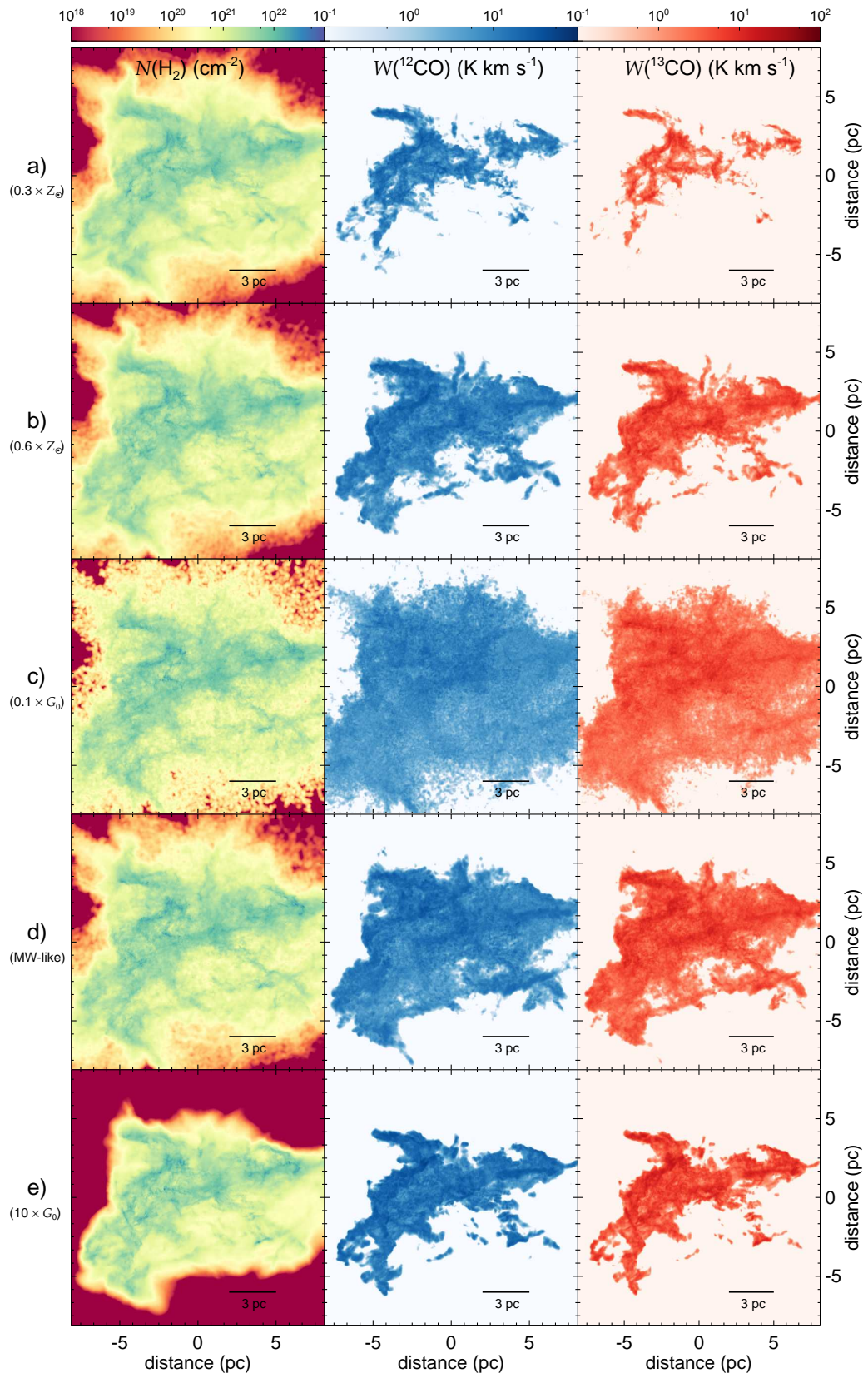


Figure 3.1: H<sub>2</sub> column density map and the <sup>12</sup>CO and <sup>13</sup>CO integrated emission maps.

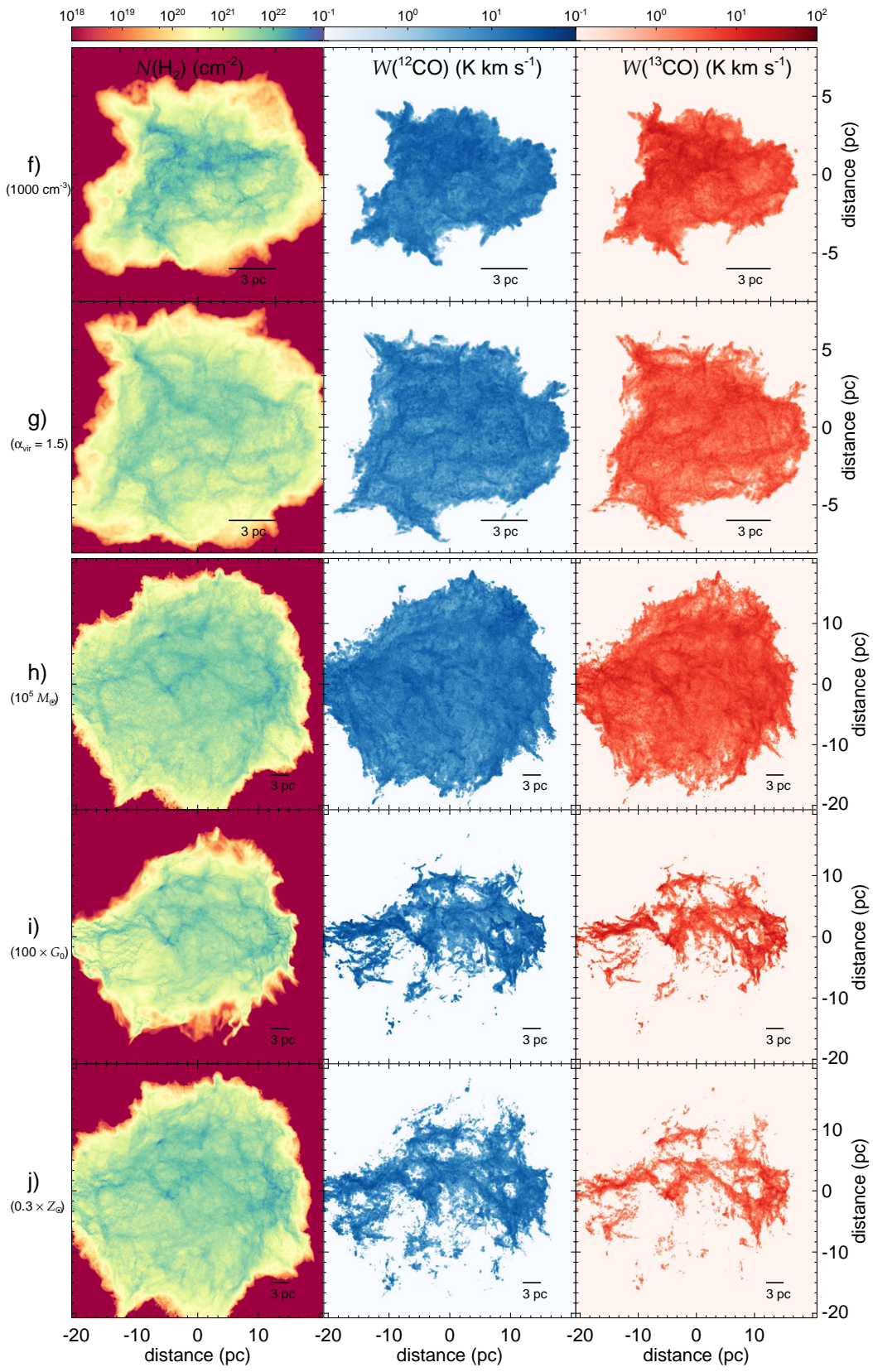


Figure 3.1: (continued)

in the  $M_{\text{cloud}} = 10^4 M_{\odot}$  case. For the  $M_{\text{cloud}} = 10^5 M_{\odot}$  simulations the map size is  $43 \text{ pc} \times 43 \text{ pc}$  with a spatial resolution of  $0.084 \text{ pc}$ . The former resolution is comparable to single-dish sub-millimetre observations of low-mass, nearby molecular clouds, such as the Taurus cloud (Pineda et al., 2010), while the latter is from a factor of 3 to an order of magnitude better than resolution observed for distant, Galactic high-mass molecular cloud complexes, such as W43 (Carlhoff et al., 2013) and  $\eta$  Carinae (Yonekura et al., 2005). Besides the similar observational resolution in the high-mass cloud case, the resolution is also limited by the available computer random access memory<sup>3</sup> for the radiative transfer modelling. The emission is considered in a  $\pm 6 \text{ km s}^{-1}$  velocity range around rest frame wavelengths of the transitions. The spectral resolution is set to  $0.09 \text{ km s}^{-1}$ . For the calculations we use the RADMC-3D<sup>4</sup> radiative transfer tool, described in Dullemond (2012).

The critical  $\text{H}_2$  number density for the CO molecule  $J = 1 \rightarrow 0$  transition – at which the collisional rate and the spontaneous de-excitation rate are equal – is about  $2200 \text{ cm}^{-3}$ . Above this value the rotational energy levels are expected to be populated according the thermal distribution (i.e. LTE applies). However, non-negligible CO emission already emerges where the number density reaches a few hundred particles per  $\text{cm}^3$ . Here, the CO excitation temperature is lower than the kinetic temperature and therefore the LTE approximation of radiative transfer is not applicable. By volume, such regions dominate the simulation domains. Furthermore, in the optically thick regions the higher energy levels might be more populated than in LTE, due to repeated excitation by trapped photons (see Section 16.3.1 in Wilson et al., 2009). To account for the sub-thermal excitation and photon trapping, we adopt the Large Velocity Gradient (LVG, Sobolev, 1957; Ossenkopf, 1997; Shetty et al., 2011a) method. In the LVG approximation, the global problem of radiation propagation is localized by correlating the escape probability of photons from a cell with the velocity gradient to the adjacent cells. Ossenkopf (1997) showed that the approximation is reliable within 20% even when the large gradient criterion does not strictly apply (e.g. in regions of in- or outflow).

Besides the number density distribution of the species in question, the properties (i.e. density and cross-section) of the collisional partners and the velocity vector field are also necessary for the LVG radiative transfer calculations. Due to their high abundance, hydrogen molecules are the most probable collisional partners for CO. We account for the two spin isomers of  $\text{H}_2$  with an ortho-to-para number density ratio of  $3 \times 10^{-5}$  (i.e. the thermal ratio at 15 K. Keep in mind however, the exact choice of the ratio has only a few per cent effect on the emission, see section 2.4.1). The collisional rates and the line properties are adopted from the Leiden Atomic and Molecular Database<sup>5</sup> (Schöier et al., 2005; Yang et al., 2010). The resolved velocity field is taken from the hydrodynamical simulations and interpolated to the regular grids. The velocity dispersion on sub-voxel scales may have a non-negligible contribution to the emission line width. To account for this contribution, we assume that the velocity dispersion follows the scaling relation between size scale and line width (i.e. velocity dispersion),  $v_{\text{unres}} = 1.1 \times (\Delta x[\text{pc}])^{0.38} [\text{km s}^{-1}]$  (Larson, 1981),

<sup>3</sup>In this study we used a workstation with 96 GB total RAM. This limits our maximum grid size to  $768^3$ . However, we find that a grid size of  $512^3$  zones is sufficient for convergence in total emission (see Appendix B).

<sup>4</sup><http://www.ita.uni-heidelberg.de/~dullemond/software/radmc-3d/>

<sup>5</sup><http://home.strw.leidenuniv.nl/~moldata/>

where  $\Delta x$  is the linear size of a pixel. [Heyer and Brunt \(2004\)](#) show that, due to the universality of turbulence, the correlation holds on sub-GMC scales, justifying our choice. The  $10^4$  and the  $10^5 M_\odot$  models yield unresolved velocity dispersions of  $0.29$  and  $0.42 \text{ km s}^{-1}$ , respectively. In case (d), the emission is also modelled without the unresolved velocity dispersion component for comparison and to constrain the effect of the chosen value on the emission and on the derived parameters (such as the virial mass).

The result of the radiative transfer calculations are  $^{12}\text{CO}$  and  $^{13}\text{CO}$  PPV emission cubes for each of our cloud simulations. The maps are converted to brightness temperature ( $[T_b] = \text{K}$ ) units for the sake of consistency with the observations.

For a more detailed description of the radiative transfer modelling and the data preparation procedure we refer to [section 2.4](#), [Appendix B.1](#) and [Appendix B.2](#).

### 3.4 METHODS FOR CLOUD MASS ESTIMATION

There are several methods in the literature for inferring GMC masses. In this chapter we focus on those which are based on the measurement of CO emission. The most commonly used techniques include the measurement of CO isotope column density (e.g. [Pineda et al., 2008](#); [Roman-Duval et al., 2010](#)), the virial analysis (e.g. [MacLaren et al., 1988](#); [Hughes et al., 2010](#)) and the conversion of emission to  $\text{H}_2$  column density with the  $X_{\text{CO}}$ -factor (see review in [Bolatto et al., 2013](#)). In this section we describe the aforementioned methods and apply them to the emission maps calculated from the simulations. We aim to test which methods work best under which conditions.

We restrict our analysis to brightness temperatures above certain contour levels. The choice of these levels are inspired by detection limits of real observations. We choose the  $^{12}\text{CO}$  and the  $^{13}\text{CO}$  detection limits to be  $0.6 \text{ K}$  and  $0.3 \text{ K}$ , respectively. These are comparable to the currently achievable per channel  $3\sigma_{\text{rms}}$  (root-mean-square noise) threshold of nearby ([Lee et al., 2014](#)), galactic ([Roman-Duval et al., 2010](#)) and Large Magellanic Cloud ([Hughes et al., 2010](#)) GMC observations. The limits are applied consistently in each methods. When the method requires the PPV cubes as input (i.e. the column density estimation and the virial mass estimation) each PPV location which is below the limit has its value set to 0. When the method requires 0th moment maps (i.e. velocity channel integrated), as in case of the CO-to- $\text{H}_2$  conversion factor method, then we calculate the masked moment maps (e.g. [Dame et al., 2001](#)): In a given line of sight, only the channels with brightness temperatures higher than the detection limit are considered in the integration. We neglect any additional uncertainties resulting from the intrinsic noise of the observational data and possible calibration errors.

#### 3.4.1 COLUMN DENSITY DETERMINATION

In this approach, the column density of an optically thin molecular gas tracer (usually  $^{13}\text{CO}$  or  $\text{C}^{18}\text{O}$ ) is first calculated, then an abundance ratio between the observed species and  $\text{H}_2$  is assumed (this implicitly contains the conversion to  $^{12}\text{CO}$  first) and the column density of the latter is calculated. The molecular gas column density is then spatially integrated over the chosen contour level to give the total  $\text{H}_2$  mass above the limit.

We use the  $^{13}\text{CO}$  emission maps derived from our simulations. The  $^{13}\text{CO}$  column density, analogous to what we would measure from observations, is determined following the concepts presented in Chapter 15.4 of [Wilson et al. \(2009\)](#) for linear molecules in LTE. The method involves a set of additional assumptions, such as that all CO isotopes have a uniform excitation temperature along a line of sight and that their emission originates from the same volume. Additionally, it is assumed that the optical depth of the  $J = 1 \rightarrow 0$  transition is much larger than 1 for  $^{12}\text{CO}$  and much smaller than 1 for  $^{13}\text{CO}$ . Furthermore, the only source of background radiation is the 2.7 K cosmic microwave background. It is known that some of these assumptions are invalid in realistic conditions or only hold over a limited column density range ([Kennicutt and Evans, 2012](#)). For instance, the  $^{13}\text{CO}$  emission becomes optically thick around a few  $\times 10^{16} \text{ cm}^{-2}$  column density, and provides only a lower limit at higher  $N(^{13}\text{CO})$ , where a significant mass fraction of the  $^{13}\text{CO}$  mass resides. Similarly, the excitation temperature inferred from  $^{12}\text{CO}$  emission might differ considerably from the real excitation temperature ([Padoan et al., 2000](#); [Molina, 2013](#)).

Despite these issues, many observational studies rely on this method (e.g. [Goldsmith et al., 2008](#); [Pineda et al., 2008, 2010](#)). Considering all the effects, the method is expected to overestimate the mass in certain column density ranges, while underestimating the CO and total cloud mass. We show, however, in section 3.6 that it might be good measure of column density over a limited range, which depends on the cloud environment.

To determine the column density of  $^{13}\text{CO}$ , first we have to estimate the “effective” excitation temperature along the lines of sight (see [Molina, 2013](#), for a discussion of the choice of an extinction temperature measure) and the optical depth ( $\tau$ ) of the emission line in question. Generally, the intensity of an emission line can be derived from the radiative transfer equation (see Eq.1.39) and written as

$$I_{\text{line}} = (S - I_0)(1 - e^{-\tau}), \quad (3.1)$$

where  $S$  denotes the source function, which is defined as the ratio of the emission and the absorption coefficients, and  $I_0$  is the incident background intensity.

In the Rayleigh-Jeans regime the brightness temperature is strictly proportional to the kinetic temperature of the gas emitting it. In fact,  $T_b$  is defined as the temperature, which, when inserted to the Rayleigh-Jeans law, would give the measured intensity;

$$T_b = I_\nu \frac{c^2}{2\nu k_B}, \quad (3.2)$$

where  $c$  is the speed of light in  $\text{cm s}^{-1}$ ,  $\nu$  is the transition frequency (115.271 GHz and 110.201 GHz for the lowest  $J$  rotational transition of  $^{12}\text{CO}$  and  $^{13}\text{CO}$ , respectively) and  $k_B$  is the Boltzmann constant in CGS units. Assuming that the source function and the initial (background) intensity follow black body spectral distributions with temperatures of  $T_{\text{ex}}$  and  $T_{\text{bg}} = 2.71 \text{ K}$ , equations 3.1 and 3.2 can be combined to

$$T_b = T_0 \left( \frac{1}{e^{T_0/T_{\text{ex}}} - 1} - \frac{1}{e^{T_0/T_{\text{bg}}} - 1} \right) (1 - e^{-\tau}), \quad (3.3)$$

where  $T_0 = h\nu/k_B$ , with  $h$  denoting the Plack constant in CGS units. If  $\tau$  is much larger than 1 and we neglect the background radiation, then  $T_b = T_{\text{ex}}$ . Thus the

excitation temperature of an optically thick line, such as  $^{12}\text{CO}$  ( $J = 1 \rightarrow 0$ ), is given by:

$$T_{\text{ex}} = 5.5 \ln \left( 1 + \frac{5.5}{T_{\text{b,peak}}^{12} + 0.82} \right)^{-1}, \quad (3.4)$$

where the  $T_{\text{b,peak}}^{12}$  is the  $^{12}\text{CO}$  brightness temperature at the emission peak and  $5.5 \text{ K} \equiv T_0 = h\nu(^{12}\text{CO})/k_{\text{B}}$ .

We assume that the excitation temperatures of  $^{12}\text{CO}$  and  $^{13}\text{CO}$  are equal. Thus substituting the  $^{12}\text{CO}$  excitation temperature with the  $^{13}\text{CO}$  brightness temperature in Eq. 3.3 we solve for

$$\tau_{13}(\nu) = -\ln \left[ 1 - \frac{T_{\text{b}}^{13}(\nu)}{5.3} \left\{ \exp \left( \frac{5.3}{T_{\text{ex}}} - 1 \right)^{-1} - 0.16 \right\}^{-1} \right], \quad (3.5)$$

where  $T_{\text{b}}^{13}(\nu)$  is the  $^{13}\text{CO}$  brightness temperature spectrum around the  $J = 1 \rightarrow 0$  line and  $5.3 \text{ K} = h\nu(^{13}\text{CO})/k_{\text{B}}$ . The optical depth calculated in this way is an indicator for the column density of  $^{13}\text{CO}$  molecules in the lower  $J$  state of the transition (in this case the ground state). To convert this to the total  $^{13}\text{CO}$  column density, we must sum over all energy levels of the molecule. Assuming LTE conditions (i.e.  $T_{\text{ex}} = T_{\text{kin}}$  for all energy states) and that the Boltzmann distribution applies, we can thus estimate the population of all states (see equations 15.32 to 15.35 in [Wilson et al., 2009](#)).

Finally, the column density of  $^{13}\text{CO}$  is calculated according to

$$N(^{13}\text{CO}) = 3.0 \times 10^{14} \frac{T_{\text{ex}} \int \tau_{13}(\nu) d\nu}{1 - \exp(-5.3/T_{\text{ex}})}, \quad (3.6)$$

where the beam (i.e. pixel) average column density is in the units of  $\text{cm}^{-2}$ , the line temperatures are in K, and the velocities ( $v = 10^{-5} c (1 - \nu/\nu(^{12}\text{CO}))$ ) are in  $\text{km s}^{-1}$ . After [Wilson et al. \(2009\)](#), we call this method *W2009\_col* for the remainder of the chapter.

[Roman-Duval et al. \(2010\)](#) adopts a slightly different method (*RD2010\_col*); instead of calculating an effective excitation temperature along a line of sight, they calculate it for each velocity channel. Consequently,  $\tau_{13}$  becomes a function of velocity (i.e. frequency), and cannot be moved out from the integral in Eq. 3.6.

The  $^{13}\text{CO}$  column densities are then converted to  $^{12}\text{CO}$  column densities by multiplying with the isotopic ratio. The CO isotopic ratio can differ by a factor of few from the elemental  $^{12}\text{C}/^{13}\text{C}$  ratio. The reason for this is selective photodissociation in the low density, high temperature and moderately shielded cloud regimes, or the chemical fractionation, which takes place in moderate volume density, better shielded, cool gas (Figure 2.4). Nevertheless, the often adopted ratio of the elemental isotopes is uniform in most studies. In one instance we will also apply this approximation with the isotope ratio of 60. In the other case, we use the results from section 2.3.3 and infer the isotope ratio as a function of  $^{13}\text{CO}$  column density using the fitting formula.

In the final step, the  $^{12}\text{CO}$  column density is converted to  $\text{H}_2$  column density. For this, we assume that all the available carbon is incorporated in CO. In case of the Solar metallicity model, this means a relative abundance to  $\text{H}_2$ ,

$n(^{12}\text{CO})/n(\text{H}_2) = 2.8 \times 10^{-4}$ , with an  $\text{H}_2$  fractional abundance relative to the total hydrogen nuclei of 0.5. For the lower metallicity cases, this value scales proportionally to  $Z$ . With this choice of the  $n(^{12}\text{CO})/n(\text{H}_2)$  ratio, the CO implied  $\text{H}_2$  column density at the low end of the distribution is expected to systematically overestimate the true distribution. The reason for this is the efficient destruction of CO by photodissociation in the weakly shielded, low visual extinction gas (van Dishoeck and Black, 1988; Visser et al., 2009a). Nevertheless, when only CO observations are available for a given GMC this approximation might be considered as the “best guess”. Pineda et al. (2010) for example finds, when comparing  $\text{H}_2$  column densities derived from CO isotope emission and visual extinction, that in their Mask 1 region the  $n(^{12}\text{CO})/n(\text{H}_2)$  ratio varies strongly, while in the Mask 2 region, it can be approximated with a single value of  $1.1 \times 10^{-4}$ .

### 3.4.2 VIRIAL MASS

The virial mass analysis is based on the measurement of the size and the average turbulent line width of the cloud. If these quantities are known and the radial density profile is given, then the mass of the cloud under the assumptions of virial equilibrium and spherical symmetry can be calculated using the equation:

$$M_{\text{vir}} = \frac{3(5-2k)}{G(3-k)} R_{\text{pc}} \Delta V^2, \quad (3.7)$$

where  $k$  is the exponent of the radial density distribution (i.e.  $\rho(r) \propto r^{-k}$ ),  $G$  is the gravitational constant ( $G \approx 1/232 \text{ M}_{\odot}^{-1} \text{ pc km}^2 \text{ s}^{-2}$ ),  $R_{\text{pc}}$  is the linear cloud size in pc and  $\Delta V$  is the full width at half-maximum (FWHM) of the line in  $\text{km s}^{-1}$ . The numerical coefficient consists of a factor depending on the exponent of radial density profile, a constant factor for converting line width to velocity dispersion and the gravitational constant. Assuming a density profile with  $k = 1$  the value of the coefficient is  $1040 \text{ M}_{\odot} \text{ pc}^{-1} \text{ km}^{-2} \text{ s}^2$ , while with an exponent of  $k = 2$  it is  $700 \text{ M}_{\odot} \text{ pc}^{-1} \text{ km}^{-2} \text{ s}^2$  (MacLaren et al., 1988). The appropriate exponent for realistic clouds and the expected error emerging from an incorrect choice of the exponent are discussed in section 3.6.2.

We measure the cloud size and velocity dispersion in the  $^{12}\text{CO}$  position-position-velocity data cube using the moment-based method developed by Rosolowsky and Leroy (2006,  $RL_{2006_{\text{vir}}}$  hereafter) and frequently adopted in observational studies (e.g. Hughes et al., 2010). The cloud is defined by a brightness temperature iso-surface, such that all the connected pixels brighter than the limit  $T_{\text{b,edge}}$  are associated with the cloud. We set the limit to be  $T_{\text{b,edge}} = 0.6 \text{ K}$  (in the case of  $^{12}\text{CO}$ ). The data cubes are then rotated such that the  $x$  and  $y$  axis are aligned with the major and minor axis of the cloud, respectively (see Eq. 1 in Rosolowsky and Leroy, 2006). The root-mean-square cloud size is given by the geometric mean of the second spatial moments along the major and minor axis. The velocity dispersion is computed analogously, by taking the second moments along the velocity axis. Assuming a Gaussian line profile, the velocity dispersion is related to the FWHM value via  $\Delta V(T_{\text{b,edge}}) = \sqrt{8 \ln(2)} \sigma_{\text{v}}(T_{\text{b,edge}})$ , where  $\sigma_{\text{v}}(T_{\text{b,edge}})$  is the velocity dispersion. Considering a  $k = 1$  radial density distribution exponent, Eq. 3.7 can be written as

$$M_{\text{vir}}(T_{\text{b,edge}}) = 1040 \times R_{\text{pc}}(T_{\text{b,edge}}) \times \sigma_{\text{v}}^2(T_{\text{b,edge}}) [\text{M}_{\odot}]. \quad (3.8)$$

We use the `CPROPS`<sup>6</sup> implementation of this recipe. An additional feature of `CPROPS` is the possibility of extrapolating the cloud properties (size and velocity dispersion) to the  $T_{\text{b,edge}} = 0$  K contour level (i.e. to correct for emission falling below the detection limit). We do not use this option for the sake of consistency with the other methods.

[MacLaren et al. \(1988, \*ML1988<sub>vir</sub>\*\)](#) proposed a slightly different analysis by suggesting the use of both  $^{12}\text{CO}$  and  $^{13}\text{CO}$  emission. They argue that the virial theorem gives a reliable result only if the considered  $\Delta V$  describes the average line-width over the whole cloud, including the central core regions. The typically optically thick  $^{12}\text{CO}$  emission provides information only from the cloud surface region (where the optical depth is about 1), while  $^{13}\text{CO}$  remains optically thin until larger depths and monitors the velocity structure deeper in the cloud. On the other hand, due to the selective photo-dissociation,  $^{13}\text{CO}$  has a larger  $A_V$  formation threshold than  $^{12}\text{CO}$ , and cloud size estimations based on it would underestimate the true value. In our implementation of the *ML1988<sub>vir</sub>* method, we use the same procedure as *RL2006<sub>vir</sub>* to calculate the cloud size and the velocity dispersion, but use  $^{12}\text{CO}$  emission to obtain the former, and  $^{13}\text{CO}$  emission to obtain the latter.

The virial mass of the cloud is a measure of the total cloud mass within the detection limit contour level, that is the He content should be subtracted from it to arrive at the  $\text{H}_2$  mass. We do so to remain consistent with the other methods presented in the chapter.

### 3.4.3 THE $\text{CO}$ -TO- $\text{H}_2$ CONVERSION FACTOR

In the case of nearby GMCs the  $\text{H}_2$  column density can be estimated by measuring the diffuse  $\gamma$ -rays and the  $\text{HI}$  21 cm hyperfine electronic transition fluxes. The diffuse  $\gamma$ -ray are produced when high energy cosmic-ray particles interact with atomic hydrogen, atomic helium and  $\text{H}_2$ , thus the  $\gamma$ -ray flux is proportional to their combined column density. The contribution of He and  $\text{HI}$  are then removed by assuming a He abundance and subtracting the  $\text{HI}$  column density measured from the 21 cm line emission. A series of studies (e.g. [Dickman, 1978](#); [Sanders et al., 1984](#)) found that the  $\text{H}_2$  column density calculated this way is proportional to the velocity-integrated intensity of the  $^{12}\text{CO}$  ( $J = 1 \rightarrow 0$ ) line ( $W_{\text{CO}} = \int T_{\text{B}}^{12}(v) dv$ , in units of  $\text{K km s}^{-1}$ ). The proportionality is often expressed with the so-called  $X_{\text{CO}}$ -factor:

$$X_{\text{CO}} \equiv \frac{N_{\text{H}_2}}{W_{\text{CO}}}. \quad (3.9)$$

A number of independent studies (see a review of [Bolatto et al., 2013](#)) find an constant  $X_{\text{CO}}$  value of  $2 \times 10^{20} \text{ cm}^{-2} \text{ K}^{-1} \text{ km}^{-1} \text{ s}$  with 30% uncertainty in the Milky Way disk environment (i.e.  $Z = Z_0, G = G_0$ ).

The  $X_{\text{CO}}$ -factor is, however, expected to vary on small scales and to correlate with the cloud properties and the (galactic) environment. In general, the variation in the conversion factor is due to the combined effects of changes in the chemical and excitation properties of the GMC with scale, environment and/or composition. In low metallicity environments, such as dwarf irregular galaxies, the  $X_{\text{CO}}$  factor might increase drastically, with multiple orders of magnitude in the bulk of the clouds. As an example, [Bolatto et al. \(2011\)](#) find and increase about 2 orders of

<sup>6</sup><https://github.com/low-sky/cprops>

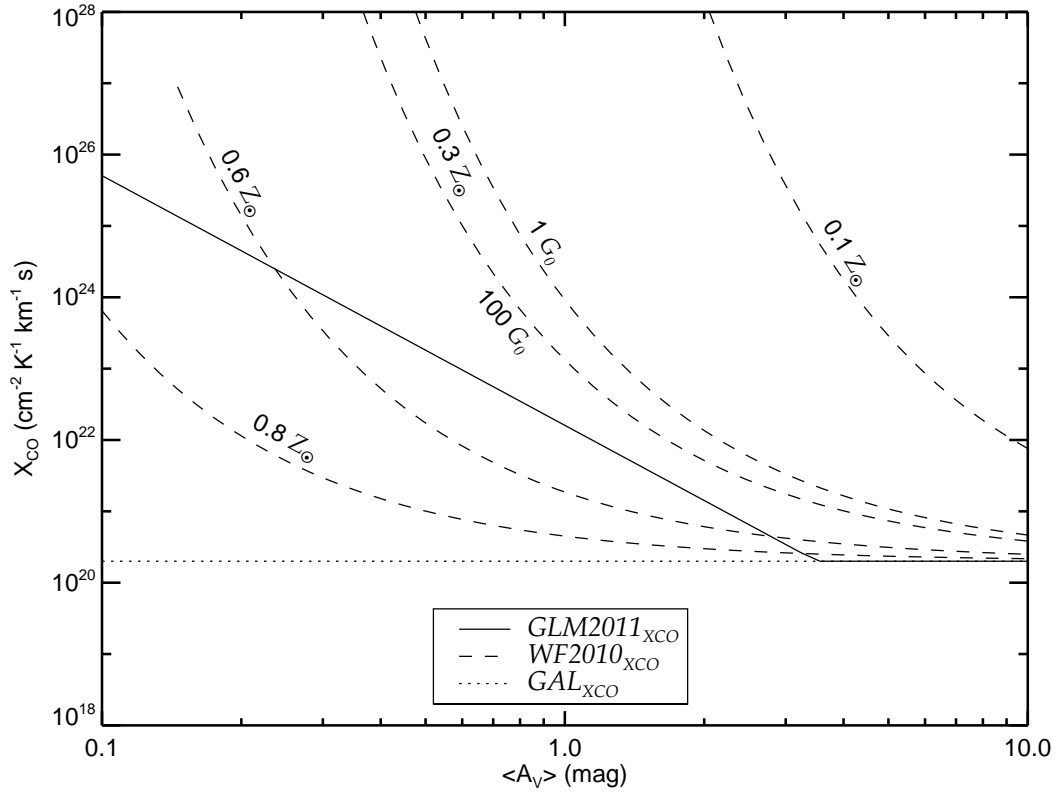


Figure 3.2: Comparison of prescriptions for the mean visual extinction and metallicity dependent  $X_{\text{CO}}$ -factors. In the case of the  $\text{GML2011}_{X_{\text{CO}}}$  method, the metallicity dependence enters implicitly, via the scaling of the dust to gas ratio with  $Z$ . The  $\text{WF2010}_{X_{\text{CO}}}$  method accounts for the metallicity and the ISRF dependence explicitly. In this case,  $X_{\text{CO}}$  strongly depends on the metallicity, while the ISRF dependence is much weaker. At high  $\langle A_V \rangle$  all models converge by construction to the Galactic value, while at low mean  $A_V$  values there is a wide distribution of possible conversion factors. The  $\text{GML2011}_{X_{\text{CO}}}$  empirical fit is roughly consistent with the 0.3 and 0.6  $Z_{\odot}$  metallicity  $\text{WF2010}_{X_{\text{CO}}}$  curves.

magnitude in the Small Magellanic Cloud, compared to the Milky Way value. The reasons could be traced back to both the lower abundance of carbon and oxygen available for CO production and the reduction of dust particles that are absorbing and scattering the incident ultraviolet radiation, thus shielding the CO molecules from photodissociation. The H<sub>2</sub> and CO molecules are formed through qualitatively different chemical processes and the efficiency of their destruction by the ISRF differs. H<sub>2</sub> mainly forms on dust grains and its abundance depends primarily on the available time (e.g. in conditions typical to the Milky Way clouds the equilibrium abundance is reached in  $\sim 2$  Myr). CO, on the other hand, forms primarily in the gas phase via the relatively fast ion-neutral and the somewhat slower neutral-neutral reactions and due to its less efficient shielding it gets destroyed even at higher cloud depths (see section 2.2.2), thus its abundance is set mainly by the shielding available. With decreasing metallicity, the CO shielding decreases, therefore the CO emitting zone shrinks to enclose only the highest (column) density regions of the clouds, while the H<sub>2</sub> rich gas still remains extended. This results in an increasing  $X_{\text{CO}}$  factor.

Similarly, when the incident ISRF is strong, e.g. in the Galactic center and starburst environments, the CO-abundant zone retreats to higher total column densities, thus the  $X_{\text{CO}}$  factor rises. The stronger irradiation, however, also boosts the excitation temperature in the CO-rich zones. This in turns increases the brightness of the CO line. As a result, the conversion factor decreases. In certain cases these two effects might cancel each other, resulting in a  $X_{\text{CO}}$  factor close to the Milky Way value (Liszt et al., 2010). Glover & Clark (in prep.) investigate the radiation field strength dependence of the  $X_{\text{CO}}$  factor by exposing a cloud to progressively increasing ISRF strength values (from 1 to  $10^4 G_0$ ). They find that the excitation temperature increase in itself can not compensate for the CO photodissociation at low column densities. However, when the mean cloud density is also increased, then a  $X_{\text{CO}}$  factor close to Galactic value can be found.

The numerical simulations of Glover and Mac Low (2011) and the analytical calculations of Wolfire et al. (2010) and Bolatto et al. (2013) offer theoretical calibrations for the environment dependence of the  $X_{\text{CO}}$  factor. Glover and Mac Low (2011) perform turbulent, three-dimensional magneto-hydrodynamic simulations with self-consistent chemistry and thermal balance, while neglecting self-gravity. They explore solar and sub-solar metallicities and various mean cloud densities (from  $n_0 = 30$  to  $1000 \text{ cm}^{-3}$ ) and determine the mean  $X_{\text{CO}}$  factor as a function of the cloud-average visual extinction ( $\langle A_V \rangle$ ). At low  $\langle A_V \rangle$  values the conversion factor follows a power law, while above 3.5 mag mean visual extinction, the  $X_{\text{CO}}$ -factor converges to the Galactic disk value. We adopt the following functional form of their result:

$$X_{\text{CO}} = \begin{cases} 2 \times 10^{20} \left( \frac{\langle A_V \rangle}{3.5} \right)^{-3.5} \text{ cm}^{-2} \text{ K}^{-1} \text{ km}^{-1} \text{ s} & \text{if } \langle A_V \rangle < 3.5 \text{ mag} \\ 2 \times 10^{20} \text{ cm}^{-2} \text{ K}^{-1} \text{ km}^{-1} \text{ s} & \text{if } \langle A_V \rangle \geq 3.5 \text{ mag.} \end{cases} \quad (3.10)$$

In the remainder of the chapter we reference the H<sub>2</sub> mass calculated with the  $X_{\text{CO}}$  value derived this way as  $GML2011_{X_{\text{CO}}}$ .

Bolatto et al. (2013) determine the metallicity dependence of the conversion factor following the analytical argument of Wolfire et al. (2010, hereafter  $WF2010_{X_{\text{CO}}}$ ). They assume a spherically symmetric molecular cloud with a radial density profile

of  $\rho \propto r^{-1}$  and calculate the difference in visual extinction between the CO-abundant (i.e. the cloud depth where the  $^{12}\text{CO}$  becomes optically thick) and the  $\text{H}_2$ -dominated layers (i.e. the depth where the gas is half molecular) of the cloud. This is given by

$$\Delta A_V = 0.53 - 0.045 \times \log_{10} \left( \frac{G}{n} \right) - 0.097 \log_{10}(Z), \quad (3.11)$$

where  $n$  is the mean gas density (assumed to be  $300\text{cm}^{-3}$ ),  $G$  and  $Z$  are the ISRF strengths and the metallicity in the units of  $G_0$  and  $Z_\odot$ , respectively. The  $X_{\text{CO}}$  factor is assumed to be proportional to the mass ratio of the CO bright and the total molecular gas masses, which is written as  $X_{\text{CO}} \propto M(R(\text{H}_2))/M(R(\text{CO})) = \exp(-4\Delta A_V/\langle A_V \rangle)$ . The metallicity dependence is introduced through the visual extinction, by assuming that the dust to gas ratio decreases with metallicity (Draine et al., 2007), thus  $\langle A_V \rangle(Z) = \langle A_V \rangle(Z_\odot) \times Z$ . The metallicity dependence of  $X_{\text{CO}}$  is then derived from the ratio  $M(R(\text{H}_2))/M(R(\text{CO}))$  at metallicity  $Z$  and the Solar value ( $Z_\odot$ );

$$X_{\text{CO}} = 2 \times 10^{20} \exp \left( \frac{4\Delta A_V}{\langle A_V \rangle} \right) \exp \left( \frac{-4\Delta A_V}{\langle A_V \rangle/Z} \right) \text{cm}^{-2} \text{K}^{-1} \text{km}^{-1} \text{s}. \quad (3.12)$$

In the first exponent,  $\langle A_V \rangle$  denotes the mean visual extinction measured at metallicity  $Z$ . In the second exponent  $\langle A_V \rangle/Z$  stands for the mean visual extinction that could be measured for the same cloud, if its metallicity were  $Z_\odot$ . This assumes a visual extinction, which scales linearly with the metallicity.

Figure 3.2 compares the  $X_{\text{CO}}$ -factors and their respective dependencies in the physical conditions, according to the  $GML_{2011X_{\text{CO}}}$  and the  $WF_{2010X_{\text{CO}}}$  methods. For comparison we also show the Galactic  $X_{\text{CO}}$  ( $GAL_{X_{\text{CO}}}$ ) on the figure.

Here, we calculate the total  $\text{H}_2$  mass of the cloud by the following prescription: first we integrate the  $^{12}\text{CO}$  ( $J = 1 \rightarrow 0$ ) PPV cubes along the velocity dimension to obtain the two-dimensional  $W_{\text{CO}}$  map. The PPV brightness temperatures, which are below the  $3\sigma_{^{12}\text{CO}} = 0.6$  K detection limit (see 3.3) are omitted from the integration. Then the  $W_{\text{CO}}(x, y) \leq 0$  K pixels are rejected from the velocity-integrated map, and the arithmetic mean intensity value of the remaining pixels is calculated. With the latter step, the effects of small scale  $X_{\text{CO}}$  variations are lessened. The mean visual extinction is the average of the true visual extinctions (determined from the hydrogen nuclei column density via Eq. 2.2) over all lines of sight (i.e. pixels) used to calculate the mean intensity. The total  $\text{H}_2$  mass estimate is then the product of the mean intensity, the adopted  $X_{\text{CO}}$ -factor, the surface area associated with the averaging and the  $\text{H}_2$  molecule mass.

### 3.5 RESULTS

Figure 3.3 summarizes the  $\text{H}_2$  masses estimated with the methods described above for all of the simulations. In addition to the molecular mass estimate, it also lists the true molecular mass above the CO brightness temperature threshold, the total  $\text{H}_2$  mass and the true CO-dark molecular gas fraction (i.e. the ratio of  $\text{H}_2$  mass below the detection limit and the total  $\text{H}_2$  mass).

We find that most methods provide a “good”, i.e. within a factor of 2-4, mass estimate, unless the metallicity of the cloud is low ( $<0.6 \times Z_\odot$ ). The exceptions is

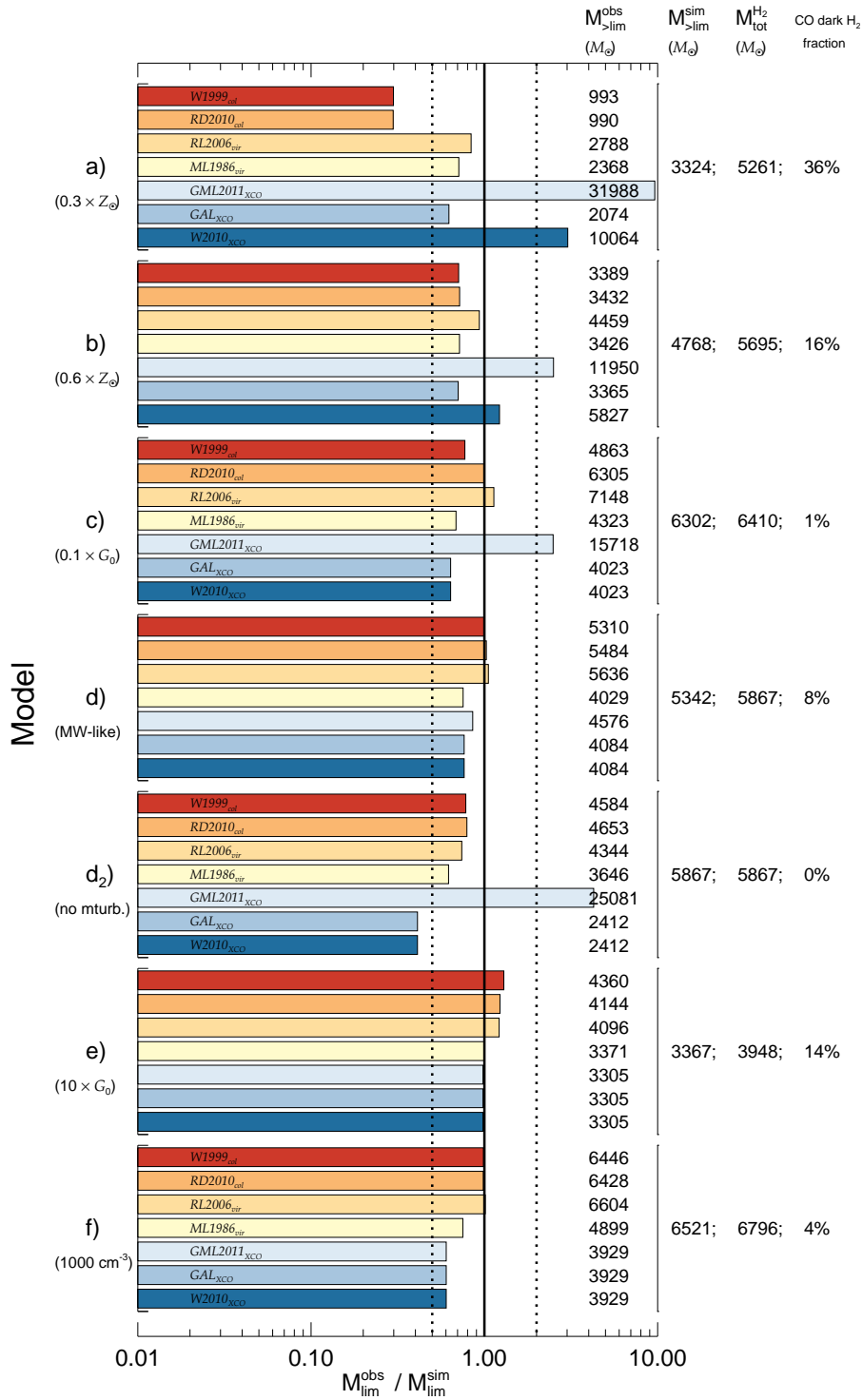


Figure 3.3: Comparison of cloud masses derived using different methods from our simulations. The horizontal axis shows the ratio of the measured  $\text{H}_2$  mass and the true  $\text{H}_2$  mass above the detection limit. The latter is known from the simulation. The numerical values of the  $\text{H}_2$  mass and its estimates can be read from the right side of the figure. The total  $\text{H}_2$  content of the GMCs and their CO-dark  $\text{H}_2$  fraction are also shown. The solid vertical line shows the one-to-one ratio of the estimate and the true  $\text{H}_2$  mass, while the dotted vertical lines indicate a factor of 2 deviation from it.

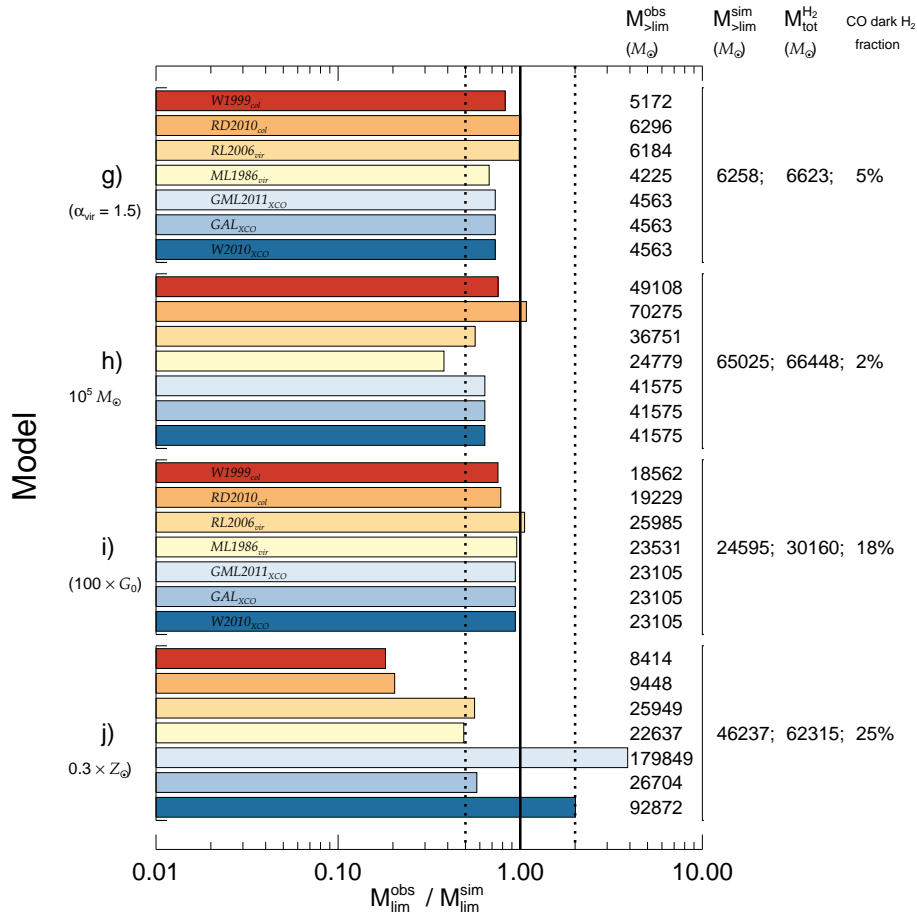


Figure 3.3: (continued)

the *GML2011<sub>XCO</sub>* method, which yields about an order of magnitude error in the lowest metallicity cases, and in other, non-Milky Way-like conditions traces the total cloud mass rather than the CO-bright  $H_2$  mass.

The CO isotope column density measurement based methods (*W2009<sub>col</sub>* and *RD2010<sub>col</sub>*) tend to perform very similarly, with the largest discrepancy of  $\sim 20\%$ , and in all cases the *RD2010<sub>col</sub>* estimate providing a better approximation for the true  $H_2$  mass. These methods work best for Solar metallicity and  $G = 1 \times G_0$  conditions, and underestimate the  $H_2$  mass severely when the metallicity is low. Their mass estimate is slightly affected by the ISRF strength change and these methods prove to be the least affected by the choice of the unresolved velocity dispersion (i.e. “micro-turbulent” velocity).

The virial analysis based methods (*RL2006<sub>vir</sub>* and *ML1986<sub>vir</sub>*) seem to work the most consistently for each model. This is not too surprising, since our clouds are close to virial equilibrium. Nevertheless, we discuss the reason for the good match in detail in section 3.6.2. The purely  $^{12}CO$  emission based *RL2006<sub>vir</sub>* method performs better from the two in all cases except when the ISRF strength is high. In those cases it overestimates the  $H_2$  mass, while the *ML1986<sub>vir</sub>* method, which consistently yields about 30% lower masses, provides a more precise estimate.

The CO-to- $H_2$  conversion factor methods exhibit a large variation in the reliability of their mass estimates. The determining quantity in the values of the  $X_{CO}$  factor in *GML2011<sub>XCO</sub>* and *W2010<sub>XCO</sub>* is the metallicity. The dependence is implicit in the

first case, through the metallicity dependent visual extinction value, and explicit in the latter. The  $GML_{2011XCO}$  method tend to perform the poorest in the low metallicity cases (see models a, b and j). The  $W_{2010XCO}$  method overestimates the  $H_2$  mass in these cases by a similar factor (about 3) as the  $GAL_{XCO}$  underestimates it.

The  $GAL_{XCO}$  method provides an estimation consistent with the true  $H_2$  mass within a factor of 2. The Galactic  $X_{CO}$  value works the best when the ISRF is strong and the metallicity is high (e and i)<sup>7</sup>. In these cases CO is photodissociated at low visual extinctions, where the CO-to- $H_2$  conversion factor is more uncertain and changes significantly with depth, but it remains abundant in the dense bulk of the cloud, thus tracing the dense regions better (see panels e and i in Figure 3.1), where the conversion factor is closer to the Galactic.

The CO-dark (sometime called “CO-faint”) molecular gas fraction and its environmental dependence is a major focus of research in both the Galactic and extragalactic ISM studies. Dust emission based analysis of nearby GMCs finds that the CO-dark  $H_2$  fraction is about  $\sim 30\%$  (Planck Collaboration et al., 2011), and hints at a metallicity dependence. The individual GMC scale PDR models presented in (Wolfire et al., 2010) and the galactic scale hydrodynamic simulations of Smith et al. (2014) in a Milky Way-like setup find this fraction to be 30% and 42% respectively. The former also finds that the fraction is insensitive to cloud properties and environment. We note that there are two main components of the CO-dark molecular gas: translucent clouds with low total visual extinction and the translucent envelopes of dense GMCs. The models of (Wolfire et al., 2010) are informative on the envelopes of dense clouds, while the Smith et al. (2014) models take both components into account. The simulations presented in this chapter are more similar to the individual cloud models of Wolfire et al. (2010). We are probably underestimating the CO-dark molecular gas fraction, due to isolated nature and the isotropic density sphere initial condition of the simulations. Nevertheless, the models may provide insight into systematic changes with metallicity, ISRF strength and the adopted CO-based mass measurement method.

We find the largest CO-dark  $H_2$  mass fraction in the low metallicity simulations (a and j,  $Z = 0.3 \times Z_\odot$ ), where it is between 25% and 36%. As the metallicity doubles (b), the fraction decreases by about a factor of 2 to 16%. At solar metallicity, it halves again to about 8%. The ISRF strength increase affects the fraction similarly to the decreasing metallicity, although to a smaller extent. These changes in the extent of gas traced by CO can be followed on the corresponding panels of Figure 3.1. A similar trend seems to apply for the  $10^5 M_\odot$  cloud (h, i and j); the dark gas fraction drops by more than a factor of 10 from (j) to (h) as metallicity decreases.

### 3.6 DISCUSSION

In the previous section we showed that in general the described methods works within a factor of 2 certainty under moderate conditions. In the Milky Way environment ( $G = G_0$ ,  $Z = Z_\odot$ ) the match could be even better. But why do these methods work in those conditions and not in others? How good are the column density estimate methods at recovering the true  $H_2$  column density distribution? Why do

<sup>7</sup>We note that all method gives the Galactic  $X_{CO}$  factor for these models

the virial analysis methods work so well in the whole studied parameter range? What is the problem with the  $A_V$  dependent  $X_{\text{CO}}$ -factors, and what is the smallest scale on which the CO-to- $\text{H}_2$  conversion factor might work? In the following section we discuss these questions.

### 3.6.1 INFERRING $\text{H}_2$ COLUMN DENSITY FROM CO ISOTOPE EMISSION

In the previous section we showed that the molecular mass derived from the CO emission inferred  $\text{H}_2$  column density gives a reasonable mass estimate, unless the metallicity is lower than the Solar metallicity. Does this mean that the column density distribution derived with these methods follows the true  $\text{H}_2$  column density distribution?

To answer this question, we compare the true  $\text{H}_2$  column density distribution to those inferred using the  $RD_{2010_{col}}$  method. We also calculate the true  $^{12}\text{CO}$  column density distribution from the simulation. Figure 3.4 shows for the probability density functions of the column density distributions for all 10 models. The solid black lines represent the true  $\text{H}_2$  distributions. In each case they follow relatively narrow log-normal distributions, with peak locations between  $10^{21}$  and  $10^{22}\text{cm}^2$ . The  $^{12}\text{CO}$  column densities are transformed to  $\text{H}_2$  column density using a constant  $^{12}\text{CO}/\text{H}_2$  ratio. We assume that all carbon atoms are incorporated in CO molecules, thus the abundance ratio is  $2 \times x_{C,tot} = 2.8 \times 10^{-4}$  in the case of solar metallicity and scales with the adopted  $Z$ . The factor of two is due to the  $x_{\text{H}_2} = 0.5$  fractional abundance of  $\text{H}_2$ . The blue long-dashed line indicates the  $^{12}\text{CO}$  column density distribution taken directly from the simulation. The remaining curves represent the two distributions inferred from the CO isotope emission maps. In one case, we assume a constant  $^{12}\text{CO}/^{13}\text{CO}$  isotopic ratio equal to 60 (orange dotted line), while in the other, a  $^{13}\text{CO}$  column density dependent isotopic ratio (green dot-dashed line) is adopted. The former choice is consistent with the frequently assumed value in observations (see the discussion in section 2.5). The latter is a result from our simulations. The fitting formula is given in section 2.3.4.

The most striking feature of Figure 3.4 is that the CO-inferred distributions fall short of the true  $\text{H}_2$  distribution over the whole column density range. Their PDF peak locations are shifted, on average, to an order of magnitude lower column densities and their distributions are a factor of 2-3 wider than those of the true  $\text{H}_2$  column density.

The true  $N(\text{CO})$  distribution – scaled with the given  $\text{CO}/\text{H}_2$  abundance ratio – (blue long-dashed line) only follows the true  $\text{H}_2$  distribution in the high column density wing. This suggests that the chosen  $^{12}\text{CO}/\text{H}_2$  ratio provides a good approximation only at the highest (column) densities, and thus the ratio is not uniform over the whole detectable cloud. In fact, the true abundance value decreases significantly in the low column density lines of sight, thus widening the inferred column density distributions towards lower values. In the case of run (d), the mean  $^{12}\text{CO}$  fractional abundance ( $x_{^{12}\text{CO}}$ , the number density ratio with the hydrogen nuclei per unit volume; note that this is half of the  $^{12}\text{CO}/\text{H}_2$  ratio when the hydrogen is fully molecular) changes between  $1.4 \times 10^{-4}$  (i.e. all carbon in CO) at  $A_V$  values greater than 2 mag, to a few  $\times 10^{-5}$  at visual extinctions between 1 and 2 mag. The main reason for the abundance gradient is the gradual build up of CO shielding from the dissociative ISRF. At lower column densities, where photodissociation is efficient,

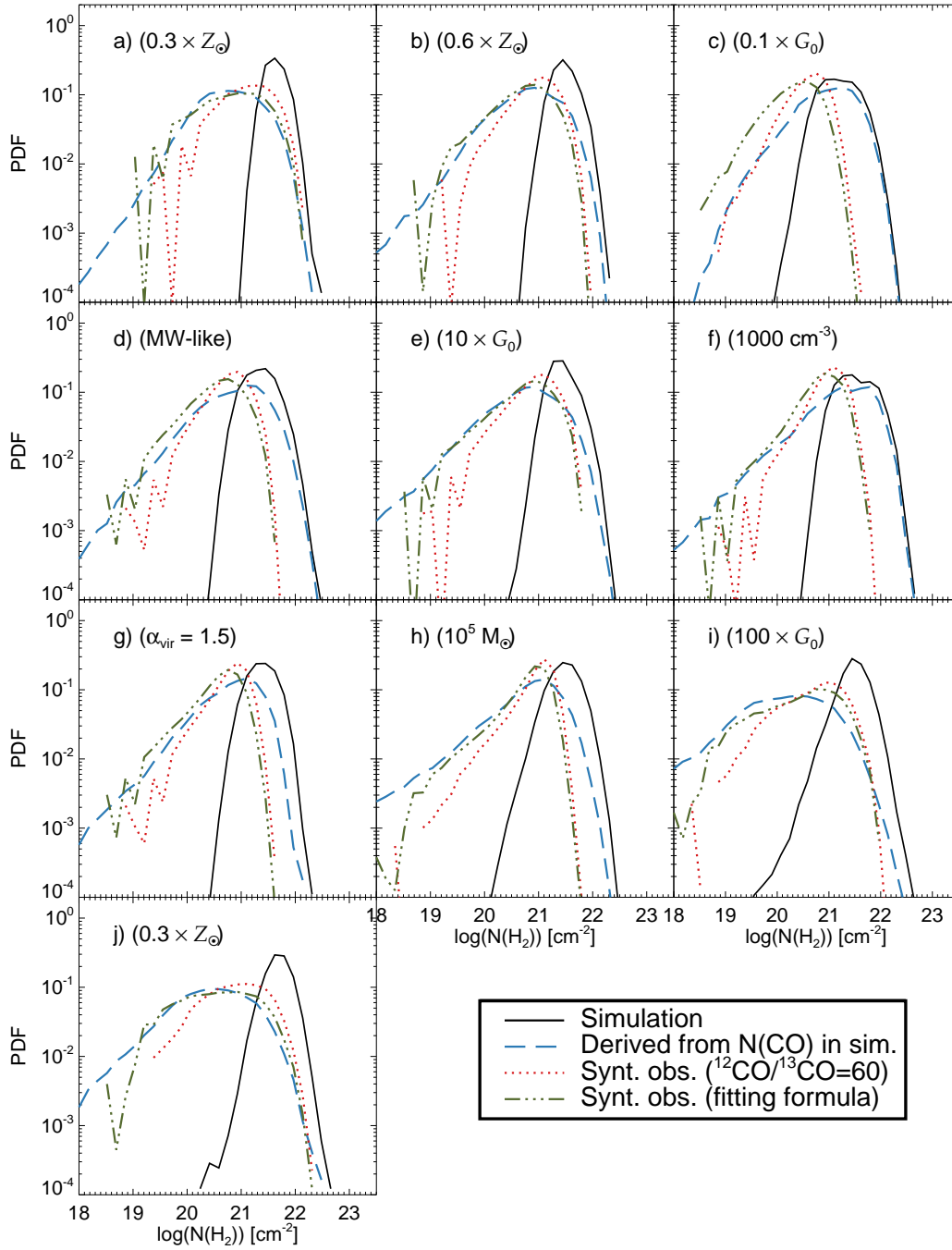


Figure 3.4:  $\text{H}_2$  column density distributions, taken directly from the simulation (black solid line) and inferred from the  $^{12}\text{CO}$  column density distributions, which are derived under various assumptions (see text in section 3.6.1).

$C^+$  dominates the carbon budget (see Figure 2.13 for an example of the  $C^+$ -to-CO transition) and the remaining small amount of CO follows a different correlation with  $H_2$  than its well-shielded counterparts. Note also, that in reality the true CO distribution does not trace the  $H_2$  column density distribution even at the higher column densities, since in those lines of sight CO is expected to deplete from the gas phase and freeze-out onto dust grains (see chapter 4).

In addition to the error inherited from the incorrect guess for the  $^{12}CO/H_2$  abundance ratio, the  $H_2$  column densities derived from the CO emission (orange dotted and green dash-dotted lines) are also affected by the insufficient detection sensitivity at the low column density end, and saturated, optically thick  $^{13}CO$  emission at the high column density end. The former is marked by a cut-off around  $N_{H_2} = 4 \times 10^{18} \text{cm}^{-2}$  and fluctuations in the PDF at slightly higher column densities, while the latter is shown by the cut-off at the high end. In the cases of strong radiation fields or low metallicities (e.g. runs a, e, i, j), where much of the low density CO is destroyed, the  $RD_{2010_{col}}$  method provides a good representation of the high column density CO distribution. It is also clear from this figure, that the adopted  $^{12}CO/^{13}CO$  isotope ratio becomes important in the intermediate column density range ( $10^{19} \text{cm}^{-2} < N(H_2) < 10^{21} \text{cm}^{-2}$ , equivalent to  $4 \times 10^{14} \text{cm}^{-2} < N(^{12}CO) < 4 \times 10^{16} \text{cm}^{-2}$ ), where the observations can trace the underlying true CO column density (although not the  $N(H_2)$ ) well.

We conclude that the  $W_{2009_{col}}$  and  $RD_{2010_{col}}$  methods are affected by high optical depths at high column densities. They can reproduce the CO column densities relatively well over a limited intermediate column density range (e.g. Kennicutt and Evans, 2012), if corrections for the depth dependent  $^{12}CO/^{13}CO$  isotope ratio are applied (section 2.3.4). In general, however, the  $H_2$  column density inferred from CO emission does not follow the true distribution, due to chemical effects.

### 3.6.2 WHY DOES THE VIRIAL MASS ESTIMATE WORK?

We show that the virial mass estimates are reliable measures of the  $H_2$  mass in most of our simulations, but why is this technique so robust within the covered parameter range?

The virial mass analysis relies on 3 main requirements: the  $^{12}CO$  ( $J = 1 \rightarrow 0$ ) line width should trace the overall velocity dispersion and therefore the mass of the cloud. The second requirement is that the cloud should be close to virial equilibrium. Finally, the radial mass distribution profile should follow a power law. In our case – as often in observational studies – the power law exponent is assumed to be  $-1$ .

Table 3.2 compares the true velocity dispersion ( $\sigma_{1D,intrinsic}$ ), measured in the line of sight to those inferred from the  $^{12}CO$  and  $^{13}CO$  line widths. In both cases the line-width inferred velocity dispersion is typically consistent with the true value within  $\sim 30$ -40 per cent. In contrast with the suggestion of MacLaren et al. (1988), we find that the  $^{13}CO$  velocity dispersion does not provide a better estimate for the simulated intrinsic line of sight velocity dispersion. We find that the  $\sigma_{1D,measured}$  calculated from the  $^{12}CO$  line systematically overestimates the true value, while those from the  $^{13}CO$  line do the opposite.

As summarized in Table 3.1 our simulated clouds are very close to virial equilibrium at the time of the analysed snapshots. The left panel of Figure 3.5 shows the

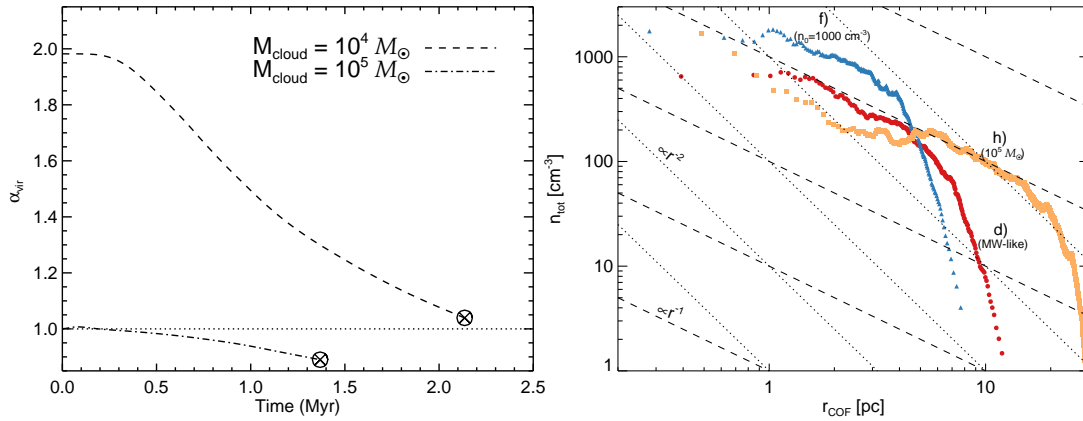


Figure 3.5: Left panel: the virial parameter defined according Eq. 3.13 as a function of time for the high mass and low mass clouds. The dotted line indicates the equilibrium virial parameter value. Right panel: the radial number density profile of the modelled clouds compared to the theoretical assumption of power law indices often used in virial mass measurements.

temporal evolution of the virial parameter, defined as

$$\alpha_{\text{vir}} = \frac{2 \times E_{\text{kin}}}{|E_{\text{pot}}|}, \quad (3.13)$$

where  $E_{\text{kin}}$  and  $E_{\text{pot}}$  are the total kinetic and potential energies of the cloud, respectively. The total kinetic energy of the cloud is calculated as the sum of the kinetic energies of individual SPH particles (i.e.  $E_{\text{kin}} = mv^2/2$ , with the particle mass  $m$  being  $0.005 M_{\odot}$ ), while the total potential energy is calculated implicitly in the hydrodynamic simulation, taking the irregular mass distribution fully into account. If  $\alpha_{\text{vir}}$  is close to 1, then the virial cloud mass estimate is expected to be reliable. The virial parameter of the  $10^4 M_{\odot}$  simulations (dashed line) stagnates during the first  $\sim 0.3$  Myr, then falls off as a power law (see the first paragraph of section 2.2.4), while in the case of the massive clouds (dot-dashed line),  $\alpha_{\text{vir}}$  first increases slightly, then decreases below the equilibrium value on a Myr time scale

The radial density profile of the GMCs,  $\rho(r)$  or  $n(r)$ , depending whether the mass or number density is concerned, is the quantity determining the numerical value of the multiplier in Eq. 3.8. The right panel of Figure 3.5 shows the average number density of the selected clouds as a function of cloud radius. The figure was constructed by dividing the total number of particles in small  $\delta r$  radius spherical shells around the center of gravity by the shell volume. We only show three representative models, since the radial profile of the clouds in runs (a), (b), (c), (e) are very similar to (d). The same is true for simulations (i), (j) and the Solar case, (h). The  $10^4 M_{\odot}$  models yield relatively flat distributions in the inner 1 pc, then they follow  $n(r) \propto r^{-1}$ , until the sharp cut-off at the cloud edges. The  $10^5 M_{\odot}$  runs are very similar, with the exception of a steeper profile in the inner cloud. On relatively large size scales, where the bulk of the mass is located, the radial number density profile follows the expected correlation remarkably well. This is especially curious, because the simulations starts with completely homogeneous and isotropic

Table 3.2: Intrinsic and  $^{12}\text{CO}$  emission line inferred line of sight velocity dispersions. For the details of the calculation we refer to section 2.4.1 with the difference that here we analyse the  $^{12}\text{CO}$  emission.

Model	$^{12}\text{CO}$ ( $J = 1 \rightarrow 0$ )			$^{13}\text{CO}$ ( $J = 1 \rightarrow 0$ )	
	$\sigma_{1D,intrinsic}$ ( $\text{km s}^{-1}$ )	$\sigma_{1D,measured}$ ( $\text{km s}^{-1}$ )	relative deviation %	$\sigma_{1D,measured}$ ( $\text{km s}^{-1}$ )	relative deviation %
a	1.39	1.10	20.8	1.06	23.7
b	1.26	1.28	1.6	1.10	12.7
c	0.93	1.58	69.8	0.99	6.5
d	1.09	1.46	33.9	1.11	1.8
e	1.32	1.20	9.1	1.14	13.6
f	1.61	1.71	6.2	1.37	14.9
g	1.39	1.46	5.0	1.02	13.7
h	2.08	1.84	11.5	1.30	37.5
i	2.06	1.62	21.4	1.48	28.2
j	2.06	1.60	22.3	1.42	31.1

density distributions, with a mean number density of  $300 \text{ cm}^{-3}$ . We believe that the radial density profile is not an artefact in the simulation, since it is very similar in both the low mass and the high mass runs. For these runs we used different seed fields to produce the initial, random velocity fluctuations and also choose different amplitudes for the turbulent velocities (by changing the cloud mass and the virial parameter). We speculate that the near  $-1$  power law exponent might correlate with the turbulent power spectrum imposed as initial condition. To investigate this, further simulations are needed. This task, however, is left for the future.

In short, we find that the virial mass estimation from the simulations works well because the emission lines do a good job of tracing the true velocity dispersion. The virial parameter is close to unity in all of our simulations. This is not always expected to hold for every real cloud; CO-rich GMCs formed in large scale colliding flows might inherit large velocity dispersions, and thus large virial parameters (e.g. [Vázquez-Semadeni et al., 2007](#); [Kauffmann et al., 2013](#)). Finally, the cloud radial density profiles in our simulations are consistent with the often chosen exponent of  $-1$ .

### 3.6.3 THE CO-TO-H<sub>2</sub> FACTOR AT LOW VISUAL EXTINCTIONS AND ON SMALL SCALES

The  $GML_{2011XCO}$  method severely overestimates the H<sub>2</sub> mass in runs (a) and (j), while for these models, the  $W_{2010XCO}$  method traces the total cloud mass rather than its H<sub>2</sub> content. One explanation for the major overestimation in the case of  $GML_{2011XCO}$  is the neglect of self-gravity in the simulations run by [Glover and Mac Low \(2011\)](#) to derive this relationship. Due to self-gravity the gas forms higher density, clumpy structures, which can provide sufficient shielding to allow CO to survive, even when the metallicity is low ([Glover and Clark, 2012c](#)). At low metallicity, the total CO emission of the cloud is dominated by these small, dense,

self-gravitating clumps, but these are absent in the [Glover and Mac Low \(2011\)](#) simulations. Another factor that might contribute to the large error is the adopted detection limit in our analysis. With the per channel  $^{12}\text{CO}$  brightness temperature limits of 0.6 K, the mean visual extinction in the area enclosed by the detection limit is found to be 1.6 mag in the case of simulation (a). This yields an  $X_{\text{CO}}$  factor of  $3.08 \times 10^{21} \text{cm}^{-2} \text{K}^{-1} \text{km}^{-1} \text{s}$  and an  $\text{H}_2$  mass of  $3.2 \times 10^4 M_{\odot}$ . If the detection limit is increased to 1 K, then  $\langle A_V \rangle$  is 2.22 mag, which in turn implies a conversion factor value of  $9.8 \times 10^{20} \text{cm}^{-2} \text{K}^{-1} \text{km}^{-1} \text{s}$ . The inferred  $\text{H}_2$  mass is then  $4185 M_{\odot}$ , a factor of 2.4 overestimation of the true  $\text{H}_2$  mass above the increased detection limit ( $1747 M_{\odot}$ ).

Surprisingly, the Galactic  $X_{\text{CO}}$  factor provides a reasonably good estimate of the  $\text{H}_2$  mass above the CO detection limit, even when the metallicity is low. This might be explained by invoking the argument used by [Liszt et al. \(2010\)](#) to explain close to Galactic  $X_{\text{CO}}$  factors in diffuse gases: They separate the  $X_{\text{CO}}$  factor into two coupled and competing contributions:

$$\frac{1}{X_{\text{CO}}} = \frac{W(\text{CO})}{N(\text{CO})} \times \frac{N(\text{CO})}{N(\text{H}_2)}, \quad (3.14)$$

where the first factor accounts for radiative transfer and CO molecule excitation effects, while the second accounts for the chemistry. On one hand the  $N(\text{CO})/N(\text{H}_2)$  decreases with decreasing metallicity (i.e. less dust shielding leads to more CO photodissociation and even in well-shielded regions there is less carbon and oxygen available); on the other hand, the  $W(\text{CO})/N(\text{CO})$  ratio increases due to the higher gas and excitation temperatures. It can be shown, that the decrease of one factor might be compensated by the other ([Pety et al., 2008](#)). When models (a) and (d) are compared, in fact we find, that along the high column density line of sights, where the abundance change is approximately a factor of 3, the line of sight mass weighted gas temperature changed with a similar factor, which is on the order of 2.

A coexisting issue that also needed to be mentioned is the combined effect of increasing CO-dark  $\text{H}_2$  mass fraction with decreasing metallicity (and/or increasing ISRF strength) and the application of a brightness temperature detection limits in CO emission. Due to the increasing CO-dark mass fraction  $X_{\text{CO}}$  also increases. By imposing a detection limit, we discard these CO-dark (or rather CO-faint) lines of sight and hence weaken the metallicity (or ISRF) dependence of the  $X_{\text{CO}}$  factor (see e.g. the discussion in [Bolatto et al., 2013](#)).

It is widely accepted in the literature (e.g. [Glover and Mac Low, 2011](#); [Shetty et al., 2011a,b](#); [Bolatto et al., 2013](#)) that the  $X_{\text{CO}}$  conversion factor breaks down on small scales. The clumpy nature of molecular clouds leads to an inhomogeneous radiation field within them. This in turn regulates the CO abundances and excitation conditions, resulting in sizeable changes on the sub-parsec scales. None of the  $X_{\text{CO}}$  methods discussed in this chapter claim to provide reliable conversion factors for individual pixels. In fact, they are recommended to be used on the cloud-averaged quantities, in order to smooth the small scale fluctuations. Arguably, the  $X_{\text{CO}}$  factor should not even be used on the scale of individual clouds, but as averages over whole populations ([Kennicutt and Evans, 2012](#)). We would however, like to test the validity of the methods on small scales, for resolved and coherent structures in the integrated emission maps. For this we identify hierarchical structures in the maps using the dendrogram analysis technique ([Houllahan and Scalo, 1992](#); [Rosolowsky](#)

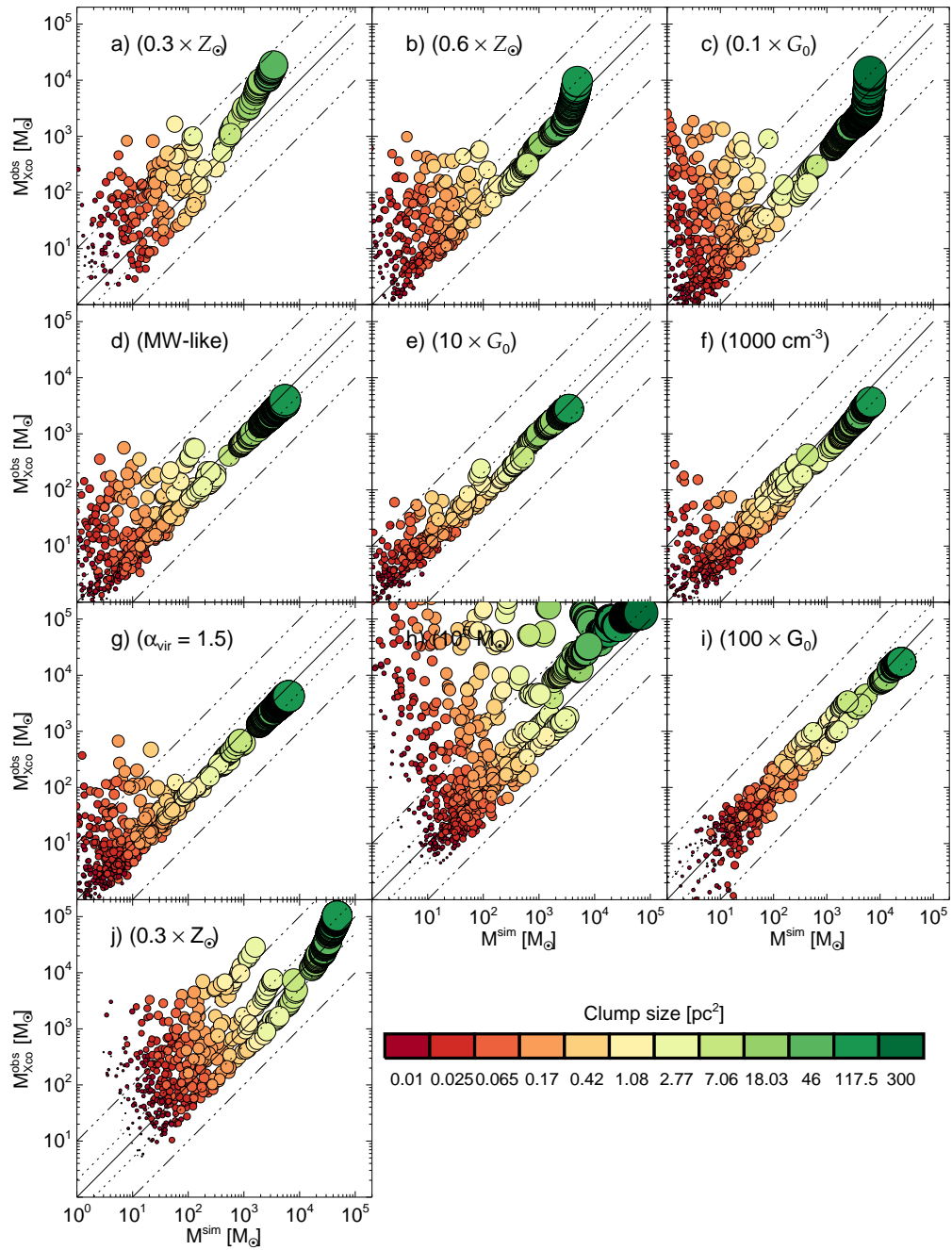


Figure 3.6: The  $\text{H}_2$  mass of sub-cloud structures, measured by the  $GML_{2011XCO}$  method, plotted as a function of the true mass of the corresponding structures. The circle size and colour code indicates the structure size. The solid line represents the perfect match between the measured and true structure  $\text{H}_2$  mass. The dotted and dash-dotted lines show a factor of 2 and an order of magnitude errors.

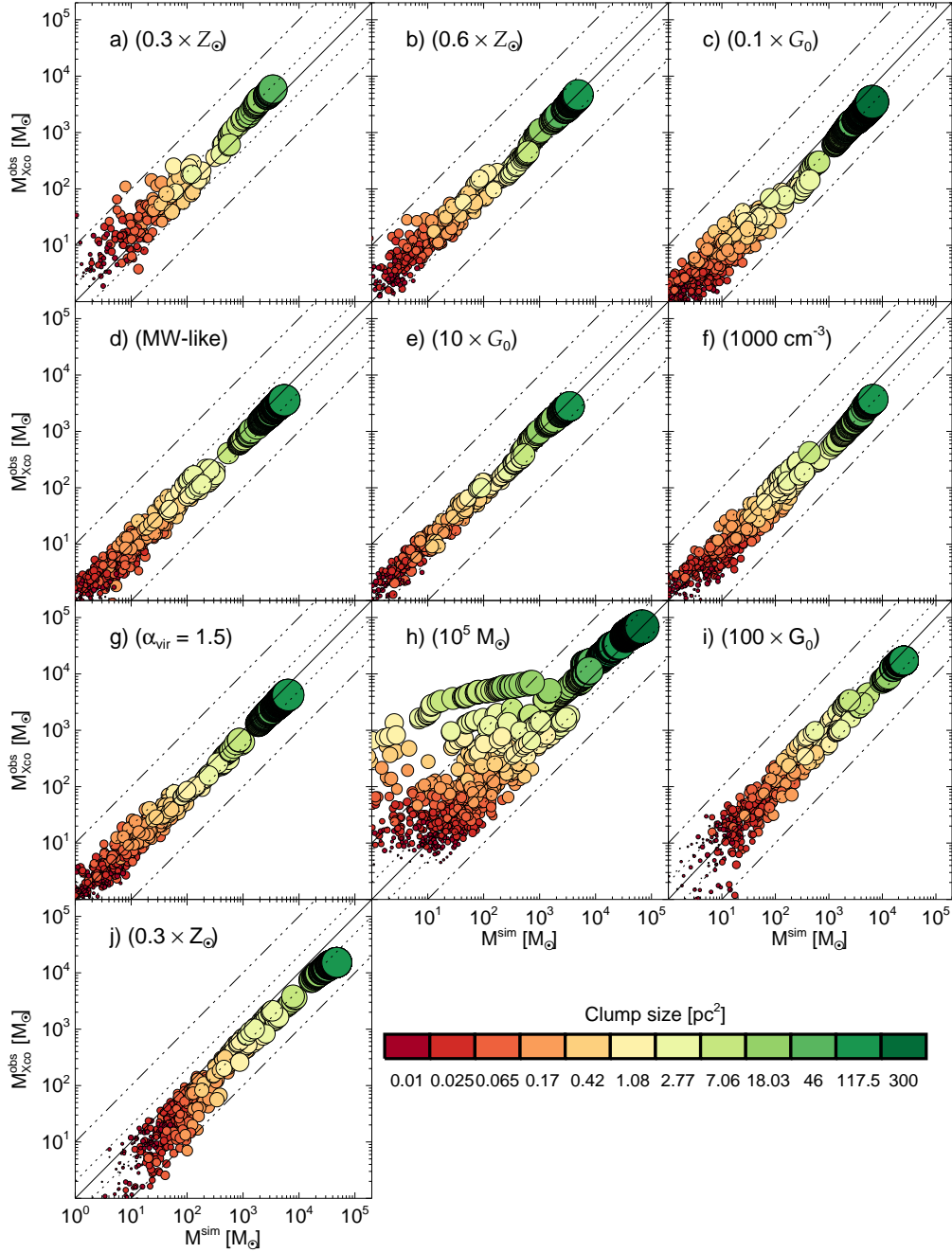


Figure 3.7: Similar to Fig. 3.6, but here the  $WF2010_{XCO}$  method was used to infer the  $X_{CO}$  factor.

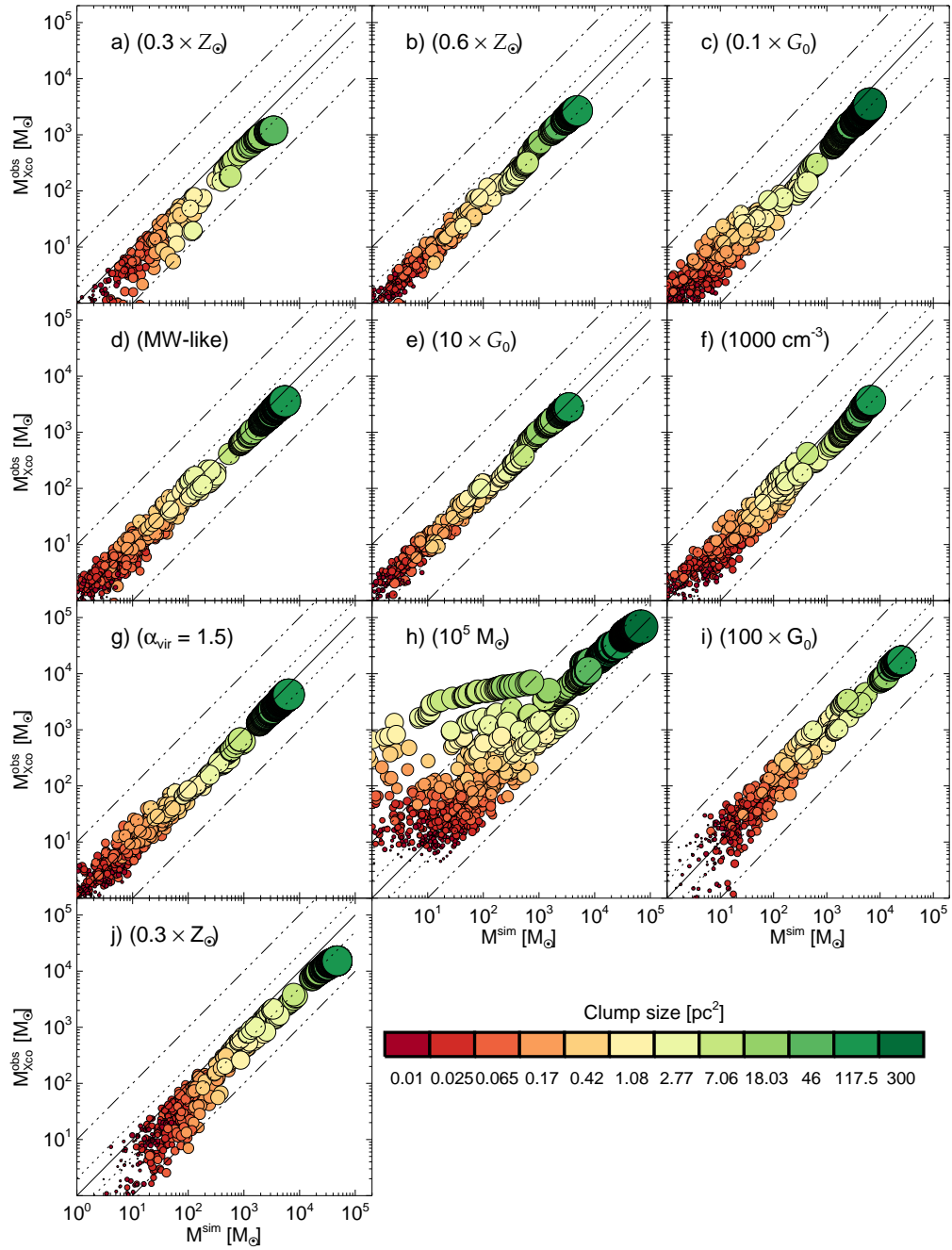


Figure 3.8: Similar to Fig. 3.6, but here the Galactic  $X_{CO}$  is used ( $GML2011_{XCO}$ ).

et al., 2008; Beaumont et al., 2013, and see also Appendix D).

In short, dendrograms are used to quantify and visualize the hierarchical nature of GMCs (i.e. higher density or emission regions are embedded in low density or emission regions, which themselves are embedded in even lower contour regions). The advantage of using dendrograms is that the identification of structures does not depend on arbitrary choices of contour levels, but rather on the intrinsic topology of the map. The control parameters of the analysis method, such as the minimum number of pixels in a leaf, the threshold contour level and the minimum contour difference before the first merge can take place, are used to discard unwanted identifications (in a procedure called pruning) and they do not modify the remaining structures. We take 10 pixels,  $0.6 \text{ K km s}^{-1}$  integrated brightness temperature and  $3 \text{ K km s}^{-1}$  contour level difference for the parameter values mentioned above and use the DENDRO<sup>8</sup> implementation of the algorithm.

Once the coherent structures are identified in the emission maps, we calculate the true  $\text{H}_2$  mass associated with the feature (i.e. clump, filament or core) and the  $X_{\text{CO}}$ -inferred molecular mass. The comparison of these masses are shown on Figures 3.6 ( $GML_{2011X_{\text{CO}}}$ ), 3.7 ( $WF_{2010X_{\text{CO}}}$ ) and 3.8 ( $GAL_{X_{\text{CO}}}$ ). The circle size and the colour code indicate the structure size. The diagonal solid, dotted and dash-dotted lines represent the 1:1 correlation, a factor of 2 and an order of magnitude discrepancy, respectively.

The  $GML_{2011X_{\text{CO}}}$  method produces about 2 orders of magnitude scatter at small scales, preferentially overestimating the mass of the features. The large scatter in the mass estimate is inherited from the similarly large scatter in the mean visual extinctions on small scales. The scatter is propagated into the  $X_{\text{CO}}$ , because in the  $GML_{2011X_{\text{CO}}}$  prescription, it depends directly on the  $A_V$ . At scales larger than a few  $\text{pc}^2$  area and masses larger than a few hundred  $M_{\odot}$ , the scatter vanishes, but the mass remains overestimated in the low metallicity cases. At the largest scales, where the method was designed to work, the method tries to compensate for the metallicity effects, but it overshoots the true value by an order of magnitude.

At non-solar metallicities, the  $WF_{2010X_{\text{CO}}}$  method behaves similarly to the  $GML_{2011X_{\text{CO}}}$  on largest scales. On small scales, it does not exhibit such large scatter. This is due to the relative  $A_V$  dependence in Eq. 3.12 (i.e. the mean visual extinction at metallicity  $Z$ ,  $\langle A_V \rangle$ , is compared to the visual extinction at Solar metallicity,  $\langle A_V \rangle / Z$ ). At Solar metallicities this method essentially gives the same result as the Galactic  $X_{\text{CO}}$  factor.

Finally, the Galactic  $X_{\text{CO}}$ -factor ( $GAL_{X_{\text{CO}}}$ ) provides the most consistent method over all parameter ranges. The constant factor seems to work on all scales within a factor of 2 error. At solar metallicity the scatter is around the 1-to-1 correlation between the true and measured masses. At lower metallicities, they systematically shift towards the right, thereby underestimating the true mass. The shift correlates with the metallicity of the model.

### 3.7 SUMMARY

In this chapter we investigate the validity of the most often used CO emission based  $\text{H}_2$  mass and column density measurement methods. We use hydrodynamic

<sup>8</sup><https://github.com/ChrisBeaumont/Dendro>

simulations with realistic thermal balance and chemical modelling and explore a range of metallicities, ISRF strengths, cloud densities, cloud masses and virial parameters. Emission maps are then constructed from the simulated (molecular) number densities, velocity fields and gas temperatures, in the LVG approximation. No observational noise was added to the emission maps, but we only consider PPV pixels in the analysis, which are above a given detection limit (i.e. 0.6 K and 0.3 K for  $^{12}\text{CO}$  and  $^{13}\text{CO}$ , respectively). The chosen detection limits are comparable to the  $3\sigma_{\text{rms}}$  levels of current-day single dish observations.

We investigate three main methods; the inference of  $\text{H}_2$  column density and mass from the LTE measurement of the  $^{13}\text{CO}$  column density, the virial analysis and the CO emission-to- $\text{H}_2$  column density conversion factor (i.e.  $X_{\text{CO}}$  factor). We also test slightly different, alternative implementation of these methods. The main results are as follows:

1. All methods provide mass estimates within a factor of 2 error over a large range of parameters, given that the metallicity is not too low. If the conditions are similar to those in the Milky Way (for which the methods were originally calibrated), all methods give a very good estimate (less than a factor of 2 error) of the true  $\text{H}_2$  mass.
2. The LTE column density measurement of  $^{13}\text{CO}$  might trace the true CO column density distribution well within the  $4 \times 10^{14} \text{ cm}^{-2} < N(^{12}\text{CO}) < 4 \times 10^{16} \text{ cm}^{-2}$ , or  $10^{19} \text{ cm}^{-2} < N(\text{H}_2) < 10^{21} \text{ cm}^{-2}$  range, if the fitting formula of chapter 2 for the  $^{12}\text{CO}/^{13}\text{CO}$  ratio is used, but it is a very bad indicator of the true  $\text{H}_2$  column density, due to the lack of a single abundance ratio, which would hold over most of the column density range.
3. The virial mass, measured from the  $^{12}\text{CO}$  emission, provides the best measure for the true  $\text{H}_2$  mass of the cloud in almost all simulations. This is because the virial parameters of the simulated clouds are close to 1, the turbulence and self-gravity develops a radial density distribution which is close to the  $n(r) \propto r^{-1}$  distribution which is assumed in the analysis and because the emission line widths trace the true line of sight velocity dispersion relatively well. We also find that the purely  $^{12}\text{CO}$  emission based  $RL2006_{\text{vir}}$  method performs systematically better than the  $ML1988_{\text{vir}}$  method, which uses both the  $^{12}\text{CO}$  and the  $^{13}\text{CO}$  isotope. This is because of the different visual extinction thresholds for CO isotope formation; the cloud size estimate from  $^{12}\text{CO}$  includes zones near the cloud edge, which do not contribute to the line width, measured from  $^{13}\text{CO}$  line, due to their faint in  $^{13}\text{CO}$  emission.
4. The  $X_{\text{CO}}$  factor provides a good molecular mass estimate over a range of values in ISRF strength, initial density, cloud mass and even in substructures within a cloud, unless the metallicity is low. This might be a result of the excitation temperature balancing the CO abundance (Liszt et al., 2010). And/or it might be a result of a bias, originating from the adoption of a CO brightness temperature limit (Bolatto et al., 2013). At low metallicities the Galactic value consistently underestimates the true  $\text{H}_2$  mass, usually by a factor of 2, while the  $\langle A_V \rangle$  and metallicity dependent methods of Wolfire et al. (2010) and Glover and Mac Low (2011) tend to overestimate the true mass, occasionally by more than an order of magnitude.

## 4 ON THE COUPLING OF LARGE CHEMICAL NETWORKS TO DYNAMIC SIMULATIONS

*Adapted from Szűcs, Glover, Semenov, & Klessen, in prep.<sup>1</sup>*

### ABSTRACT

Numerous observations point toward a large chemical diversity in molecular clouds and dense cores. It is also clear that most of the observed species are not in chemical equilibrium and their formation and destruction timescales are comparable to the dynamical timescales (e.g. crossing time, free-fall time) of cloud and core. Thus, a comprehensive theoretical treatment of the chemistry in such environments requires the coupling of chemical models to multi-dimensional (magneto-) hydrodynamical simulations. The difficulty of building such simulations lies in the fact that chemical modelling is computationally expensive compared to the pure hydrodynamics or to the calculation of gravitational interactions. Most chemo-dynamical simulations so far focused on modelling only a handful of species. These were chosen either because of their distinguished role in determining the thermal state of gas and/or for their significance in characterizing the atomic-to-molecular transition.

In this chapter we present a method for inferring the evolution and spatial distribution of a number of observational tracer and organic molecules from a hydrodynamical molecular cloud simulation. Most of the considered molecules were completely neglected from earlier simulations. Our approach relies on a robust reduced chemical network for following the chemistry of the major gas coolants within the simulation and a formalism of hydrodynamics, which operates with Lagrangian tracer particles. Once the simulation is run, the density, temperature and radiation history of selected tracer particles is extracted and fed into a fully time dependent chemical model, designed for evolving chemical networks with various complexity. As preliminary results, we present a comparison of approaches for the modelling of CO chemistry with or without accretion onto dust grains. We discuss briefly the spatial distribution and depletion of a few (high) density and kinetic temperature tracer molecules ( $\text{NH}_3$ ,  $\text{N}_2\text{H}^+$ ,  $\text{H}_2\text{O}$  and  $\text{HCN}$ ), modelled in a dense core analogous to low mass starless cores and infrared dark clouds. Finally, we show similar data for organic molecules ( $\text{CH}_3\text{OH}$ ,  $\text{CH}_3\text{CN}$ ,  $\text{HCOOCH}_3$ ) and compare the modelled column densities to those observed in real clouds.

### 4.1 INTRODUCTION

Observational studies have identified more than 180 interstellar molecules<sup>2</sup> up to date. Most of these were found in giant molecules clouds (GMC), photon dominated regions (PDRs) and warm dense cores, heated by star formation activity. Their

---

<sup>1</sup>See page xi for details on authorship.

<sup>2</sup><http://www.astrochymist.org>

detection hints for the existence of a large number of so far unidentified species, which are necessary to explain the existence of those observed. In the inventory of known interstellar atoms and molecules, there are a few key species (e.g.  $\text{H}_2$ ,  $\text{C}^+$ , O, CO), which have a considerable impact on gas dynamics, either by acting as an efficient coolant or by controlling the ionization state of the gas, and thus influencing the coupling between matter and magnetic fields. There are a handful of relatively abundant molecules (e.g. CO,  $\text{NH}_3$ ,  $\text{N}_2\text{H}^+$ , HCN), which are known to correlate with gas properties, such as density and temperature. The emission, absorption and line ratios of these species is therefore often utilized as tracers of the physical conditions (e.g. [van Dishoeck and Blake, 1998](#)). Yet another group of interstellar molecules provides a less clear measure for physical properties (e.g.  $\text{CH}_3\text{OH}$ ,  $\text{HCOOCH}_3$ ), but their presence or absence might hint for the evolutionary stage of the medium ([Beuther et al., 2009](#)).

Most of these species, however, are probably out of chemical equilibrium in typical GMC conditions (e.g. [Leung et al., 1984](#)), and their abundance is a complicated function of density, temperature, local radiation field and possibly dynamical history ([Glover et al., 2010](#)). What is more, the interstellar matter itself is not in steady state. There is an amounting evidence for supersonic, turbulent motions providing the dominant support for molecular clouds against gravitational collapse on large scales. At the same time, turbulence enhances gas density on small scales, leading to local collapse and star formation. The interplay between gas motions on different scales leads to dynamically complex molecular clouds (see [Mac Low and Klessen, 2004](#), for a review). Therefore, if we want to understand the formation and destruction mechanisms, abundances and physical history dependence of molecules in space, it is necessary to couple their chemical models to models of turbulent interstellar gas dynamics.

The rapid advancement of computational power made the inclusion of astrochemical models into multi-dimensional simulation of turbulent gas motions feasible in the past two decades (e.g. [Nelson and Langer, 1997, 1999](#); [Glover et al., 2010](#); [Glover and Clark, 2012b](#)). Although, even the most advanced of these simulation follows the time dependent chemistry for only a few tens of species. This is a tiny fraction of those molecules which can be modelled in “pseudo” time-dependent, from one zone to two dimensional chemical codes. The main factors limiting the modelable chemistry in hydrodynamical simulations are the large number of zones modelled (i.e an Eulerian simulation with  $128^3$  cells already means more than 2 million one-zone chemical models), the frequent hydrodynamical timesteps, after which the chemistry has to be updated and the fact that the computational cost of solving the ordinary differential equation system, which describes the chemical reaction network, scales as the cube of the number of species considered (e.g. [Semenov, 2004](#); [Glover and Clark, 2012b](#)). The chemo-dynamical model of [Glover and Mac Low \(2011\)](#), for instance, includes only about a hundred reactions between 32 atomic and molecular species. From these only 14 are non-equilibrium species and explicitly evolved with the reaction network. In their simulations, about 80 per cent of the total computational time is taken up by solving the chemical rate equations. It is clear with such high computational cost the modelling of the full gas-phase and grain surface chemistry in hydrodynamic simulations is at least impractical if not infeasible.

In this chapter we aim to propose a partial solution to this problem and to

extend our chemical models to species, which are often observed, but almost always neglected from numerical simulations. We do so by implementing a post-processing technique. First, we perform the hydrodynamical cloud simulations with a limited chemical network, which is required for a realistic thermal model. Then a domain of interest, such as a protostellar core, is selected within the computational volume for further analysis. The chemical history of the gas, from which the selected domain consists of is then modelled with the aid of a fully time-dependent chemical code. This utilizes a number of species and reactions comparable to modern pseudo time-dependent chemical models.

The outline of the chapter is as follows: In section 4.2 we introduce the post-processing procedure and explain how it is linked to the hydrodynamical simulations described in the earlier chapters. We also describe the chemical modelling code, `ALCHEMIC` (Semenov et al., 2010), which we use for the post-processing and give an account on the modifications we implemented to fulfil the needs of this study. In section 4.3 we show a possible application for the method and analyse a dense core, similar to low-mass starless cores and infrared dark clouds (IRDCs). Thereafter, in section 4.4 we present preliminary results on benchmarking the simplified CO chemistry network (4.4.1), on the distribution and abundance of high density tracers and complex organic molecules (4.4.2). We also compare the modelled column densities of these species to the column densities measured by Gerner et al. (2014) for a large sample of IRDCs. Finally, in section 4.5 we summarize the post-processing technique and the preliminary results, and give an outlook on future applications.

## 4.2 A RECIPE FOR POST-PROCESSING

The basic concept of our post-processing method is very similar to those presented in Visser et al. (2009b). In that paper the authors investigated the chemical evolution CO and H<sub>2</sub>O ices as material accretes from a protostellar core to the newly formed protoplanetary disk in a two-dimensional, semi-analytic core-collapse model. The core-collapse model provided them with trajectories, along which Lagrangian fluid elements may travel during the viscous evolution of the envelope-disk system. The physical conditions, such as the gas density, the temperature (dust temperature in their case) and the attenuation of stellar and interstellar radiation fields were recorded at each points along the trajectory, as a function of time. This information constitutes the physical history of the fluid element that travelled along the trajectory. The physical histories were then fed into a fully time dependent chemical code, which while evolving the chemical network with time, also updates the physical conditions. By selecting a number of points of origin in the protostellar core/envelope they explored many different trajectories and mapped the chemical composition as a function of final position in the disk.

We model the dynamic and chemical evolution of a molecular cloud within the Lagrangian frame with the aid of Smoothed Particle Hydrodynamic (SPH, see section 1.2.2 in the introduction) numerical simulations. The method of following the physical history of selected tracer particles naturally translates and can be generalized to the SPH. While the SPH particles themselves are tracers of the continuous fluid quantities, such as density, velocity field and internal energy. An additional benefit of SPH is that it already utilizes an interpolation kernel, that can

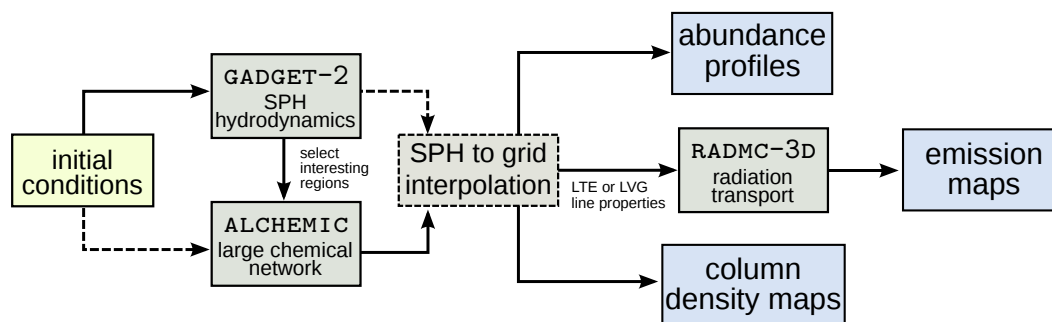


Figure 4.1: Schematic work flow of the chemical post-processing.

also be used to produce rectangular maps of the spatial distribution of the modelled molecules.

The conceptual picture of the post-processing steps are summarized in Fig. 4.1. We start with a set of initial conditions. These include the physical and chemical characteristics of the modelled cloud (see 2.2.4) and the initial abundances of species followed only in the post-processing step. The numerical hydrodynamic simulation is then run in GADGET-2 code (Springel, 2005) with frequent snapshot outputs, until the first sink particles form. The final snapshot is then analysed and domains of interest, e.g. future sites of star formation, are selected. The history of SPH particles landing in a given radius around the selected locations are traced back in the snapshots and stored. In the next step, the SPH particle histories and supplementary initial conditions are imparted to the post-processing chemical code ALCHEMIC. At the end of the chemical post-processing step, the abundances of a large number of chemical species within the selected SPH particles are known. This information with additional data from the hydrodynamic simulation (e.g. velocity field) is then further processed. The particles are interpolated onto a three-dimensional regular grid, for the more convenient visualization. The grids contains the mass density, species specific number density, dust and gas temperature distributions, and the velocity field. These can then be used to produce column density maps or abundance profiles. With additional information on the excitation properties of molecules (e.g. collisional cross sections and Einstein coefficients), radiative transfer models and emission maps can be calculated with e.g. the RADMC-3 code (Dullemond, 2012).

The main ingredients for our post-processing method are the history of physical conditions along the selected SPH trajectories, a chemical network describing the formation and destruction reactions of the species of interest, a code for evolving the chemical network with the changing physical conditions and the initial abundances. In the following sections we describe these, one-by-one.

#### 4.2.1 HYDRODYNAMIC SIMULATION

For the purpose of this chapter we use the Solar metallicity and  $G_0$  radiation field  $10^4 M_\odot$  mass GMC simulation, referred as model (d) in the earlier chapters. For the detailed description of the simulation setup and the exact simulation parameters see section 2.2 and table 3.1, respectively. The chemistry in the simulation was modelled

using the NL99 network (see section 4.2.2), while the attenuation of the interstellar radiation field was approximated by the TreeCol algorithm (section 1.5.2). The H<sub>2</sub> self- and dust shielding are treated according to [Draine and Bertoldi \(1996\)](#), while for the CO self-shielding and shielding by H<sub>2</sub> we adopted the tabulated shielding coefficients from [Visser et al. \(2009a\)](#). The visual extinction dependence of the CO dust shielding, with the free-space CO photodissociation rate coefficient are also taken from [Visser et al. \(2009a\)](#) (see also section 2.2.2).

To construct the physical history of the SPH particles we take all snapshots from the start of the simulation to the one before the formation of the first sink particle. A snapshots are written in a 1.27 kyr interval in simulation time, while the first sink particle forms at 2.14 Myr, thus the total number of snapshots is 168. The final time represents the epoch of the initiation of star and cluster formation. The upper limitation is due to the fact that we are not modelling the thermal and kinetic (i.e. stellar winds and jets) feedback from the newly formed stars. The feedback would heat up the stellar surroundings, thus releasing molecules previously locked up in ices within grain mantels to the gas-phase. The energy provided by the star would also activate reactions channels with endothermic components, thus initiating a large diversity in chemical composition. Additionally, newly formed stars would quickly become the dominant sources of far-ultraviolet photons, thus photodissociation and photoionization. The modelling of these latter feedback processes is out of the scope of this work. However, we would note that such ingredients can be implemented and modelled well in SPH hydrodynamic simulations (e.g. [Dale et al., 2012, 2014](#)).

#### 4.2.2 CHEMICAL NETWORKS

We use two chemical networks, distinct in motivation and complexity. One is the approximate network developed for modelling the major carbon-bearing species, the C<sup>+</sup>-C-CO transition and the gas-phase CO abundance ([Nelson and Langer, 1999](#)). This is supplemented with the hydrogen network of ([Glover and Mac Low, 2011](#)). The other network is based on the 2006 and 2008 releases of the Ohio State University (OSU) chemical rate file ([Smith et al., 2004; Garrod and Herbst, 2006](#)) and contains gas-phase, gas-grain and grain surface reactions for the formation and destruction of 598 chemical species. The reaction network contains more than 7000 reactions (see [Semenov et al., 2010](#)).

For more details we refer to sections 1.3.6.1 and 1.3.6.2 in the introduction.

#### 4.2.3 SOLVING THE CHEMICAL NETWORK

The ordinary differentiation equation (ODE) system, constructed according the physical conditions, the network and the initial abundances, is solved in the `ALCHEMIC` (AcceLerated CHEMical Code; [Semenov et al., 2008, 2010](#)) code. `ALCHEMIC` is based on the publicly available `DVODPK`<sup>3</sup> (Differential Variable-coefficient Ordinary Differential equation solver with the Preconditioned Krylov method GMRES for the solution of linear systems) ODE solver package. The Jacobi matrix of the ODE system is determined automatically and used as a left-hand preconditioner. In astrochemical applications it is common that the Jacobi matrix is sparse, therefore the efficient solution of the corresponding linearized system of equations require

<sup>3</sup><http://computation.llnl.gov/casc/odepack/>

a specialized spars matrix solver. For this we use the high-performance sparse unsymmetric MA48 solver from the Harwell Mathematical Software Library<sup>4</sup>, and gain about a factor of 100 speed-up compared to the standard DVODPK method. The accuracy of the resulting chemical abundances are controlled by the absolute and relative error parameters. Although a larger accuracy is always desirable, it means a trade-off with the computational time. Following [Semenov \(2004\)](#), we set these to  $\epsilon_{\text{abs}} = 10^{-16}$  and  $\epsilon_{\text{rel}} = 10^{-8}$ , for a reliable abundance estimation at a reasonable computational cost.

ALCHEMIC was originally designed to model the pseudo time-dependent chemical evolution of dense cores and protoplanetary disks. When modelling dense starless cores, the main input parameters are the gas density and temperature, the interstellar radiation field (ISRF) strength in units of the Draine field, the “effective” visual extinction towards the ISRF, the H<sub>2</sub> and CO shielding coefficients (originally calculated according [Draine and Bertoldi, 1996](#); [Lee et al., 1996](#)), the cosmic ray ionization rate of H and the initial abundances. Additionally, the starting and ending times of the evolution, with the number of intervening outputs are given as parameters. The internal timestep of the ODE solver is adaptive and determined automatically. The results are the chemical abundances of modelled species at the defined output times.

The pseudo time-dependence means that the network is evolved with time and the resulting abundances are also functions of time, but the physical conditions (e.g. density, temperature and ISRF strength and cosmic ray flux), consequently, the reaction rate coefficients, do not change as time progresses. If the dynamical timescales of the problem are much longer than the chemical timescales, this is a good approximation. In the case of molecular clouds, however, we aim to model the chemical evolution on a few Myr timescale. During this time, the density, temperature and visual extinction that certain SPH particles experience might change from a few hundred to  $10^6 \text{ cm}^{-3}$ , from 100 K to 15 K and from less than 0.1 mag to few 10 magnitudes, respectively. Furthermore, some particles might experience repeated low and high density periods, which might leave a mark on their chemical composition.

For these reasons, to be suitable for our aims, there are a number of modifications we implemented into the original code:

1. We implement full time dependency into ALCHEMIC (i.e. for both physical conditions and chemistry). We do so by introducing an additional, physical condition cycle above the already existing chemical cycle in hierarchy. The procedure of solving the chemistry along the time evolution of an SPH particle is as follows: In the first physical timestep we calculate the rate coefficients for each reactions. These stay constant until the next physical timestep. Then, we build the Jacobian using the rate coefficients and the initial abundances. The ODE solver is called with the integration time set to the temporal length of the physical step. When the solver provides the abundances, they are stored along with the rate coefficients (for analytical purposes). Thereafter the second physical timestep starts. The physical conditions are updated and the new rate coefficients are calculated accordingly. The initial abundances in the second steps are set to final abundances of the preceding step. The ODE solver is then

---

<sup>4</sup><http://www.hsl.rl.ac.uk/catalogue/ma48.html>

called again, the rate coefficients and final abundances of the step are stored. From the third step the procedure is the same as for the second. This continues until the final physical condition step is reached. Then the abundance and rate coefficient data as functions of the physical times are saved and the code terminates. In short, this means that we are solving a pseudo time dependent problem in each physical timestep. The repeated calling of the ODE solver cost computational speed; the time required to solve the same network scales close to linearly with the number of physical timesteps. We compensate for this by running the chemical models parallel on up to a hundred computer cores.

2. In the original `ALCHEMIC` implementation the dust and gas temperatures are assumed to be equal. In low density environments, typical for molecular cloud, this is generally not true (see e.g. the dotted and dot-dashed lines in Fig. 2.13). The dust and gas temperatures differs because gas and dust are heated and cooled by qualitatively different processes (see section 1.2.4) and the heat transfer between them requires frequent gas-grain collisions, thus high density. Therefore we need to treat the dust and gas temperatures separately, keeping in mind which is the relevant for the process in question. The gas temperature is the relevant temperature in the Arrhenius equation (Eq. 1.24) for gas-phase reactions and in the expression for the accretion rate onto grains (Eq. 1.27), while the dust temperature is needed in Eq. 1.28 for the calculation of thermal desorption rate from grains.
3. Finally, we need to take the three-dimensional nature of the hydrodynamical code into account when calculating the photochemical rates. In the simulation a parcel of gas is irradiated from  $4\pi$  sr solid angle. In each direction this irradiation is attenuated differently, depending on the line of sight density distribution. As previously described, we use the `TreeCol` algorithm for tracking the hydrogen nuclei (i.e. visual extinction),  $\text{H}_2$  and  $\text{CO}$  column densities (see sections 1.4 and 1.5.2) in 48 equally spaced directions. Therefore, in each timestep for each SPH particles, the effective rate coefficient of a photochemical reaction is given by the average of the rate coefficients induced by the arriving radiation from each of the 48 directions and calculated according Eq. 1.34. We pass the complete `TreeCol` data (i.e.  $3 \times 48$  values per particle per timestep) to `ALCHEMIC` to calculate the appropriate effective rates. In the original implementation of `ALCHEMIC` only a single irradiation line of sight was taken into account.

#### 4.2.4 INITIAL ABUNDANCES

The initial abundance are set consistently in case of both networks, according [Sembach et al. \(2000\)](#). The abundances are consistent with the warm neutral medium at Solar metallicity. The “low metal” abundances of [Lee et al. \(1998\)](#) are more frequently chosen for observation inspired chemical models as initial conditions ([Semenov et al., 2010](#); [Gerner et al., 2014](#)), because they thought to reproduce the observed abundances in dense cores and protoplanetary disks better. Compared to those the initial abundances adopted here are a factor of a few higher for carbon, oxygen and nitrogen, while 3 – 4 orders of magnitude higher for the

Table 4.1: The adopted initial fractional abundances (relative to the hydrogen nuclei)

Species	NL99	OSU
H <sub>2</sub>	5.000(-1)	5.000(-1)
He	7.900(-2)	7.900(-2)
C <sup>+</sup>	1.400(-4)	1.400(-4)
O	3.200(-4)	3.200(-4)
N	-	7.590(-5)
Si <sup>+</sup>	-	1.500(-5)
Fe <sup>+</sup>	-	1.000(-7)
M <sup>+</sup>	1.000(-7)	-
e <sup>-</sup>	1.401(-4)	1.551(-4)

The abundances are adopted from [Sembach et al. \(2000\)](#) and thought to resemble the composition of the warm interstellar medium at Solar metallicity. We note that the frequently adopted “low metal” abundances from [Lee et al. \(1998\)](#) are a factor of a few lower in C, O and N abundances, while about 3-4 orders of magnitude depleted in Fe and Si. The values are given in  $a(x) = a \times 10^x$  form.

low ionization potential metals, such as Fe<sup>+</sup> and Si<sup>+</sup>. These large differences in the initial composition should be kept in mind when comparing results to the literature (e.g. in section 4.4).

The adopted initial fractional abundances relative to the hydrogen nuclei are summarized in table 4.1. When possible we assume the same fractional abundances in both networks. Similarly to the earlier chapters, we adopt fully molecular conditions for hydrogen, while the carbon and oxygen are assumed to be fully ionized and fully neutral forms, respectively. The helium is also neutral and its abundance corresponds to a mass fraction of 24 per cent.

In addition to the hydrogen-carbon-oxygen based NL99 network, we also introduce nitrogen (N) and silicon (Si) to the extended network. Initially, the complete reservoir of nitrogen is chosen to be neutral and all silicon is ionized. These choices are motivated by the fact, that nitrogen, likewise to oxygen, has a higher ionization potential than 13.6 eV, while sulphur, similarly to carbon, is ionized easily by less energetic photons and thus not shielded by hydrogen ionization events.

The initial ionization state of the gas is due to carbon and low ionization potential metals. The latter are represented as a combined species in the NL99 network (M<sup>+</sup>), while in our OSU model it is constituted by Si<sup>+</sup> and Fe<sup>+</sup>. The combined abundance of the latter two are slightly higher than the former.

We assume that the dust-to-gas ratio is uniform over the cloud and has the standard value of 0.01. In this case, the visual extinction is calculated according Eq. 1.26.

### 4.3 A PRESTELLAR DENSE CORE

The fundamental idea behind applying a post-processing method for chemistry is that we try to save computational time by focusing our attention only to certain

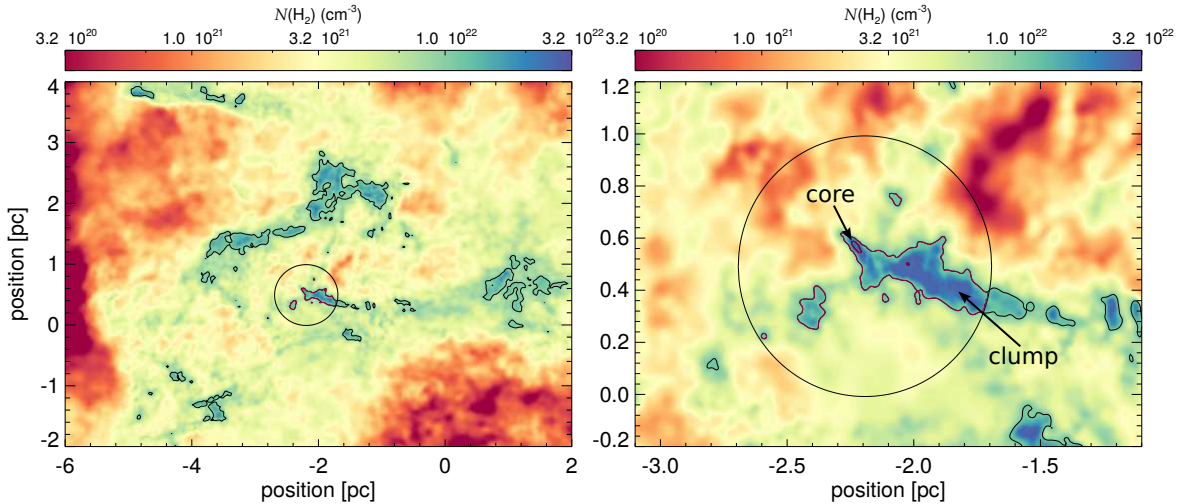


Figure 4.2: The selected high density region in simulation (d), marked by red contour. The contours indicate regions with  $\text{H}_2$  column density higher than  $10^{22} \text{ cm}^{-2}$ . The left panel shows the environment of the core on a few parsec scale, while the right panel shows its direct surroundings. The black circle has a radius of 0.5 pc and indicates the projection of a sphere around the high density peak. We analysed SPH particles which were within this spherical zone at the last snapshot before the first sink particle formed. For an overlook of the whole simulation domain we refer to Fig.3.1.

domains of the simulation volume. We are primarily interested in the chemical composition of future sites for star formation. The hydrodynamical simulation contains a range of such sites, from massive cores and filaments forming multiple sink particles, to small, sub-parsec scale cores with initial masses on the order of a few Solar masses. For testing purposes and preliminary studies we prefer the latter, small mass objects. These typically contain only a few thousand SPH particles, hence they can be modelled relatively quickly. For these reasons, we choose a single object based on its peak density and total mass just before star formation commences in the simulation.

The selected structure is shown in Fig. 4.2 with red contour lines. The outer and inner contours indicate the  $10^{22} \text{ cm}^{-2}$  and  $3 \times 10^{22} \text{ cm}^{-2}$  column density levels, respectively. We classify the structure associated with the lower contour level as a clump. The higher contour level within is an indicator for a core-like structure, hence we refer to it as such. Both of them are located in a dynamically active region.

In fact, the clump is formed by a gas stream, arriving from the upper right corner in the figures. The larger filament or clump complex above the selected core is also formed by a flow, coming from the upper left corner. The flows converge in the region and thus enhance the local density. The local density then reaches the critical density for sink particle formation and the dense core and the slightly more dilute clump will start to form stars in the next timesteps. In a few more kyr self-gravity becomes dominant over the turbulent support and the whole clump collapses. The density enhancement towards the lower left corner and still within the selected

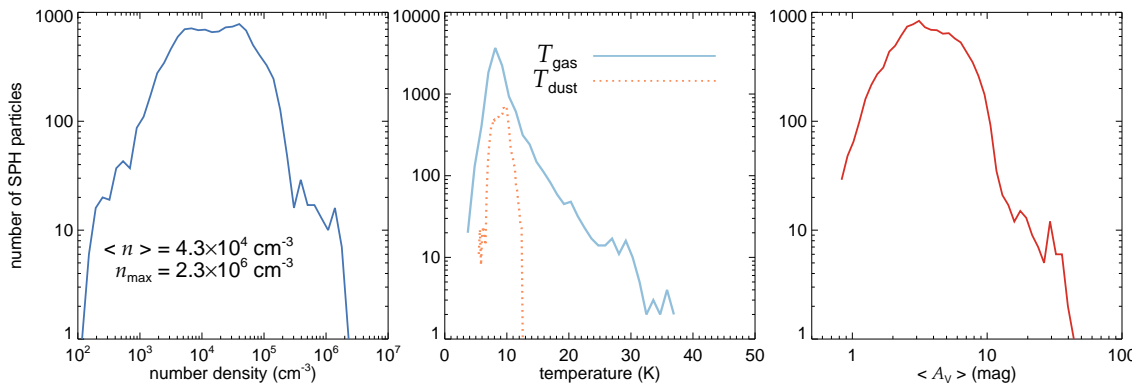


Figure 4.3: The number density, gas and dust temperature and effective visual extinction distribution of particles forming the studied core at  $t = 2.14$  Myr. The total number of SPH particles plotted there is 11054.

region is prohibited of sink formation and disperses on a short timescale. By the time of the last considered snapshot (at 2.14 Myr) the dense core accumulated a total mass between  $3 M_{\odot}$  and  $5 M_{\odot}$ , depending on the choice of the core border, while the total mass of the clump (including the dense core) is about  $54 M_{\odot}$ .

For a detailed analysis we select the SPH particles within a 0.5 pc radius zone, centred approximately around the dense core. The two-dimensional projection of this zone is indicated by the circles in Fig. 4.2. The number density, gas temperature, dust temperature and mean visual extinction distribution of particles within the region 2.14 Myr after the start of the simulation, are shown in Fig. 4.3. The number density distribution is relatively broad. The mean value is a few  $10^4 \text{ cm}^{-3}$ , while the few densest particle reaches number densities above  $10^6 \text{ cm}^{-3}$ . The temperatures are generally low and they peak around 10 K. The dust and gas temperatures are not coupled completely: the dust is always below 15 K, while in some gas parcels the gas temperature may reach above 20 K.  $\langle A_V \rangle$  is the averaged visual extinctions measured in 48 directions, from the particle center towards the cloud surface, by the TreeCol method. Hence, it is not equivalent to the visual extinction that a distant observer would measure towards the cores. The former indicates to what extent the ISRF is attenuated at the particle center, while the latter is a tracer of the total line of sight column density. Most of the particles are well shielded by dust columns equivalent to 3 – 4 mag visual extinctions. In the center of the dense core, this can reach up to 40 mag. The physical properties of the selected core are very similar to those measured in observational works for low-mass prestellar cores and clumps (e.g. Hartquist et al., 1993; Bergin and Tafalla, 2007). Therefore we expect our model is a reasonably good analogue for real star formation sites, early in their evolution.

The clump described above consists of 11054 SPH particles. We post-processed the particles with both the OSU and the NL99 networks. The latter serves the purpose of checking whether the post-processing method reproduces the chemistry, modelled internally in the GADGET-2 simulation. The 2.14 Myr chemical evolution of this particle assembly, with the post-processing method, took in total 344.2 CPU hours for the OSU and 1.92 CPU hours for the NL99 networks. The former is comparable to the runtime of the hydrodynamical simulation with the NL99 chemical model for

2 million particles, which was approximately 500 CPU hours<sup>5</sup>.

#### 4.4 PRELIMINARY RESULTS

The following results are preliminary and based on the outcomes of test simulations, which are not meant for journal publication in their current state. Here we present them to illustrate potential applications for the post-processing method.

##### 4.4.1 CARBON CHEMISTRY

As a consistency check, first we investigate how the spatial distribution and time evolution of the main carbon-bearing species compares between the GADGET-2 and the ALCHEMIC (post-processing) implementations of the NL99 network. We are also interested in how well the reduced network is capable of recovering the chemical properties, modelled by the more complete OSU network.

The comparison of implementations for the NL99 network is presented in Fig. 4.4. The left panel shows the time evolution of the median abundances for SPH particles, which reach a number density  $10^5 \text{ cm}^{-3}$  or higher by the last analysed snapshot and are within the clump. The left panel shows the median abundances for all SPH particles within the clump, at the time of the last snapshot (2.14 Myr) as a function of mean visual extinction (an average over the  $4\pi\text{sr}$  sky for each particle). The solid lines represent abundance profiles from the internal chemical model of the gadget-2 simulation, while the large-dotted curves indicate abundance profiles from the post-processing method. At low visual extinctions and early times, the chemistry is dominated by photoionization of carbon atoms and photodissociation of CO molecules (for a details see section 1.3.2. In these cases we find an excellent agreement between the approaches, proving that the multi-dimensionality of photochemistry is correctly implemented into the ALCHEMIC code. Deeper in the cloud and at later times, the CO and  $\text{C}^+$  abundances are still well match. However, the neutral carbon show a sizeable difference, up to about an order of magnitude). The reason of the discrepancy is unclear, but likely related to how the cosmic ray particle induced photodissociation of CO is treated in the codes. The clarification requires further modelling, from which we leave aside here.

Apart from the discrepancy of the neutral carbon abundance deep within the clump, we conclude that the post-processing method can reproduce the chemistry of the GMC simulations well and that we transfer the SPH data from the simulation to the post-processing chemical tool correctly. Thus the method is also suitable to be used with more complex networks.

Next, we compare the abundance evolution and spatial distribution of the major carbon-bearing species modelled with the NL99 and the more complete OSU networks (dashed lines in Fig. 4.4. Again, at early times and low visual extinction, where the chemistry is controlled by the radiation, the agreement is good. The simplified model slightly overestimates the  $\text{C}^+$  and underestimates the CO abundances. This is due to the fact that the larger network has multiple, less efficient

<sup>5</sup>The post-processing calculations were run on a workstation with  $2 \times$  Intel(R) Xeon(R) CPU E5645 @ 2.40 GHz CPU (12 cores) and 98 GB RAM, while the GADGET-2 simulation was run on 64 cores of the Kolob cluster, each node equipped with  $2 \times$  Intel(R) Xeon(R) E5410 @ 2.33 GHz CPU (8 cores) and 24 GB RAM

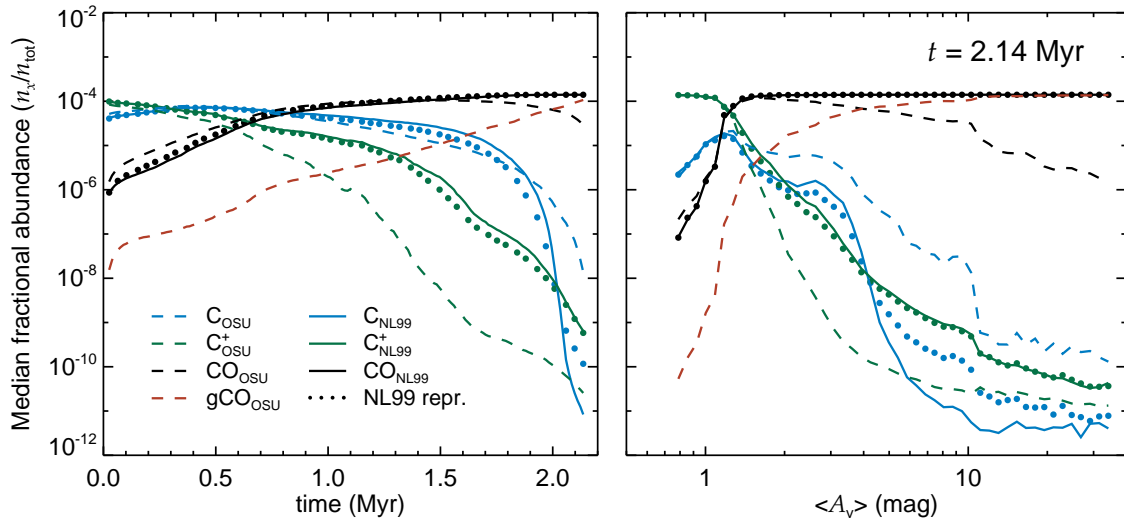


Figure 4.4: Comparison of the major carbon-bearing species modelled with the OSU and the NL99 networks. The dashed lines indicate post-processed abundances, modelled with the OSU network, while the solid lines show abundances calculated implicitly in the hydrodynamical simulation, adopting the NL99 network. The large-dotted curves are the abundance profiles found with the NL99 network implemented in `ALCHEMIC`. Left panel: the time evolution of abundances within SPH particles which reach a final number density of  $10^5 \text{ cm}^{-3}$  or higher at the end of the simulation. The abundances shown here are the median values at a given time for the particles fulfilling the criterion. Right panel: fractional abundance of the same species at the end of the simulation, as a function of the mean visual extinction.

formation routes for CO which are active at early times. For instance, the direct formation of CO from grain surface species gC and gO and gC and gOH are such reactions. These combined, may result in a noticeable, but weak increase in its abundance. Once the  $\text{C}^+$ -to-CO transition is complete, the differences grow larger: due to the shielding which allows the transition at the first place, the temperature also decreases. This combined with an increasing gas density results in an efficient accretion of CO to dust grains, thus reducing its gas-phase abundance. This process is neglected from the NL99 network. At high visual extinctions, the NL99 model predicts by up to two orders of magnitude more  $\text{C}^+$  than neutral carbon. The trend is switched in case of the OSU network. This difference can be understood by considering the processes for  $\text{C}^+$  destruction once its recombination with electrons becomes inefficient. In the NL99 network  $\text{C}^+$  is consumed by reactions with OH, producing  $\text{HCO}^+$  and with  $\text{H}_2$ , light producing hydrocarbon ions. In addition to these, the OSU network also includes Si, with which the charge transfer reaction of  $\text{C}^+$  is very efficient. In fact, this might dominate  $\text{C}^+$  destruction in certain conditions. The enhanced recombination rate leads to reduced  $\text{C}^+$  and enhanced C abundances. We note, however, that at those cloud depths the abundance of both neutral and

ionic carbon atoms are very low. The main charge carriers by then are  $\text{H}_3^+$  and  $\text{He}^+$ , which are produced by cosmic ray particles. Thus, such discrepancies in C and  $\text{C}^+$  abundances probably do not have a significant effect on the overall chemical state of the gas.

All things considered, we conclude that the NL99 network does a good job modelling the carbon chemistry in low to intermediate visual extinction environments, even when compared to more complete chemical networks. At higher visual extinctions, however, the freeze-out becomes the dominant process for controlling the gas-phase CO abundance. Therefore, we suggest the addition of this process to the reduced network for numerical simulations.

#### 4.4.2 HIGH DENSITY TRACERS AND ORGANIC MOLECULES

The typical used  $\text{H}_2$  column density and mass tracer, the emission of CO isotopes becomes less feasible measure of physical properties in dense clumps and cores. One difficulty is that clumps and cores are usually embedded in lower density and lower visual extinction gas, which is abundant in CO. Therefore the CO emission might already become optically thick before the core. This can be partially overcome by using more optically thin isotopes, such as  $^{13}\text{CO}$  and  $\text{C}^{18}\text{O}$ . An other problem emerges, however, deeper in the clump/core: the typical temperatures are between 10 - 20 K and the density is also high, resulting in a rapid CO freeze-out onto dust grains (see Fig. 4.4). Therefore, alternative tracers are used in this regime. In this section we present the column density distributions and morphologies of several high density, temperature and depletion tracer molecules from the post-processed numerical simulations.

Fig. 4.5 show the column density distribution of a  $\text{H}_2$  and a number of often observed molecule, for the latter we also present the column densities of their grain surface peers for a comparison. The contour lines represent the  $5 \times 10^{21} \text{ cm}^{-2}$ ,  $1.25 \times 10^{22} \text{ cm}^{-2}$  and  $3 \times 10^{22} \text{ cm}^{-2}$  levels in  $\text{H}_2$  column density, respectively. These contours are overlayed to the column density distributions of the tracer molecules for a comparisons. The column densities of each species, measured at the location of the dense core are summarized in Table. 4.2. We also calculate depletion fractions for the molecules according  $\text{d.f.} = (\langle N(x) \rangle_{\text{gas}} + \langle N(x) \rangle_{\text{grain}}) / \langle N(x) \rangle_{\text{gas}}$ .

The CO column density distribution follows the elongated ridge of the clump, and it does not trace the dense core. Consistently with this, the column density of the grain surface CO peaks at the  $\text{H}_2$  density peak (i.e. at the core location). The depletion factor is about 3, meaning that about 33 per cent of the total CO reservoir is in the gas-phase. This compares well to the CO depletion values that Lippok et al. (2013) measured in low mass starless cores. As the CO is removed from the gas-phase in the core, the  $\text{N}_2\text{H}^+$  molecular ion is expected to increase in abundance (e.g. Caselli et al., 1999). This is due to the fact that the reaction with CO is the main destruction path of  $\text{N}_2\text{H}^+$  (Bergin et al., 2002). The model follows this expectation well.

The gas-phase water follows a similar distribution as CO and it is depleted by a factor of 50. Through most of the cloud,  $\text{H}_2\text{O}$  forms on grain surfaces, while it might be also formed by dissociative recombination of  $\text{H}_3\text{O}^+$  in the gas-phase. Its peak gas-phase abundance reaches about  $10^{-7}$ , while the abundance of water ice might be as high as  $10^{-5}$ .

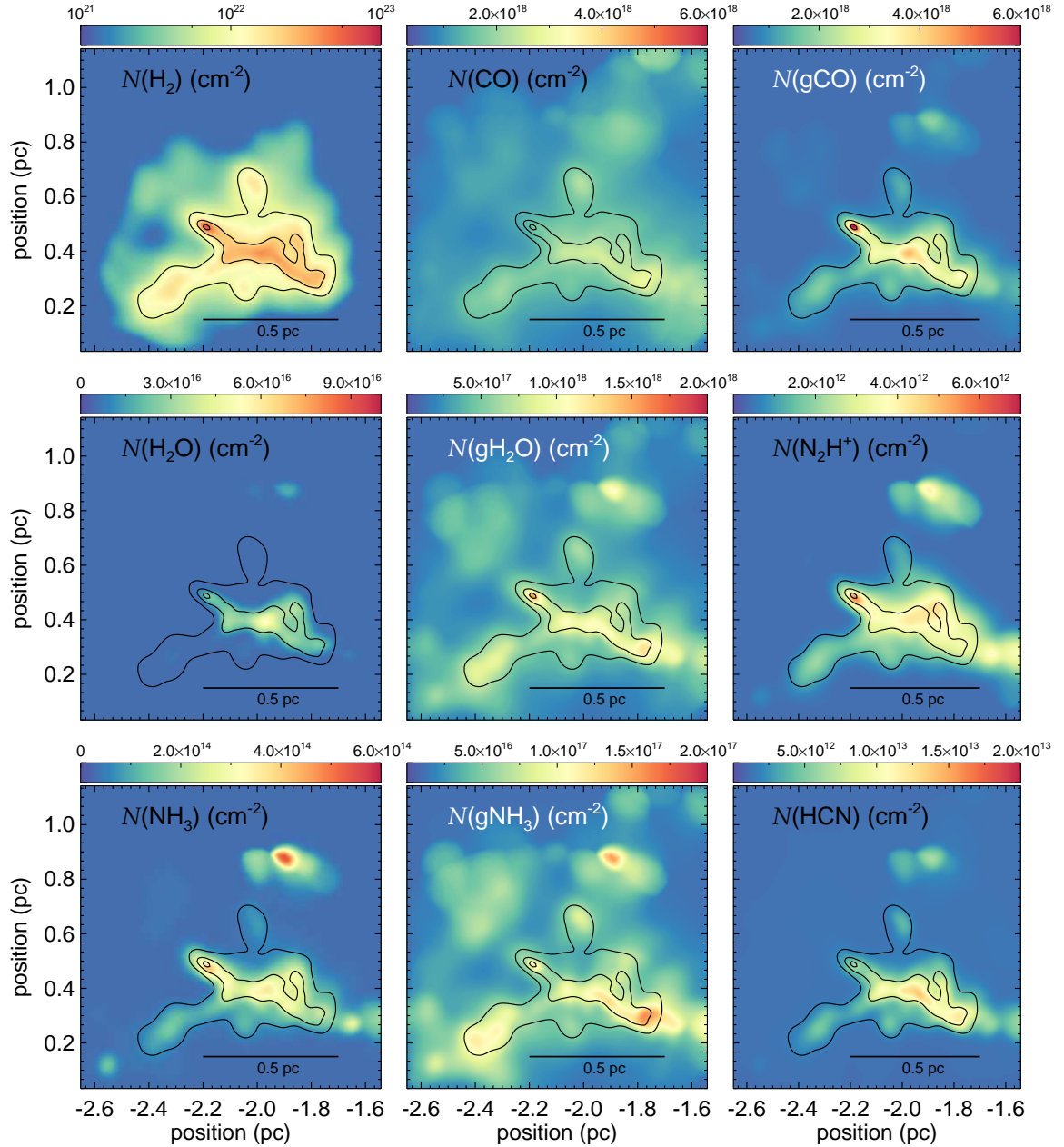


Figure 4.5: An inventory of frequently observed density, high-density and temperature tracer molecules and their ice peers. For each species we show the integrated column density through the analysed volume (i.e. contribution from the diffuse gas and coinciding structures in the GMC are neglected). The contour lines indicate  $N(\text{H}_2) = 5 \times 10^{21} \text{ cm}^{-2}$ ,  $1.25 \times 10^{22} \text{ cm}^{-2}$  and  $3 \times 10^{22} \text{ cm}^{-2}$ , respectively. Note the different colour scales for the panels.

As expected the ammonia column density also peaks at the core position. The core also shows stronger depletion in HCN than the rest of the cloud.

In Fig. 4.5 we also present the spatial distribution of a few organic molecules. Their distribution shows similar trends as found in observations (e.g. [Feng et al.](#),

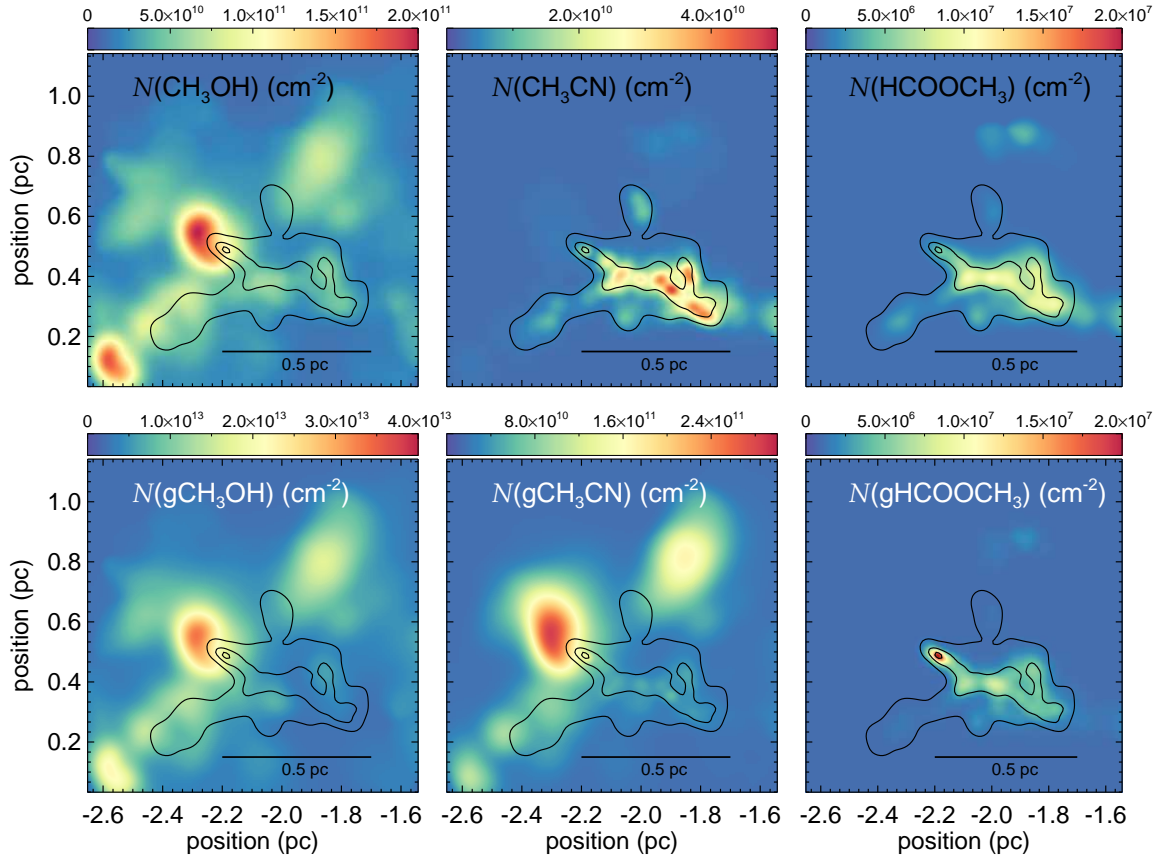


Figure 4.5: (continued)

2013).  $\text{CH}_3\text{CN}$  and  $\text{HCOOCH}_3$  peaks at the clump, while the  $\text{CH}_3\text{OH}$  column density peak shows no correlations with the dense gas. The reason for the different behaviour may lie in the dominantly gas-phase production of the former and the grain surface production of the latter.

We also present a comparison between the column densities measure towards the peak position in the simulations and those measured in Gerner et al. (2014) for infrared dark clouds (IRDCs). IRDCs are dense, high mass cores before the commencing of high mass star formation. They are historically classified by the lack of mid- and far-IR emission, which would indicate the presence of embedded stellar object(s). The typical physical conditions within IRDCs are a few  $10^5 \text{ cm}^{-3}$  and 10-20 K temperature (Bergin and Tafalla, 2007), thus they are very similar to starless low-mass cores. One major difference is the total cloud mass: the IRDC mass ranges from a few 10 to a few hundred solar masses. The selected clump in the simulation has a mass of about  $50 M_\odot$ . The column density comparison is shown in Fig. 4.6.

The comparison reveals a large discrepancy between the model and observations, even though (Gerner et al., 2014) was able to explain the measured abundances with a pseudo-time dependent chemical model, very similar to our OSU network (i.e. both is based in *ALCHEMIC*). We speculate that the reason for the large discrepancy is due to the chosen initial abundances. For instance, our model sets the initial Si abundance 4 orders of magnitude higher than the “low metals” abundances of (Lee

et al., 1998), which is adopted as initial conditions for the models of (Gerner et al., 2014).

All in all, we find that the spatial distribution and abundance trends from the simulations are consistent with the expectations, although the absolute column densities (abundances) are not matching well with the expected values.

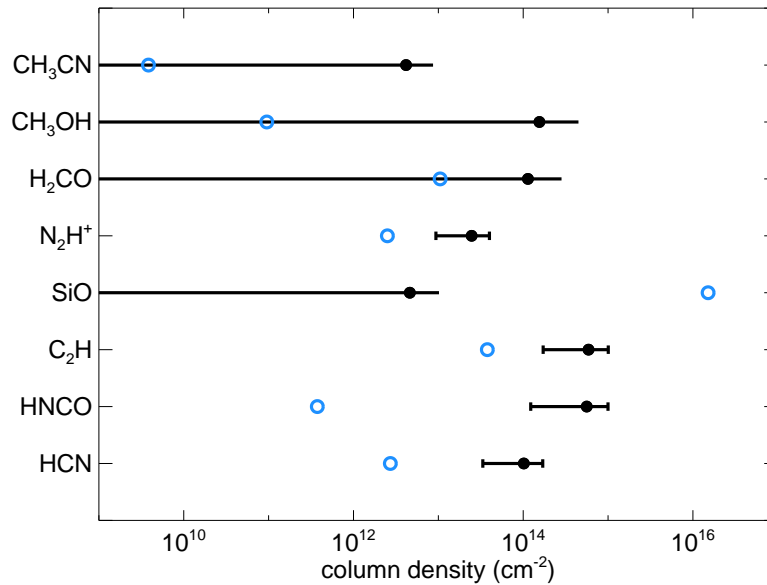


Figure 4.6: Comparison of column densities measured in your simulation towards the core position (empty circles) and column densities observed for a large set of IRDCs (filled black circles). The latter data is compiled from Table A.5 in the Appendix of Gerner et al. (2014). The errorbar indicates the standard deviation of the observational data. The upper limits are marked with continuous bars towards small column density values.

#### 4.5 SUMMARY AND FURTHER PLANS

In this chapter we presented a post-processing method for inferring the chemical evolution of a large number of chemical species from hydrodynamic simulations. The direct implementation of such large chemical network to hydrodynamic simulations is hindered by the large computational cost of solving the ODE system, which describes the network. One plausible way to get around this problem is to restrict the complex chemical analysis to a limited domain of the simulation and perform the chemical modelling after the simulation has finished. Thus, reducing the computational cost to a manageable level.

Our method builds upon an SPH-based numerical simulations, which involves a limited chemical model for the most important atomic and molecular gas coolants. After performing the simulation we select a clump with an embedded dense core from the last simulation snapshots and extract the physical history of gas within them. These are then post-processed with an external, fully time-dependent

Table 4.2: Simulated column densities of selected molecular species, measured towards the dense core.

Molecule ( $x$ )	in gas-phase		on grains		depletion factor
	$\langle N(x) \rangle$	$N_{\text{peak}}(x)$	$\langle N(x) \rangle$	$N_{\text{peak}}(x)$	
H <sub>2</sub>	1.11(+22)	4.08(+22)	–	–	–
CO	9.40(+17)	1.28(+18)	1.85(+18)	6.24(+18)	2.97
H <sub>2</sub> O	1.28(+16)	2.75(+16)	6.59(+17)	1.50(+18)	52.48
NH <sub>3</sub>	2.10(+14)	3.89(+14)	4.98(+16)	1.09(+17)	238.14
N <sub>2</sub> H <sup>+</sup>	2.51(+12)	5.34(+12)	–	–	–
HCO <sup>+</sup>	1.45(+12)	2.75(+12)	–	–	–
HCN	2.72(+12)	5.37(+12)	2.94(+14)	5.43(+14)	109.09
HNCO	3.75(+11)	7.36(+11)	2.93(+12)	4.76(+12)	8.81
H <sub>2</sub> CO	1.05(+13)	1.22(+13)	3.72(+13)	5.63(+13)	4.52
C <sub>2</sub> H	3.78(+13)	4.69(+13)	1.17(+14)	1.78(+14)	4.09
SiO	1.51(+16)	3.04(+16)	–	–	–
CH <sub>3</sub> OH	9.52(+10)	1.44(+11)	1.49(+13)	2.25(+13)	157.51
CH <sub>3</sub> CN	3.84(+09)	1.48(+10)	1.01(+11)	1.76(+11)	27.30
CH <sub>3</sub> CHO	5.31(+08)	1.54(+09)	1.21(+09)	5.71(+09)	3.28
HCOOCH <sub>3</sub>	1.54(+07)	3.92(+07)	4.98(+07)	2.11(+08)	4.23

The column densities are measured in the direction of the dense core, in an  $\sim 10000$  AU radius area, with the H<sub>2</sub> column density peak at its center. The mean column density of species  $x$  ( $\langle N_x \rangle$ ) is meant as the average within this area. The peak column density  $N_{\text{peak}}(x)$  is defined similarly. The depletion factor is calculated as the ratio of the total reservoir (grain surface + gas-phase) of species  $x$  and its gas-phase abundance, i.e. d.f. =  $(\langle N(x) \rangle|_{\text{gas}} + \langle N(x) \rangle|_{\text{grain}}) / \langle N(x) \rangle|_{\text{gas}}$ . The values in columns from the second to the fifth are given in a  $a(x) = a \times 10^x$  form.

chemical code. This includes a chemical network comparable in completeness to those used in pseudo-time dependent gas-grain models.

The post-processing method was tested by calculating the chemical evolution of the chosen clump with the same chemical network (NL99) as was used for the internal chemical model of the simulation. We find that the abundances of the main carbon bearing species are in good agreement between the methods. We also compare the abundance evolution and spatial distribution of these species, when they are modelled with the NL99 and the more complete OSU networks. At early times and low visual extinction, where the chemistry is driven by photoionization and photodissociation, the agreement is good. In the well-shielded gas, the differences grow larger: freeze-out depletes CO from the gas-phase by a factor of a few even at moderate (3 – 5 mag)  $A_V$  values. The neutral carbon abundance is increased at the expense of C<sup>+</sup> due to the efficient charge transfer reaction with Si in the latter model.

We conclude that the NL99 network is in a good agreement with the more complex OSU network when the visual extinction is low or moderate. At high  $A_V$ , however, the freeze-out becomes the governing process for the CO abundance. From the perspective of the chemistry and synthetic observations, this effect should be in-

cluded. In numerical simulations focusing primarily on gas dynamics, disregarding freeze-out may still be a good approximation, because at densities where depletion becomes serious already the dust continuum emission is the main coolant.

The method also provides abundances and column density maps for high density tracer and organic molecules. We find good qualitative agreement with the expectations regarding the morphology of the molecules. The gas-phase CO is depleted in the core, while it remains more abundant in the rest of the clump. The  $\text{N}_2\text{H}^+$  shows the expected anti-correlation with this: it reaches its peak towards the core. The ammonia column density also peaks at the core position. The core also shows stronger depletion in HCN than the rest of the cloud. The least depleted molecules in the simulations is CO, while  $\text{H}_2\text{O}$  is depleted by a factor of 50.  $\text{NH}_3$  is depleted by a factor of 500, but this might be explained by the fact that ammonia forms almost exclusively on grain surfaces. The absolute column densities are typically underestimate those measured for IRDCs by at least an order of a magnitude. The discrepancy is likely the result of the difference choices of initial abundances. We plan redo the comparison with more consistent initial conditions.

The column density maps of organic molecules show similar trends as found in observations:  $\text{CH}_3\text{CN}$  and  $\text{HCOOCH}_3$  peaks at the clump, while the  $\text{CH}_3\text{OH}$  column density peak shows no correlations with the dense gas. The reason for the different behaviour may lie in the dominantly gas-phase production of the former and the grain surface production of the latter.

After further testing of the method, our objectives are to investigate the following problems:

In observational studies, the chemical ages of clumps are often used as indicators for their physical age. The chemical age is estimated by matching the measured abundances with pseudo time-dependent chemical models. The age is then taken to be equivalent to the model age with abundances fitting the observed data the best (e.g. [Gerner et al., 2014](#)). However, the chemical age might differ considerably from the physical age. Turbulent mixing or violent events are expected to alter or entirely reset chemical ages ([van Dishoeck and Blake, 1998](#)). We plan to use the method presented here to constrain these effects.

Numerical simulations can also be used to test the detectability of core collapse signatures. For instance, [Smith et al. \(2012, 2013\)](#) modelled line emission profiles of collapsing high mass cores from large scale cloud simulations. They used both optically thick (CS, HCN) and optically thin ( $\text{N}_2\text{H}^+$ ) tracers and find that the optically thick line profiles are very variable with viewing angle and that CS is not a good indicator of collapse, since its emission peaks in the outer envelope. Their model, however, uses either constant abundances (e.g. for  $\text{N}_2\text{H}^+$  and HCN) or parametrized formula (for CS). We plan to follow up on their work, using self-consistently calculated chemical abundances and to extend the investigation to additional species. Such models might also help to constrain projection effects in  $\text{NH}_3$  emission based virial core mass estimates ([Kauffmann et al., 2013](#)).

We are also interested in conducting a statistical comparison of chemical composition for cores formed in quiescent environment (i.e. where gravity dominates) to those cores which are formed dynamically within colliding flows.

## 5 SUMMARY

The aim of this thesis has been to improve the understanding of physical and chemical processes influencing the observational techniques, which are used to infer the state of interstellar molecular gas. As tools, we used numerical experiments accounting for a range of relevant processes, from turbulent hydrodynamics to self-gravity and from radiation transport to molecular chemistry.

In chapter 2 we investigated the effects of selective photodissociation and chemical fractionation on the  $^{12}\text{CO}/^{13}\text{CO}$  ratio in self-consistently modelled, turbulent giant molecule clouds, which were irradiated by an external uniform radiation field. The direct determination of the isotope ratio is often not feasible from solely the millimetre wavelength emission, and thus a uniform isotope ratio is frequently adopted as a best guess. We aimed to improve this assumption or at the least to constrain the error introduced by its use.

We find a direct correlation between the  $^{12}\text{CO}$  column density and the isotope ratio. This is robust over moderate ranges of radiation field strengths and metallicities. The effect of the isotope selective photodissociation of  $^{13}\text{CO}$ , for the most part of the cloud can be neglected. The chemical fractionation reaction enhances the  $^{13}\text{CO}$  abundance, and thus reduces the isotope ratio. The reduction is upto a factor of 3 and it is the strongest on the  $10^{15} \text{ cm}^{-2} < N(^{12}\text{CO}) < 10^{17} \text{ cm}^{-2}$  column density range. Coincidentally this is the same range, where the CO column density can be measured with the largest confidence – as we showed in chapter 3 – and therefore accounting for the true isotope ratio is important. For this purpose we construct a fitting formula between the CO isotope column densities and the ratio.

We find the formula to be consistent with millimetre-wavelength  $^{12}\text{CO}/^{13}\text{CO}$  column density ratio measurements. While it underestimates the ratio measured in ultraviolet absorption by a factor of 2-3. The discrepancy is due to the qualitatively different cloud type (strong irradiation and/or weak attenuation) that UV absorption might trace and the clouds modelled here.

In chapter 3 we use the same set of simulations, extended with several realizations of a higher mass GMC, to test the validity of the most often used CO emission based  $\text{H}_2$  mass and column density measurement methods. These are the LTE measurement of the  $^{13}\text{CO}$  column density, the virial analysis and the CO emission-to- $\text{H}_2$  column density conversion factor (i.e.  $X_{\text{CO}}$  factor). The physical quantities, such as density, temperature, abundances from the simulations are translated to emission using the large velocity gradient approximation of radiative transfer. This is then analysed according the above mentioned techniques and the results are compared to the true values, known from the simulations.

We find that all methods provide mass estimates within a factor of 2 error over a large range of parameters, if the cloud's metallicity is not too low. The LTE column density measurement of  $^{13}\text{CO}$  traces the true CO column density distribution well within an intermediate column density range. However, it is a very bad indicator for the true  $\text{H}_2$  column density, due to the fact that the CO abundance compared to  $\text{H}_2$  changes drastically over the column density range. The virial mass, derived

from the cloud size and line width, proves to be the most reliable tracer of true mass in the simulations. This is partially not surprising, since the simulated clouds are close to virial equilibrium. On the other hand we also find that the CO line widths trace the underlying velocity dispersion well and that the assumption on the cloud's radial density profile is surprisingly close to the true value in each case. A constant, galactic  $X_{\text{CO}}$  factor provides a reasonable molecular mass estimate over a large range of parameters. This might be a result of the excitation temperature balancing the CO abundance (Liszt et al., 2010). And/or it might be a result of a bias, originating from the adoption of a CO brightness temperature limit (Bolatto et al., 2013). The  $X_{\text{CO}}$  factor based methods, which aim to correct for the metallicity dependence tend to overestimate the true molecules masses, if the metallicity is low.

Finally, in chapter 4, we considered core and clump scale structure instead of large scale molecular clouds, and introduced a post-processing technique for efficiently inferring abundances of high density tracers and organic molecules from hydrodynamical simulations. The procedure is as follows: first the hydrodynamic simulation is run with a limited chemical network. Then a domain of interest, such as a protostellar core, is selected from the simulation volume and the thermal, density and irradiation history of gas within the chosen structure is traced back. The chemical history in turn, is modelled using the physical information and a fully time-dependent code for chemical modelling, utilizing an extensive gas-grain chemical network.

The preliminary results show that the post-processing method works well, and it is able to reproduce the chemical composition modelled in the hydrodynamics simulation with a high precision. The method can be used to identify most important reactions for modelling a given species within dynamical conditions, to predict column densities and abundances of high density tracer or organic molecules and to find molecules, which might keep a record on their environmental history. Combined with a radiative transfer model, it can also provide emission maps and line profiles of species of interest.

## APPENDIX A

### THE REACTION RATES OF THE NL99 CHEMICAL NETWORK

Table A.1: Reactions in the NL99 chemical network, supplemented with the [Glover and Mac Low \(2007a\)](#) hydrogen network.

	<i>Reaction</i>	<i>Rate coefficient</i>
1	$\text{H}_2 + \text{CRP} \rightarrow \text{H}_2^+ + \text{e}^-$	$2 \times \zeta_{\text{H}} \text{s}^{-1}$
2	$\text{H}_2^+ + \text{H}_2 \rightarrow \text{H}_3^+ + \text{H}$	$2.24 \times 10^{-9} \left(-\frac{T_{\text{g}}}{300\text{K}}\right)^{-0.042} \times \exp\left(-\frac{4660\text{K}}{T_{\text{g}}}\right) \text{cm}^{-3}\text{s}^{-1}$
3	$\text{He} + \text{CRP} \rightarrow \text{He}^+ + \text{e}^-$	$1.09 \times \zeta_{\text{H}} \text{s}^{-1}$
4	$\text{C} + \text{H}_3^+ \rightarrow \text{CH}_x + \text{H}_2$	$2 \times 10^{-9} \text{cm}^{-3}\text{s}^{-1}$
5	$\text{O} + \text{H}_3^+ \rightarrow \text{OH}_x + \text{H}_2$	$8 \times 10^{-10} \text{cm}^{-3}\text{s}^{-1}$
6	$\text{CO} + \text{H}_3^+ \rightarrow \text{HCO}^+ + \text{H}_2$	$1.7 \times 10^{-9} \text{cm}^{-3}\text{s}^{-1}$
7	$\text{He}^+ + \text{H}_2 \rightarrow \text{He} + \text{H} + \text{H}^+$	$3.7 \times 10^{-14} \exp\left(-\frac{35\text{K}}{T_{\text{g}}}\right) \text{cm}^{-3}\text{s}^{-1}$
8	$\text{He}^+ + \text{CO} \rightarrow \text{C}^+ \text{O} + \text{He}$	$1.6 \times 10^{-9} \text{cm}^{-3}\text{s}^{-1}$
9	$\text{C}^+ + \text{H}_2 \rightarrow \text{CH}_x + \text{H}$	$4 \times 10^{-16} \text{cm}^{-3}\text{s}^{-1}$
10	$\text{C}^+ + \text{OH}_x \rightarrow \text{HCO}^+$	$1 \times 10^{-9} \text{cm}^{-3}\text{s}^{-1}$
11	$\text{O} + \text{CH}_x \rightarrow \text{CO} + \text{H}$	$2 \times 10^{-10} \text{cm}^{-3}\text{s}^{-1}$
12	$\text{C} + \text{OH}_x \rightarrow \text{CO} + \text{H}$	$5.8 \times 10^{-12} \left(-\frac{T_{\text{g}}}{300\text{K}}\right)^{0.5} \text{cm}^{-3}\text{s}^{-1}$
13	$\text{He}^+ + \text{e}^- \rightarrow \text{He} + h\nu$	$9 \times 10^{-11} \left(-\frac{T_{\text{g}}}{300\text{K}}\right)^{-0.64} \text{cm}^{-3}\text{s}^{-1}$
14	$\text{H}_3^+ + \text{e}^- \rightarrow \text{H}_2 + \text{H}$	$6.8 \times 10^{-8} \left(-\frac{T_{\text{g}}}{300\text{K}}\right)^{-0.52} \text{cm}^{-3}\text{s}^{-1}$
15	$\text{C}^+ + \text{e}^- \rightarrow \text{C} + h\nu$	$4.67 \times 10^{-12} \left(-\frac{T_{\text{g}}}{300\text{K}}\right)^{-0.61} \text{cm}^{-3}\text{s}^{-1}$
16	$\text{HCO}^+ + \text{e}^- \rightarrow \text{CO} + \text{H}$	$1.1 \times 10^{-7} \left(-\frac{T_{\text{g}}}{300\text{K}}\right)^{-1} \text{cm}^{-3}\text{s}^{-1}$
17	$\text{M}^+ + \text{e}^- \rightarrow \text{M} + h\nu$	$3.8 \times 10^{-10} \left(-\frac{T_{\text{g}}}{300\text{K}}\right)^{-0.65} \text{cm}^{-3}\text{s}^{-1}$
18	$\text{H}_3^+ + \text{M} \rightarrow \text{M}^+ + \text{H}_2 + \text{H}$	$2 \times 10^{-9} \text{cm}^{-3}\text{s}^{-1}$
19	$\text{C} + h\nu \rightarrow \text{C}^+ + \text{e}^-$	$1.77 \times 10^{-10} G \exp(-3 A_V) \text{s}^{-1}$
20	$\text{CH}_x + h\nu \rightarrow \text{C} + \text{H}$	$1 \times 10^{-9} G \exp(-1.5 A_V) \text{s}^{-1}$
21	$\text{CO} + h\nu \rightarrow \text{C} + \text{O}$	$2.6 \times 10^{-10} G \Theta_{\text{CO}} \exp(-3.53 A_V) \text{s}^{-1}$
22	$\text{OH}_x + h\nu \rightarrow \text{O} + \text{H}$	$5 \times 10^{-10} G \exp(-1.7 A_V) \text{s}^{-1}$
23	$\text{M} + h\nu \rightarrow \text{M}^+ + \text{e}^-$	$2 \times 10^{-10} G \exp(-1.9 A_V) \text{s}^{-1}$
24	$\text{HCO}^+ + h\nu \rightarrow \text{CO} + \text{H}^+$	$1.5 \times 10^{-9} G \exp(-2.5 A_V) \text{s}^{-1}$
<i>The Glover and Mac Low (2007a) hydrogen network</i>		
25	$\text{H} + \text{H} + \text{grain} \rightarrow \text{H}_2 + \text{grain}$	
26	$\text{H}_2 + \text{H} \rightarrow \text{H} + \text{H} + \text{H}$	
27	$\text{H}_2 + \text{H}_2 \rightarrow \text{H}_2 + \text{H} + \text{H}$	
28	$\text{H}_2 + h\nu \rightarrow \text{H} + \text{H}$	$3.3 \times 10^{-11} G \Theta_{\text{H}_2} \exp(-3.74 A_V)$
29	$\text{H} + \text{CRP} \rightarrow \text{H}^- + \text{e}^-$	$\zeta_{\text{H}}$
30	$\text{H} + \text{e}^- \rightarrow \text{H}^+ + \text{e}^- + \text{e}^-$	
31	$\text{H}^+ + \text{e}^- \rightarrow \text{H} + h\nu$	
32	$\text{H}^+ + \text{e}^- \text{grain} \rightarrow \text{H} + \text{grain}$	



## APPENDIX B

### ON THE GRIDDING OF SMOOTHED PARTICLE HYDRODYNAMIC SIMULATIONS

#### B.1 INTERPOLATION TO A REGULAR GRID

To interpret the results from our Lagrangian hydrodynamic simulations we interpolate the SPH particles to a regular grid. We construct a  $512^3$  grid centred on the geometrical midpoint of the uniform density sphere defined in the initial conditions. The sides of the grid are 16.2 pc long. The 2D-projected resolution of the grid is therefore  $0.032 \times 0.032$  pc<sup>2</sup>. This resolution is comparable to the current observationally achievable resolution for nearby star-forming regions in millimetre-wavelength CO line emission (e.g. 0.03 pc linear resolution for Taurus in [Pineda et al., 2010](#)). The interpolated quantities are the total volume density, the gas and dust temperatures, the velocity field and the H<sub>2</sub>, <sup>12</sup>CO and <sup>13</sup>CO number densities.

The density of a voxel (3D pixel) is accumulated from the contribution of SPH particles lying strictly within the voxel and from the contribution of those which have common section with it (i.e. particles with centre coordinates outside of the voxel could contribute). If  $r$  is the distance between the centres of the voxel and an SPH particle, the contribution is given by the smoothing kernel (eq. 1.9). The smoothing kernel has units of cm<sup>-3</sup>, and when multiplied with the particle mass gives the contribution of an SPH particle to the voxel density. In case of the other quantities the contribution is the SPH particle value multiplied by the ratio of the density contribution and the total density of the SPH particle.

The interpolation to a regular grid is necessary for the grid based radiation transfer modelling described in section 2.4. For consistency we also analyse the grid interpolated quantities in section 2.3.

#### B.2 GRID RESOLUTION TEST

By design the SPH based hydrodynamical simulations concentrate the highest spatial resolution where the gas is the densest. In GMC simulations, where multiple size scales are needed to be considered (from tens of parsec scales in dilute gas to the dense protostellar cores on the order of thousands of astronomical units in size), such feature is often required. The radiative transfer code, RADMC-3D, applied here, is however, designed to work on gridded input data (see B.1). By interpolating the variable spatial resolution SPH data to a fixed sized grid, we necessarily lose information on density, temperature and excitation conditions of the smallest and densest structures. Such structures, due to their high density and high gas phase CO abundance (in the absence of freeze-out), might add significant contribution to the total CO emission, specially if they are relatively warm. If our choice of

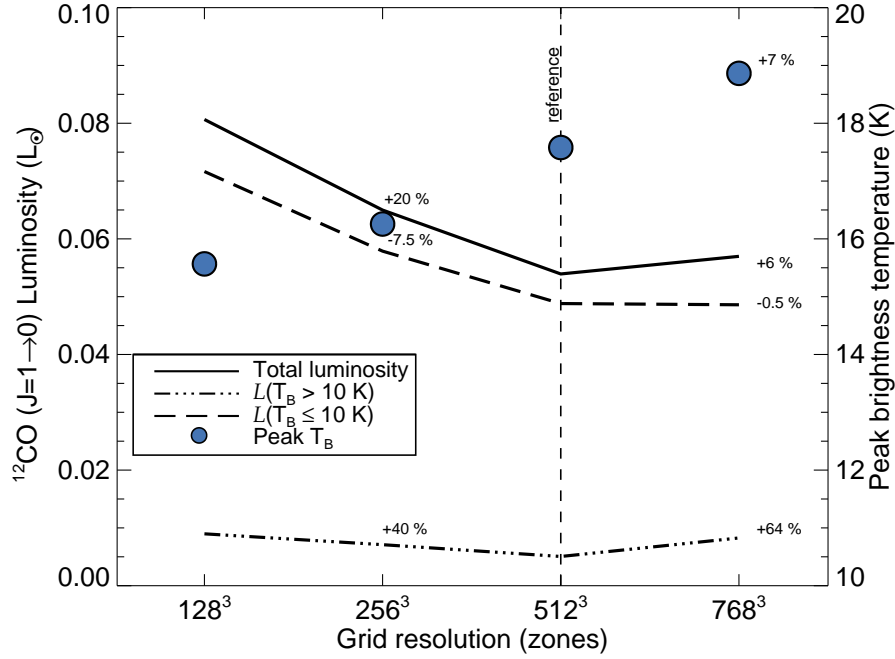


Figure B.1: The total luminosity (lines) and the peak brightness temperature (circle) of  $^{12}\text{CO}$  ( $J = 1 \rightarrow 0$ ) emission maps with increasing grid resolution. The solid line represents the total luminosity, while the dash-dotted and dashed lines the luminosity above 10 K and below 10 K, respectively. The numerical values of increase or decrease are compared to the reference resolution of  $512^3$  zones

grid spatial resolution is not high enough, then the radiative transfer models might underestimate the total and peak brightness of the GMCs.

To quantify how the grid resolution affects the emergent total and peak intensity of a GMC, we calculated the  $^{12}\text{CO}$  and  $^{13}\text{CO}$   $J = 1 \rightarrow 0$  emission of model d) with  $128^3$ ,  $256^3$ ,  $512^3$  and  $768^3$  zone resolutions. The highest resolution is set by the maximum amount of random access memory available in the workstation<sup>1</sup> used for this thesis.

The Figure B.1 show the total luminosity and the peak brightness temperatures of the  $^{12}\text{CO}$   $J = 1 \rightarrow 0$  transition, calculated for the aforementioned grid resolutions. The overall luminosity decreases by about a factor of 2 while going from the lowest resolution to  $512^3$  zones, while from  $512^3$  to  $768^3$  zones it slightly increases ( $\approx 6\%$ ). The reason for the former can be understood by examining the velocity integrated brightness temperature maps (Figure B.2). On one hand, the low resolution maps slightly underestimate the peak intensity in a matching feature compared to the high resolution. At the same time, they overestimate the area associated with intermediate brightness temperatures. The adopted interpolation scheme conserves the mass and uses a weighting by the SPH particle density. Due to self-gravity the dense structures are concentrated on small scales. These together result in an overestimated density in much of the volume of a pixel, if that pixel is much larger than the dense region within. Since quantities such as abundances and temperatures are weighted by density, these will be also overestimated too. This, overall leads to

<sup>1</sup>Reference configuration: 2× Intel(R) Xeon(R) CPU E5645 @ 2.40GHz (12 cores) with 94 GB RAM

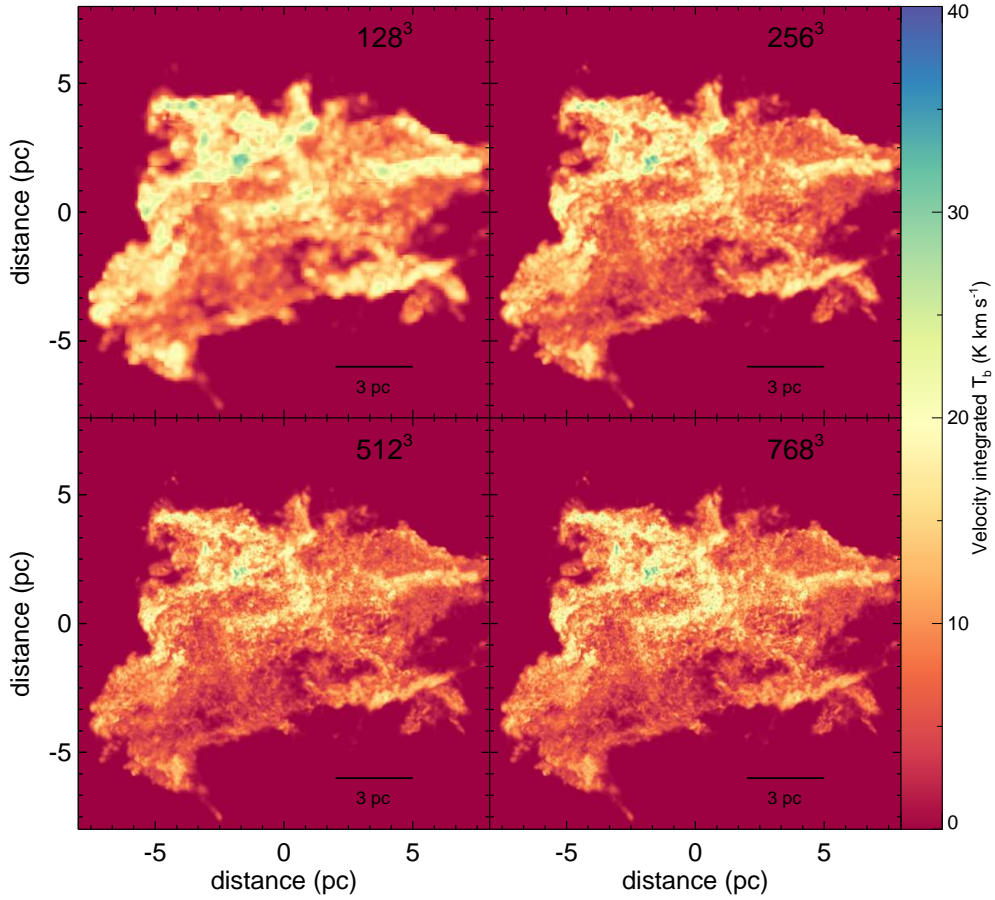


Figure B.2: The  $^{12}\text{CO}$  ( $J = 1 \rightarrow 0$ ) emission maps with increasing grid resolution, plotted with the same colour scale.

a larger emission flux from a low resolution pixel than from the equivalent volume in the higher resolution case. The latter effect is much stronger, resulting in an anticorrelating cloud luminosity with the resolution. The small increase at the highest resolution is due to the contribution of small, bright clumps, which are not yet fully resolved with  $512^3$  zones.

Going from  $128^3$  to  $256^3$  grid, the total luminosity changes by about 20%, while from  $256^3$  to  $512^3$ , the change is about 15%. The further increase of resolution causes about 6% change. Even though the convergence is not perfect, the typical error is expected to be below 10%, thus the  $512^3$  resolution is acceptable, specially if the factor of 8 increase in memory required is considered for a factor of 2 increase in linear pixel size.



## APPENDIX C

### THE EFFECT OF THE INITIAL CHEMICAL COMPOSITION

In most of the simulations presented in this paper, we adopted initial conditions in which we assumed that the hydrogen was fully molecular (i.e. all of it started in the form of  $\text{H}_2$  and none as atomic hydrogen). In reality, however, molecular clouds form from initially diffuse gas which is a mixture of ionized, neutral and molecular hydrogen. By assuming fully molecular initial conditions we overestimate the  $\text{H}_2$  column density and therefore the  $\text{H}_2$  self- and CO shielding. Self-consistent modelling of the initial chemical composition of clouds, as discussed in e.g. [Clark et al. \(2012b\)](#); [Smith et al. \(2014\)](#) is out of the scope of this paper, but we investigate the validity of our findings in the other extreme case, when fully atomic initial conditions, with all of the hydrogen in the form of  $\text{H}$ , are adopted. The simulation with atomic initial composition is model g). All other model parameters have the fiducial value (i.e. as in simulation d). Some of the characteristic quantities of model g) are indicated in Tables 2.2 to 2.5 for comparison.

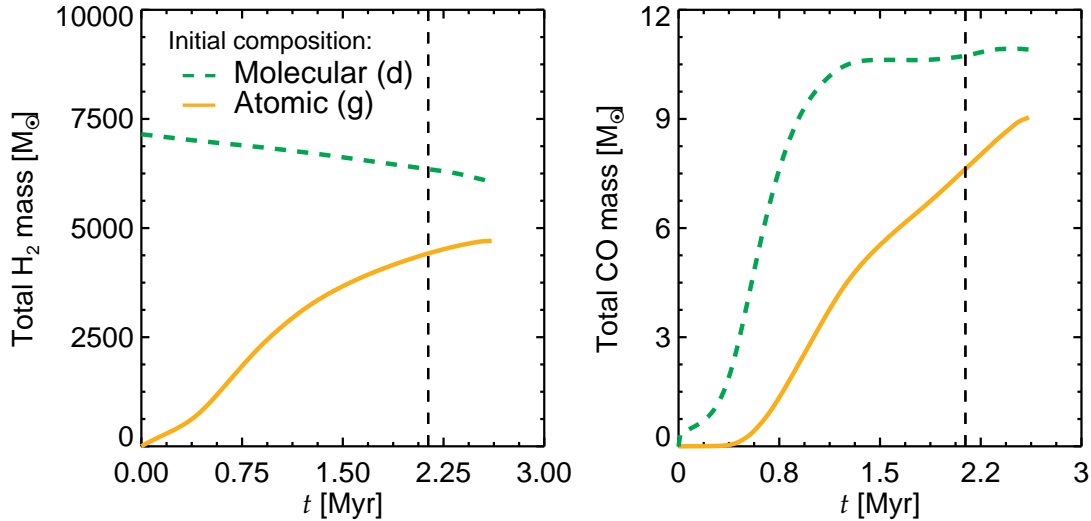


Figure C.1: Left panel: the total  $\text{H}_2$  mass of the cloud as a function of time. The total mass of the cloud is  $10^4 M_\odot$ . Right panel: the total CO mass as a function of time. In the fully molecular case the final mass is higher and the formation is faster than in the atomic case. Both simulations are analysed at 2.150 Myrs, the time marked by the vertical dashed line.

The chemical composition of models d) and g) show a very different evolution. The  $\text{H}_2$  mass content (Fig. C.1) in d) (dashed line) slightly decreases with time due to  $\text{H}_2$  photodissociation and a relatively long  $\text{H}_2$  formation time scale. In the case of g) (solid line) the  $\text{H}_2$  mass gradually increases with time and reaches  $\sim 4800 M_\odot$  ( $\sim 70$  per cent of the initial  $\text{H}_2$  mass in d) by the end of the simulation. The CO

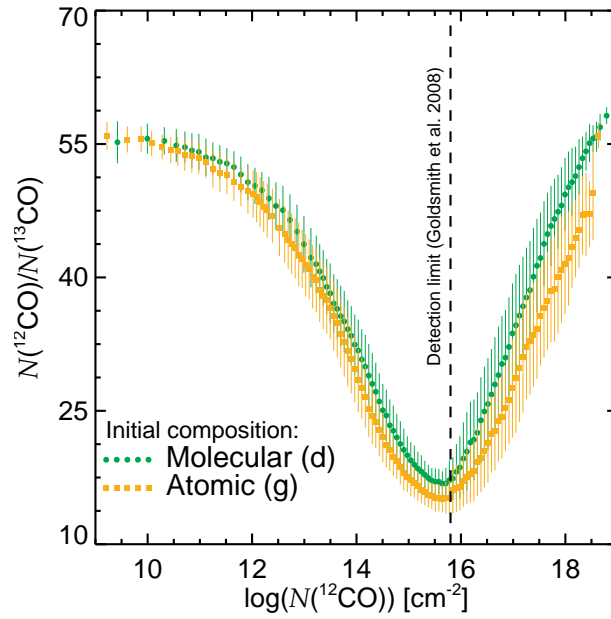


Figure C.2: The isotopic ratio as a function of  $^{12}\text{CO}$  column density in the case of molecular and atomic initial compositions.

mass evolution shows similar trends, but in g) it is significantly delayed and the equilibrium CO mass is not reached by the end of the simulation.

Regardless of the lower  $\text{H}_2$  mass and delayed CO formation, the CO isotope ratio - column density relation hold in case of atomic initial conditions (Fig. C.2). The distributions overlap at low column densities, and model g) produces slightly lower isotope ratios at high CO column density. The behaviour of the  $^{12}\text{CO}/^{13}\text{CO}$  ratio in case of d) and g) could be understood as follows. In the simulation with fully atomic initial conditions, there is less shielding of CO by  $\text{H}_2$ , owing to the lower molecular content of the cloud, and hence the CO formation threshold shifts to slightly higher densities and extinctions. Lines of sight with column densities  $10^{16} < N(^{12}\text{CO}) < 10^{18} \text{ cm}^{-2}$  therefore probe denser regions of the cloud with higher dust extinctions in model g) than in model d). This gas tends to be colder, meaning that the the effect of chemical fractionation is more pronounced, leading to a lower  $^{12}\text{CO}/^{13}\text{CO}$  ratio.

## APPENDIX D

### DENDROGRAMS

Dendrograms are suitable tools for visualizing and analysing the hierarchical structure of emission maps (Houlahan and Scalo, 1992; Rosolowsky et al., 2008; Beaumont et al., 2013). The dendrogram tree is characterized by leaves, branches and the trunk. The leaf is on the top of the hierarchy and it is defined by an intensity contours and area that incorporates exactly one local maximum. The size of this area is a free parameter and it defines the level of details in the tree. Here, the area is set to  $7 \times 7$  pixels. The next level in the hierarchy is represented by the branch. The branch connects two leaves or two branches or one leaf and one branch and it is defined by the highest common intensity level between the connected entities. This intensity is called the “merger” level. Below the merger level, the branch represents the union of contours, associated with the features it connects. The trunk is the lowest level element of the tree, it is similar to a branch, but it is not connected to any lower contour feature. See figure D.1 for the graphical representation. The  $y$  axis of the tree representation shows the intensity or contour levels (e.g. in  $\text{K km s}^{-1}$ ), while the  $x$  axis usually does not indicate any location information, rather, the leaves and branches are ordered horizontally to avoid crossing between vertical lines.

The noise in the observed data might lead features, that the algorithm might identify falsely as leaves. To remove these artefacts, several criteria are imposed on the leaves, in a procedure called “pruning”. The local maxima below a given threshold value (here  $0.6 \text{K km s}^{-1}$  for the  $^{12}\text{CO}$  emission maps) are rejected. Neighbouring leaves are merged, if the contour difference between the highest intensity of the two and their merger level is smaller than  $3 \text{K km s}^{-1}$ . In principle, leaves are also rejected if the contour associated with them do not encompass at least a minimum number of the pixels. We set this number to 10, which is effectively means no rejection based on this criteria in our case (i.e. it is a smaller number of pixels than those required at the local maxima identification).

The dendrogram tree is a useful tool to identify and analyse coherent structures or clusters of structures in the emission maps. The structures then can be marked in the original dataset, and physical quantities, such as the size or the virial parameter can be calculated.

Dendrograms are also helpful when different, but still linked quantities are compared. As an example, Beaumont et al. (2013) compares structures in the three-dimensional density distributions, resulting from numerical simulations, to features in the PPV emission cubes, that are computed from the same simulations. After converting the position-position-position density distribution to position-position-velocity space, they build the dendrogram tree for both the density and intensity distribution. The overlap between every density feature and intensity feature is then calculated and the most features with the highest degree of overlap are identified with each other.

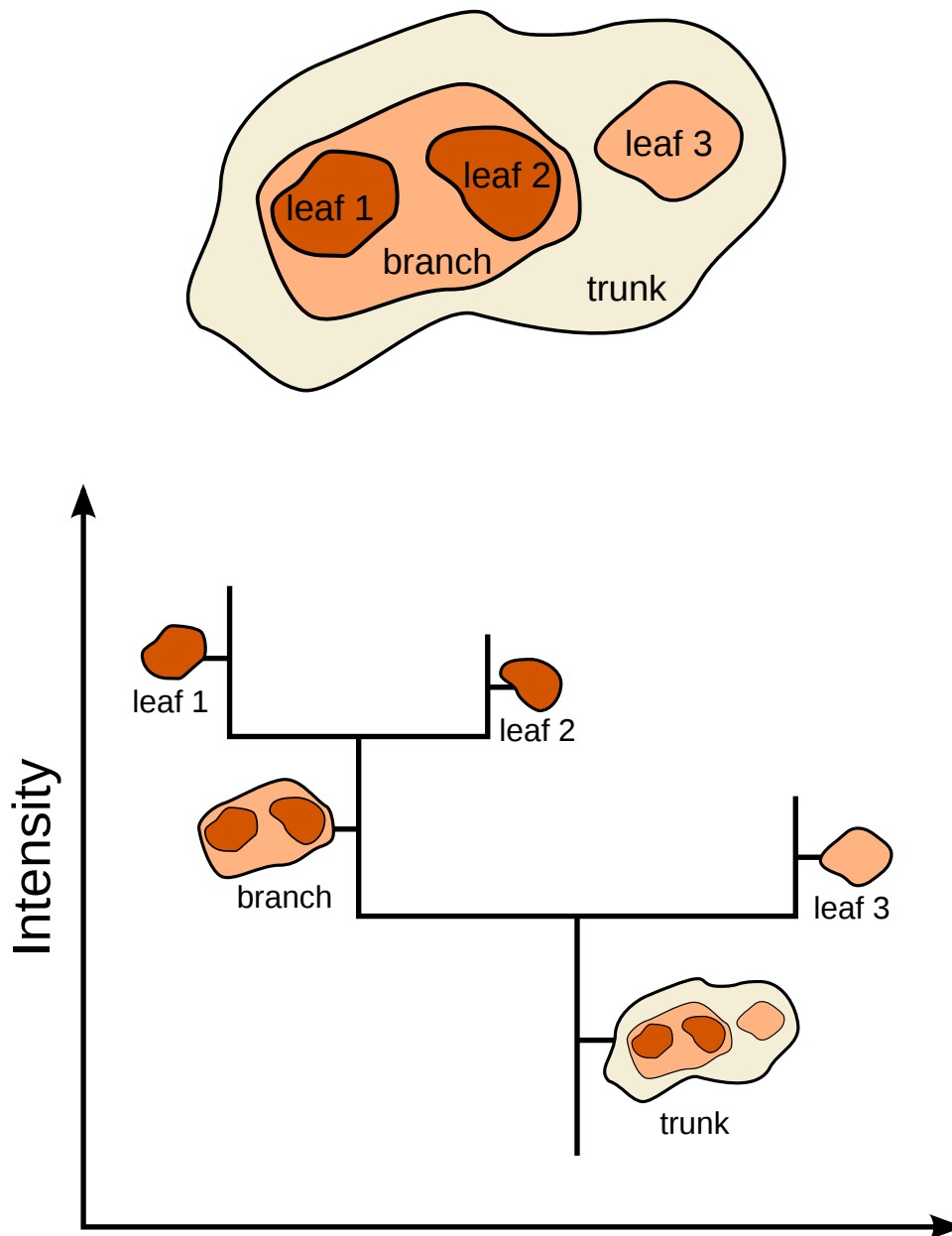


Figure D.1: The basic concept of the dendrogram tree construction in two-dimensions. The upper figure show an emission emission feature with hierarchical structure, while the lower plot shows its tree representation. The figures are adapted from Chris Beaumont.

## BIBLIOGRAPHY

- Albertsson, T., Semenov, D. A., Vasyunin, A. I., Henning, T., and Herbst, E. (2013). New Extended Deuterium Fractionation Model: Assessment at Dense ISM Conditions and Sensitivity Analysis. *ApJS*, 207:27.
- Armitage, P. J. (2010). *Astrophysics of Planet Formation*.
- Audouze, J., Lequeux, J., and Vigroux, L. (1975). Isotopes of carbon, nitrogen and oxygen as probes of nucleosynthesis, stellar mass losses and galactic evolution. *A&A*, 43:71–83.
- Bacmann, A., Lefloch, B., Ceccarelli, C., Castets, A., Steinacker, J., and Loinard, L. (2002). The degree of CO depletion in pre-stellar cores. *A&A*, 389:L6–L10.
- Bakes, E. L. O. and Tielens, A. G. G. M. (1994). The photoelectric heating mechanism for very small graphitic grains and polycyclic aromatic hydrocarbons. *ApJ*, 427:822–838.
- Balsara, D. S. (1995). von Neumann stability analysis of smooth particle hydrodynamics—suggestions for optimal algorithms. *Journal of Computational Physics*, 121:357–372.
- Barnes, J. and Hut, P. (1986). A hierarchical  $O(N \log N)$  force-calculation algorithm. *Nature*, 324:446–449.
- Bate, M. R., Bonnell, I. A., and Price, N. M. (1995). Modelling accretion in protobinary systems. *MNRAS*, 277:362–376.
- Bates, D. R. (1951). Rate of formation of molecules by radiative association. *MNRAS*, 111:303.
- Beaumont, C. N., Offner, S. S. R., Shetty, R., Glover, S. C. O., and Goodman, A. A. (2013). Quantifying Observational Projection Effects Using Molecular Cloud Simulations. *ApJ*, 777:173.
- Bergin, E. A., Alves, J., Huard, T., and Lada, C. J. (2002).  $N_2H^+$  and  $C^{18}O$  Depletion in a Cold Dark Cloud. *ApJ*, 570:L101–L104.
- Bergin, E. A., Hartmann, L. W., Raymond, J. C., and Ballesteros-Paredes, J. (2004). Molecular Cloud Formation behind Shock Waves. *ApJ*, 612:921–939.
- Bergin, E. A. and Tafalla, M. (2007). Cold Dark Clouds: The Initial Conditions for Star Formation. *ARA&A*, 45:339–396.
- Beuther, H., Zhang, Q., Bergin, E. A., and Sridharan, T. K. (2009). Chemical Diversity in High-Mass Star Formation. *AJ*, 137:406–418.

- Bigiel, F., Leroy, A., Walter, F., Brinks, E., de Blok, W. J. G., Madore, B., and Thornley, M. D. (2008). The Star Formation Law in Nearby Galaxies on Sub-Kpc Scales. *AJ*, 136:2846–2871.
- Black, J. H. (1994). Energy Budgets of Diffuse Clouds. In Cutri, R. M. and Latter, W. B., editors, *The First Symposium on the Infrared Cirrus and Diffuse Interstellar Clouds*, volume 58 of *Astronomical Society of the Pacific Conference Series*, page 355.
- Blitz, L., Fukui, Y., Kawamura, A., Leroy, A., Mizuno, N., and Rosolowsky, E. (2007). Giant Molecular Clouds in Local Group Galaxies. *Protostars and Planets V*, pages 81–96.
- Bohlin, R. C., Savage, B. D., and Drake, J. F. (1978). A survey of interstellar H I from L-alpha absorption measurements. II. *ApJ*, 224:132–142.
- Bolatto, A. D., Leroy, A. K., Jameson, K., Ostriker, E., Gordon, K., Lawton, B., Stanimirović, S., Israel, F. P., Madden, S. C., Hony, S., Sandstrom, K. M., Bot, C., Rubio, M., Winkler, P. F., Roman-Duval, J., van Loon, J. T., Oliveira, J. M., and Indebetouw, R. (2011). The State of the Gas and the Relation between Gas and Star Formation at Low Metallicity: The Small Magellanic Cloud. *ApJ*, 741:12.
- Bolatto, A. D., Wolfire, M., and Leroy, A. K. (2013). The CO-to-H<sub>2</sub> Conversion Factor. *ARA&A*, 51:207–268.
- Bourke, T. L., Myers, P. C., Robinson, G., and Hyland, A. R. (2001). New OH Zeeman Measurements of Magnetic Field Strengths in Molecular Clouds. *ApJ*, 554:916–932.
- Brunt, C. M. (2010). The density variance - Mach number relation in the Taurus molecular cloud. *A&A*, 513:A67.
- Burgh, E. B., France, K., and McCandliss, S. R. (2007). Direct Measurement of the Ratio of Carbon Monoxide to Molecular Hydrogen in the Diffuse Interstellar Medium. *ApJ*, 658:446–454.
- Burkhart, B. and Lazarian, A. (2012). The Column Density Variance- $\langle \Sigma_{\text{cal M}} \rangle_s$  Relationship. *ApJ*, 755:L19.
- Cami, J., Bernard-Salas, J., Peeters, E., and Malek, S. E. (2010). Detection of C<sub>60</sub> and C<sub>70</sub> in a Young Planetary Nebula. *Science*, 329:1180–.
- Carlhoff, P., Nguyen Luong, Q., Schilke, P., Motte, F., Schneider, N., Beuther, H., Bontemps, S., Heitsch, F., Hill, T., Kramer, C., Ossenkopf, V., Schuller, F., Simon, R., and Wyrowski, F. (2013). Large scale IRAM 30 m CO-observations in the giant molecular cloud complex W43. *A&A*, 560:A24.
- Carroll, B. and Ostlie, D. (2007). *An Introduction to Modern Astrophysics*. Pearson Addison-Wesley.
- Carruthers, G. R. (1970). Rocket Observation of Interstellar Molecular Hydrogen. *ApJ*, 161:L81.
- Caselli, P., Hasegawa, T. I., and Herbst, E. (1998). A Proposed Modification of the Rate Equations for Reactions on Grain Surfaces. *ApJ*, 495:309–316.

- Caselli, P., Walmsley, C. M., Tafalla, M., Dore, L., and Myers, P. C. (1999). CO Depletion in the Starless Cloud Core L1544. *ApJ*, 523:L165–L169.
- Clark, P. C., Glover, S. C. O., and Klessen, R. S. (2012a). TreeCol: a novel approach to estimating column densities in astrophysical simulations. *MNRAS*, 420:745–756.
- Clark, P. C., Glover, S. C. O., Klessen, R. S., and Bonnell, I. A. (2012b). How long does it take to form a molecular cloud? *MNRAS*, 424:2599–2613.
- Clark, P. C., Glover, S. C. O., Klessen, R. S., and Bromm, V. (2011). Gravitational Fragmentation in Turbulent Primordial Gas and the Initial Mass Function of Population III Stars. *ApJ*, 727:110.
- Cleeves, L. I., Bergin, E. A., Alexander, C. M. O. O., Du, F., Graninger, D., Öberg, K. I., and Harries, T. J. (2014). The ancient heritage of water ice in the solar system. *Science*, 345:1590–1593.
- Colín, P., Vázquez-Semadeni, E., and Gómez, G. C. (2013). Molecular cloud evolution - V. Cloud destruction by stellar feedback. *MNRAS*, 435:1701–1714.
- Colombo, D., Hughes, A., Schinnerer, E., Meidt, S. E., Leroy, A. K., Pety, J., Dobbs, C. L., García-Burillo, S., Dumas, G., Thompson, T. A., Schuster, K. F., and Kramer, C. (2014). The PdBI Arcsecond Whirlpool Survey (PAWS): Environmental Dependence of Giant Molecular Cloud Properties in M51. *ApJ*, 784:3.
- Crutcher, R. M. (1999). Magnetic Fields in Molecular Clouds: Observations Confront Theory. *ApJ*, 520:706–713.
- Dale, J. E., Ercolano, B., and Bonnell, I. A. (2012). Ionizing feedback from massive stars in massive clusters - II. Disruption of bound clusters by photoionization. *MNRAS*, 424:377–392.
- Dale, J. E., Ngoumou, J., Ercolano, B., and Bonnell, I. A. (2014). Before the first supernova: combined effects of H II regions and winds on molecular clouds. *MNRAS*, 442:694–712.
- Dame, T. M., Hartmann, D., and Thaddeus, P. (2001). The Milky Way in Molecular Clouds: A New Complete CO Survey. *ApJ*, 547:792–813.
- Dickey, J. M. and Lockman, F. J. (1990). H I in the Galaxy. *ARA&A*, 28:215–261.
- Dickman, R. L. (1978). The ratio of carbon monoxide to molecular hydrogen in interstellar dark clouds. *ApJS*, 37:407–427.
- Dobbs, C. L., Bonnell, I. A., and Pringle, J. E. (2006). The formation of molecular clouds in spiral galaxies. *MNRAS*, 371:1663–1674.
- Dobbs, C. L., Krumholz, M. R., Ballesteros-Paredes, J., Bolatto, A. D., Fukui, Y., Heyer, M., Mac Low, M.-M., Ostriker, E. C., and Vázquez-Semadeni, E. (2013). Formation of Molecular Clouds and Global Conditions for Star Formation. *ArXiv e-prints*.
- Draine, B. T. (1978). Photoelectric heating of interstellar gas. *ApJS*, 36:595–619.

- Draine, B. T. and Bertoldi, F. (1996). Structure of Stationary Photodissociation Fronts. *ApJ*, 468:269.
- Draine, B. T., Dale, D. A., Bendo, G., Gordon, K. D., Smith, J. D. T., Armus, L., Engelbracht, C. W., Helou, G., Kennicutt, Jr., R. C., Li, A., Roussel, H., Walter, F., Calzetti, D., Moustakas, J., Murphy, E. J., Rieke, G. H., Bot, C., Hollenbach, D. J., Sheth, K., and Teplitz, H. I. (2007). Dust Masses, PAH Abundances, and Starlight Intensities in the SINGS Galaxy Sample. *ApJ*, 663:866–894.
- Dullemond, C. P. (2012). RADMC-3D: A multi-purpose radiative transfer tool. *Astrophysics Source Code Library*.
- Dullemond, C. P., Hollenbach, D., Kamp, I., and D’Alessio, P. (2007). Models of the Structure and Evolution of Protoplanetary Disks. *Protostars and Planets V*, pages 555–572.
- Evans, II, N. J., Dunham, M. M., Jørgensen, J. K., Enoch, M. L., Merín, B., van Dishoeck, E. F., Alcalá, J. M., Myers, P. C., Stapelfeldt, K. R., Huard, T. L., Allen, L. E., Harvey, P. M., van Kempen, T., Blake, G. A., Koerner, D. W., Mundy, L. G., Padgett, D. L., and Sargent, A. I. (2009). The Spitzer c2d Legacy Results: Star-Formation Rates and Efficiencies; Evolution and Lifetimes. *ApJS*, 181:321–350.
- Federrath, C., Banerjee, R., Clark, P. C., and Klessen, R. S. (2010). Modeling Collapse and Accretion in Turbulent Gas Clouds: Implementation and Comparison of Sink Particles in AMR and SPH. *ApJ*, 713:269–290.
- Feldmann, R., Gnedin, N. Y., and Kravtsov, A. V. (2012). The X-factor in Galaxies. I. Dependence on Environment and Scale. *ApJ*, 747:124.
- Feng, S., Beuther, H., Semenov, D., Henning, T., and Palau, A. (2013). Resolving the Chemical Substructure of Orion-KL. In *Protostars and Planets VI Posters*, page 19.
- Gammie, C. F. (1996). Layered Accretion in T Tauri Disks. *ApJ*, 457:355.
- Garrod, R. T. and Herbst, E. (2006). Formation of methyl formate and other organic species in the warm-up phase of hot molecular cores. *A&A*, 457:927–936.
- Geiss, J. (1988). Composition in Halley’s Comet: Clues to Origin and History of Cometary Matter. In Klare, G., editor, *Reviews in Modern Astronomy*, volume 1 of *Reviews in Modern Astronomy*, pages 1–27.
- Gerner, T., Beuther, H., Semenov, D., Linz, H., Vasyunina, T., Bühr, S., Shirley, Y. L., and Henning, T. (2014). Chemical evolution in the early phases of massive star formation. I. *A&A*, 563:A97.
- Glover, S. C. O. and Clark, P. C. (2012a). Approximations for modelling CO chemistry in giant molecular clouds: a comparison of approaches. *MNRAS*, 421:116–131.
- Glover, S. C. O. and Clark, P. C. (2012b). Is molecular gas necessary for star formation? *MNRAS*, 421:9–19.
- Glover, S. C. O. and Clark, P. C. (2012c). Star formation in metal-poor gas clouds. *MNRAS*, 426:377–388.

- Glover, S. C. O., Federrath, C., Mac Low, M.-M., and Klessen, R. S. (2010). Modelling CO formation in the turbulent interstellar medium. *MNRAS*, 404:2–29.
- Glover, S. C. O. and Mac Low, M.-M. (2007a). Simulating the Formation of Molecular Clouds. I. Slow Formation by Gravitational Collapse from Static Initial Conditions. *ApJS*, 169:239–268.
- Glover, S. C. O. and Mac Low, M.-M. (2007b). Simulating the Formation of Molecular Clouds. II. Rapid Formation from Turbulent Initial Conditions. *ApJ*, 659:1317–1337.
- Glover, S. C. O. and Mac Low, M.-M. (2011). On the relationship between molecular hydrogen and carbon monoxide abundances in molecular clouds. *MNRAS*, 412:337–350.
- Godard, B., Falgarone, E., and Pineau Des Forêts, G. (2009). Models of turbulent dissipation regions in the diffuse interstellar medium. *A&A*, 495:847–867.
- Goldsmith, P. F., Heyer, M., Narayanan, G., Snell, R., Li, D., and Brunt, C. (2008). Large-Scale Structure of the Molecular Gas in Taurus Revealed by High Linear Dynamic Range Spectral Line Mapping. *ApJ*, 680:428–445.
- Górski, K. M., Hivon, E., Banday, A. J., Wandelt, B. D., Hansen, F. K., Reinecke, M., and Bartelmann, M. (2005). HEALPix: A Framework for High-Resolution Discretization and Fast Analysis of Data Distributed on the Sphere. *ApJ*, 622:759–771.
- Goto, M., Usuda, T., Takato, N., Hayashi, M., Sakamoto, S., Gaessler, W., Hayano, Y., Iye, M., Kamata, Y., Kanzawa, T., Kobayashi, N., Minowa, Y., Nedachi, K., Oya, S., Pyo, T.-S., Saint-Jacques, D., Suto, H., Takami, H., Terada, H., and Mitchell, G. F. (2003). Carbon Isotope Ratio in  $^{12}\text{CO}/^{13}\text{CO}$  toward Local Molecular Clouds with Near-Infrared High-Resolution Spectroscopy of Vibrational Transition Bands. *ApJ*, 598:1038–1047.
- Gredel, R., Lepp, S., and Dalgarno, A. (1987). The C/CO ratio in dense interstellar clouds. *ApJ*, 323:L137–L139.
- Habing, H. J. (1968). The interstellar radiation density between 912 Å and 2400 Å. *Bull. Astron. Inst. Netherlands*, 19:421.
- Harada, N., Herbst, E., and Wakelam, V. (2010). A New Network for Higher-temperature Gas-phase Chemistry. I. A Preliminary Study of Accretion Disks in Active Galactic Nuclei. *ApJ*, 721:1570–1578.
- Hartmann, L., Ballesteros-Paredes, J., and Bergin, E. A. (2001). Rapid Formation of Molecular Clouds and Stars in the Solar Neighborhood. *ApJ*, 562:852–868.
- Hartmann, L., Ballesteros-Paredes, J., and Heitsch, F. (2012). Rapid star formation and global gravitational collapse. *MNRAS*, 420:1457–1461.
- Hartquist, T. W., Rawlings, J. M. C., Williams, D. A., and Dalgarno, A. (1993). The Regulatory and Diagnostic Roles of Chemistry in Low-Mass Star Formation. *QJRAS*, 34:213.

- Hasegawa, T. I., Herbst, E., and Leung, C. M. (1992). Models of gas-grain chemistry in dense interstellar clouds with complex organic molecules. *ApJS*, 82:167–195.
- Hennebelle, P. and Pérault, M. (2000). Dynamical condensation in a magnetized and thermally bistable flow. Application to interstellar cirrus. *A&A*, 359:1124–1138.
- Herbst, E. (1993). *Gas-Grain Chemistry in Quiescent Dense Interstellar Clouds*, page 183.
- Herbst, E. and Klemperer, W. (1973). The Formation and Depletion of Molecules in Dense Interstellar Clouds. *ApJ*, 185:505–534.
- Heyer, M. H. and Brunt, C. M. (2004). The Universality of Turbulence in Galactic Molecular Clouds. *ApJ*, 615:L45–L48.
- Hockney, R. W. and Eastwood, J. W. (1988). *Computer simulation using particles*.
- Hollenbach, D. and McKee, C. F. (1979). Molecule formation and infrared emission in fast interstellar shocks. I Physical processes. *ApJS*, 41:555–592.
- Hollenbach, D. and Salpeter, E. E. (1971). Surface Recombination of Hydrogen Molecules. *ApJ*, 163:155.
- Houllahan, P. and Scalo, J. (1992). Recognition and characterization of hierarchical interstellar structure. II - Structure tree statistics. *ApJ*, 393:172–187.
- Hughes, A., Wong, T., Ott, J., Muller, E., Pineda, J. L., Mizuno, Y., Bernard, J.-P., Paradis, D., Maddison, S., Reach, W. T., Staveley-Smith, L., Kawamura, A., Meixner, M., Kim, S., Onishi, T., Mizuno, N., and Fukui, Y. (2010). Physical properties of giant molecular clouds in the Large Magellanic Cloud. *MNRAS*, 406:2065–2086.
- Jappsen, A.-K., Klessen, R. S., Larson, R. B., Li, Y., and Mac Low, M.-M. (2005). The stellar mass spectrum from non-isothermal gravoturbulent fragmentation. *A&A*, 435:611–623.
- Jura, M. (1975). Interstellar clouds containing optically thin H<sub>2</sub>. *ApJ*, 197:575–580.
- Kauffmann, J., Pillai, T., and Goldsmith, P. F. (2013). Low Virial Parameters in Molecular Clouds: Implications for High-mass Star Formation and Magnetic Fields. *ApJ*, 779:185.
- Kawamura, A., Mizuno, Y., Minamidani, T., Filipović, M. D., Staveley-Smith, L., Kim, S., Mizuno, N., Onishi, T., Mizuno, A., and Fukui, Y. (2009). The Second Survey of the Molecular Clouds in the Large Magellanic Cloud by NANTEN. II. Star Formation. *ApJS*, 184:1–17.
- Kennicutt, R. C. and Evans, N. J. (2012). Star Formation in the Milky Way and Nearby Galaxies. *ARA&A*, 50:531–608.
- Kennicutt, Jr., R. C. (1989). The star formation law in galactic disks. *ApJ*, 344:685–703.
- Kennicutt, Jr., R. C. (1998). The Global Schmidt Law in Star-forming Galaxies. *ApJ*, 498:541–552.

- Koda, J., Scoville, N., Sawada, T., La Vigne, M. A., Vogel, S. N., Potts, A. E., Carpenter, J. M., Corder, S. A., Wright, M. C. H., White, S. M., Zauderer, B. A., Patience, J., Sargent, A. I., Bock, D. C. J., Hawkins, D., Hodges, M., Kembell, A., Lamb, J. W., Plambeck, R. L., Pound, M. W., Scott, S. L., Teuben, P., and Woody, D. P. (2009). Dynamically Driven Evolution of the Interstellar Medium in M51. *ApJ*, 700:L132–L136.
- Krumholz, M. R., Leroy, A. K., and McKee, C. F. (2011). Which Phase of the Interstellar Medium Correlates with the Star Formation Rate? *ApJ*, 731:25.
- Langer, W. D. and Penzias, A. A. (1990). C-12/C-13 isotope ratio across the Galaxy from observations of C-13/O-18 in molecular clouds. *ApJ*, 357:477–492.
- Larson, R. B. (1981). Turbulence and star formation in molecular clouds. *MNRAS*, 194:809–826.
- Le Petit, F., Nehmé, C., Le Bourlot, J., and Roueff, E. (2006). A Model for Atomic and Molecular Interstellar Gas: The Meudon PDR Code. *ApJS*, 164:506–529.
- Lee, H.-H., Herbst, E., Pineau des Forets, G., Roueff, E., and Le Bourlot, J. (1996). Photodissociation of H<sub>2</sub> and CO and time dependent chemistry in inhomogeneous interstellar clouds. *A&A*, 311:690–707.
- Lee, H.-H., Roueff, E., Pineau des Forets, G., Shalabiea, O. M., Terzieva, R., and Herbst, E. (1998). Bistability in large chemical networks: a global view. *A&A*, 334:1047–1055.
- Lee, M.-Y., Stanimirović, S., Wolfire, M. G., Shetty, R., Glover, S. C. O., Molina, F. Z., and Klessen, R. S. (2014). The CO-to-H<sub>2</sub> Conversion Factor across the Perseus Molecular Cloud. *ApJ*, 784:80.
- Leung, C. M., Herbst, E., and Huebner, W. F. (1984). Synthesis of complex molecules in dense interstellar clouds via gas-phase chemistry - A pseudo time-dependent calculation. *ApJS*, 56:231–256.
- Lippok, N., Launhardt, R., Semenov, D., Stutz, A. M., Balog, Z., Henning, T., Krause, O., Linz, H., Nielbock, M., Pavlyuchenkov, Y. N., Schmalzl, M., Schmiedeke, A., and Bieging, J. H. (2013). Gas-phase CO depletion and N<sub>2</sub>H<sup>+</sup> abundances in starless cores. *A&A*, 560:A41.
- Liszt, H. S. (2007). Formation, fractionation, and excitation of carbon monoxide in diffuse clouds. *A&A*, 476:291–300.
- Liszt, H. S. and Lucas, R. (1998). CO in absorption and emission toward compact extragalactic radio continuum sources. *A&A*, 339:561–574.
- Liszt, H. S., Pety, J., and Lucas, R. (2010). The CO luminosity and CO-H<sub>2</sub> conversion factor of diffuse ISM: does CO emission trace dense molecular gas? *A&A*, 518:A45.
- Lucas, R. and Liszt, H. (1998). Interstellar isotope ratios from mm-wave molecular absorption spectra. *A&A*, 337:246–252.

- Lucy, L. B. (1977). A numerical approach to the testing of the fission hypothesis. *AJ*, 82:1013–1024.
- Mac Low, M.-M. and Klessen, R. S. (2004). Control of star formation by supersonic turbulence. *Reviews of Modern Physics*, 76:125–194.
- Mac Low, M.-M., Klessen, R. S., Burkert, A., and Smith, M. D. (1998). Kinetic Energy Decay Rates of Supersonic and Super-Alfvénic Turbulence in Star-Forming Clouds. *Physical Review Letters*, 80:2754–2757.
- MacLaren, I., Richardson, K. M., and Wolfendale, A. W. (1988). Corrections to virial estimates of molecular cloud masses. *ApJ*, 333:821–825.
- Maloney, P. R., Hollenbach, D. J., and Tielens, A. G. G. M. (1996). X-Ray-irradiated Molecular Gas. I. Physical Processes and General Results. *ApJ*, 466:561.
- McElroy, D., Walsh, C., Markwick, A. J., Cordiner, M. A., Smith, K., and Millar, T. J. (2013). The UMIST database for astrochemistry 2012. *A&A*, 550:A36.
- Mihalas, D., Auer, L. H., and Mihalas, B. R. (1978). Two-dimensional radiative transfer. I - Planar geometry. *ApJ*, 220:1001–1023.
- Mitchell, G. F. and Maillard, J.-P. (1993). The C-12/C-13 abundance ratio in NGC 2264. *ApJ*, 404:L79–L82.
- Miura, R. E., Kohno, K., Tosaki, T., Espada, D., Hwang, N., Kuno, N., Okumura, S. K., Hirota, A., Muraoka, K., Onodera, S., Minamidani, T., Komugi, S., Nakanishi, K., Sawada, T., Kaneko, H., and Kawabe, R. (2012). Giant Molecular Cloud Evolutions in the Nearby Spiral Galaxy M33. *ApJ*, 761:37.
- Mokrane, H., Chaabouni, H., Accolla, M., Congiu, E., Dulieu, F., Chehrouri, M., and Lemaire, J. L. (2009). Experimental Evidence for Water Formation Via Ozone Hydrogenation on Dust Grains at 10 K. *ApJ*, 705:L195–L198.
- Molina, F. (2013). Statistical analysis of simulated molecular clouds. *PhD Thesis, submitted to the Heidelberg University*.
- Monaghan, J. J. (1992). Smoothed particle hydrodynamics. *ARA&A*, 30:543–574.
- Monaghan, J. J. and Gingold, R. A. (1983). Shock simulation by the particle method SPH. *j-J-COMPUT-PHYS*, 52(2):374–389.
- Nelson, R. P. and Langer, W. D. (1997). The Dynamics of Low-Mass Molecular Clouds in External Radiation Fields. *ApJ*, 482:796–826.
- Nelson, R. P. and Langer, W. D. (1999). On the Stability and Evolution of Isolated BOK Globules. *ApJ*, 524:923–946.
- Neufeld, D. A. and Kaufman, M. J. (1993). Radiative Cooling of Warm Molecular Gas. *ApJ*, 418:263.
- Neufeld, D. A., Lepp, S., and Melnick, G. J. (1995). Thermal Balance in Dense Molecular Clouds: Radiative Cooling Rates and Emission-Line Luminosities. *ApJS*, 100:132.

- Ossenkopf, V. (1997). The Sobolev approximation in molecular clouds. *New Astronomy*, 2:365–385.
- Padoan, P., Juvela, M., Bally, J., and Nordlund, Å. (2000). A Comparison of  $^{13}\text{CO}$  Local Thermodynamic Equilibrium and True Column Densities in Molecular Cloud Models. *ApJ*, 529:259–267.
- Pety, J., Lucas, R., and Liszt, H. S. (2008). Imaging galactic diffuse gas: bright, turbulent CO surrounding the line of sight to NRAO150. *A&A*, 489:217–228.
- Pineda, J. E., Caselli, P., and Goodman, A. A. (2008). CO Isotopologues in the Perseus Molecular Cloud Complex: the X-factor and Regional Variations. *ApJ*, 679:481–496.
- Pineda, J. L., Goldsmith, P. F., Chapman, N., Snell, R. L., Li, D., Cambrésy, L., and Brunt, C. (2010). The Relation Between Gas and Dust in the Taurus Molecular Cloud. *ApJ*, 721:686–708.
- Planck Collaboration, Ade, P. A. R., Aghanim, N., Arnaud, M., Ashdown, M., Aumont, J., Baccigalupi, C., Balbi, A., Banday, A. J., Barreiro, R. B., and et al. (2011). Planck early results. XIX. All-sky temperature and dust optical depth from Planck and IRAS. Constraints on the “dark gas” in our Galaxy. *A&A*, 536:A19.
- Prasad, S. S. and Tarafdar, S. P. (1983). UV radiation field inside dense clouds - Its possible existence and chemical implications. *ApJ*, 267:603–609.
- Qi, C., Öberg, K. I., and Wilner, D. J. (2013).  $\text{H}_2\text{CO}$  and  $\text{N}_2\text{H}^+$  in Protoplanetary Disks: Evidence for a CO-ice Regulated Chemistry. *ApJ*, 765:34.
- Röllig, M. and Ossenkopf, V. (2013). Carbon fractionation in photo-dissociation regions. *A&A*, 550:A56.
- Roman-Duval, J., Jackson, J. M., Heyer, M., Rathborne, J., and Simon, R. (2010). Physical Properties and Galactic Distribution of Molecular Clouds Identified in the Galactic Ring Survey. *ApJ*, 723:492–507.
- Rosolowsky, E. (2005). The Mass Spectra of Giant Molecular Clouds in the Local Group. *PASP*, 117:1403–1410.
- Rosolowsky, E. and Leroy, A. (2006). Bias-free Measurement of Giant Molecular Cloud Properties. *PASP*, 118:590–610.
- Rosolowsky, E. W., Pineda, J. E., Kauffmann, J., and Goodman, A. A. (2008). Structural Analysis of Molecular Clouds: Dendrograms. *ApJ*, 679:1338–1351.
- Sanders, D. B., Solomon, P. M., and Scoville, N. Z. (1984). Giant molecular clouds in the Galaxy. I - The axisymmetric distribution of  $\text{H}_2$ . *ApJ*, 276:182–203.
- Schöier, F. L., van der Tak, F. F. S., van Dishoeck, E. F., and Black, J. H. (2005). An atomic and molecular database for analysis of submillimetre line observations. *A&A*, 432:369–379.

- Scoville, N., Kleinmann, S. G., Hall, D. N. B., and Ridgway, S. T. (1983). The circumstellar and nebular environment of the Becklin-Neugebauer object - 2-5 micron wavelength spectroscopy. *ApJ*, 275:201–224.
- Sembach, K. R., Howk, J. C., Ryans, R. S. I., and Keenan, F. P. (2000). Modeling the Warm Ionized Interstellar Medium and Its Impact on Elemental Abundance Studies. *ApJ*, 528:310–324.
- Semenov, D. (2004). Dust and gas in protoplanetary discs. *PhD Thesis, submitted to the Astrophysical Institute of the Friedrich Schiller University, Jena.*
- Semenov, D., Hersant, F., Wakelam, V., Dutrey, A., Chapillon, E., Guilloteau, S., Henning, T., Launhardt, R., Piétu, V., and Schreyer, K. (2010). Chemistry in disks. IV. Benchmarking gas-grain chemical models with surface reactions. *A&A*, 522:A42.
- Semenov, D., Pavlyuchenkov, Y., Henning, T., Wolf, S., and Launhardt, R. (2008). Chemical and Thermal Structure of Protoplanetary Disks as Observed with ALMA. *ApJ*, 673:L195–L198.
- Sheffer, Y., Rogers, M., Federman, S. R., Lambert, D. L., and Gredel, R. (2007). Hubble Space Telescope Survey of Interstellar  $^{12}\text{CO}/^{13}\text{CO}$  in the Solar Neighborhood. *ApJ*, 667:1002–1016.
- Shetty, R., Glover, S. C., Dullemond, C. P., and Klessen, R. S. (2011a). Modelling CO emission - I. CO as a column density tracer and the X factor in molecular clouds. *MNRAS*, 412:1686–1700.
- Shetty, R., Glover, S. C., Dullemond, C. P., Ostriker, E. C., Harris, A. I., and Klessen, R. S. (2011b). Modelling CO emission - II. The physical characteristics that determine the X factor in Galactic molecular clouds. *MNRAS*, 415:3253–3274.
- Shu, F. (1991). *Physics of Astrophysics, Vol. II: Gas Dynamics*. University Science Books.
- Shu, F. H., Adams, F. C., and Lizano, S. (1987). Star formation in molecular clouds - Observation and theory. *ARA&A*, 25:23–81.
- Smith, D. and Adams, N. G. (1980). Laboratory studies of isotope fractionation in the reactions of  $\text{C}/+/\text{C}$  and  $\text{HCO}/+/\text{HCO}$  with CO - Interstellar implications. *ApJ*, 242:424–431.
- Smith, I. W. M., Herbst, E., and Chang, Q. (2004). Rapid neutral-neutral reactions at low temperatures: a new network and first results for TMC-1. *MNRAS*, 350:323–330.
- Smith, R. J., Glover, S. C. O., Clark, P. C., Klessen, R. S., and Springel, V. (2014). CO-dark gas and molecular filaments in Milky Way-type galaxies. *MNRAS*, 441:1628–1645.
- Smith, R. J., Shetty, R., Beuther, H., Klessen, R. S., and Bonnell, I. A. (2013). Line Profiles of Cores within Clusters. II. Signatures of Dynamical Collapse during High-mass Star Formation. *ApJ*, 771:24.

- Smith, R. J., Shetty, R., Stutz, A. M., and Klessen, R. S. (2012). Line Profiles of Cores within Clusters. I. The Anatomy of a Filament. *ApJ*, 750:64.
- Sobolev, V. V. (1957). The Diffusion of  $L\alpha$  Radiation in Nebulae and Stellar Envelopes. *Soviet Ast.*, 1:678.
- Solomon, P. M., Rivolo, A. R., Barrett, J., and Yahil, A. (1987). Mass, luminosity, and line width relations of Galactic molecular clouds. *ApJ*, 319:730–741.
- Solomon, P. M. and Sage, L. J. (1988). Star-formation rates, molecular clouds, and the origin of the far-infrared luminosity of isolated and interacting galaxies. *ApJ*, 334:613–625.
- Sonnentrucker, P., Welty, D. E., Thorburn, J. A., and York, D. G. (2007). Abundances and Behavior of  $^{12}\text{CO}$ ,  $^{13}\text{CO}$ , and  $\text{C}_2$  in Translucent Sight Lines. *ApJS*, 168:58–99.
- Springel, V. (2005). The cosmological simulation code GADGET-2. *MNRAS*, 364:1105–1134.
- Springel, V. (2010). Smoothed Particle Hydrodynamics in Astrophysics. *ARA&A*, 48:391–430.
- Springel, V. and Hernquist, L. (2002). Cosmological smoothed particle hydrodynamics simulations: the entropy equation. *MNRAS*, 333:649–664.
- Srivastava, S. K., Chutjian, A., and Trajmar, S. (1975). Absolute elastic differential electron scattering cross sections in the intermediate energy region. I.  $\text{H}_2$ . *The Journal of Chemical Physics*, 63(6).
- Tafalla, M., Myers, P. C., Caselli, P., and Walmsley, C. M. (2004). On the internal structure of starless cores. I. Physical conditions and the distribution of  $\text{CO}$ ,  $\text{CS}$ ,  $\text{N}_2\text{H}^+$ , and  $\text{NH}_3$  in L1498 and L1517B. *A&A*, 416:191–212.
- Tielens, A. G. G. M. (2013). The molecular universe. *Reviews of Modern Physics*, 85:1021–1081.
- Tielens, A. G. G. M. and Hagen, W. (1982). Model calculations of the molecular composition of interstellar grain mantles. *A&A*, 114:245–260.
- Troland, T. H. and Crutcher, R. M. (2008). Magnetic Fields in Dark Cloud Cores: Arecibo OH Zeeman Observations. *ApJ*, 680:457–465.
- van der Tak, F. F. S., Black, J. H., Schöier, F. L., Jansen, D. J., and van Dishoeck, E. F. (2007). A computer program for fast non-LTE analysis of interstellar line spectra. With diagnostic plots to interpret observed line intensity ratios. *A&A*, 468:627–635.
- van Dishoeck, E. F. (1998). The Chemistry of Diffuse and Dark Interstellar Clouds. *The Molecular Astrophysics of Stars and Galaxies*, edited by Thomas W. Hartquist and David A. Williams. Clarendon Press, Oxford, 1998., p.53, 4:53.
- van Dishoeck, E. F. and Black, J. H. (1988). The photodissociation and chemistry of interstellar CO. *ApJ*, 334:771–802.

- van Dishoeck, E. F. and Blake, G. A. (1998). Chemical Evolution of Star-Forming Regions. *ARA&A*, 36:317–368.
- Vasyunin, A. I., Semenov, D., Henning, T., Wakelam, V., Herbst, E., and Sobolev, A. M. (2008). Chemistry in Protoplanetary Disks: A Sensitivity Analysis. *ApJ*, 672:629–641.
- Vasyunin, A. I., Semenov, D. A., Wiebe, D. S., and Henning, T. (2009). A Unified Monte Carlo Treatment of Gas-Grain Chemistry for Large Reaction Networks. I. Testing Validity of Rate Equations in Molecular Clouds. *ApJ*, 691:1459–1469.
- Vázquez-Semadeni, E. (2010). Molecular Cloud Evolution. In Kothes, R., Landecker, T. L., and Willis, A. G., editors, *The Dynamic Interstellar Medium: A Celebration of the Canadian Galactic Plane Survey*, volume 438 of *Astronomical Society of the Pacific Conference Series*, page 83.
- Vázquez-Semadeni, E., Gómez, G. C., Jappsen, A. K., Ballesteros-Paredes, J., González, R. F., and Klessen, R. S. (2007). Molecular Cloud Evolution. II. From Cloud Formation to the Early Stages of Star Formation in Decaying Conditions. *ApJ*, 657:870–883.
- Visser, R., van Dishoeck, E. F., and Black, J. H. (2009a). The photodissociation and chemistry of CO isotopologues: applications to interstellar clouds and circumstellar disks. *A&A*, 503:323–343.
- Visser, R., van Dishoeck, E. F., Doty, S. D., and Dullemond, C. P. (2009b). The chemical history of molecules in circumstellar disks. I. Ices. *A&A*, 495:881–897.
- Wakelam, V., Herbst, E., Loison, J.-C., Smith, I. W. M., Chandrasekaran, V., Pavone, B., Adams, N. G., Bacchus-Montabonel, M.-C., Bergeat, A., Béroff, K., Bierbaum, V. M., Chabot, M., Dalgarno, A., van Dishoeck, E. F., Faure, A., Geppert, W. D., Gerlich, D., Galli, D., Hébrard, E., Hersant, F., Hickson, K. M., Honvault, P., Klippenstein, S. J., Le Picard, S., Nyman, G., Pernot, P., Schlemmer, S., Selsis, F., Sims, I. R., Talbi, D., Tennyson, J., Troe, J., Wester, R., and Wiesenfeld, L. (2012). A KInetic Database for Astrochemistry (KIDA). *ApJS*, 199:21.
- Wakelam, V., Smith, I. W. M., Herbst, E., Troe, J., Geppert, W., Linnartz, H., Öberg, K., Roueff, E., Agúndez, M., Pernot, P., Cuppen, H. M., Loison, J. C., and Talbi, D. (2010). Reaction Networks for Interstellar Chemical Modelling: Improvements and Challenges. *Space Sci. Rev.*, 156:13–72.
- Walmsley, C. M., Pineau des Forêts, G., and Flower, D. R. (1999). Silicon chemistry in PDRs. *A&A*, 342:542–550.
- Watson, W. D. (1973). The Rate of Formation of Interstellar Molecules by Ion-Molecule Reactions. *ApJ*, 183:L17.
- Watson, W. D., Anicich, V. G., and Huntress, Jr., W. T. (1976). Measurement and significance of the equilibrium reaction  $C-13/+ + /C-12/O$  yields  $C-12/+ + /C-13/O$  for alteration of the C-13/C-12 ratio in interstellar molecules. *ApJ*, 205:L165–L168.

- Williams, J. P., Bergin, E. A., Caselli, P., Myers, P. C., and Plume, R. (1998). The Ionization Fraction in Dense Molecular Gas. I. Low-Mass Cores. *ApJ*, 503:689–699.
- Williams, T. and Kelley, C. e. (2011). Gnuplot 4.5: an interactive plotting program.
- Wilson, R. W., Jefferts, K. B., and Penzias, A. A. (1970). Carbon Monoxide in the Orion Nebula. *ApJ*, 161:L43.
- Wilson, T. L. (1999). Isotopes in the interstellar medium and circumstellar envelopes. *Reports on Progress in Physics*, 62:143–185.
- Wilson, T. L., Rohlfs, K., and Hüttemeister, S. (2009). *Tools of Radio Astronomy*. Springer-Verlag.
- Wolfire, M. G., Hollenbach, D., and McKee, C. F. (2010). The Dark Molecular Gas. *ApJ*, 716:1191–1207.
- Wolfire, M. G., McKee, C. F., Hollenbach, D., and Tielens, A. G. G. M. (2003). Neutral Atomic Phases of the Interstellar Medium in the Galaxy. *ApJ*, 587:278–311.
- Wolfire, M. G., McKee, C. F., Hollenbach, D. J., and Tielens, A. G. G. M. (1993). Multiphase Structure of the Galactic Halo. In *American Astronomical Society Meeting Abstracts*, volume 25 of *Bulletin of the American Astronomical Society*, page 114.03.
- Yang, B., Stancil, P. C., Balakrishnan, N., and Forrey, R. C. (2010). Rotational Quenching of CO due to H<sub>2</sub> Collisions. *ApJ*, 718:1062–1069.
- Yonekura, Y., Asayama, S., Kimura, K., Ogawa, H., Kanai, Y., Yamaguchi, N., Barnes, P. J., and Fukui, Y. (2005). High-Mass Cloud Cores in the  $\eta$  Carinae Giant Molecular Cloud. *ApJ*, 634:476–494.
- Yoshida, N., Abel, T., Hernquist, L., and Sugiyama, N. (2003). Simulations of Early Structure Formation: Primordial Gas Clouds. *ApJ*, 592:645–663.
- Zaragoza-Cardiel, J., Font, J., Beckman, J. E., García-Lorenzo, B., Erroz-Ferrer, S., and Gutiérrez, L. (2014). Two physical regimes for the giant H II regions and giant molecular clouds in the Antennae galaxies. *MNRAS*, 445:1412–1423.
- Zuckerman, B., Turner, B. E., Johnson, D. R., Lovas, F. J., Fourikis, N., Palmer, P., Morris, M., Lilley, A. E., Ball, J. A., and Clark, F. O. (1975). Detection of interstellar trans-ethyl alcohol. *ApJ*, 196:L99–L102.



## ACKNOWLEDGMENTS

First of all, I would like to thank to my supervisor, Simon Glover, for his support, patience, efforts and encouragement over this past three years. I would also like to express my gratitude to Dmitry Semenov, to whom I could always turn to with chemistry related questions and to Kees Dullemond, who taught me a lot about radiative transfer, hydrodynamics, planet formation and scientific thinking in general. I am grateful to them and to Ralf Klessen for the opportunity to work on this project and to be a member of ITA.

I am grateful to my colleagues, Paul Clark, Volker Gaibler, Nanase Harada, Jens Kauffmann, Ralf Klessen, Ágnes Kóspál, Helen Morrison, Johan Olofsson, Ilaria Pascucci, Thushara Pillai, Jon Ramsey and Rahul Shetty for their guidance and collaboration, the fruitful discussions and their interest in my work. I also owe thanks to my previous advisers, Dániel Apai, Ilaria Pascucci and József Vinkó for their continuous trust in me and for their support over the years. Special thanks to Jon and Volker for our always inspiring conversations about scientific data visualization, programming practices, linux desktop environments, philosophy and politics, these truly changed my outlook on the World.

Furthermore, I thank Simon Glover, Helen Morrison and Nanase Harada for proofreading this thesis. They helped a lot in improving the text and the scientific content and I truly appreciate that they were available for this even on a short notice. I am also indebted to Volker Gaibler for his prompt help in the German translation of the abstract. I am grateful for Thomas Henning, Matthias Bartelmann and Eva Grebel in my thesis committee for taking their time with this thesis.

The project would have not been possible without the financial support of the Deutsche Forschungsgemeinschaft through the SFB 881 project, "The Milky Way System", subproject B3. I am also grateful for the conscientious work of Christian Fendt, and that I could have enjoyed the social connections, professional advices, tasty barbecues and the fun retreats that the IMPRS Heidelberg offered.

The warm atmosphere in the basement office, the weekly board gaming sessions, the Thursdays spent fighting sorcerer kings in the world of Athas and the frequent hikes and travels, even the occasional flat painting projects made my time in Heidelberg really memorable and enjoyable. Helen, Fredrik, Maria, Mei, Svitlana, Christian, Joanna, Wini, Jon, Volker, Nanase, Sebastian and Örs, thank you for these good times and for your friendship. I would like to dedicate this thesis to you all.

Finally, I would also like to say thanks to those who I left behind in Hungary and who welcomed me back at those rare occasions when I visited them; to Nóra, Gábor, Balázs and to my family.